Additive Manufacturing of Engineered Polymeric Flexible Structures

by

Ajay Jayswal

A dissertation submitted to the Graduate Faculty of
Auburn University
in partial fulfillment of the
requirements for the Degree of
Doctor of Philosophy

Auburn, Alabama
August 5, 2023

Keywords: Additive manufacturing (AM), fabrics, finite element modeling, composite filament, viscoelasticity, creep modeling

Approved by

Sabit Adanur, Chair, Professor of Mechanical Engineering, Auburn University
Dan Marghitu, Professor of Mechanical Engineering, Auburn University
Nima Shamsaei, Professor of Mechanical Engineering, Auburn University
Russell Mailen, Assistant Professor of Aerospace Engineering, Auburn University
Jordan Roberts, Senior Lecturer of Mechanical Engineering, Auburn University
University Reader: Anwar Ahmed, Professor of Aerospace Engineering, Auburn University

Abstract

Polymer-based additive manufacturing (AM) processes allow the flexibility, rapid, and low-cost fabrication of complex geometries. In recent years, fused filament fabrication (FFF), also known as fused deposition modeling (FDM) has attracted the attention of researchers to fabricate flexible fabric structures. Several researchers attempted to additively manufacture fabric structures, but the mechanical property evaluation was not performed due to the complexity of the geometry and the loading difficulty on the testing fixture. In addition, poly(lactic) acid (PLA) is mostly explored. It is brittle in nature and has elongation at break in the range of 2.5 – 6.0 %, which limits its application in fabrics and fashion industries. In this context, this dissertation deals with the design, additive manufacturing, and mechanical properties characterization of fabric structures. In addition, it discusses the manufacture and characterization of novel composite filaments to use in FDM. The creep behavior of 3D printed composite filaments is also modeled.

In chapter 3, the design, 3D printing and analysis of mechanical and microstructural behavior of interlaced fibrous structures were assessed. It was found that the mechanical strength is higher in warp direction as compared to that of in weft direction for 2/1 twill weave fabrics. The flexural strength of weft knitted fabrics is lower in course direction. The cylindrical braids are capable of holding compressive displacement of more than 25 mm. The printed samples contained voids which decreased the mechanical strength.

In chapter 4, the effect of heat treatment on 2/1 twill weave fabrics and dog-bone samples were studied. They were compared in terms of mechanical properties and crystallinity. The crystallinity of both samples improved significantly when they were heat treated at temperatures above the glass transition temperature (T_g) of the material. But an improvement in mechanical properties of twill weave fabric was not observed whereas they were improved for dog-bone samples.

In chapter 5, a multi-physics computational model is utilized to study a coupled thermo-mechanical-viscoelastic properties of 3D printed plain weave fabrics at and above T_g. The temperatures considered for this study are 60 ℃, 65 ℃, and 70 ℃, and the viscoelastic properties is represented by a Prony series. In this study, unit cells were 3D printed, and then using dynamic mechanical analysis (DMA), the tensile and compression tests were conducted in a closed thermal environment at temperatures mentioned above. The computational analysis was performed in ABAQUS simulation software, and the results were compared with the

experimental results. The relative error percentages in the peak forces at each temperature were 23.60% at 60 ℃, −8.85% at 65 ℃, and – 6.25% at 70 ℃. A better agreement in peak forces was seen for unit cells above T_g. The computational model developed for unit cells was used to predict the thermo-mechanical-viscoelastic response of large additively manufactured fabric structures which is difficult to evaluate experimentally.

In chapter 6, composite filaments using PLA and TPU were manufactured using twin-screw and single-screw extruders. Different material characterization methods were utilized to study the material properties of the composite filaments. The tensile stress and Young's modulus of the filaments decreased whereas the elongation increased by more than 500 %. The crystallinity of the materials were increased which were studied using differential scanning calorimetry (DSC) and polarized optical microscope (POM). The analysis also showed a partial miscibility of the polymer constituents.

In chapter 7, the effect of a plasticizer on mechanical, thermal, chemical, and morphological properties were studied. Poly(ethylene) glycol (PEG) was used as a plasticizer in PLA/TPU composition. It was found that although the yield stress decreased, the ultimate tensile stress of the filaments did not show a drop in their values. This might have happened due to the plasticizing effect of PEG. Finally, the composite filament was used to 3D print a plain weave fabric structure which demonstrates its feasibility in 3D printing applications.

The last chapter of this dissertation discusses the creep behavior and computational modeling of 3D printed composite filaments. The composite filaments were used to 3D print creep samples. The creep test was performed under a constant tensile load of 100 N. A computational model is developed using the Generalized Voigt-Kelvin solid model and three terms in the Prony series. The experimental results and computational results were compared and found that the maximum error is approximately 6 %. This proved the reliability of the model developed and can be used to predict creep response of similar polymers.

Keywords: Additive manufacturing, polymers, fabrics, heat treatment, crystallinity, multi-physics finite element modeling, composite filament, material characterization, creep modeling.

Acknowledgements

I would like to thank my Ph.D. advisor, Dr. Sabit Adanur for his supervision during my Ph.D. study. He gave me freedom to explore my ideas and learn by failure and success methodology. This learning has boosted up my confidence to work as an independent researcher starting from generating the ideas, finding the research gaps, design of methodologies, conducting the experiments, computational modeling, and presenting the results. I am also thankful to him for allowing me to work on the design of novel facemasks to fight against the COVID-19 pandemic and teaching me the way to contribute, being a researcher, to unforeseeable future epidemics/pandemics.

I would also like to thank Dr. Dan Marghitu, Dr. Nima Shamsaei, Dr. Russell Mailen, and Dr. Jordan Roberts for serving on my committee and providing me the valuable suggestions to improve the quality of this dissertation. I am very thankful to Dr. Russell Mailen for teaching me the computational modeling stuffs. It would not have been possible to conduct the research mentioned in Chapter 5 without his help. He is very intelligent and well informed in computational modeling of polymers. I must thank Dr. Anwar Ahmed, professor of Aerospace Engineering, for serving as a university reader and providing me the useful comments regarding this dissertation.

I am very grateful to the Department of Mechanical Engineering for supporting my Ph.D. journey and providing me with the opportunity to work as a Graduate Teaching Assistant (GTA) during my whole Ph.D. study at Auburn. The GTA role taught me how to teach in the classroom, deliver the lecture notes, interact with the students, public speaking, grading assignments, and projects, and providing feedbacks. I am also grateful to the Interdisciplinary Center for Advanced Manufacturing Systems (ICAMS) located in the Department of Industrial and Systems Engineering for providing me the Research Assistant (RA) position and financial support for my research for 1 year starting from 8 May 2022 to 7 May 2023. This support accelerated my working pace and helped me complete chapter 5, chapter 7, and chapter 8 within 1 year. Specifically, I would like to thank Dr. Jia Liu and Dr. Gregory Harris for believing in me and providing me with the opportunity to work with ICAMS.

I would also like to thank Dr. Ramsis Farag for teaching me the mechanical properties characterization methods on Instron such as tensile, bending, and flexural tests. Most of the tests were conducted at the Center for Polymers and Advanced Composites (CPAC) lab, and I am really obliged to the center because this research would have been impossible to complete without their help.

Moreover, I am thankful to my friends Lokesh Silwal, Ashutosh Mishra, Arun Poudel, and all other friends who supported me directly and indirectly. They supported me and helped me overcome tough times and made my stay pleasant at Auburn. I am also thankful to Dr. Nima Alizadeh, Dr. Archana Bansode, Dr. Yuyang Wang, Debabrata Mondal, and Syed Hassan Shah for their help during my Ph.D.

Finally, I express my gratitude to my parents, and all my dear family members including Nilam, Kayara, Bijay, Sarita, Sanjay, Arati, Akriti, Amrit, and Sushant. They have supported me unconditionally. Whenever I felt emotionally broken, I talked with them, and it helped me raise again. Without their love, support and understanding, I would never finish my Ph.D.

Table of Contents

List of Tables

List of Figures

List of Abbreviations

ABS	Acrylonitrile butadiene styrene
AM	Additive manufacturing
AMPS	Acrylamido-2-methylpropanesulfonate
ANOVA	Analysis of variance
ASTM	American Society for Testing and Materials
CAD	Computer aided design
CD	Cross-print direction
DB	Dog bone
DH	Degree of hydrolysis
DIW	Direct ink writing
DMA	Dynamic mechanical analysis
DMF	N,N-dimethylformamide
DN	Double network
DSC	Differential scanning calorimetry
DTG	Derivative thermogravimetric
ED	Energy density
EPA	Environmental protection agency
FDM	Fused deposition modeling
FDT	Final thermal degradation temperature
FEA	Finite element analysis
FEM	Finite element modeling
FFF	Fused filament fabrication
FH	Fully hydrolyzed
FTIR	Fourier transform infrared spectroscopy
GF	Glass fiber
HCH	Heat-cool-heat
HDA	Hexadecylamine
HS	Hard segments
HT	Heat treatment
HTPLA	High-temperature polylactic acid
ISO	International Organization for Standardization

MBAA	N,N′-methylenebis(acrylamide)
MDI	diphenylmethane-4.4-diisocyanate
MFI	Melt flow index
MW	Molecular weight
NHT	Non-heat-treated
NRDC	Natural Resources Defense Council
OM	Optical microscope
PBF	Powder bed fusion
PC	Polycarbonate
PD	Print direction
PDI	Polymer dispersity index
PDLA	Poly-D-lactic acid
PDMS	Polydimethyl-siloxane
PEBA	Polyester block amide
PEEK	Polyether ether ketone
PEG	Poly(ethylene) glycol
PEO	polyethylene oxide
PLA	Poly(lactic) acid
PLLA	Poly-L-lactic acid
PMMA	Poly(methyl methacrylate)
POE	polyoxyethylene
POM	Polarized optical microscope
PP	Polypropylene
PS	Polystyrene
PTMG	Poly(tetramethylene glycol)
PVA	Poly(vinyl) alcohol
RVE	Representative volume element
SAN	Styrene-acrylonitrile
SEM	Scanning electron microscope
SLM	Selective laser melting
SLS	Selective laser sintering
SS	Soft segments
STL	Standard Tessellation Language or STereoLithography

TG	Thermogravimetric
TGA	Thermogravimetric analysis
THF	Tetrahydrofuran
TPU	Thermoplastic polyurethane
TTSP	Time-temperature superposition principle
UTS	Ultimate tensile stress
WLF	Williams-Landel-Ferry

Chapter 1
Introduction

1.1. Background

Fabrics are one of the most demanding needs of human beings. With the increasing sophistication of the modern world, the demand has been increasing with everchanging property requirements in every industry including architecture, construction, composites, filtration, geosynthetics, medicine, military and defense, papermaking, safety and protection, sports and recreation, transportation, and agriculture. The current fabric manufacturing methods have some major issues: (i) long manufacturing times, (ii) requirements for highly skilled workers, (iii) large production areas and storage space, (iv) cost, and (v) post consumption solid waste production.

Traditional fabric manufacturing process starts with the production of fibers from polymers using one of the 3 fiber spinning processes: melt spinning, dry spinning, and wet spinning. Then, a number of fibers are spun together to form a yarn with one of the 4 yarn spinning methods: ring spinning, open-end (rotor) spinning, air-jet spinning and friction spinning. The yarns are combined in a certain pattern to obtain fabrics in which the interlacing, interloping and entanglement pattern determines the structure and properties of the fabrics. The main fabric production methods are weaving, knitting, braiding, tufting and nonwoven manufacturing [1][2]. Hence, the whole process consumes a lot of time to produce fabrics. Similarly, a huge number of workers are required at every stage starting from fiber production to yarn manufacturing to design of fabrics to production of fabrics. In general, for different fabric designs, different machines and different skilled workers are required. Moreover, it requires large and complex machinery which occupies large spaces. Fabric manufacturing is also a chemical-intensive process and requires a high volume of water throughout its operations. Textile plants produce textiles solid wastes, wastewater containing different pollutants, and billions of tons of soot. According to the United States Environmental Protection Agency (EPA), the textile solid waste generation was 17.05 million tons in 2018, out of which more than 11.29 million tons were landfilled [3]. According to Natural Resources Defense Council (NRDC) website, the apparel industry is one of the biggest polluters on the planet. Textile mills generate one-fifth of the world's industrial water pollution and use 20,000 chemicals, many of which are carcinogenic, to make clothes [4]. These wastes cause a negative

impact on the environment and therefore, there have been increasing concerns regarding the disposal of fabric waste around the globe.

The above-mentioned problems can be resolved by continuously working on research projects for an alternative method of fabric manufacturing and studying different materials useful for production. To make fabric manufacturing sustainable, a scientific selection of materials and manufacturing methods become important. Although traditional fibrous structure manufacturing has advanced the industrial revolution, it holds shortcomings as discussed above, and as an alternative, additive manufacturing or 3D printing method should be explored in this important area. 3D printing is not just a mere emerging technology but also has the potential to become a truly transformative technology within the near future. Its ability to build almost any designable object increases efficiency, reduces waste, and makes manufacturing more sustainable. The time it takes for the products to get to the markets is much shorter because it eliminates most of the time-consuming processes in the design and manufacturing stages of fibrous structure.

1.2. Objectives

The research outline is divided into two parts with their own specific objectives as shown in Figure 1.1. The proposed works will contribute to the additive manufacturing, materials, and textile industry as a whole towards the development of future fabrics.

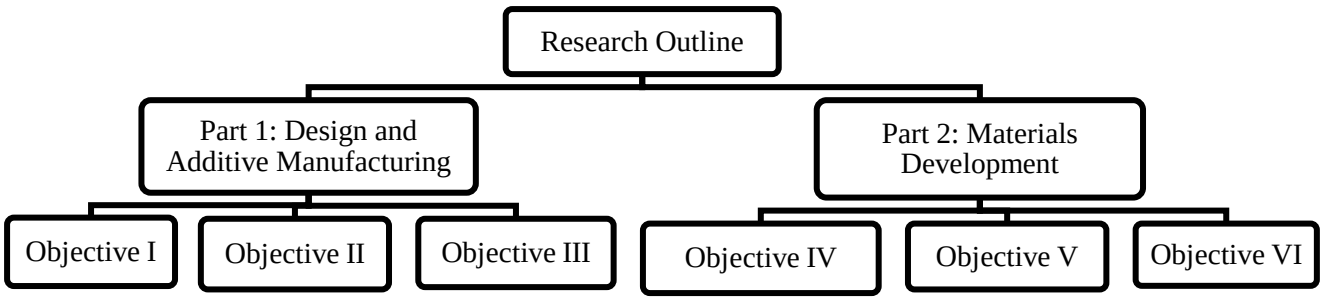

Figure 1.1. Research outline.

The objectives are described below.

I. Design and additive manufacturing of interlaced fibrous structures.

II. Study the effect of heat treatment on crystallinity and mechanical properties of 3D printed structures.

III. Computational modeling of 3D printed woven fabrics.

IV. Manufacturing of PLA/TPU composite filaments for 3D printing

V. Effect of a plasticizer on PLA/TPU composite filaments .

VI. Modeling creep behavior of 3D printed structures using composite filament.

Objective I. Design and additive manufacturing of interlaced fibrous structures

The goal of this objective is to design, 3D print and analyze mechanical as well as microstructural behavior of interlaced fibrous structures. A series of plain weave, twill weave, weft-knitted and braided fabric structures are designed using computer-aided design (CAD) software, Solidworks and 3D printed using Fused Deposition Modeling (FDM) machine to determine the best model that could be printable. The structures are designed in such a way that the fabricated yarns with pure polylactic acid (PLA) are not sticking to each other in the plain weave and twill weave fabric structure. The plain weave, twill weave and braided fabric specimens are printed in vertical orientation and weft-knitted structure in horizontal orientation. Tensile and three-point bending (flexural) tests are conducted for twill weave and weft-knitted fabrics whereas compression test is performed for braided structures. Optical microscope is used to study the microscopic structures of the yarns and fabric structures.

Objective II. Study the effect of heat treatment on crystallinity and mechanical properties of 3D printed structures.

The goal of this objective is to 3D print 2/1 twill weave fabric structures using poly (lactic) acid (PLA) and study the effect of heat treatment on crystallization and mechanical behavior. The printed samples are heat–treated in a temperature–controlled lab oven at different temperatures for 1 hour and then allowed to cool slowly in the oven by a process called furnace cooling. The samples are heat–treated at 50 ℃, 75 ℃, 100 ℃, and 125 ℃ for 1 hour. The mechanical properties and crystallinity of twill weave fabrics are studied. For comparison, an ASTM standard dog-bone specimen is 3D printed, heat-treated using the identical conditions as that of twill weave fabrics. Its crystallization and mechanical behaviors are studied as well.

Objective III. Computational analysis of 3D printed woven fabrics.

The goal of this objective is to study the coupled thermo-mechanical-viscoelastic behavior of additively manufactured plain weave fabrics at and above glass transition temperature (T_g) using a multi-physics finite element model. Unit cells of plain weave fabrics are additively manufactured using poly(lactic) acid (PLA). Tensile and compression tests were performed in a thermal environment using dynamic mechanical analysis (DMA). The experimental results are compared with that of computational results; good agreement between them is observed, with an error percentage in peak forces having approximately 24% at 60 ℃, -9% at 65 ℃ and

-6% at 70 ℃. The computational model developed for unit cells is used to predict the coupled thermo-mechanical-viscoelastic response of large additively manufactured fabric structures which is difficult to evaluate experimentally.

Objective IV. Manufacturing of PLA/TPU composite filaments for 3D printing.

The goal of this objective is to manufacture a composite filament having high mechanical strength and high flexibility. Polylactic acid (PLA) and thermoplastic polyurethane (TPU) pellets are blended using the twin–screw and single–screw extruders, and novel composite filaments have been obtained. The amounts of TPU polymer in the blend are 10 wt%, 20 wt%, 30 wt%, and 40 wt% of the total weight of the respective composition. The filaments manufactured have varying diameters but the filaments having diameter in the range of 1.60 mm to 1.90 mm were used for the analyses. The properties are characterized by using several analytical instruments such as tensile test, differential scanning calorimetry (DSC), thermogravimetric analysis (TGA), dynamic mechanical analysis (DMA), Fourier transform infrared spectroscopy (FTIR), polarized optical microscope (POM), rheology, and scanning electron microscopy (SEM). Finally, the TPU_30 (PLA – 70% and TPU – 30%) filament is used to 3D printed plain weave fabric structure using the fused deposition modeling (FDM) method which demonstrated the feasibility of these filaments to be used in 3D printing of fabrics.

Objective V. Effect of a plasticizer on PLA/TPU composite filaments.

The goal of this objective is to study the effect of a plasticizer such as poly(ethylene) glycol (PEG) on the properties of PLA/TPU composite filaments. The amount of TPU content in the composition is kept constant either being 30% or 40%. PLA and PEG are added in varying weight percentages. The filaments produced had varying diameters, but the diameter in the range of 1.70 mm to 1.80 mm is considered for this study. The properties of the filaments are studied using various material characterization methods such as uniaxial tensile test, differential scanning calorimetry (DSC), thermogravimetric analysis (TGA), dynamic mechanical analysis (DMA), Fourier transform infrared spectroscopy (FTIR), and scanning electron microscope (SEM).

Objective VI. Creep modeling of 3D printed structures using composite filaments.

The goal of this objective is to experimentally characterize and computationally model the creep behavior of 3D printed samples using the composite filaments. The composite filaments are employed in the 3D printing of creep samples. The samples are tested under a constant

tensile load of 100 N. The computational model is developed by using the Generalized Voigt-Kelvin solid model and three terms in Prony series. The experimental creep displacements and strains are compared with computational results, and a good agreement between them is observed. The maximum error percentages in computational result is approximately 6 % as compared to the experimental result. Hence, the computational model developed is reliable and can be used to study the creep behavior of similar polymers and polymer composites.

1.3. References

[1] Sabit. Adanur, *Handbook of Weaving*. Technomic Publishing Co. Inc., 2001.

[2] S. Adanur, "Wellington Sears Handbook of Industrial Textiles," Technomic Publishing Co. Inc., 1995, pp. 273–294.

[3] United States Environmental Protection Agency, "Facts and Figures about Materials, Waste and Recycling," 2022. https://www.epa.gov/facts-and-figures-about-materials-waste-and-recycling/national-overview-facts-and-figures-materials#Landfilling (accessed Sep. 03, 2022).

[4] NRDC, "Encourage Textile Manufacturers to Reduce Pollution." https://www.nrdc.org/issues/encourage-textile-manufacturers-reduce-pollution#:~:text=Textile mills generate one-fifth,by burning coal for energy (accessed Sep. 05, 2022).

Chapter 2

Literature review

(Jayswal, A., and Adanur, S., *"An overview of additive manufacturing methods, materials, and applications for flexible structures",* Journal of Industrial Textiles, vol. 52, pp. 1-42, 2022)

Abstract

Various types of additive manufacturing (AM) methods (also called 3D printing), and materials have been increasingly studied in the field of additive manufacturing of flexible structures such as fabrics, and flexible electronics. Polymer-based AM processes allow the flexibility, rapid, and low-cost fabrication of complex geometries depending on the types of materials used. The purpose of this literature review is to summarize the major AM methods, materials, and their emerging applications to additively manufacture the flexible structures. In the AM methods section, Fused Deposition Modeling (FDM), and Selective Laser Sintering (SLS) are reviewed for fabrics, and Direct Ink Writing (DIW) for electronics. In the Materials section, the manufacturing methods, chemical structures, properties, advantages, and limitations of some of the widely used materials in three-dimensional (3D) printing of polymers are reviewed. Third, the applications of these methods and materials for fabrics and electronics are covered. Finally, the associated opportunities and challenges in 3D printing process of flexible structures are described. The future research should be related to the exploration of combinations and development of innovative materials, printing process parameters, detail study on improving the properties, and hybrid 3D printing process.

2.1. Introduction

The international standard ISO/ASTM 52900 defines additive manufacturing (AM) as a "process of joining materials to make parts from three-dimensional (3D) model data, usually layer upon layer" [1]. AM methods are classified into seven categories: material extrusion, material jetting, binder jetting, sheet lamination, vat photopolymerization, powder bed fusion, and directed energy deposition [1]. These methods are further classified into sub-categories depending on the type of materials used and the process of material deposition. The materials may be in the form of powder, filaments, liquid, hydrogels or ink, and sheets [2]. In this method of manufacturing, materials are added layer upon layer forming a 3D solid object. A computer-aided-design (CAD) model is developed and sliced into several layers by using slicing software. The generated model is saved as 'g-code' which is finally used by the 3D printers to

produce the solid object. The schematic diagram showing the working principle of AM processes using unit material is shown in Figure 2.1.

The conventional manufacturing methods such as subtractive machining, casting, forging, and powder metallurgy [3][2] take longer time and produce waste. As a result, the cost of fabrication and final product becomes higher whereas AM methods fabricate the parts in a minimal time with little or no wastes [2][4][5]. Another aspect is the diverse forms of material availability, which is accelerating its applications in many industries and becoming an integral part of modern product development [4][6]. AM methods are mostly used in automotive, aerospace, textiles, pharmaceuticals, medical, tissue engineering, flexible electronics, and sensors. This has increased the competition in the world economy [7].

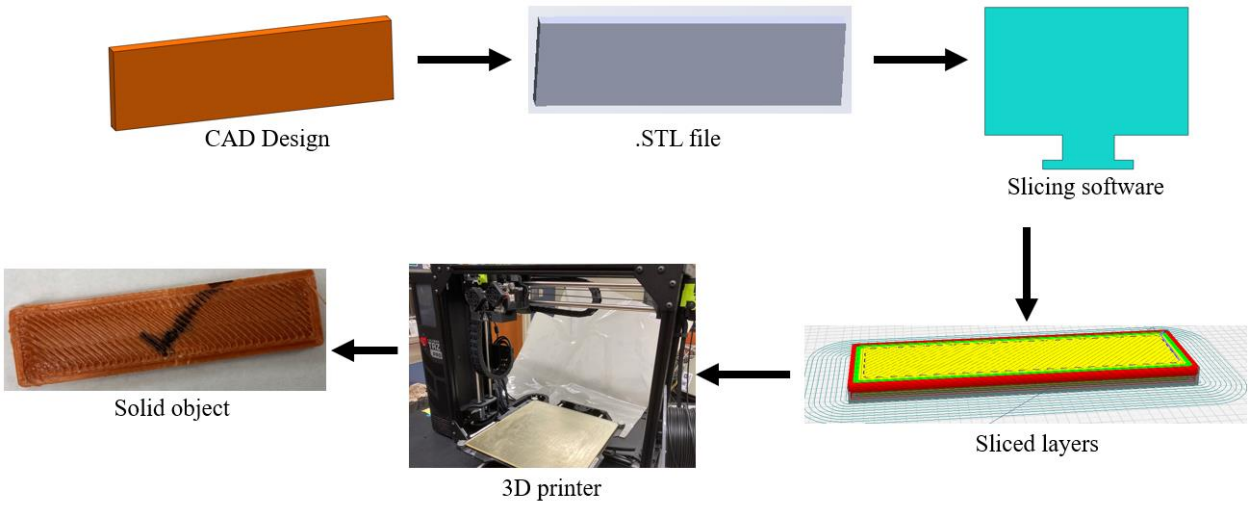

Figure 2.1. Schematic diagram of working principle of additive manufacturing process (Modified after ref. [8].)

In recent years, AM methods have attracted attention to fabricating flexible structures such as fabrics and flexible electronics. The main conventional methods of fabric production are weaving, knitting, braiding, tufting and nonwoven manufacturing [9]. Among all these methods, weaving is the most common method, in which warp and weft yarns are interlaced in a defined pattern. A particular fabric manufacturing method is used according to the required fabric design. All the traditional fabric manufacturing processes consume a lot of time and generate wastes. This is one of the reasons that has attracted the attention of AM researchers. Similarly, the research on flexible and wearable electronics is fascinating. 3D printing has made it possible to integrate functional electrical/electronic components into 3D printed products, such as sensors, and circuits. The expansion of 3D printing has opened the way for exciting

new applications, and opportunities. It has been possible to 3D print stretchable, flexible, and bio-compatible electronic devices which can be adjusted over irregularly shaped mounting surfaces. In summary, AM has offered great potential and unique capabilities to fabricate parts with multiple functionalities [10][11][12][13].

This chapter is organized into different sections. In the Additive Manufacturing (3D Printing) Methods section, the working principles and schematic diagrams, advantages, limitations, prospective applications, and summary of the three methods that are the most widely used for 3D printing of flexible structures are described. In the Materials section, the production, chemical compositions and structures, properties, advantages, and limitations of the materials are presented. The Applications section is divided into two parts. The first part covers the application of 3D printing methods to produce flexible fabric structures, whereas the second part includes the 3D printing methods to produce flexible electronic structures. The associated challenges and future opportunities are discussed as well.

2.2. Additive Manufacturing (3D Printing) Methods

With the advancements of AM technology, its applications have been widely explored in various fields. Different methods are exploited by researchers, manufacturers, and innovators. Some of the methods that are used in 3D printing of flexible structures such as fabrics, sensors, and electronics are briefly discussed in this section. The methods reviewed in this chapter are highlighted in Figure 2.2. FDM and SLS methods are reviewed for 3D printing of fabrics, and DIW for 3D printing of flexible electronic components.

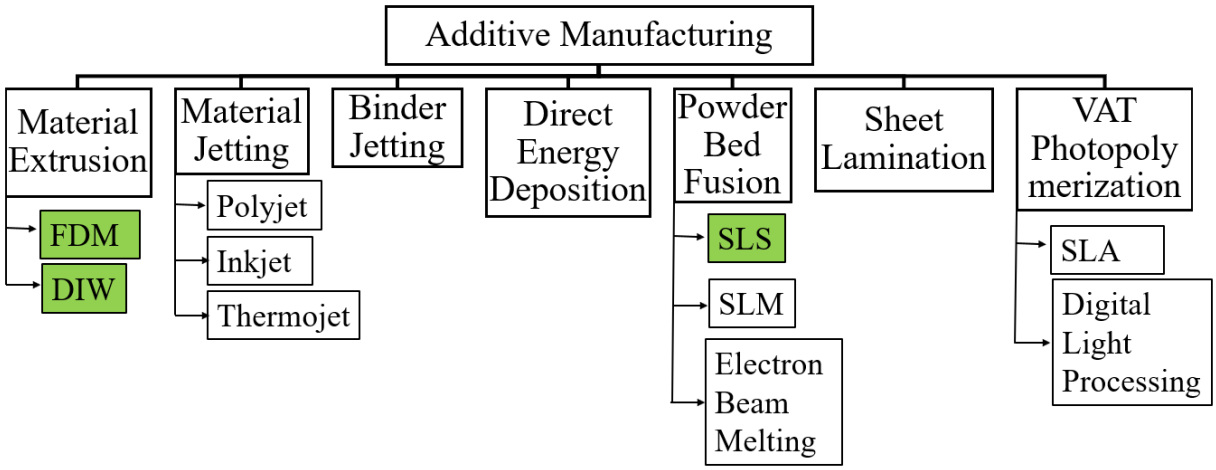

Figure 2.2. Summary of different additive manufacturing methods.

2.2.1. Fused Deposition Modeling (FDM)

FDM method works on the principle of material extrusion as shown in Figure 2.3. In this method, a thermoplastic polymer is melted and then extruded through a nozzle on a build platform. The movement of the nozzle depends on the program (g-code) generated by the slicing software for a specific design. The melted polymer is deposited layer by layer and produces the three-dimensional (3D) object. For structures having hanging parts, water or chemical dissolvable support material is used. Although the AM process produces near-net-shape products, sometimes, it may require post-processing such as support removal, cleaning, and finishing. Post-processing usually improves the properties and aesthetic of the products. Few examples of materials which are commonly used in this technique are poly(lactic) acid (PLA), acrylonitrile butadiene styrene (ABS), thermoplastic polyurethane (TPU), polypropylene (PP), nylon, polycarbonate, polyether ether ketone (PEEK), ULTEM, glass and metals [14] [15].

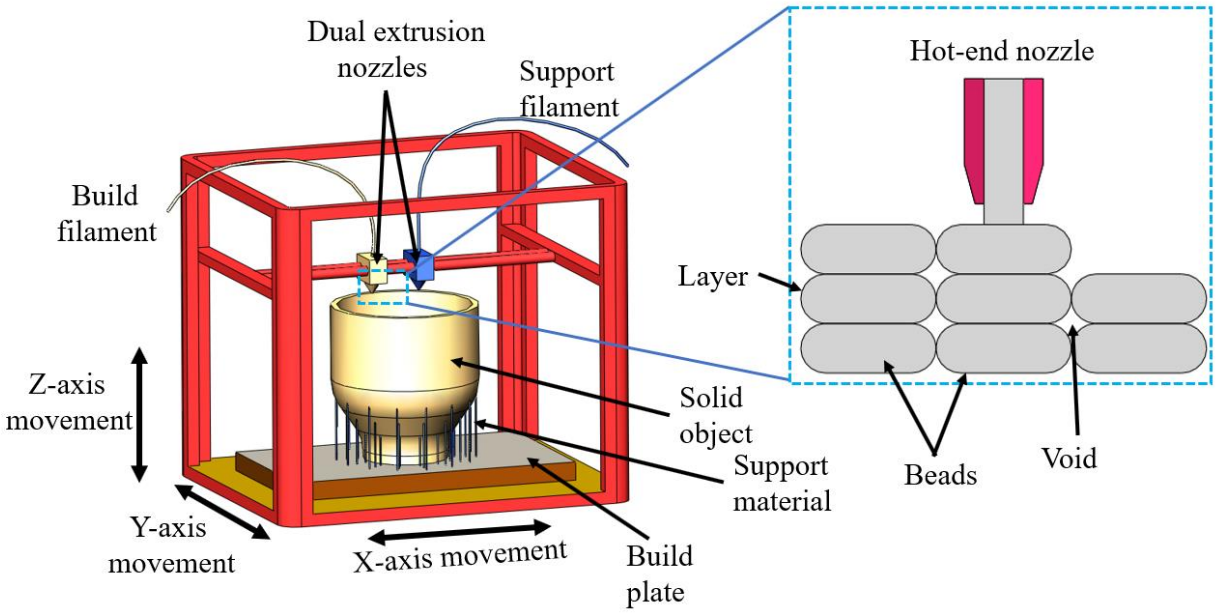

Figure 2.3. Schematic of fused deposition modeling (FDM) method employed to 3D print a cup with support materials.

The main advantages of this method are processability of a wide variety of materials, low maintenance costs, no toxic chemicals involved, rapid production, overall tolerance of 0.1 mm, and easy material change. The main disadvantages are surface roughness, relatively slow process, restricted dimensions, appearance of voids and lower mechanical properties [16].

Some of the approaches to overcome these disadvantages are optimization of 3D printing process parameters and using polymer composite filaments.

Process parameters include layer thickness, raster angle, print orientation, print temperature, infill pattern and density, and others. Durgun and Ertan [16] found that raster angle and orientation affected the surface roughness, mechanical properties, and production costs. In particular, the build orientation exhibited a significant effect on surface roughness and mechanical properties of the parts rather than the raster angle. Poor surface quality caused by stair-stepping effect is generally seen in layer manufacturing processes. Several studies show that a smaller layer thickness can bring lower surface roughness but this can increase the production time [17] [18]. Chacón, et. al. [19] investigated the effects of build orientation, layer thickness and feed rate on the strength of 3D printed parts. They found that vertical print orientation showed the lowest mechanical properties whereas on-edge and flat orientations the highest. They also observed an increase in mechanical properties with increasing layer thickness and decrease with increasing feed rate for upright orientation whereas the layer thickness and feed rate play insignificant role for on-edge and flat orientations.

Several researchers investigated the effect of heat treatment on mechanical properties of 3D printed parts. This method could increase the bonding between the layers and rasters. Avila et. al. [20] worked on 3D printing of parts using different materials such as PC, PMMA, and PEEK and investigated the effect of heat treatment at 90% of glass-transition temperature on their mechanical properties. They found an improvement in tensile strength of about 10 MPa for PC, 20 MPa for PMMA and a slight change for PEEK. Yang et al. [21] studied various thermal processing conditions in 3D printing of PEEK materials and found that different degrees of crystallinity and mechanical properties can be found.

Kaynak and Varsavas [22] examined the mechanical performance of neat PLA, glass fiber (GF)-reinforced PLA, and TPU-blended PLA composites using injection molding and 3D printing methods. They used twin-screw extruders and manufactured composite filaments for 3D printing using 10 wt% of TPU and 15 wt% of GF in PLA matrix. Using the filaments obtained, they 3D printed dog-bone specimens and compared their performance with the dog-bone samples obtained from injection molding. They did not find significant differences in their strength obtained from tensile and flexural tests. However, they noticed that the elastic modulus values of 3D printed specimens were slightly higher than that of injection molded specimens due to the stiffening action of the slightly textured structure formed during 3D-printing.

2.2.2. Direct Ink Writing (DIW)

Direct ink writing is a 3D printing method based on the principle of material extrusion as shown in Figure 2.4a; it is also known as Robocasting. As its name suggests, the material used in this method is in the "ink" form, which is a highly viscous liquid, and has the ability to retain its shape after deposition. Although it operates on a similar principle as FDM, it has a major difference that it does not depend on drying or solidification of deposited material to retain the shape when the ink exits the nozzle. A different variety of materials or a combination of materials can be used ranging from ceramics, plastics, and food to living cells. Hence it is an extremely versatile technology. Post-processing such as drying, heating or sintering may be required to harden the printed part and improve its mechanical properties [15] [23] [24].

This printing method follows three steps: 3D design, generation of a path file for nozzle and extrusion of ink. After the completion of the 3D model in CAD software, the 2D layer-by-layer or 3D movement path profile for nozzle is generated and exported to the printer. The nozzle moves in a 2D path of each layer generated by the slicing software and deposits the ink layer-by-layer and subsequently builds the 3D object. Alternatively, a 3D object can be printed directly by the movement of nozzle in three dimensions which does not involve a layer-by-layer approach. This method demands specific material strategies to hold the printed structure after deposition. The strategies are: (i) to deploy the intrinsic properties of ink such as the facile oxidation and solidification of liquid metal filaments in air, which can help maintain the 3D structures, and (ii) to fabricate 3D object within a supportive matrix [13] [25] [26].

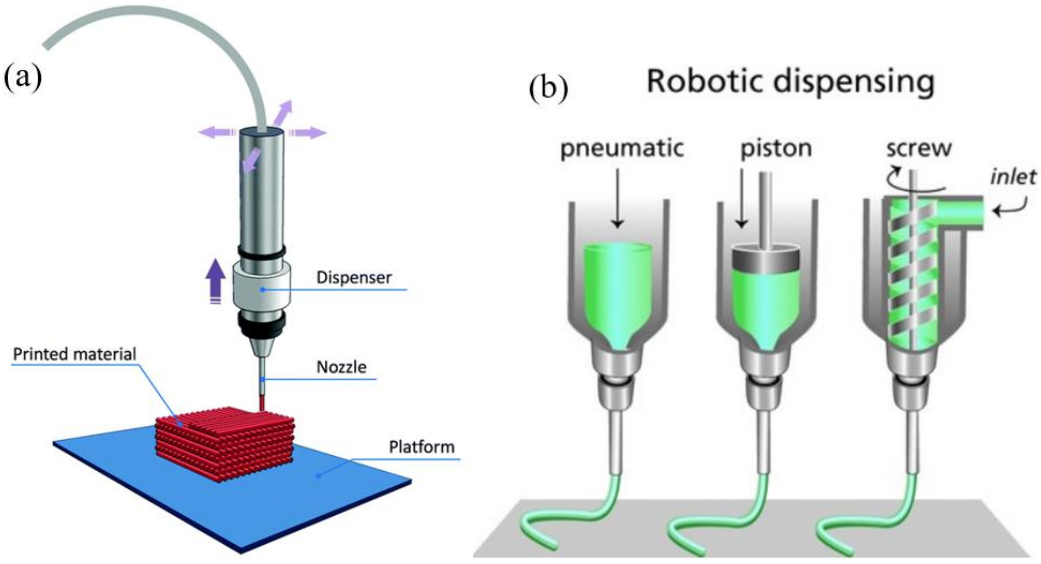

Figure 2.4. (a) Schematic of direct ink writing process [23] (Reproduced with permission from ref. [23]. Copyright John Wiley and Sons.), and (b) Different dispensers used in DIW process [24] (Reproduced with permission from ref. [24]. Copyright Wiley-VCH GmbH.)

Depending on the type of material, viscosity and density of ink, and particle size within, the type of dispenser is selected to push the ink through the nozzle. Some common dispensers available are pneumatic, piston, and screw as shown in Figure 2.4b. Piston based dispensers provide more direct control over the flow of hydrogel from the nozzle than in the pneumatic dispensers due to the delay of the compressed gas volume. Screw systems provide more spatial control and are useful for the applications requiring ink of higher viscosities to be deposited through the nozzle. However, this method of dispensing can cause a huge pressure drop at the nozzle which can damage the embedded cells. Hence, the design of screw has to be revised in order to make the printing of biomaterials possible [24].

The polymers used for DIW often have limited mechanical properties and experience fatigue under repeated stress, which causes limitations in their applications. This limitation can be addressed by improving the hydrogel used. Gong et al. [27] [28] introduced the concept of modifying the hydrogel used for fabrication by inducing a double network (DN) structure for various combinations of hydrophilic polymers. The DN hydrogels contained 60 – 90 % water and exhibited a fracture strength of a few to several tens of megapascals and high wear resistance due to extremely low friction coefficients of the gels. Yang et. al. [29] demonstrated a two-step method to fabricate a DIW object using DN hydrogels as shown in Figure 2.5. In the first step, they prepared a 3D printable gel by mixing N,N′-methylenebis(acrylamide) (MBAA), Irgacure 2959, Laponite RDS, sodium 2-acrylamido-2-methylpropanesulfonate (AMPS) and water in specific concentrations. This ink was used to 3D print an object and then cure it with UV light. In the second step, they mixed acrylamide, MBAA, Irgacure 2959, and water and cured the gel prepared. After that, the gel prepared in the first step was soaked in the gel prepared in the second step, and the fully soaked gel was cured again. With various ratio of polyacrylamide to cross-linker, the compressive strength and elastic modulus can be increased to 61.9 MPa and 0.44 MPa, respectively. Similarly, the maximum values of compressive and tensile strength can be obtained up to 93.5 MPa and 1.417 MPa, respectively.

The ink formulation and printing parameters such as ink exiting speed, nozzle size, dispenser moving speed, temperature, and external environment directly influence the final product.

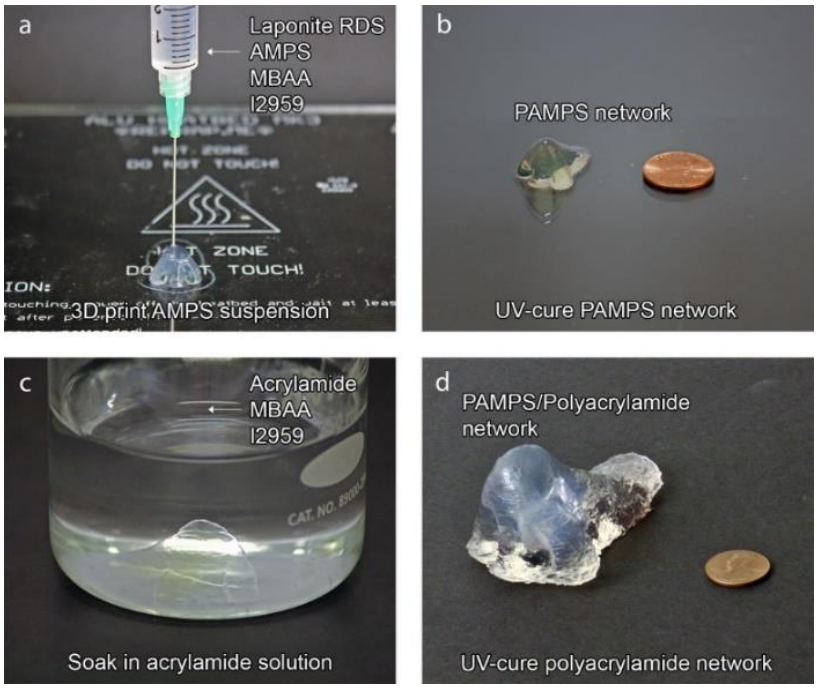

Figure 2.5. 3D printing procedures of DN hydrogels: (a) DIW printing of AMPS network, (b) Curing to get PAMPS network under UV light, (c) Soaking of PAMPS network into acrylamide solution, and (d) Curing of PAMPS/polyacrylamide network [29]. (Reprinted with permission from ref. [29]. Copyright 2017 American Chemical Society.)

2.2.3. Selective Laser Sintering (SLS)

Selective laser sintering is a widely used powder bed fusion (PBF) AM technique which uses powder form of materials. In this method, complex 3D parts can be generated by the fusion of powder material on top of each layer in an enclosed chamber using thermal energy supplied by a focused laser beam. Following the CAD model, the cross section of each layer is scanned by using a beam deflection system (Galvano mirrors) and then the successive powder layers are deposited having a thickness in the range of 20 to 150 μm, and is monitored by a powder deposition system [30] [31].

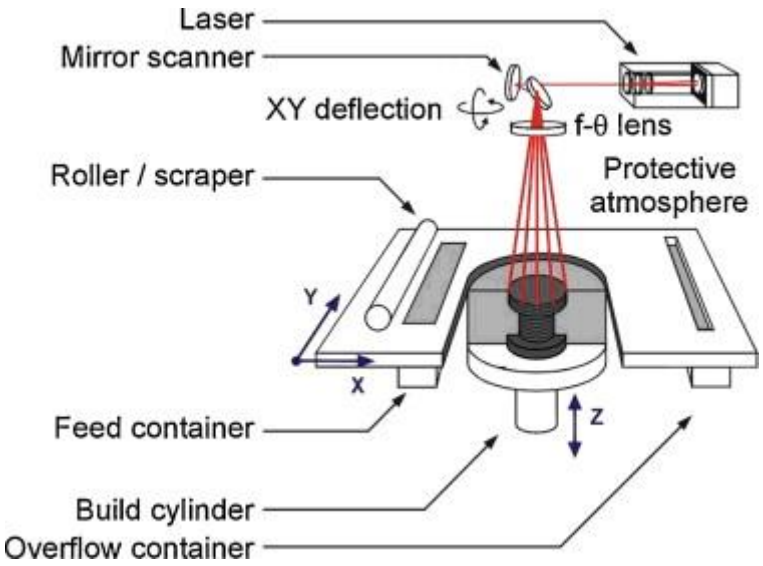

Figure 2.6. A typical Selective Laser Sintering Additive Manufacturing (SLS – AM) set up [32]. (Reproduced with permission from ref. [32]. Copyright 2014 Elsevier.)

Figure 2.6 shows the schematic diagram of a SLS-AM set-up. The SLS-AM system contains laser, mirror scanner, roller, feed container, build cylinder and N_2 atmosphere. First, the powder is spread over the building platform by using the spreading mechanism which consists of a slot feeder and roller/scraper. Next, the powder is fused by the application of a high-power laser which heats it to a temperature below its melting point such that the fusion occurs. After the formation of the first layer, the platform moves downward depending on the G-code generated from the CAD model of the final product. The role of scanner is to adjust the focus of laser on each layer and determine the height of powder bed. The process continues until the final 3D product is obtained, and allowed to cool down, and the un-sintered powder is removed. Lastly, the product is taken out from the printer [30] [31].

The products manufactured by this method have high dimensional accuracy, which depends on several parameters such as accuracy of the STL model converted from CAD model, cutting into layers, machine resolution, beam offset, layer thickness, material shrinkage, laser beam speed, laser power, temperature of working platform, and hatch distance. The properties of the manufactured products such as surface quality, mechanical properties, dimensional accuracy, and manufacture time can be adjusted based on the printing parameters. Improved mechanical properties can be obtained by improving the sintering between each layer and is dependent on the laser beam density [33]. There must be adequate supply of laser power to get

a high-quality product with better sintering between the layers (Figure 2.7a). If the supplied laser power is not sufficient, the powder will not fuse together and in case of higher energy, the products deform, and high dimensional inaccuracy is seen (Figure 2.7b). Hence, the energy density is quite important to consider while working with the SLS method.

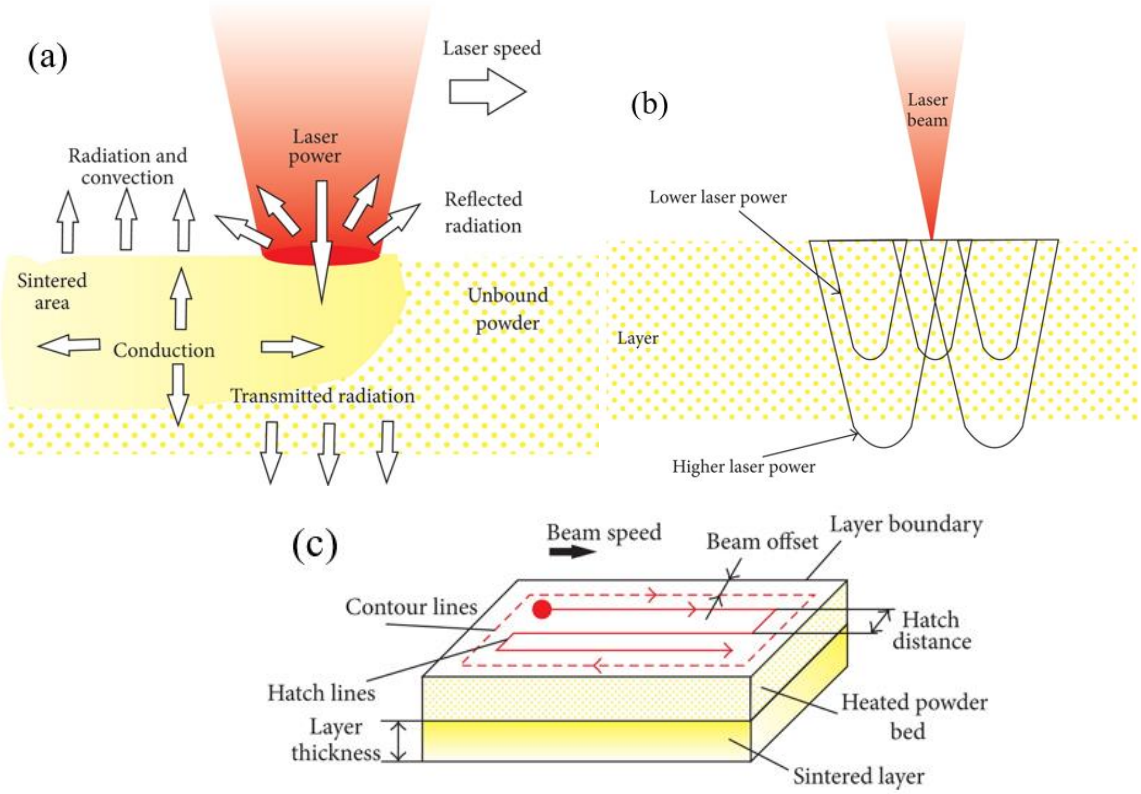

Figure 2.7. SLS system: (a) Effect of laser power on the sintering process of powders, (b) Effects of lower and higher laser power, (c) Hatch distance [33]. (Adapted from ref. [33]. Copyright 2014 Hindawi Publishing Corporation.)

Equation (2.1) represents the equation of energy density required in the SLS method to print a product. It is defined as the amount of energy input per unit area [31] [33] [34].

$$ED = \frac{P}{v.h} \times \frac{d}{h} \qquad (2.1)$$

where, *ED* is energy density, *P* is the laser power, *v* is laser beam speed, *d* is laser beam diameter, and *h* is hatch distance (Figure 2.7c). Hatch distance is the spacing between two laser beams.

The powder can be fused together following different binding mechanisms [30] [35] [36].

(a) **Solid state sintering:** It is a thermal process which requires the heating of a material powder to a temperature above half of its melting temperature ($T_m/2$) and below the melting temperature (T_m). The fusion of the adjacent powder particles is initiated by the formation and growth of a neck between them when the surface energy is reduced by the implication of temperature induced by laser.

(b) **Chemically induced binding:** This method is useful for ceramic materials. For example, if SiC ceramics are heated to a very high temperature, partial decomposition of SiC into Si and C occurs and Si combines further with oxygen and forms SiO_2, which acts as a binder between the particles. This produces full dense objects.

(c) **Liquid phase sintering – Partial melting:** In this method, a binder/additive material having lower melting temperature is added into the main building material having higher melting temperature. When the laser energy heats the material to its melting temperature, additives melt first before the main material. The molten additive materials attract the main material together due to the capillary action which results in high density, rearranged grains of the product, and filled pores between the particles. This makes a rigid object. This method is generally used to manufacture 3D parts using ceramic materials.

(d) **Full melting or Selective Laser Melting (SLM):** This method is suitable for metals and ceramics rather than polymers. In this mechanism, the material is melted completely by the use of laser power. This results in nearly full dense objects, good mechanical properties and prevents the lenghty post-processing steps.

Some of the advantages of this method are as follows [37]:

(i) It is one of the faster forms of 3D printing.

(ii) Support structures are not required since the parts are supported by the material powder.

(iii) Multiple components can be nested within the powder bed to speed up production.

(iv) The resolution can be achieved to around 0.1 mm.

(v) By adjusting the laser power either less or high, different types of material powders such as polymers, metals, ceramics, and glass can be successfully sintered.

(vi) Various polymers have been laser sintered to manufacture products such as TPU, polystyrene (PS), polyester block amide (PEBA), PEEK, and blends of polyamide (nylon), including glass-reinforced grades.

SLS has the following shortcomings [37]:

(i) Due to the high cost of laser, the machine can be expensive.

(ii) Limited availability of different types of thermoplastic powder materials to make the parts.

(iii) The manufactured products may have porous surface finish which requires post-processing.

In summary, the working principles, advantages, and disadvantages of the additive manufacturing methods discussed above are presented in Table 2.1.

Table 2.1. Summary of different 3D printing methods.

Method	Materials	Principle	Advantages	Disadvantages	References
FDM	Filament form of PLA, ABS, TPU, PC, Nylon, PEEK, glass, metal.	Extrusion	Processable with a wide variety of materials, can produce multi-material structures, low maintenance costs, no toxic chemicals involved, rapid production, overall tolerance of 0.1 mm, and easy material change.	Surface roughness, rather slow process, restricted dimensions, appearance of voids and lower mechanical properties.	[14] [15]
DIW	Ink form of plastics, ceramics, food, living cells, composites	Extrusion	Huge application areas such as photonics, microelectronics, advanced ceramics, micro fuel cells and batteries, sensors, and biological applications.	Requires post-processing, low resolution.	[15] [25]

SLS	Powder form of metals, polymers, ceramics, and glass.	Powder bed fusion	Rapid production, high dimensional accuracy, resolution around 0.1 mm, support not required.	Expensive, limitations of thermoplastics, requires post-processing.	[31] [33] [37]

2.3. Materials

Researchers have explored various additive manufacturing (3D printing) methods. Depending on the method used, the required materials are selected. In this section, an overview of the manufacturing, chemical composition, structure, properties, advantages, and limitations of some of the widely used materials is presented. The materials reviewed in this paper are highlighted in Figure 2.8.

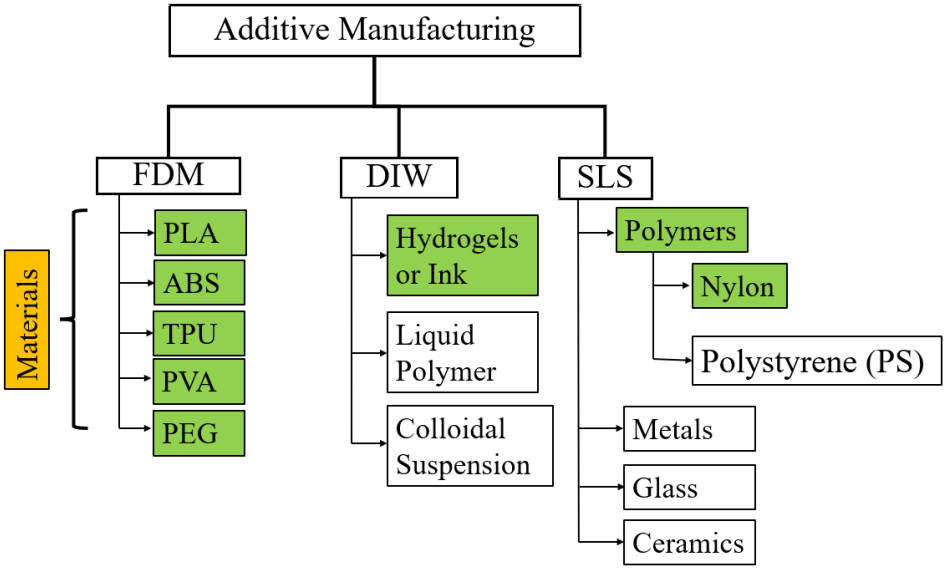

Figure 2.8. Materials commonly used for different additive manufacturing methods.

2.3.1. Poly(lactic) acid (PLA)

PLA is a biodegradable and renewable thermoplastic polymer that is derived from starch obtained from renewable resources such as corn, wheat, rice, and sugarcane [38] [39]. It has been extensively used in pharmaceutical and biomedical applications [40], electrochemical energy conversion and storage [41], packaging and tissue engineering [42], fabric and fashion industries [14] [43] [44] [45].

PLA is manufactured by processing and polymerization of lactic acid monomers which exist in two optically active configurations: L(+) and D(−) isomers as shown in Figure 2.9 [46] [47] [48]. The weight percentages of these isomers directly influences the crystallinity, mechanical properties and degradation characteristics of PLA [49]. If the content of D isomers is less than 2% in the L-D blends, then a highly crystalline PLA can be obtained whereas if it is higher than 20%, a highly amorphous PLA can be produced [47] [50]. Hence, these lactides are mixed in an appropriate proportion to produce either semi-crystalline PLLA (poly-L-lactic acid) or amorphous PDLA (poly-D-lactic acid) by a ring opening polymerization process.

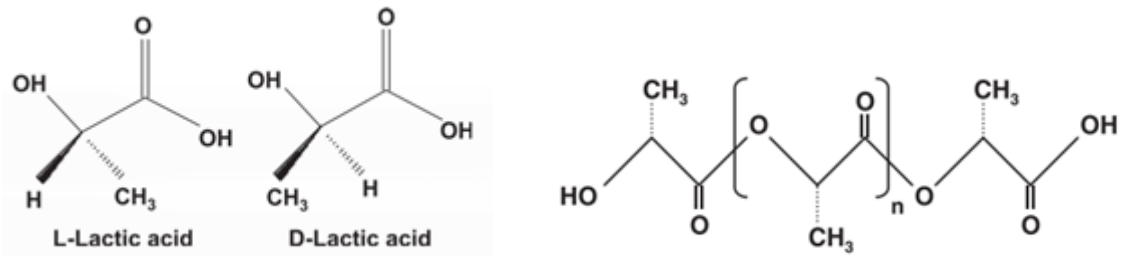

Figure 2.9. Chemical structure of L and D isomers of lactic acid (left) and high molecular weight PLA formed by ring opening polymerization (right) [47].

The lower glass transition temperature (T_g = 60 – 65 ℃), melting temperature (T_m = 170 – 180 ℃), lower coefficient of thermal expansion [40], and non-adherence to the printing surface makes it a suitable candidate for 3D printing purposes [39] [51]. Its production consumes carbon dioxide [52] [53] and does not produce toxic or carcinogenic effects [52]. It requires 25% – 55% less energy to produce than petroleum-based products [54]. The end products made of PLA have high strength and high stiffness. It is relatively easy to print without warping and its mechanical properties depend on the printing parameters and geometries [14] [55]. However, the properties such as low thermal stability, high degradation rate during processing, brittle in nature with less than 10% elongation at break [54] [56], low toughness and moisture sensitivity limit its applications [51] [57]. Soft PLA (PLA + softener) provides better elongation-at-break properties (up to 200%) [58]. It is a potential candidate because of its availability, low cost, and lower printing temperature; it can also be used to make dimensionally accurate parts, with printing details down to 0.8 mm and minimum features down to 1.2 mm [59]. Therefore, it is suitable for parts with fine details.

Figure 2.10 shows the Differential Scanning Calorimetry (DSC) curve of a 3D printed PLA material exhibiting the first heating cycle, cooling cycle and second heating cycle for

exothermic process in an upward direction. The spectra determines important features of semi-crystalline thermoplastic PLA, such as glass transition temperature T_g, exothermic cold crystallization temperature T_{cc} and associated enthalpy ΔH_c, endothermic melting temperature T_m and enthalpy ΔH_m [39]. The sample is first heated from 40 ℃ to 200 ℃ and then cooled from 200 ℃ to 40 ℃ at heating and cooling rates of both 10 ℃/min [60]. Cold crystallization peaks are visible when the polymer chains do not get enough time to fully get ordered. It is seen after the glass transition temperature when the chains get chance to move and get ordered. Crystallization peak is visible during the cooling cycle which happens due to the polymer chain mobility and ordering in the PLA material [61]. Sometimes, first heating cycle is performed to remove the thermal history pre-existing on the sample [62] [63]. During the second heating cycle, two endothermic melting peaks (as observed in Ref. [64]) can be seen at ~158 ℃ and ~166 ℃ which has been formed due to the presence of multiple crystalline states (α' and α) of PLA during thermal cycling [39] [65] [66]. The first peak present at the lower temperature is associated with the melting of the α′ crystalline state and its recrystallization into the α form, whereas the second peak at higher temperature is related to the melting of the α state. Hence, the melting of the α′ form and its recrystallization into α form can be said as the α′– α phase transition [66].

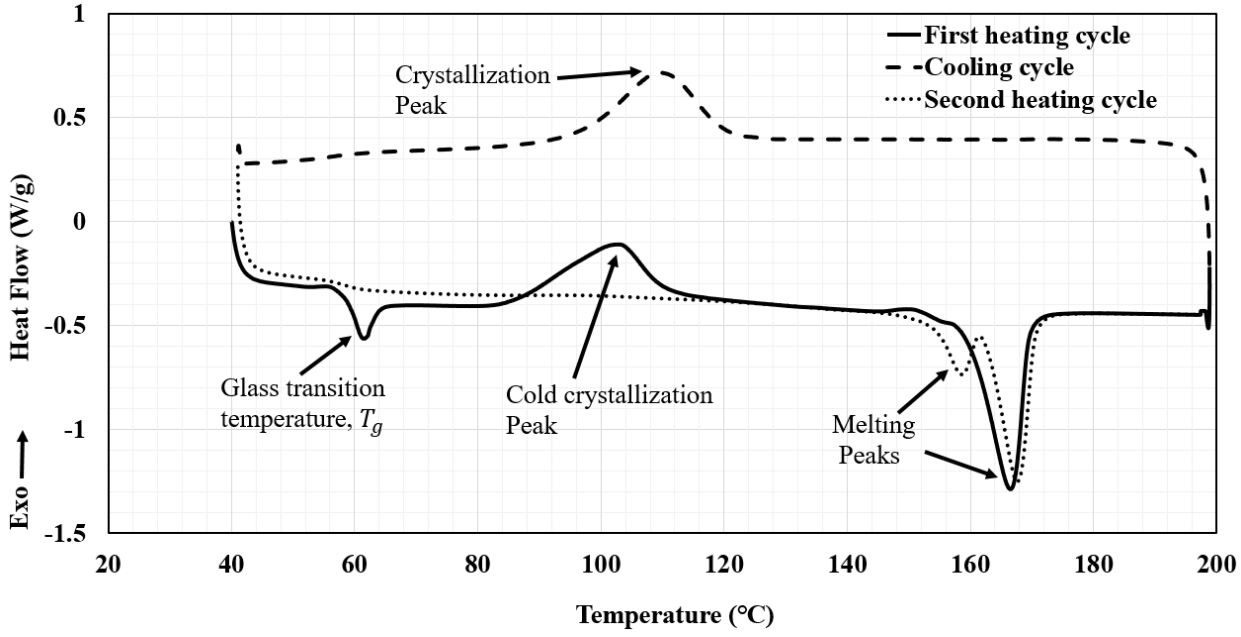

Figure 2.10. DSC curve of a 3D printed PLA showing the first heating cycle, cooling cycle and second heating cycle.

2.3.2. Acrylonitrile butadiene styrene (ABS)

ABS is a popular thermoplastic material in 3D printing which is formed by a systematic polymerization of monomers of 15% – 35% acrylonitrile (A), 5% – 30% butadiene (B) and 40% – 60% styrene (S) [67]. The chemical structures of these monomers are shown in Figure 2.11 [68]. Two different phases of ABS terpolymer exist: a continuous phase of styrene-acrylonitrile (SAN) and a dispersed phase of polybutadiene as shown in Figure 2.12 [69].

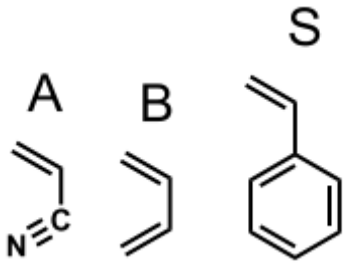

Figure 2.11. Monomer units constituting the ABS filament [68].

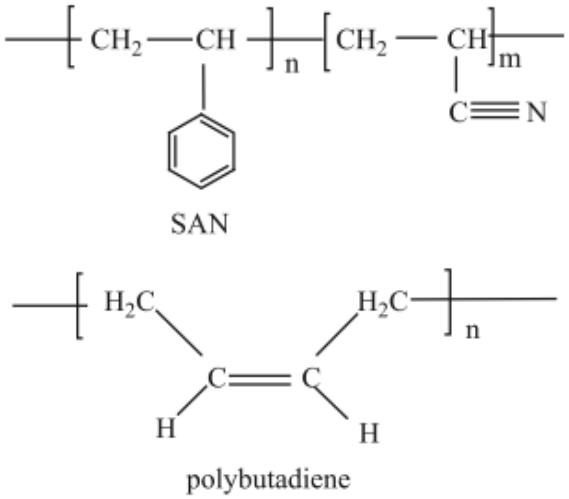

Figure 2.12. Chemical structure of ABS: SAN phase of ABS (left), Butadiene rubber phase of ABS (right) [69].

ABS is low cost and is used to fabricate lightweight, rigid and molded products [70]. It has good dimensional stability, impact strength, abrasion resistance, low coefficient of thermal expansion and can withstand many chemical reagents [69]. In addition, it is easy to shape but tough to break, as it melts and becomes pliable when heated at 220 ℃; then, it sets quickly which makes it suitable for 3D printing [14]. The matrix composition, molecular mass, type of rubber, rubber particle size, grafted rubber structure, additive content, volume ratio of rubber to SAN phase determines the properties of ABS. For example, the optimized impact strength

can be achieved by controlling the rubber particle size, its distribution and micro-structure. It is hydrophobic and shows an absorption of up to 1.5 % of water upon storage in aqueous media due to the presence of residual emulsifier and the polarity of the nitrile side groups [69]. It has a elongation at break in the range of 3 – 20 % and flexural strength up to 48 – 110 MPa [8] [71]. It has the following limitations:

(a) It does not attach satisfactorily to cold print beds. This results in distorted products. Hence, it is suggested to keep the bed heated to at least 120 ℃ [14].
(b) Fumes are produced when this filament is melted during extrusion in the nozzle, which is not safe to breathe. That's why the printer should be kept in a well-ventilated area.
(c) It gets fractured by UV radiation if it is used for a long time in the sun.

2.3.3. Thermoplastic polyurethane (TPU)

TPU is a biocompatible, biodegradable and linear segmented block copolymer [72] [73], which is synthesized by the reaction of polyols with aliphatic or aromatic diisocyanates. The polyols may be ether-, ester-, and carbonate-based diols with average molecular weight in the range of 1000 to 3000 g/mol. These polyols form the soft segments of the material whereas the diisocyanates such as diphenylmethane-4.4-diisocyanate (MDI) make the hard segments of TPU by addition of a chain extender such as butanediol. The soft segment interconnects two hard segments and the hard segments are bonded together with the presence of hydrogen bonds and form physical crosslinks [74] [75] [76]. The chemical structure of the materials showing the hard segments and soft segments are shown in Figure 2.13. Its properties vary from being a high-performance elastomer to tough thermoplastic polymer [77] [78]. It gets its rigidity and hardness from HS domains whereas the flexibility and elastomeric behavior is gained from SS domains [79]. It is used for high tensile strength, abrasion resistance, tear resistance, low temperature flexibility and high versatility in chemical structures [74]. It can be used in several applications such as textile, footwear industry, tubing, biomaterials, and adhesives.

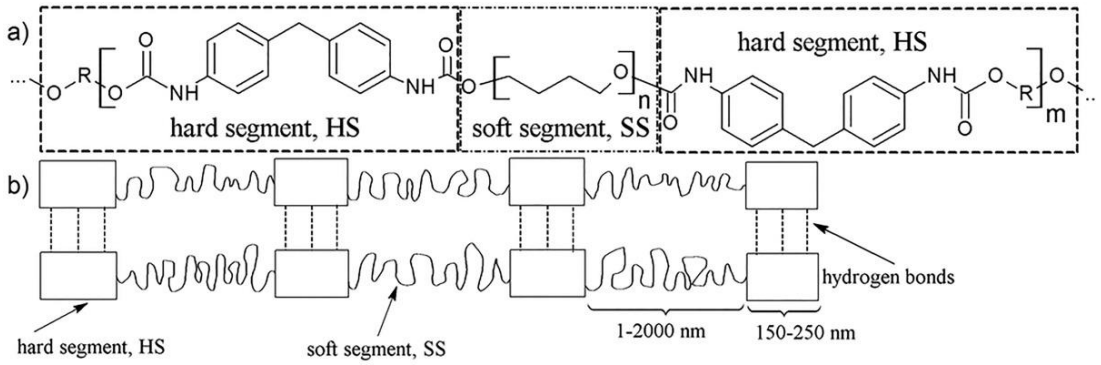

Figure 2.13. (a) Chemical structure of TPU consisting of hard and soft segments, (b) Schematic structure of TPU [76]. (Reproduced with permission from ref. [76]. Copyright 2017 John Wiley and Sons.)

TPU's easy printability has made it a good candidate to be explored for 3D printing. It provides high flexibility, and strength to the final products. Like most elastomers, it is melt-processable, recyclable, and elastic. It can be processed by compression, blow, and injection molding and extrusion, which is the basis for fused deposition modeling (FDM) method of 3D printing [80]. It possesses the elasticity of vulcanized rubber as well as the processability of thermoplastics and it can be as soft as rubber or as hard as rigid plastic; thus, TPU bridges the gap between rubber and plastic [81]. TPU suffers from the following limitations:

(a) Its production is highly dependent on non-renewable fossil-based polyols and isocyanates. The gradual exhaustion of conventional fossil fuels makes its applications limited unless it is produced from renewable sources [82].
(b) It has lower thermal stability and mechanical strength [83].

2.3.4. Poly(vinyl) alcohol (PVA)

Polyvinyl alcohols are non-toxic, water-soluble, bio-degradable, bio-compatible, semi-crystalline, and synthetic polymers which are prepared by polymerizing vinyl acetate following the hydrolysis or partial hydrolysis methods [84] [85]. Therefore, it can be classified into two groups; fully hydrolyzed PVA (FH-PVA) (1–2 mol% acetate groups) and partially hydrolyzed (PH-PVA) (10–15 mol% acetate groups) [86]. The chemical structures of PH-PVA and FH-PVA are shown in Figure 2.14 [87]. FH-PVA has the higher chemical stability, water resistance, and excellent physical and mechanical properties, which have led to its wide use, especially in the textile industry [88] [89]. PH-PVA is used in packaging for bleaches, bath salts, insecticides, and disinfectants [86]. The properties of PVA are highly dependent on the degree of hydrolysis under acidic or alkaline conditions and the length of vinyl acetate polymer.

These properties are molecular weight, solubility, flexibility, strength, and adhesiveness. It is an odorless, tasteless, translucent, white or cream-colored granular powder [90].

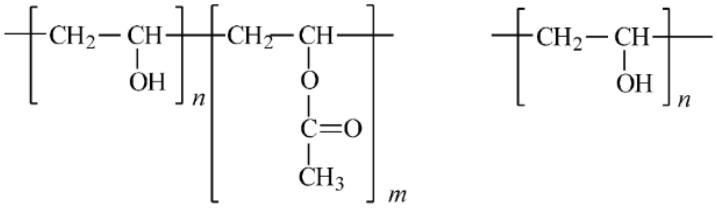

Figure 2.14. Chemical structure of PVA: partially hydrolyzed (left), and fully hydrolyzed (right) [87].

The thermoplastic PVA has a glass transition temperature of T_g = 34 ℃, melt temperature of 174 – 178 ℃, density of ρ = 1.27 gm/cm^3 [91] [92], and printing temperature of 190 – 220 ℃, which makes it a suitable candidate to be used in 3D printing. It has adhesiveness, water solubility property, and similar extruding temperature as PLA which is why many researchers use it as a support material with PLA being the polymer matrix. It provides flexibility to print support structures and rafts in complex components and prototypes [93] [94]. PVA has been extensively used in textile and paper industries [87], pharmaceutical industries [95][96], and tissue engineering [97]. A few limitations of this polymer are:

(a) **Storage:** Since PVA is hydrophilic in nature, it has a tendency of absorbing any form of moisture even from air and the final print can bubble or crack, degrading the final quality and strength [98].

(b) **Expensive:** It is expensive in comparison with most typical polymeric filaments. It costs around two or three times as much as PLA or ABS filaments [98].

(c) **Clogging and oozing:** Sometimes PVA can clog the nozzle. If the temperature is set too high or even the nozzle if left idle for too long, then it will ooze or degrade inside the nozzle and clog it. To avoid this problem, it is recommended to use ooze shield for constant cooling of nozzle during the printing process. It is also suggested to remove any unused PVA from the printer when it is not in use to protect it from the exposure to humid air [98].

(d) It does not have cell-adhesive property [99].

2.3.5. Poly(ethylene) glycol (PEG)

PEG is also known as polyethylene oxide (PEO), polyoxyethylene (POE), and polyoxirane [100]. It is a linear or branched, neutral polyether, available in a variety of

molecular weights (MWs) from 200 to tens of thousands, and soluble in water, toluene, methylene chloride, and most organic solvents. It is insoluble in ethyl ether, hexane, and ethylene glycol. PEGs having MW less than 1000 are viscous, colorless liquids, water soluble and hygroscopic at room temperature. The higher molecular weight PEGs are waxy white solids. PEG-2000 has a solubility of about 60% in water at 20 ℃ . Its melting point is dependent on its molecular weight and exhibits a plateau at about 67 ℃ [101] [102]. It is biocompatible [103][104], yields non-immunogenicity, non-antigenicity, protein rejection, and non-toxic. That's why it has gained popularity among researchers. The chemical structure is shown in Figure 2.15. It is most popular in pharmaceutical industries, tissue engineering [105] and medicals. PEG-based wound healing especially in diabetic wounds causes skin cells to grow faster and accelerates the healing [106].

$$HO{-}(CH_2CH_2O)_n{-}CH_2CH_2OH$$

Figure 2.15. Chemical structure of PEG.

The properties of the materials used in FDM 3D printing are summarized in Table 2.2.

Table 2.2. Mechanical, thermal, and chemical properties of materials used in FDM.

Materials	Mechanical	Thermal	Chemical	References
PLA	ρ: 1.21 – 1.25 g/cm^3 σ: 21 – 60 MPa E: 0.35 – 3.5 GPa ∈: 2.5 – 6.0 % σ_F: 65 – 157 MPa E_F : 2.50 GPa σ_I: 4.25 − 13.7 kJ/m^2	T_g : 45 – 60 ℃ T_m : 170 – 180 ℃ ΔH_m^0 = 93.6 (J/g) χ = 10 – 30 (%)	• Optically active configurations: L – lactide and D – lactide. • Optically pure PLLA and PDLA are crystalline. • If the content of D isomers is less than 2% in the L-D blends then a highly crystalline PLA can be obtained whereas if it is higher than 20%, a highly amorphous PLA can be produced.	[14][47] [50][107] [108][109] [110][111]

ABS	ρ: 1.01 – 1.20 g/cm^3 σ: 36 – 72 MPa E: 0.1 – 2.4 GPa ∈: 3 – 20 % σ_F: 48 – 110 MPa E_F: 2.250 GPa IZOD impact, notched: 106 J/m	T_g : 105 – 110 ℃ T_m : 230 – 270 ℃	• SAN determines the chemical properties of ABS. • High resistance to acids, alkalis, fats, or aqueous solutions of salts. • Hydrophobic. • Contact angle between ABS and water is 81.0 ± 0.6°. • Insoluble in paraffinic hydrocarbons. • SAN phase is soluble in halogenated hydrocarbons, aromatics, esters, and ketones. • Oxidizing agents, especially inorganic acids, break up the chains and cause degradation of the polymer.	[8] [14][16] [69][71] [112]
TPU	ρ: 1.10 g/cm^3 σ: 50 MPa ∈: 550 % E_F: 68.9 MPa	T_g: – 33 ℃ MFI = 32 g/10 min α = 161 × 10^{-6} mm/mm/ ℃	• Semi-crystalline, and hygroscopic • Can be polyether-based or polyester-based. • Ether-bonded compounds are often poorly biodegradable.	[113][114] [115]
PVA	ρ = 1.27 g/cm^3 σ: 17.84 ± 1.01 MPa E: 5.60 ± 0.26 MPa (at 10% strain)	MFI = 39 ± 8 g/10 min T_g : 34 ℃ T_m : 178 ℃	• Hydrophilic polymer with excellent biocompatibility. • PVA with low degree of hydrolys (DH) shows	[91] [99]

	∈: 2.18 ± 0.21 (mm/mm)	ΔH_m^0 = 161 J/g χ = ~ 20 (%)	higher solubility in water at low temperature. • PVA with high DH, must be heated above 70°C to dissolve in water. • Residual acetate groups (hydrophobic in nature) weaken the intra – and intermolecular hydrogen bonds of adjoining –OH groups.	

Note: ρ = Density; σ = Tensile strength; E = Tensile modulus; ∈: = Tensile elongation; $\boldsymbol{\sigma_F}$ = Flexural strength; $\boldsymbol{E_F}$ = Flexural modulus; $\boldsymbol{\sigma_I}$ = Impact strength; $\boldsymbol{T_g}$ = Glass transition temperature; $\boldsymbol{T_m}$ = Melting temperature; $\boldsymbol{\Delta H_m^0}$ = Melting enthalpy of 100% crystalline polymers; χ = Crystallinity; MFI = Melt flow index; α = Coefficient of linear thermal expansion.

2.3.6. Hydrogels (Ink) for DIW

The printable ink for DIW can be fabricated by mixing fillers, binders, additives, and solvents as shown in Figure 2.16a [25]. Valentine et. al. [116] prepared two types of ink: insulating ink and conductive ink. For insulating ink, they mixed TPU (Elastollan soft 35A) in cosolvent prepared from 1:4 ratio by volume (v/v) of *N*,*N*-dimethylformamide (DMF) and tetrahydrofuran (THF). For conductive ink, they mixed TPU (Elastollan Soft 35A) in DMF and then silver flakes, and APS 2–5 μm (Inframat Advanced Materials) were added. Lastly, the inks were centrifuged to remove the air bubble and made ready for 3D printing. They 3D printed flexible and wearable sensors using DIW method.

Jason et. al. [117] immersed a bottle containing water in an oil bath heated at 100 °C. When the water started boiling, hexadecylamine (HDA) and copper chloride ($CuCl_2.2H_2O$) were added and stirred for 30 minutes at 1000 rpm. When the color of solution changed to sky blue, α or β D-glucose (Merck) was added, then the color of solution changed from pale brown to dark brown. After stirring for 6 hours, the solution was removed from oil bath and centrifuged, and hence the ink was ready to use as shown in Figure 2.16b.

Wang et. al. [118] prepared electrode layer ink by dissolving TPU (Elastollan 35A, BASF) in DMF at 1:1.5 ratio of TPU:DMF. Then, silver microflakes (≈ 5 μm) were added into the solution and mixed well using planetary mixer. They also prepared sensing layer ink by adding NaCl crystals as the sacrificial template. For this, the grain size of NaCl crystals was reduced to < 100 μm, and then mixed with carbon black and TPU (dissolved in twice its weight of DMF). This solution was mixed thoroughly, and a porous and conductive ink was obtained.

Lacey et. al. [119] produced additive-free and aqueous carbon-based ink by oxidizing holey graphene (hG), which is a highly porous carbon nanomaterial. They obtained holey graphene oxide (hGO), which is nano porous and hydrophilic in nature. Then hGO was mixed with water at high concentration of ≈ 100 mm/mL, and hence a printable ink with shear thinning behavior was produced as shown in Figure 2.16c. The produced ink was used to 3D print a complex structure, stacked mesh structure.

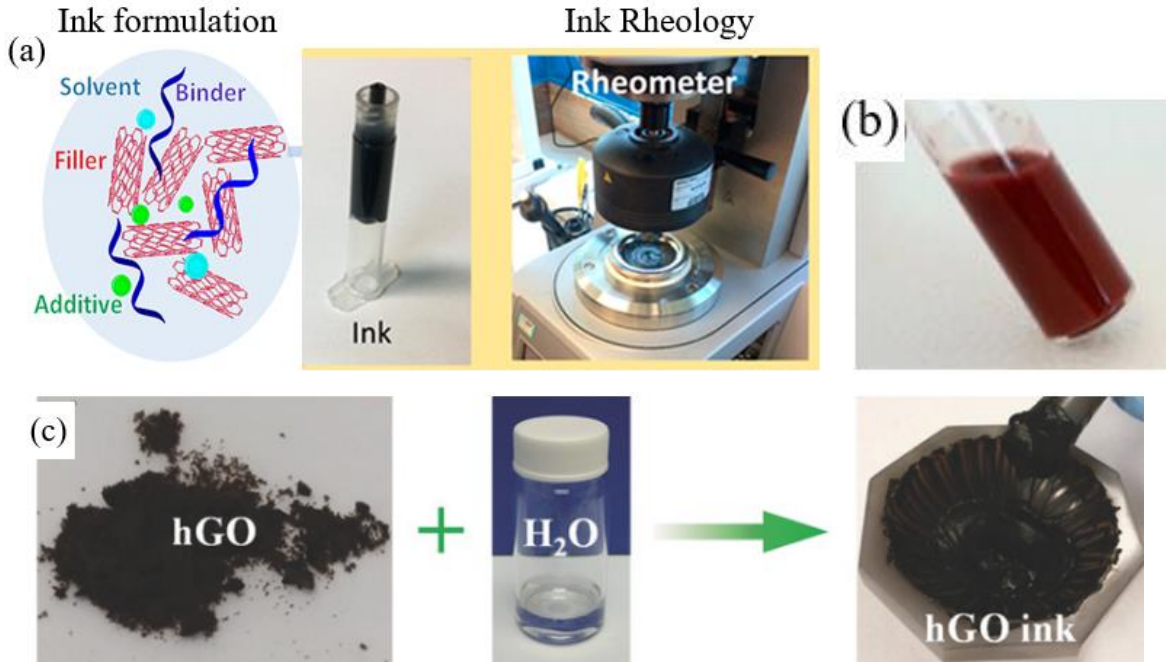

Figure 2.16. Images showing (a) Ink formulation and rheology for DIW 3D printing [25] (Reprinted with permission from ref. [25]. Copyright 2019 American Chemical Society.), (b) Ink formulated by using copper nanowires, HDA and water [117] (Reprinted with permission from ref. [117]. Copyright 2015 American Chemical Society.), and (c) Image showing the steps of preparing the additive free ink using holey graphene and water [119]. (Reproduced with permission from ref. [119]. Copyright Wiley-VCH GmbH.)

The composition of inks determines the mechanical properties, resolution, and conductivity of the printed electronics. The inks must possess two important characteristics: shear thinning behavior and viscoelasticity [120] [121]. These characteristics of inks allow

them to extrude smoothly from the dispenser, rapid curing, fusion with previously deposited layers and to maintain a fixed shape of object after printing due to its higher storage modulus and yield strength [122]. In addition, the rheology of inks can be optimized by adding nanomaterials as fillers to improve their electrochemical, conductivity and mechanical properties.

The flow of inks is observed when the applied shear stress (τ) is greater than yield point (τ_y) of the inks. The relationship between shear stress, shear rate and viscosity can be expressed by Eq. (2.2).

$$\tau = \eta\dot{\gamma} = \tau_y + K\dot{\gamma}^n \qquad (2.2)$$

where, η is apparent viscosity, $\dot{\gamma}$ is shear rate, K is viscosity parameter, and n is the power law exponent.

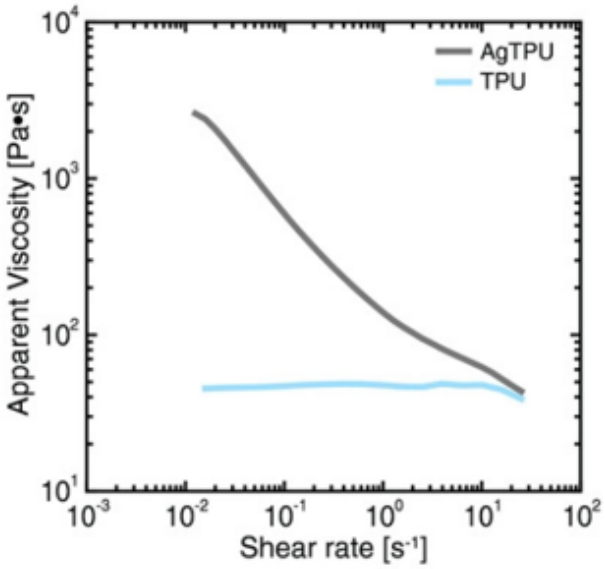

Figure 2.17. Rheological behavior of TPU ink prepared for direct ink writing of soft electronics [116]. (Reproduced with permission from ref. [116].Copyright Wiley-VCH GmbH.) (For interpretation of the references to color in this figure legend, the reader is referred to the web version of this article.)

The inks having lower viscosity extrudes easily from the nozzle but have to be cured rapidly to retain the final shape. TPU ink having low viscosity, around 10^1 to 10^2 Pa.s, was extruded through a 200 μm nozzle which behaved as a Newtonian fluid (η is independent of the shear rate) (shown by blue curve in Figure 2.17). After printing, the product was cured at 80 ℃ within 2 hours. The inks having shear thinning behavior exhibits lower viscosity with

increasing shear rates, $\dot{\gamma}$ (n < 1). This type of rheological characteristics allows the continuous and stable ink flow through a nozzle. The mixing of silver flakes causes the rheology of ink to change from Newtonian flow to shear thinning behavior (shown by gray curve in Figure 2.17) and become gel-like upon the removal of shear stress and help to retain the shape of final product [25] [116].

2.3.7. Nylon powders for SLS

Nylon is a widely used thermoplastic material because of its light weight, excellent mechanical properties, superior flexibility, low moisture absorption, chemical resistant and good dimensional stability [123]. Many forms of nylon are available in the market such as Nylon 6, Nylon 11, Nylon 12, Nylon 46, and Nylon 6,6. The semi-crystalline forms of nylon such as Nylon 11 and 12 (Figure 2.18) are easy to sinter using the SLS method.

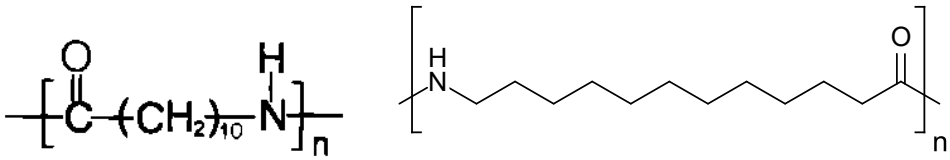

Figure 2.18. Chemical structures of Nylon: Nylon 11 (left) and Nylon 12 (right) [124].

Nylon 12 can be produced through two routes. These routes are explained briefly.

First route: In this process, the polycondensation of ω-aminolauric acid, a bifunctional monomer with one amine and one carboxylic acid group takes place as shown in Eq. *(2.3)* [124]:

$$n\,H_2N(CH_2)_{11}CO_2H \;\rightarrow\; [(CH_2)_{11}CONH]_n + nH_2O \qquad (2.3)$$

Second route: In this process, a ring – opening polymerization of laurolactan at 260 – 300 ℃ takes place, which is carried out by cationic or anionic initiators. The cationic initiators are used commercially since the products formed by it are less stable and oxidized relatively faster than that of anionic initiators. Ring – opening polymerization is widely used method for commercial production as shown in Eq. (2.4) [124].

$$n\,[(CH_2)_{11}CONH] \;\rightarrow\; [(CH_2)_{11}CONH]_n \qquad (2.4)$$

The melting temperature of nylon 11 and 12 is 170 – 180 ℃. Nylon 12 is used in various industries including as films for packaging materials in the food industry, pharmaceutical and medical fields, sintered powder for coating metals, textile industry and many others.

Higher mechanical properties can be achieved from nylon 11 and 12 than their amorphous forms [125]. This is one of the reasons for being widely used by the researchers with the SLS process. However, shrinkage during crystallization can be an obstacle in production of accurate parts. It provides sufficient time to recrystallize and achieve better products by the proper fusion of newer layers with the older ones [125]. Similarly, molecular weight is an important aspect to consider while sintering polymer. It affects the melting viscosity and hence melt flow index (MFI). Higher MFI is related to lower melting viscosity and lower molecular weight of polymer [126]. The relationship between molecular weight and melting viscosity can be given by Eq. *(2.5)*:

$$\eta_0 = k\ (M_w)^n \qquad (2.5)$$

where, η_0 is the viscosity of polymer, *k* is constant, and M_w is molecular weight. Every polymer has its critical molecular weight, M_c. If $M_w < M_c$, then n = 1, and if $M_w > M_c$, then n = 3.4.

Similarly, for a better SLS process and product quality, Frenkel proposed a model for predicting melting viscosity. This model considers the sintering rate of two adjacent materials and is given by Eq. (2.6) and Figure 2.19 [126].

$$\left(\frac{x}{r}\right)^2 = \frac{3\sigma t}{2\pi\eta_0} \qquad (2.6)$$

where, $\sigma\ and\ t$ are the surface tensions of the polymer materials and the time required to scan a dot by the laser, respectively, r is the radius of powder grains, and x is the width of sintered layers between the particles. If $x\ /\ r = 0.5$, it was proposed that sintering process has completed. In this way, Eq. *(2.6)* can predict the melting viscosity of the polymer material.

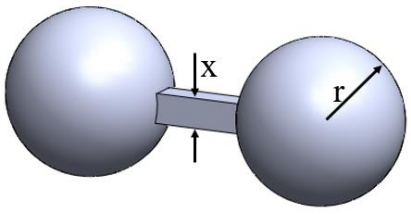

Figure 2.19. Frenkel sintering model (Modified after ref. [126]).

2.4. Applications

In this section, a review of additive manufacturing of fabrics and flexible electronics is presented.

2.4.1. Additive manufacturing of fabrics

The use of different additive manufacturing (3D printing) methods is in its infancy; they have been extensively used in textile and fabrics industries. The most widely used materials are PLA, ABS, TPU, Nylon, etc. The desired traits of printable materials for textile applications are printability, flexibility, biocompatibility, good mechanical, and structural properties. In this section, the application of different 3D printing methods along with the suitable materials for 3D printing of fabrics is presented.

2.4.1.1. Fused deposition modeling (FDM)

FDM is the dominating 3D printing technology in fashion and textile industries. Several researchers worked on design and 3D printing of fabrics by using FDM method. Some of this research is reviewed briefly in this section.

Melnikova et. al. used FDM printer X400 and different types of materials such as PLA, soft PLA, and BendLay [107]. They printed weft knitted structures as shown in Figure 2.20. The knitted structure was printed using BendLay and with support material. It was realized that support structure was hard to remove, which destroyed the model as shown in Figure 2.20a. Hence, they concluded that it was not possible to print a fine model by FDM. However, using soft PLA and without support material, they could obtain the structure having separated loops and exhibiting similar properties to knitted fabrics as shown in Figure 2.20b. The surface roughness and fine fibers between loops could be easily observed on a macroscopic level.

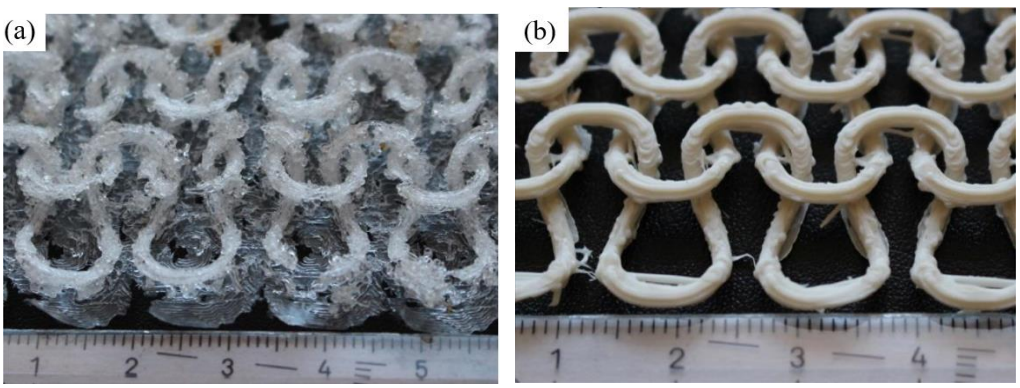

Figure 2.20. Weft knitted fabric structure 3D printed by using FDM method: (a) BendLay with support materials, and (b) Soft PLA without support materials [107]. (Copyright 2014 IOP Publishing Ltd)

Spahiu et. al. designed a 3D model of fabric as shown in Figure 2.21a, in which the shape of structure is an arrowhead with negative Poisson's ratio having dimensions of 130 mm × 130 mm [127]. A structure having negative Poisson's ratio is called auxetic structure. They used the material, FilaFlex manufactured by Recreus with shore hardness A82 to fabricate the lattice structures. They printed several lattice structures and then using a Dikale 07A 3D Pen, all the parts were joined with each other in a definite pattern. Finally, a complete 3D printed dress was obtained as shown in Figure 2.21b. However, they concluded that more research is needed to achieve the properties of textile materials to replace the traditional way of garment manufacturing.

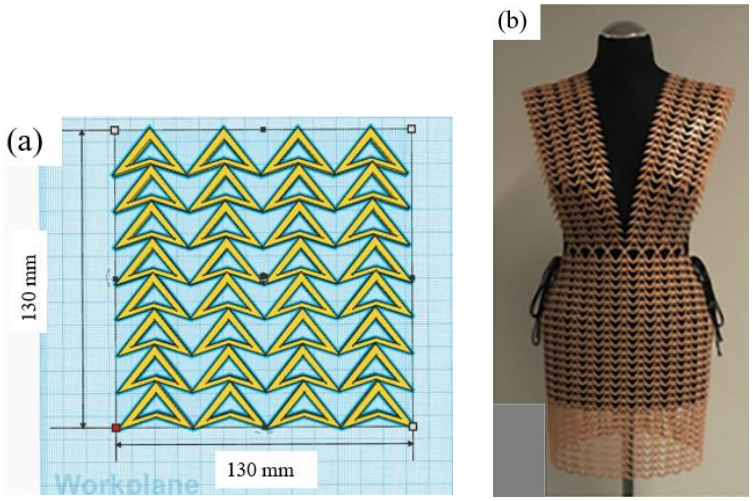

Figure 2.21. FDM 3D printed fabric structure: (a) 3D modeled lattice structure for fabric, and (b) A complete 3D printed dress over a mannequin [127]. (Copyright 2020 Journal of Engineered Fibers and Fabrics.)

Kim et. al. 3D printed unit cell of fabric structures using TPU as main building material as shown in Figure 2.22a [128]. Their fabric design was inspired by the spider web and used triangles of different sizes and shapes. They designed the final silhouette of the to-be-3D-printed clothing using the software, Rhinoceros and then modelled the fabric structure by using another software, Grasshopper as shown in Figure 2.22b. After 3D printing of the unit cells,

they assembled them together producing the final 3D printed cloth. They used different connection methods to join the triangles such as sewing, and copper wire. A complete 3D printed dress wrapped over the traditionally manufactured dress is shown in Figure 2.22c.

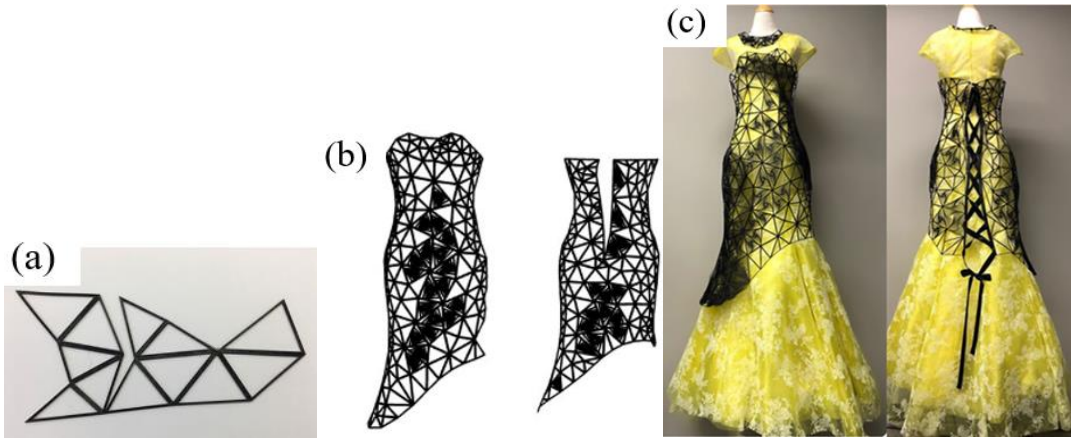

Figure 2.22. (a) 3D printed unit cell of fabric, (b) Design of to-be-3D-printed clothing, and (c) A complete 3D printed dress over a traditionally manufactured dress [128]. (Copyright 2019 Fashion and Textiles)

Uysal and Stubbs used a combination of different materials, PLA and LAY-FOMM 40, to 3D print textile – like structures using the 3D printer X400 such as gloves as shown in Figure 2.23 [129]. LAY-FOMM 40 is made of rubber-elastomeric polymer and PVA component. After rinsing in water, PVA disappears, and the remaining part becomes soft, flexible, and micro-porous. It is harmless and food-safe [130]. First, they printed the sewing patterns (Figure 2.23A) in which the surfaces were printed partially with polygons (Figure 2.23B and C) and then the patterns were sewn together to obtain the final 3D form of glove (Figure 2.23D). The authors suggested two future studies regarding joining the printed patterns: ultrasound technique and 3D printed connections to join the patterns to avoid extra needs of tools.

Figure 2.23. (A) Sewing pattern 3D printed using two materials, (B) surface design of glove, (C) flexible sewing pattern with inner lining, (D) pattern pieces sewn together to form a 3D printed glove [129]. (Reproduced with permission from ref. [129]. Copyright 2019 Tekstilec).

2.4.1.2. Selective laser sintering (SLS)

A fashion design company named, Nervous System, 3D printed different fabrics structures following kinematics methods with SLS using Nylon powder as shown in Figure 2.24. Examples of 3D printed structures include skirt, blouse, belts, jewellery, and many more. The kinematics bodice they produced was composed of 1320 hinged pieces, and was 3D printed in a single folded piece. To adjust the size of bodice into the printer, the fabric was printed in a flattened form which was produced by Kinematics folding software. The 3D printed bodice was wearable straight out of the printer since no pieces were manually assembled and no fasteners were used [131].

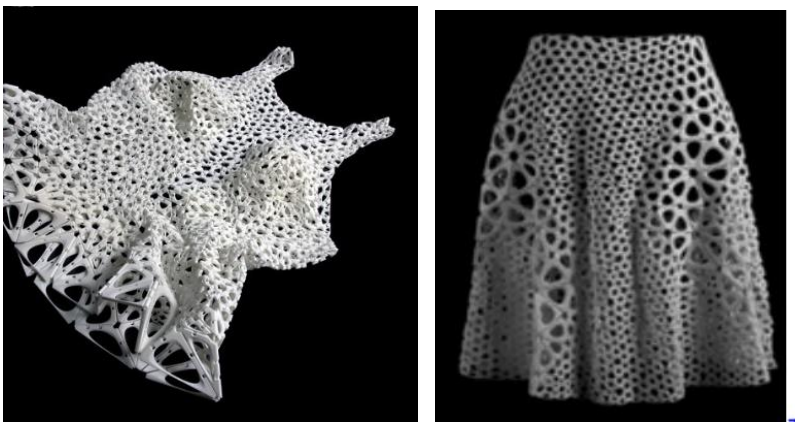

Figure 2.24. 3D printed blouse and skirt by using Kinematics method [131]. (Reproduced with permission from [131]. Copyright Nervous System.)

Beecroft 3D printed textile-based tubular structures using SLS method [123]. The material employed was nylon powder to produce flexible weft knitted structures. For 3D printing, a CAD model is required which was developed by using Rhino CAD software. The printed samples were manually compressed and stretched without any deformations in the knit, and the compressed and extended lengths were determined (Figure 2.25a and b). This tube has a compression and extension range of 95 mm, which is 52.80% of its length. Moreover, the samples were manually stretched over the conical structure repeatedly to determine the stretch and recovery properties of the tube (Figure 2.25c). It was observed that the loop structure recovered its shape but had slight deformations. In addition, each tube was bended and folded manually to see the overall flexibility and the structure recovered to its original shape (Figure 2.25d).

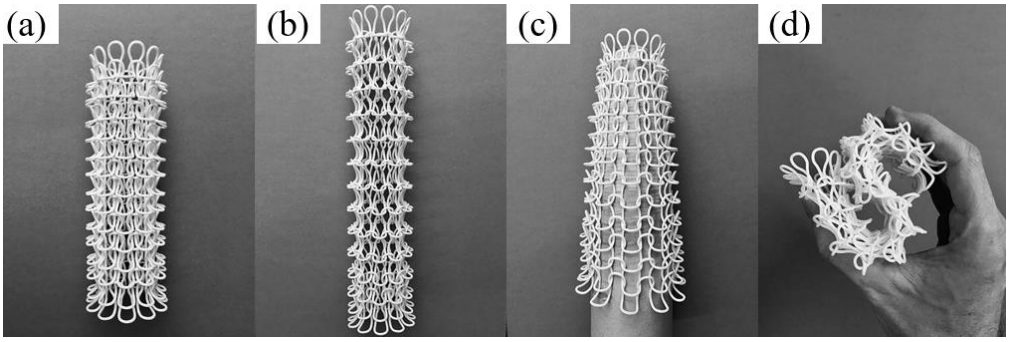

Figure 2.25. Weft knitted textile-based structures [123]. (Copyright 2019 International Journal of Fashion Design, Technology and Education)

2.4.2. Additive manufacturing of flexible electronics

Several research works on 3D printing of flexible electronics have been performed. Some relevant works along with the associated additive manufacturing method are reviewed in this section.

2.4.2.1. Direct Ink Writing (DIW)

Valentine et. al. developed a hybrid 3D printing method to fabricate flexible and wearable electronics using insulating matrix and conductive electrode inks [116]. They used thermoplastic polyurethane (TPU) elastomers which acted as insulating matrix. To make it conductive, silver flakes with dimensions of ≈ 2 μm were added to TPU matrix. These inks can be used to print in a specific layout and then both the active and passive electrical components

are merged to obtain the final electric circuit. To combine, vacuum nozzle can be employed to pick up the components from one location and place at another. The conducive traces were printed to make electrical connection between the components. The whole process is shown in Figure 2.26. They observed a strong bonding between TPU and AgTPU inks, and as a result, delamination, and cracking during or after printing were not seen. This observation solved a common problem of delamination during printing.

The conductivity of a composite conductive ink with respective to power-law theory for a percolating network is given by Eq. *(2.7)*:

$$\sigma = \sigma_0 \, (V_f - V_c)^s \qquad (2.7)$$

where, σ is conductivity of composite ink, σ_0 is bulk conductivity of silver, V_f is volumetric fraction of silver flakes in dried form, V_C is critical volume fraction at percolation (in dried form) and *s* is the power law exponent. From their experimental observations, they decided to work with 36 vol% of silver in the conductive composite ink (AgTPU ink) which contained an initial conductivity above 10^4 S cm^{-1} [116].

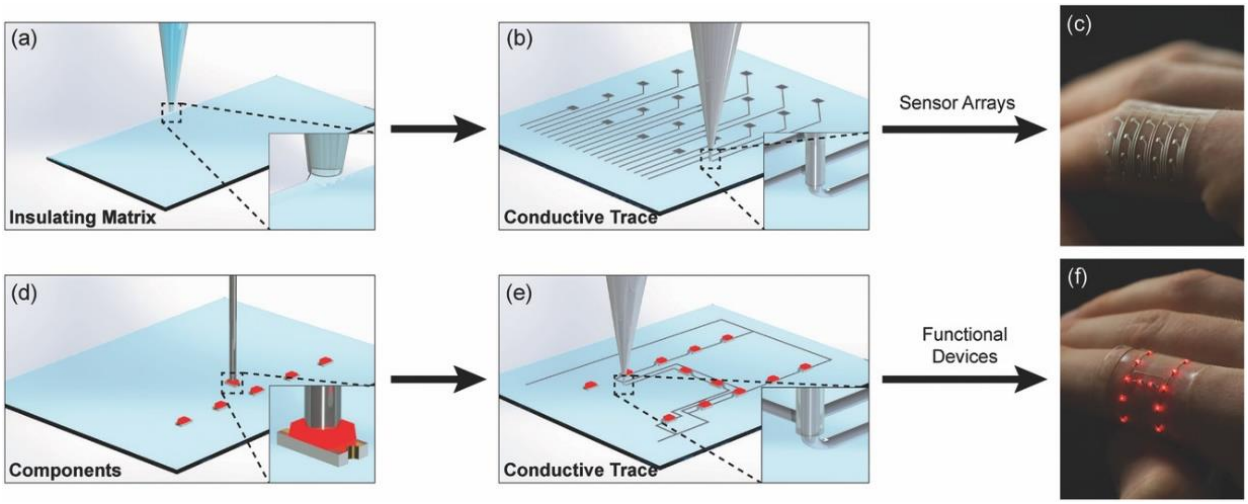

Figure 2.26. Schematic diagrams showing (a) DIW 3D printing using an insulating ink, (b) DIW 3D printing using conductive ink, (c) 3D printed wearable and flexible sensor, (d) Pick-and-place of components using vacuum nozzle, (e) Direct ink writing of AgTPU traces, and (f) A functional LED device worn on a finger [116]. (Reproduced with permission from ref. [116].Copyright Wiley-VCH GmbH.)

Boley et. al. used direct ink writing method to fabricate novel stretchable strain gauges [132]. They employed Gallium-Indium alloys such as eutectic Ga-In (EGaIn) (75% Ga, 25%

In) as ink and extruded over two silicon – based substrates: glass and Polydimethyl-siloxane (PDMS) mixed in 10:1 weight ratio. The printing setup is shown in Figure 2.27 (a – c). The ratio of the velocity of the EGaIn exiting the needle to the stage velocity, v* can be expressed by:

$$v^* = \frac{4Q}{\pi ID^2 v} \tag{2.8}$$

where, *Q* is flow rate of ink, *ID* is inner diameter of stationary syringe needle, and *v* is velocity of stage. They printed novel strain gauges directly on PDMS substrate and then encapsulated in PDMS for performance characterization. The variation in resistance increment is almost linear for strains up to 50% with an approximate slope (gauge factor) of 1.5, whereas it deviates from linear trend for strains greater than 50% making a quadratic least square fit for 100% strain. The experimental approach showing the stretchability of the printed strain gauges are shown in Figure 2.27 (d – f). This process can be useful for rapid fabrication of inductors, and capacitors with potential applications in sensing, actuating skins, robotics, medical devices, and stretchable electronics.

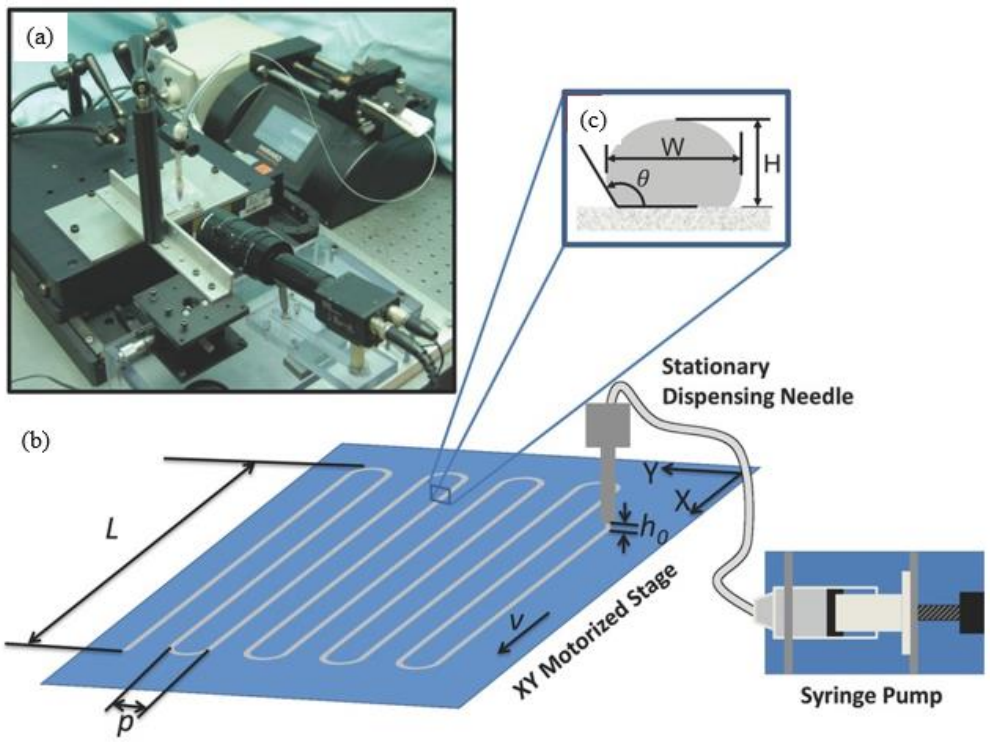

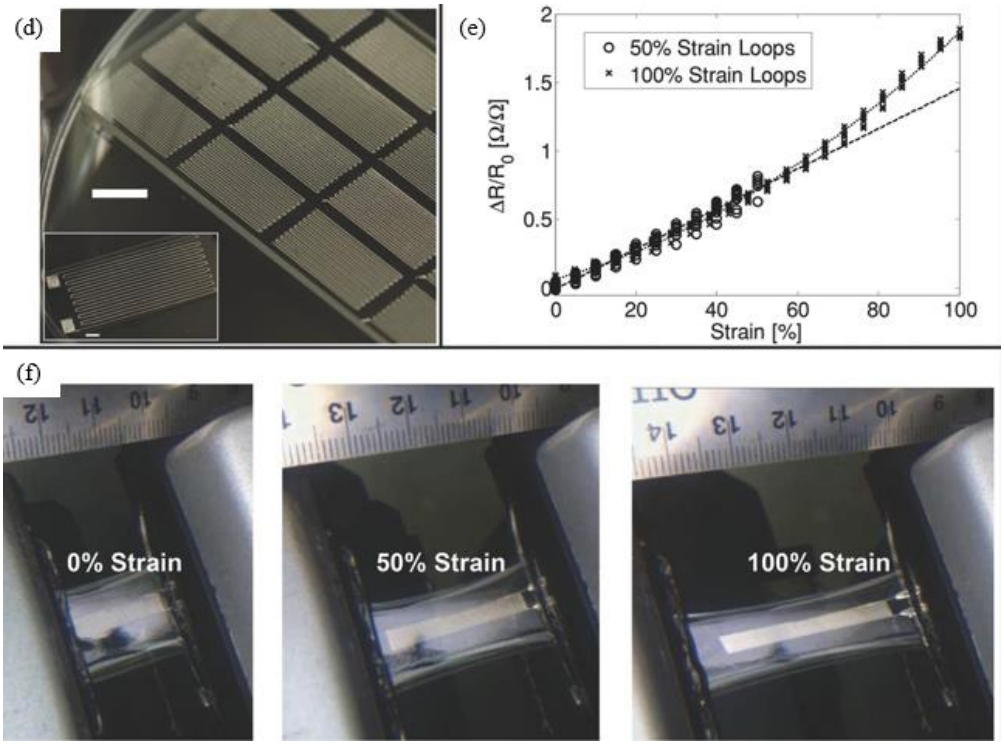

Figure 2.27. Direct ink writing of stretchable electronics: (a) DIW equipment, (b) schematic of DIW process, (c) Detailed cross-sectional view of deposited ink, (d) 3D printed stretchable strain gauge using DIW method. Scale bar is 5mm in length, (e) Comparison of performance characterization of DIW 3D printed strain gauges at 50 % and 100% strain loops repeated for 5 cycles, and (f) Strain gauges stretched at different strains [132]. (Reproduced with permission from ref. [132]. Copyright Wiley-VCH GmbH.)

2.5. Challenges and opportunities

AM methods allow to produce complex structures depending on the CAD model. The structures may be a topology of an internal architecture of a part or the whole geometry. With high degree of design and fabrication freedom comes the associated challenges and opportunities for the researchers and innovators [3] [133]. The challenges include representation, optimization, material selection, material development and 3D printing of complicated geometries.

Since the research field related to additive manufacturing of fabrics is new, it carries a lot of challenges to overcome to make an impact on human lives.

(a) The fabric structures have complex architecture, which needs a good design knowledge in CAD software. An experienced design engineer needs to be involved.

(b) The lattice structure may contain gaps between the yarns and have weaving curves. This makes the rapid prototyping of such structures a challenging task. Many printing

parameters such as printing orientation, temperature, speed, infill density, and layer thickness need to be studied.

(c) The materials available are PLA, TPU, ABS or other thermoplastics. The resulting fabrics using these materials do not possess the required fabric properties such as flexibility and strength. Hence, novel material development and its adoption to the additive manufacturing should be pursued.

(d) Most of the 3D printers are designed to fabricate parts of limited size. This brings a challenge to produce fabrics of larger size. Moreover, it is a challenging task to connect or join or stitch all the smaller parts. Therefore, research on stitching of parts is important.

All these challenges, on the other hand, bring opportunities for innovators and scientists. The additive manufacturing of flexible structures is interesting and revolutionary. It can be used to produce support structures for fabrics along with the fabrics manufactured by traditional methods.

Some of the challenges and opportunities associated with the 3D printing of electronics are as follows:

(a) To maintain the same conductivity of the 3D printed electronics is still challenging. The reason is the poor conductivity of ink which is caused by low curing temperature because of the limitation of substrate material such as cardboard and polymers. In addition, the available material types and their processing to 3D print electronic objects is also one of the major difficulties. Hence, it is recommended to explore different materials to provide adequate functionality and manufacturability for the product. Moreover, a hybrid 3D printing process should also be studied. A hybrid process combining FDM and direct ink writing shows higher applied potential, and more flexibility [10]. For example, a shoe insole was 3D printed by using multi-materials, which had embedded pressure and temperature sensor, and mounted with wireless communications chip for data transmission (Figure 2.28). The multi-layer sensors along with the insulating layers and sensing elements have been printed using hybrid printing method. This has made possible with the combination of ink jet, aerosol jet and extrusion print heads [10]. Along with all these challenges, the innovative eyes can see the opportunities. For example, one can combine 3D printed electronic elements such as sensors in completely 3D printed fabrics.

(b) One of the major challenges is to maintain the resolution of printed electronics, which directly affects their performances. An electronic component with higher resolution works better than that with lower resolution. This hinders the wider adoption of additive manufacturing technologies in electronics [134] [135] [136].

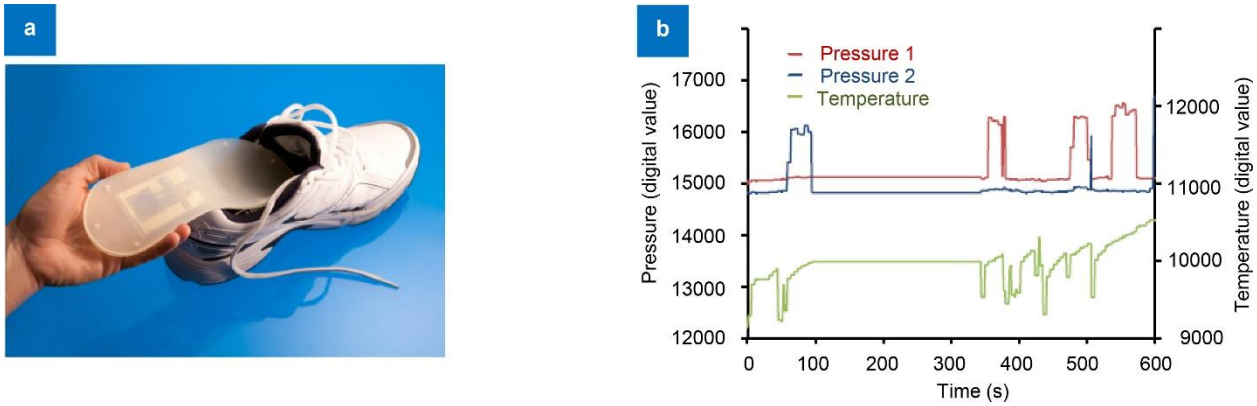

Figure 2.28. (a) 3D printed shoe insole with embedded pressure and temperature sensors with wireless communications chip for data transmission, and (b) Data generated from the chip embedded in the 3D printed shoe insole [10]. (Copyright 2018 Opto-Electronic Advances.)

2.6. Conclusions

In this chapter, several AM methods, and materials are reviewed, which have found applications for fabrication of flexible structures such as fabrics and electronics. AM is transforming the manufacturing industries providing the capability to fabricate objects ranging from simple to complex geometries. It has been adopted in almost every industry for fabricating prototypes or for research work. A group of researchers have started working on 3D printing of fabrics. Based on the design requirements, different types of fabrics have been investigated for a wide variety of materials available. The designs of fabrics studied are plain and twill weave, knitted, or some other innovative designs. The additive manufacturing methods explored are fused deposition modeling (FDM), and Selective Laser Sintering (SLS), which have been discussed in this article. The most common materials used are PLA, ABS, TPU and nylon. However, a detailed study on the mechanical properties of printed fabrics is still not seen in the literature. Moreover, literature also lacks studies on printing process parameters. This creates a future research direction on 3D printing of fabrics.

In the second part, the fabrication of electronics is discussed. There are many methods for 3D printing of electronics, but in this review the material extrusion based direct ink writing (DIW) method is discussed. This method uses the hydrogel or ink form of materials and

extrudes through the nozzle based on the CAD model. The printable ink for DIW can be fabricated by mixing fillers, binders, additives, and solvents. It is useful for a wide variety of materials such as ceramics, plastics, food and living cells. Hence, it is an extremely versatile technology. Post-processing such as drying, heating, or sintering may be required to harden the printed part and improve its mechanical properties. It fabricates flexible and wearable electronics using insulating matrix and conductive electrode inks. However, the poor conductivity, limitations of material types available, and resolution of 3D printed electronics are some of the difficulties. Future work can be on increasing the conductivity, explore different combinations of materials and/or develop innovative materials, and increasing the resolution of 3D printed electronics.

2.7. References

[1] ISO/ASTM 52900.2021, "Additive manufacturing — General principles — Fundamentals and vocabulary," Geneva, Switzerland, 2021.

[2] Y. Zhai, D. A. Lados, and J. L. LaGoy, "Additive Manufacturing: Making Imagination the Major Limitation," *JOM*, vol. 66, no. 5, pp. 808–816, 2014, doi: 10.1007/s11837-014-0886-2.

[3] A. Paolini, S. Kollmannsberger, and E. Rank, "Additive manufacturing in construction: A review on processes, applications, and digital planning methods," *Addit. Manuf.*, vol. 30, p. 100894, 2019, doi: 10.1016/j.addma.2019.100894.

[4] S. Lim, R. A. Buswell, T. T. Le, S. A. Austin, A. G. F. Gibb, and T. Thorpe, "Developments in construction-scale additive manufacturing processes," *Autom. Constr.*, vol. 21, no. 1, pp. 262–268, 2012, doi: 10.1016/j.autcon.2011.06.010.

[5] F. Calignano *et al.*, "Overview on Additive Manufacturing Technologies," *Proc. IEEE*, vol. 105, no. 4, pp. 593–612, 2017, doi: 10.1109/JPROC.2016.2625098.

[6] R. Hague, I. Campbell, and P. Dickens, "Implications on design of rapid manufacturing," *Proc. Inst. Mech. Eng. Part C J. Mech. Eng. Sci.*, vol. 217, no. 1, pp. 25–30, 2003.

[7] S. L. N. Ford, "Additive Manufacturing Technology : Potential Implications for U . S . Manufacturing Competitiveness," *J. Int. Commer. Econ.*, vol. 6, no. September, pp. 40–74, 2014.

[8] T. Campbell, C. Williams, O. Ivanova, and B. Garrett, “Could 3D Printing Change the World? Technologies, Potential, and Implications of Additive Manufacturing,” *Atl. Counc.*, pp. 1–14, 2011.

[9] S. Adanur, “Wellington Sears Handbook of Industrial Textiles,” Technomic Publishing Co. Inc., 1995, pp. 273–294.

[10] B. H. Lu, H. B. Lan, and H. Z. Liu, “Additive manufacturing frontier: 3D printing electronics,” *Opto-Electronic Adv.*, vol. 1, no. 1, pp. 1–10, 2018, doi: 10.29026/oea.2018.170004.

[11] D. Espalin, D. W. Muse, E. MacDonald, and R. B. Wicker, “3D Printing multifunctionality: Structures with electronics,” *Int. J. Adv. Manuf. Technol.*, vol. 72, no. 5–8, pp. 963–978, 2014, doi: 10.1007/s00170-014-5717-7.

[12] Y. Lu, M. Vatani, and J. W. Choi, “Direct-write/cure conductive polymer nanocomposites for 3D structural electronics,” *J. Mech. Sci. Technol.*, vol. 27, no. 10, pp. 2929–2934, 2013, doi: 10.1007/s12206-013-0805-4.

[13] J. T. Muth *et al.*, “Embedded 3D printing of strain sensors within highly stretchable elastomers,” *Adv. Mater.*, vol. 26, no. 36, pp. 6307–6312, 2014, doi: 10.1002/adma.201400334.

[14] S. Adanur and A. Jayswal, “Additive manufacturing of interlaced fibrous structures,” *Rapid Prototyp. J.*, vol. 27, no. 4, pp. 671–681, 2021, doi: 10.1108/RPJ-05-2020-0095.

[15] A. Ambrosi and M. Pumera, “3D-printing technologies for electrochemicalapplications,” *Chem. Soc. Rev.*, vol. 45, pp. 2740–2755, 2016, doi: 10.1039/C5CS00714C.

[16] I. Durgun and R. Ertan, “Experimental investigation of FDM process for improvement of mechanical properties and production cost,” *Rapid Prototyp. J.*, vol. 20, no. 3, pp. 228–235, 2014, doi: 10.1108/RPJ-10-2012-0091.

[17] L. M. Galantucci, F. Lavecchia, and G. Percoco, “Quantitative analysis of a chemical treatment to reduce roughness of parts fabricated using fused deposition modeling,” *CIRP Ann. - Manuf. Technol.*, vol. 59, no. 1, pp. 247–250, 2010, doi: 10.1016/j.cirp.2010.03.074.

[18] P. M. Pandey, N. V. Reddy, and S. G. Dhande, “Improvement of surface finish by

staircase machining in fused deposition modeling," *J. Mater. Process. Technol.*, vol. 132, no. 1–3, pp. 323–331, 2003, doi: 10.1016/S0924-0136(02)00953-6.

[19] J. M. Chacón, M. A. Caminero, E. García-Plaza, and P. J. Núñez, "Additive manufacturing of PLA structures using fused deposition modelling: Effect of process parameters on mechanical properties and their optimal selection," *Mater. Des.*, vol. 124, pp. 143–157, Jun. 2017, doi: 10.1016/J.MATDES.2017.03.065.

[20] E. de Avila, J. Eo, J. Kim, and N. P. Kim, "Heat Treatment Effect on Mechanical Properties of 3D Printed Polymers," in *MATEC Web of Conferences*, 2019, vol. 264, pp. 1–5, doi: https://doi.org/10.1051/matecconf/201926402001.

[21] C. Yang, X. Tian, D. Li, Y. Cao, F. Zhao, and C. Shi, "Influence of thermal processing conditions in 3D printing on the crystallinity and mechanical properties of PEEK material," *J. Mater. Process. Technol.*, vol. 248, no. April, pp. 1–7, 2017, doi: 10.1016/j.jmatprotec.2017.04.027.

[22] C. Kaynak and S. D. Varsavas, "Performance comparison of the 3D-printed and injection-molded PLA and its elastomer blend and fiber composites," *J. Thermoplast. Compos. Mater.*, vol. 32, no. 4, pp. 501–520, 2019, doi: 10.1177/0892705718772867.

[23] X. Tian, J. Jin, S. Yuan, C. K. Chua, S. B. Tor, and K. Zhou, "Emerging 3D-Printed Electrochemical Energy Storage Devices: A Critical Review," *Adv. Energy Mater.*, vol. 7, pp. 1–17, 2017, doi: 10.1002/aenm.201700127.

[24] J. Malda *et al.*, "25th Anniversary Article: Engineering Hydrogels for Biofabrication," *Adv. Mater.*, vol. 25, pp. 5011–5028, 2013, doi: 10.1002/adma.201302042.

[25] Y. Zhang *et al.*, "Recent Progress of Direct Ink Writing of Electronic Components for Advanced Wearable Devices," *ACS Appl. Electron. Mater.*, vol. 1, no. 9, pp. 1718–1734, 2019, doi: 10.1021/acsaelm.9b00428.

[26] Y. G. Park, H. Min, H. Kim, A. Zhexembekova, C. Y. Lee, and J. U. Park, "Three-Dimensional, High-Resolution Printing of Carbon Nanotube/Liquid Metal Composites with Mechanical and Electrical Reinforcement," *Nano Lett.*, vol. 19, no. 8, pp. 4866–4872, 2019, doi: 10.1021/acs.nanolett.9b00150.

[27] J. P. Gong, Y. Katsuyama, T. Kurokawa, and Y. Osada, "Double-Network Hydrogels with Extremely High Mechanical Strength," *Adv. Mater.*, vol. 15, no. 14, pp. 1155–

1158, 2003, doi: 10.1002/adma.200304907.

[28] J. P. Gong, “Why are double network hydrogels so tough?,” *Soft Matter*, vol. 6, pp. 2583–2590, 2010, doi: 10.1039/B924290B.

[29] F. Yang, V. Tadepalli, and B. J. Wiley, “3D Printing of a Double Network Hydrogel with a Compression Strength and Elastic Modulus Greater than those of Cartilage,” *ACS Biomater. Sci. Eng.*, vol. 3, pp. 863–869, 2017, doi: 10.1021/acsbiomaterials.7b00094.

[30] J. P. Kruth, P. Mercelis, J. Van Vaerenbergh, L. Froyen, and M. Rombouts, “Binding mechanisms in selective laser sintering and selective laser melting,” *Rapid Prototyp. J.*, vol. 11, no. 1, pp. 26–36, 2005, doi: 10.1108/13552540510573365.

[31] A. Kafle, E. Luis, R. Silwal, H. M. Pan, P. L. Shrestha, and A. K. Bastola, “3D/4D Printing of Polymers: Fused Deposition Modelling (FDM), Selective Laser Sintering (SLS), and Stereolithography (SLA),” *Polymers (Basel).*, vol. 13, no. 3101, pp. 1–37, 2021, doi: 10.3390/polym13183101.

[32] K. Shahzad, J. Deckers, Z. Zhang, J. P. Kruth, and J. Vleugels, “Additive manufacturing of zirconia parts by indirect selective laser sintering,” *J. Eur. Ceram. Soc.*, vol. 34, no. 1, pp. 81–89, 2014, doi: 10.1016/j.jeurceramsoc.2013.07.023.

[33] A. Pilipović, I. Drstvenšek, and M. Šercer, “Mathematical model for the selection of processing parameters in selective laser sintering of polymer products,” *Adv. Mech. Eng.*, vol. 2014, no. 1, pp. 1–9, 2014, doi: 10.1155/2014/648562.

[34] N. A. Charoo *et al.*, “Selective laser sintering 3D printing – an overview of the technology and pharmaceutical applications,” *Drug Dev. Ind. Pharm.*, vol. 46, no. 6, pp. 869–877, 2020, doi: 10.1080/03639045.2020.1764027.

[35] S. F. S. Shirazi *et al.*, “A review on powder-based additive manufacturing for tissue engineering: selective laser sintering and inkjet 3D printing,” *Sci. Technol. Adv. Mater.*, vol. 16, no. 3, pp. 1–20, 2015, doi: 10.1088/1468-6996/16/3/033502.

[36] M. B. Kumar, P. Sathiya, and M. Varatharajulu., “Selective Laser Sintering,” in *Advances in Additive Manufacturing Processes*, First., J. Natarajan, M. Cheepu, and Che-hua Yang, Eds. Bentham Books, 2021, pp. 28–47.

[37] R. J. Crawford and P. J. Martin, “Processing of plastics,” in *Plastics Engineering*, 4th ed., Butterworth-Heinemann, 2020, pp. 279–409.

[38] J. R. Dorgan, H. Lehermeier, and M. Mang, “Thermal and Rheological Properties of Commercial-Grade Poly (Lactic Acid)s,” *J. Polym. Environ.*, vol. 8, no. 1, pp. 1–9, 2000.

[39] M. A. Cuiffo, J. Snyder, A. M. Elliott, N. Romero, S. Kannan, and G. P. Halada, “Impact of the Fused Deposition (FDM) Printing Process on Polylactic Acid (PLA) Chemistry and Structure,” *Appl. Sci.*, vol. 7, no. 6, p. 579, Jun. 2017, doi: 10.3390/app7060579.

[40] J. Domínguez-Robles *et al.*, “Antioxidant PLA composites containing lignin for 3D printing applications: A potential material for healthcare applications,” *Pharmaceutics*, vol. 11, no. 165, pp. 1–14, 2019, doi: 10.3390/pharmaceutics11040165.

[41] M. P. Browne, E. Redondo, and M. Pumera, “3D Printing for Electrochemical Energy Applications,” *Chemical Reviews*, vol. 120, no. 5. pp. 2783–2810, 2020, doi: 10.1021/acs.chemrev.9b00783.

[42] I. Armentano *et al.*, “Multifunctional nanostructured PLA materials for packaging and tissue engineering,” *Prog. Polym. Sci.*, vol. 38, no. 10–11, pp. 1720–1747, 2013, doi: 10.1016/j.progpolymsci.2013.05.010.

[43] A. Jayswal and S. Adanur, “Effect of heat treatment on the crystallinity and mechanical properties of 3D printed flexible structures with fused deposition modeling,” *J. Ind. Text.*, 2021.

[44] “Melnikova, R., Ehrmann, A., & Finsterbusch, K. 3D printing of textile-based structures by Fused Deposition Modelling (FDM) with different polymer materials. IOP Conference Series: Materials Science and Engineering. 62. IOP Publishing Ltd. 2014.”

[45] A. Jayswal and S. Adanur, “Characterization of polylactic acid/thermoplastic polyurethane composite filaments manufactured for additive manufacturing with fused deposition modeling,” *J. Thermoplast. Compos. Mater.*, pp. 1–22, 2021, doi: 10.1177/08927057211062561.

[46] R. Auras, B. Harte, and S. Selke, “An overview of polylactides as packaging materials,” *Macromol. Biosci.*, vol. 4, no. 9, pp. 835–864, 2004, doi: 10.1002/mabi.200400043.

[47] B. Gupta, N. Revagade, and J. Hilborn, “Poly(lactic acid) fiber: An overview,” *Prog. Polym. Sci.*, vol. 32, no. 4, pp. 455–482, 2007, doi: 10.1016/j.progpolymsci.2007.01.005.

[48] A. Sodergard and M. Stolt, “Properties of polylactic acid fiber based polymers and their correlation with composition,” *Prog. Polym. Sci.*, vol. 27, no. 6, pp. 1123–1163, 2002, doi: 10.1016/S0079-6700(02)00012-6.

[49] T. Tábi, I. E. Sajó, F. Szabó, A. S. Luyt, and J. G. Kovács, “Crystalline structure of annealed polylactic acid and its relation to processing,” *express Polym. Lett.*, vol. 4, no. 10, pp. 659–668, 2010, doi: 10.3144/expresspolymlett.2010.80.

[50] J. A. Cicero, J. R. Dorgan, J. Garrett, J. Runt, and J. S. Lin, “Effects of molecular architecture on two-step, melt-spun poly(lactic acid) fibers,” *J. Appl. Polym. Sci.*, vol. 86, no. 11, pp. 2839–2846, 2002, doi: 10.1002/app.11268.

[51] I. Chiulan, A. N. Frone, C. Brandabur, and D. M. Panaitescu, “Recent advances in 3D printing of aliphatic polyesters,” *Bioengineering*, vol. 5, no. 2, pp. 2–18, 2018, doi: 10.3390/bioengineering5010002.

[52] S. Farah, D. G. Anderson, and R. Langer, “Physical and mechanical properties of PLA, and their functions in widespread applications — A comprehensive review,” *Adv. Drug Deliv. Rev.*, vol. 107, pp. 367–392, 2016, doi: 10.1016/j.addr.2016.06.012.

[53] J. R. Dorgan, H. J. Lehermeier, L. Palade, and J. Cicero, “Polylactides: properties and prospects of an environmentally benign plastic from renewable resources,” *Macromol. Symp.*, vol. 175, no. 1, pp. 55–66, 2001.

[54] R. M. Rasal and D. E. Hirt, “Toughness decrease of PLA-PHBHHx blend films upon surface-confined photopolymerization,” *J. Biomed. Mater. Res. - Part A*, vol. 88, no. 4, pp. 1079–1086, 2009, doi: 10.1002/jbm.a.32009.

[55] G. Ehrmann and A. Ehrmann, “Shape-Memory Properties of 3D Printed PLA Structures,” *Proceedings*, vol. 4, no. x, pp. 1–6, 2020, doi: 10.3390/cgpm2020-07198.

[56] M. Hiljanen-Vainio, P. Varpomaa, J. Seppälä, and P. Törmälä, “Modification of poly(L-lactides) by blending: Mechanical and hydrolytic behavior,” *Macromol. Chem. Phys.*, vol. 197, no. 4, pp. 1503–1523, 1996, doi: 10.1002/macp.1996.021970427.

[57] O. Gordobil, I. Egüés, R. Llano-Ponte, and J. Labidi, “Physicochemical properties of PLA lignin blends,” *Polym. Degrad. Stab.*, vol. 108, pp. 330–338, 2014, doi: 10.1016/j.polymdegradstab.2014.01.002.

[58] T. Gérard, T. Noto, and T. Budtova, “Tensile Properties of Pla And Phbv Blends:

Anomalous Elongation and Aging," *11th Eur. Symp. Polym. Blends - Polyblends 2012*, 2012.

[59] Ken Giang, "PLA vs. ABS: What's the difference?" https://www.hubs.com/knowledge-base/pla-vs-abs-whats-difference/ (accessed Jun. 01, 2021).

[60] S. Wasti *et al.*, "Influence of plasticizers on thermal and mechanical properties of biocomposite filaments made from lignin and polylactic acid for 3D printing," *Compos. Part B Eng.*, vol. 205, 2021, doi: 10.1016/j.compositesb.2020.108483.

[61] N. Alizadeh, D. P. Thorne, M. L. Auad, and A. D. N. Celestine, "Mechanical performance of vinyl ester—polyurethane interpenetrating polymer network composites," *J. Appl. Polym. Sci.*, vol. 138, no. 19, pp. 1–11, 2021, doi: 10.1002/app.50411.

[62] G. Ozkoc, G. Bayram, and E. Bayramli, "Effects of olefin-based compatibilizers on the morphology, thermal and mechanical properties of ABS/polyamide-6 blends," *J. Appl. Polym. Sci.*, vol. 104, no. 2, pp. 926–935, 2007, doi: 10.1002/app.25848.

[63] S. Bose, A. R.Bhattacharyya, P. V.Kodgire, and A. Misra, "Fractionated crystallization in PA6/ABS blends: Influence of a reactive compatibilizer and multiwall carbon nanotubes," *Polymer (Guildf).*, vol. 48, no. 1, pp. 356–362, 2007, [Online]. Available: https://doi.org/10.1016/j.polymer.2006.11.019.

[64] M. A. Abdelwahab, A. Flynn, B.-S. Chiou, S. Imam, W. Orts, and E. Chiellini, "Thermal, mechanical and morphological characterization of plasticized PLA-PHB blends," *Polym. Degrad. Stab.*, vol. 97, pp. 1822–1828, 2012, doi: 10.1016/j.polymdegradstab.2012.05.036.

[65] A. Jalali, M. A. Huneault, and S. Elkoun, "Effect of thermal history on nucleation and crystallization of poly(lactic acid)," *J. Mater. Sci.*, vol. 51, no. 16, pp. 7768–7779, 2016, doi: 10.1007/s10853-016-0059-5.

[66] T. Tábi, I. E. Sajó, F. Szabó, A. S. Luyt, and J. G. Kovács, "Crystalline structure of annealed polylactic acid and its relation to processing," *EXPRESS Polym. Lett.*, vol. 4, no. 10, pp. 659–668, 2010, doi: 10.3144/expresspolymlett.2010.80.

[67] V. D. Sagias, K. I. Giannakopoulos, and C. Stergiou, "Mechanical properties of 3D printed polymer specimens," *Procedia Struct. Integr.*, vol. 10, pp. 85–90, 2018, doi:

10.1016/j.prostr.2018.09.013.

[68] A. S. de León, A. Domínguez-Calvo, and S. I. Molina, “Materials with enhanced adhesive properties based on acrylonitrile-butadiene-styrene (ABS)/thermoplastic polyurethane (TPU) blends for fused filament fabrication (FFF),” *Mater. Des.*, vol. 182, p. 108044, 2019, doi: 10.1016/j.matdes.2019.108044.

[69] S. Olivera, H. B. Muralidhara, K. Venkatesh, K. Gopalakrishna, and C. S. Vivek, “Plating on acrylonitrile–butadiene–styrene (ABS) plastic: a review,” *J. Mater. Sci.*, vol. 51, no. 8, pp. 3657–3674, 2016, doi: 10.1007/s10853-015-9668-7.

[70] A. Manoj, M. Bhuyan, S. R. Banik, and M. Ravi Sankar, “Review on particle emissions during fused deposition modeling of acrylonitrile butadiene styrene and polylactic acid polymers,” *Mater. Today Proc.*, vol. 44, pp. 1375–1383, 2021, doi: 10.1016/j.matpr.2020.11.521.

[71] T. Campbell, C. Williams, O. Ivanova, and B. Garrett, “Strategic Foresight Report,” *Atl. Counc.*, no. June 2014, pp. 3–7, 2012.

[72] V. Jašo, M. Cvetinov, S. S. S. Rakič, and Z. S. Petrovič, “Bio-plastics and elastomers from polylactic acid/thermoplastic polyurethane blends,” *J. Appl. Polym. Sci.*, vol. 131, no. 22, pp. 1–8, 2014, doi: 10.1002/app.41104.

[73] H. Y. Mi *et al.*, “Characterization of thermoplastic polyurethane/polylactic acid (TPU/PLA) tissue engineering scaffolds fabricated by microcellular injection molding,” *Mater. Sci. Eng. C*, vol. 33, no. 8, pp. 4767–4776, 2013, doi: 10.1016/j.msec.2013.07.037.

[74] Q.-W. Lu and C. W. Macosko, “Comparing the compatibility of various functionalized polypropylenes with thermoplastic polyurethane (TPU),” *Polymer (Guildf).*, vol. 45, pp. 1981–1991, 2004, doi: 10.1016/j.polymer.2003.12.077.

[75] A. Frick and A. Rochman, “Characterization of TPU-elastomers by thermal analysis (DSC),” *Polym. Test.*, vol. 23, no. 4, pp. 413–417, 2004, doi: 10.1016/j.polymertesting.2003.09.013.

[76] J. Datta and P. Kasprzyk, “Thermoplastic polyurethanes derived from petrochemical or renewable resources: A comprehensive review,” *Polym. Eng. Sci.*, vol. 58, no. S1, pp. E14–E35, 2018, doi: https://doi.org/10.1002/pen.24633.

[77] N. Alizadeh *et al.*, “Synthesis and characterization of high performance interpenetrating polymer networks with polyurethane and poly(methyl methacrylate),” in *Unsaturated Polyester Resins*, Elsevier Inc., 2019, pp. 243–255.

[78] S. Jiang, G. Duan, H. Hou, A. Greiner, and S. Agarwal, “Novel Layer-by-Layer Procedure for Making Nylon-6 Nanofiber Reinforced High Strength, Tough, and Transparent Thermoplastic Polyurethane Composites,” *ACS Appl. Mater. Interfaces*, vol. 4, pp. 4366–4372, 2012.

[79] M. Nofar, M. Mohammadi, and P. J. Carreau, “Effect of TPU hard segment content on the rheological and mechanical properties of PLA/TPU blends,” *Journal of Applied Polymer Science*, vol. 137, no. 45. 2020, doi: 10.1002/app.49387.

[80] M. M. Prabhakar, A. K. Saravanan, A. H. Lenin, I. J. Leno, K. Mayandi, and P. S. Ramalingam, “A short review on 3D printing methods, process parameters and materials,” *Mater. Today Proc.*, vol. 45, pp. 6108–6114, 2020, doi: 10.1016/j.matpr.2020.10.225.

[81] X. Zhao, T. Shou, R. Liang, S. Hu, P. Yu, and L. Zhang, “Bio-based thermoplastic polyurethane derived from polylactic acid with high-damping performance,” *Ind. Crops Prod.*, vol. 154, no. 112619, 2020, doi: 10.1016/j.indcrop.2020.112619.

[82] X. Zhao, T. Shou, R. Liang, S. Hu, P. Yu, and L. Zhang, “Bio-based thermoplastic polyurethane derived from polylactic acid with high-damping performance,” *Ind. Crops Prod.*, vol. 154, no. 112619, 2020, doi: 10.1016/j.indcrop.2020.112619.

[83] D. Tabuani, F. Bellucci, A. Terenzi, and G. Camino, “Flame retarded Thermoplastic Polyurethane (TPU) for cable jacketing application,” *Polym. Degrad. Stab.*, vol. 97, no. 12, pp. 2594–2601, 2012, doi: 10.1016/j.polymdegradstab.2012.07.011.

[84] G. G. D. Silva, P. J. A. Sobral, R. A. Carvalho, P. V. A. Bergo, O. Mendieta-Taboada, and A. M. Q. B. Habitante, “Biodegradable films based on blends of gelatin and poly (vinyl alcohol): Effect of PVA type or concentration on some physical properties of films,” *J. Polym. Environ.*, vol. 16, no. 4, pp. 276–285, 2008, doi: 10.1007/s10924-008-0112-9.

[85] “Effect of molecular weight on fibrous PVA produced by electrospinning,” *Mater. Lett.*, vol. 58, pp. 493–497, 2004.

[86] S. Aruldass, V. Mathivanan, A. R. Mohamed, and C. T. Tye, “Factors affecting hydrolysis of polyvinyl acetate to polyvinyl alcohol,” *Journal of Environmental Chemical Engineering*, vol. 7, no. 5. pp. 1–7, 2019, doi: 10.1016/j.jece.2019.103238.

[87] C. C. DeMerlis and D. R. Schoneker, “Review of the oral toxicity of polyvinyl alcohol (PVA),” *FoodandChemical Toxicol.*, vol. 41, pp. 319–326, 2003, doi: 10.1300/j147v21n03_03.

[88] F. Liu *et al.*, “Preparation of fully hydrolyzed polyvinyl alcohol electrospun nanofibers with diameters of sub-200 nm by viscosity control,” *Text. Res. J.*, vol. 82, no. 16, pp. 1635–1644, 2012, doi: 10.1177/0040517512436833.

[89] C. Shao, H. Y. Kim, J. Gong, B. Ding, D. R. Lee, and S. J. Park, “Fiber mats of poly(vinyl alcohol)/silica composite via electrospinning,” *Mater. Lett.*, vol. 57, no. 9–10, pp. 1579–1584, 2003, doi: 10.1016/S0167-577X(02)01036-4.

[90] R. Nagarkar and J. Patel, “Polyvinyl Alcohol: A Comprehensive Study,” *Acta Sci. Pharm. Sci.*, vol. 3, no. 4, pp. 34–44, 2019.

[91] A. Cataldi, D. Rigotti, V. D. H. Nguyen, and A. Pegoretti, “Polyvinyl alcohol reinforced with crystalline nanocellulose for 3D printing application,” *Mater. Today Commun.*, vol. 15, pp. 236–244, 2018, doi: 10.1016/j.mtcomm.2018.02.007.

[92] N. H. A. Tran, H. Brunig, and G. Heinrich, “Controlling micro- and nanofibrillar morphology of polymer blendsin low-speed melt spinning process. Part I. Profiles of PLA/PVA-filamentparameters along the spinline,” *J. Appl. Polym. Sci.*, vol. 44258, pp. 1–14, 2016, doi: 10.1002/APP.44258.

[93] C. Duran, V. Subbian, M. T. Giovanetti, J. R. Simkins, and F. R. Beyette, “Experimental desktop 3D printing using dual extrusion and water-soluble polyvinyl alcohol,” *Rapid Prototyp. J.*, vol. 21, no. 5, pp. 528–534, 2015, doi: 10.1108/RPJ-09-2014-0117.

[94] D. Rigotti, L. Fambri, and A. Pegoretti, “Polyvinyl alcohol reinforced with carbon nanotubes for fused deposition modeling,” *J. Reinf. Plast. Compos.*, vol. 37, no. 10, pp. 716–727, 2018, doi: 10.1177/0731684418761224.

[95] A. Goyanes, P. Robles Martinez, A. Buanz, A. W. Basit, and S. Gaisford, “Effect of geometry on drug release from 3D printed tablets,” *Int. J. Pharm.*, vol. 494, no. 2, pp. 657–663, 2015, doi: 10.1016/j.ijpharm.2015.04.069.

[96] T. Tagami *et al.*, "Defined drug release from 3D-printed composite tablets consisting of drug-loaded polyvinylalcohol and a water-soluble or water-insoluble polymer filler," *Int. J. Pharm.*, vol. 543, no. 1–2, pp. 361–367, 2018, doi: 10.1016/j.ijpharm.2018.03.057.

[97] S. Jiang, S. Liu, and W. Feng, "PVA hydrogel properties for biomedical application," *J. Mech. Behav. Biomed. Mater.*, vol. 4, no. 7, pp. 1228–1233, 2011, doi: 10.1016/j.jmbbm.2011.04.005.

[98] 3D Sourced, "PVA Filament: The Complete 3D Printing Guide." https://www.3dsourced.com/3d-printer-materials/pva-filament-3d-printing-guide/ (accessed Oct. 06, 2021).

[99] A. Kumar and S. S. Han, "PVA-based hydrogels for tissue engineering: A review," *Int. J. Polym. Mater. Polym. Biomater.*, vol. 66, no. 4, pp. 159–182, 2017, doi: 10.1080/00914037.2016.1190930.

[100] N. A. Alcantar, E. S. Aydil, and J. N. Israelachvili, "Polyethylene glycol–coated biocompatible surfaces," *J. Biomed. Mater. Res. - Part A*, vol. 51, no. 3, pp. 343–351, 2000, doi: /10.1002/1097-4636(20000905)51:3.

[101] J. Chen, S. K. Spear, J. G. Huddleston, and R. D. Rogers, "Polyethylene glycol and solutions of polyethylene glycol as green reaction media," *Green Chem.*, vol. 7, pp. 64–82, 2005.

[102] J. Milton Harris, *Poly (ethylene glycol) chemistry: biotechnical and biomedical applications*. New York, 1992.

[103] L. A. Hockaday *et al.*, "Rapid 3D printing of anatomically accurate and mechanically heterogeneous aortic valve hydrogel scaffolds," *Biofabrication*, vol. 4, no. 3, pp. 1–12, 2012, doi: 10.1088/1758-5082/4/3/035005.

[104] G. M. Cruise, D. S. Scharp, and J. A. Hubbell, "Characterization of permeability and network structure of interfacially photopolymerized poly(ethylene glycol) diacrylate hydrogels," *Biomaterials*, vol. 19, no. 14, pp. 1287–1294, 1998, doi: 10.1016/S0142-9612(98)00025-8.

[105] J. A. S. Neiman *et al.*, "Photopatterning of hydrogel scaffolds coupled to filter materials using stereolithography for perfused 3D culture of hepatocytes," *Biotechnol. Bioeng.*,

vol. 112, no. 4, pp. 777–787, 2015, doi: 10.1002/bit.25494.

[106] E. Ilhan *et al.*, "Development of Satureja cuneifolia-loaded sodium alginate/polyethylene glycol scaffolds produced by 3D-printing technology as a diabetic wound dressing material," *Int. J. Biol. Macromol.*, vol. 161, pp. 1040–1054, 2020, doi: 10.1016/j.ijbiomac.2020.06.086.

[107] R. Melnikova, A. Ehrmann, and K. Finsterbusch, "3D printing of textile-based structures by Fused Deposition Modelling (FDM) with different polymer materials," *IOP Conf. Ser. Mater. Sci. Eng.*, vol. 62, no. 1, pp. 1–6, 2014, doi: 10.1088/1757-899X/62/1/012018.

[108] S. A. Raj, E. Muthukumaran, and K. Jayakrishna, "A Case Study of 3D Printed PLA and Its Mechanical Properties," *Mater. Today Proc.*, vol. 5, no. 5, pp. 11219–11226, 2018, doi: 10.1016/j.matpr.2018.01.146.

[109] S. R. Rajpurohit and H. K. Dave, "Flexural strength of fused filament fabricated (FFF) PLA parts on an open-source 3D printer," *Adv. Manuf.*, vol. 6, pp. 430–441, 2018, doi: 10.1007/s40436-018-0237-6.

[110] Z. Qu, D. Yin, H. Zhou, X. Wang, and S. Zhao, "Cellular morphology evolution in nanocellular poly (lactic acid)/thermoplastic polyurethane blending foams in the presence of supercritical N 2," *Eur. Polym. J.*, vol. 116, pp. 291–301, 2019, doi: 10.1016/j.eurpolymj.2019.03.046.

[111] C. Zhang *et al.*, "Thermal, mechanical and rheological properties of polylactide toughened by expoxidized natural rubber," *Mater. Des.*, vol. 45, pp. 198–205, 2013, doi: 10.1016/j.matdes.2012.09.024.

[112] M. Rahman, N. R. Schott, and L. K. Sadhu, "Glass Transition of ABS in 3D Printing," in *Proceedings of the 2016 COMSOL conference*, 2016, pp. 1–5.

[113] J. Xiao and Y. Gao, "The manufacture of 3D printing of medical grade TPU," *Prog. Addit. Manuf.*, vol. 2, no. 3, pp. 117–123, 2017, doi: 10.1007/s40964-017-0023-1.

[114] LNS Technologies, "Natural TPU pellets." https://www.techkits.com/products/resin-tpunat-90a/ (accessed Feb. 10, 2022).

[115] A. McElroy and M. Hyman, "Biodegradation of Ether Pollutants," in *Consequences of Microbial Interactions with Hydrocarbons, Oils, and Lipids: Biodegradation and*

Bioremediation, R. J. Steffan, Ed. Cham: Springer International Publishing, 2019, pp. 303–331.

[116] A. D. Valentine *et al.*, "Hybrid 3D Printing of Soft Electronics," *Adv. Mater.*, vol. 29, no. 1703817, pp. 1–8, 2017, doi: 10.1002/adma.201703817.

[117] N. N. Jason, W. Shen, and W. Cheng, "Copper Nanowires as Conductive Ink for Low-Cost Draw-On Electronics," *ACS Appl. Mater. Interfaces*, vol. 7, pp. 16760–16766, 2015, doi: 10.1021/acsami.5b04522.

[118] Z. Wang, X. Guan, H. Huang, H. Wang, W. Lin, and Z. Peng, "Full 3D Printing of Stretchable Piezoresistive Sensor with Hierarchical Porosity and Multimodulus Architecture," *Adv. Eng. Mater.*, vol. 29, no. 1807569, pp. 1–8, 2019, doi: 10.1002/adfm.201807569.

[119] S. D. Lacey *et al.*, "Extrusion-Based 3D Printing of Hierarchically Porous Advanced Battery Electrodes," *Adv. Mater.*, vol. 30, no. 1705651, pp. 1–9, 2018, doi: 10.1002/adma.201705651.

[120] K. Fu, Y. Yao, J. Dai, and L. Hu, "Progress in 3D Printing of Carbon Materials for Energy-Related Applications," *Adv. Mater.*, vol. 29, no. 1603486, pp. 1–20, 2017, doi: 10.1002/adma.201603486.

[121] N. W. S. Pinargote, A. Smirnov, N. Peretyagin, A. Seleznev, and P. Peretyagin, "Direct Ink Writing Technology (3D Printing) of Graphene-Based Ceramic Nanocomposites: A Review," *Nanomaterials*, vol. 10, no. 1300, pp. 1–48, 2020, doi: 10.3390/nano10071300.

[122] Z. Hou, H. Lu, Y. Li, L. Yang, and Y. Gao, "Direct Ink Writing of Materials for Electronics-Related Applications: A Mini Review," *Front. Mater.*, vol. 8, pp. 1–8, 2021, doi: 10.3389/fmats.2021.647229.

[123] M. Beecroft, "Digital interlooping: 3D printing of weft-knitted textile-based tubular structures using selective laser sintering of nylon powder," *Int. J. Fash. Des. Technol. Educ.*, vol. 12, no. 2, pp. 218–224, 2019, doi: 10.1080/17543266.2019.1573269.

[124] Wikipedia, "Nylon 12," 2021. https://en.wikipedia.org/wiki/Nylon_12#:~:text=Nylon 12 is a nylon,the name "Nylon 12". (accessed Feb. 13, 2022).

[125] H. Zarringhalam, N. Hopkinson, N. F. Kamperman, and J. J. de Vlieger, "Effects of

processing on microstructure and properties of SLS Nylon 12," *Mater. Sci. Eng. A*, vol. 435–436, pp. 172–180, 2006, doi: 10.1016/j.msea.2006.07.084.

[126] Y. Shi, Z. Li, H. Sun, S. Huang, and F. Zeng, "Effect of the properties of the polymer materials on the quality of selective laser sintering parts," *Proc. Inst. Mech. Eng. Part L J. Mater. Des. Appl.*, vol. 218, no. 3, pp. 247–252, 2004, doi: 10.1243/1464420041579454.

[127] T. Spahiu, E. Canaj, and E. Shehi, "3D printing for clothing production," *J. Eng. Fiber. Fabr.*, vol. 15, pp. 1–8, 2020, doi: 10.1177/1558925020948216.

[128] S. Kim, H. Seong, Y. Her, and J. Chun, "A study of the development and improvement of fashion products using a FDM type 3D printer," *Fash. Text.*, vol. 6, no. 9, pp. 1–24, 2019, doi: 10.1186/s40691-018-0162-0.

[129] R. Uysal and J. B. Stubbs, "A new method of printing multi-material textiles by fused deposition modelling (FDM)," *Tekstilec*, vol. 62, no. 4, pp. 248–257, 2019, doi: 10.14502/Tekstilec2019.62.248-257.

[130] MatterHackers, "PORO-LAY LAY-FOMM 40 Porous Filament - 1.75mm (0.25kg)." https://www.matterhackers.com/store/3d-printer-filament/poro-lay-lay-fomm-filament-175mm (accessed Jan. 26, 2022).

[131] Nervous System, "Kinematics Bodice," 2014. https://n-e-r-v-o-u-s.com/projects/tags/3dprint/albums/kinematics-clothing/ (accessed Nov. 03, 2021).

[132] J. W. Boley, E. L. White, G. T.-C. Chiu, and R. K. Kramer, "Direct Writing of Gallium-Indium Alloy for Stretchable Electronics," *Adv. Funct. Mater.*, vol. 24, no. 23, pp. 3501–3507, 2014, doi: 10.1002/adfm.201303220.

[133] C. C. Seepersad, "Challenges and Opportunities in Design for Additive Manufacturing," *3D Print. Addit. Manuf.*, vol. 1, no. 1, 2014, doi: 10.1089/3dp.2013.0006.

[134] H. W. Tan, T. Tran, and C. K. Chua, "A review of printed passive electronic componentsthrough fully additive manufacturing methods," *Virtual Phys. Prototyp.*, vol. 11, no. 4, pp. 271–288, 2016, doi: 10.1080/17452759.2016.1217586.

[135] S. Khan, L. Lorenzelli, and R. S. Dahiya, "Technologies for printing sensors and electronics over large flexible substrates: A review," *IEEE Sens. J.*, vol. 15, no. 6, pp. 3164–3185, 2015, doi: 10.1109/JSEN.2014.2375203.

[136] F. Cai *et al.*, “Aerosol jet printing for 3-D multilayer passive microwave circuitry,” *2014 44th Eur. Microw. Conf.*, pp. 512–515, 2014, doi: 10.1109/EuMC.2014.6986483.

Chapter 3

Additive manufacturing of interlaced fibrous structures

(Adanur, S., and Jayswal, A., *"Additive manufacturing of interlaced fibrous structures",* Rapid Prototyping Journal, vol. 27, No. 4, pp. 671-681, 2021.)
(Adanur, S., Jayswal, A., Griffin, K.O. and Hancock, J.L. *"Additive manufacturing of weft knitted and braided fabric structures with fused deposition modeling",* The Journal of the Textile Institute, 2023.)

Abstract

The purpose of this research is to design, 3D print and analyze mechanical as well as microstructural behavior of interlaced fibrous structures. A series of plain weave, twill weave, weft-knitted and braided fabric structures are designed using computer-aided design (CAD) software, Solidworks and printed using Fused Deposition Modeling (FDM) machine to determine the best model that could be printable. The structures were designed in such a way that the fabricated yarns with pure polylactic acid (PLA) were not sticking to each other in the plain weave and twill weave fabric structure. The plain weave, twill weave and braided fabric specimens were printed in vertical orientation and weft-knitted structure in horizontal orientation. Tensile and three-point bending (flexural) tests were conducted for twill weave and weft-knitted fabrics whereas compression test were performed for braided structures. optical microscope was used to study the microscopic structures of the yarns and fabric structures. Future work should include improvement of the structure and exploration of different polymers and their composites to increase the tensile, bending, and other strengths to make the 3D printed structures more flexible and stronger. Future research should also focus on the large-scale manufacturing of 3D printed fabrics. This paper supports work on wearable 3D printed fabrics.

3.1. Introduction

Typically, fabrics are formed by yarns, yarns by fiber(s), and fibers by polymer molecules [1]. A polymer is a large chain-like molecular structure produced by a combination of many small repeating molecules called monomers [2]. Textile fibers are hair-like structures whose diameter is several hundred times smaller than their lengths. Natural fibers are extracted from animals and plants [1] [3] and synthetic fibers from organic and inorganic polymers [3]. Synthetic fibers are manufactured by different spinning methods including melt, dry and wet spinning. A number of fibers are spun together to form a yarn following some yarn spinning processes such as ring spinning, open-end rotor spinning, air-jet spinning and friction spinning.

The characteristics of polymers, fibers and yarns determine certain properties of fabrics. A combination of warp yarns (also called machine-direction yarns or vertical yarns) and weft yarns (also called cross-machine direction yarns or filling yarns) forms a fabric [4]. The appearance of a fabric depends on the interlacing pattern of warp yarns and weft yarns. The main methods of fabric production are weaving, knitting, braiding, tufting and nonwoven manufacturing [2] [5]. Weaving is the most common method of fabric production which is produced by interlacing warp and weft yarns. Because of the ease of variation in interlacing pattern, different weave designs such as plain, warp rib, filling rib, twill, basket, satin, etc. and their many variations are possible to produce. A typical modern weaving machine consists of approximately 5000 parts [1]; as a result they are complicated [6] and expensive. Since the production process goes through different phases like fiber production, yarn production and many inter processes, it consumes a lot of time and human resources to manufacture fabrics.

Although traditional manufacturing has advanced the industrial revolution, it holds some shortcomings which led to the thought of new methods such as additive manufacturing (AM), which is also referred to as three-dimensional (3D) printing. 3D printing is not just a mere emerging technology but also has the potential to become a truly transformative technology within the next few decades [7]. Its ability to build almost any designable object [7] increases efficiency, reduces waste, and is making manufacturing more sustainable. The time it takes for the products to get to the markets is much shorter since it eliminates most of the time-consuming processes in the design and manufacturing stages. It does not need any extra parts and/or accessories to develop and manufacture the products. Therefore, the time and costs can be minimized with this method.

Figure 3.1 shows the comparison of fabric manufacturing processes by the traditional methods and AM method. The former method first produces the fibers from polymers by different fiber spinning methods, then, the fibers are spun together to make yarns and yarns are intertwined in a certain pattern to make a fabric. This is a lengthy process and consumes lots of energy, time, space, and human resources. In general, for different fabric designs, different machines and different skilled workers are required. On the other hand, AM eliminates all the intermediate steps and manufactures the fabrics directly from polymers which makes it an efficient manufacturing method. With a CAD model, AM can produce any design of fabrics within a short period of time without utilizing a huge number of workers.

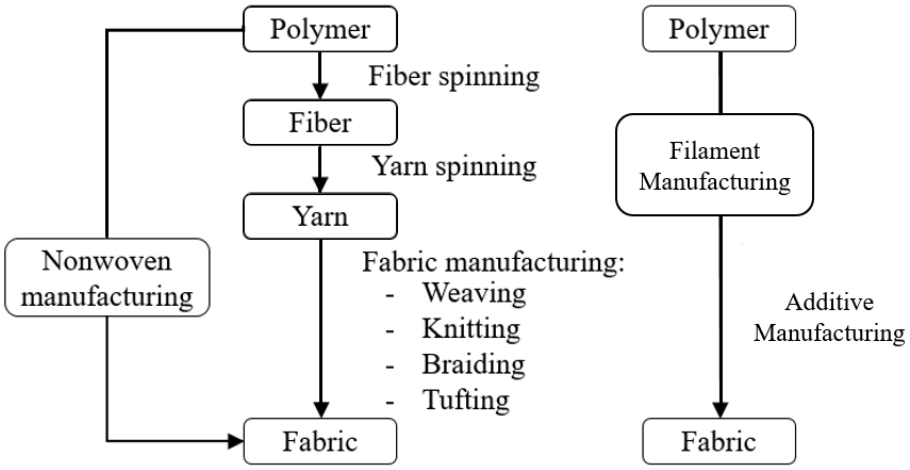

Figure 3.1. Comparison of fabric manufacturing: Traditional (left) versus AM Method (right).

Knitting involves the inter-looping of one yarn system into continuously connecting vertical columns (wales) and horizontal rows (courses) of loops to form a knitted fabric structure [2]. There are two types of knit structures: weft knit, and warp knit. Weft knit fabrics are formed by a yarn which forms into loops successively at each needle during the same knitting cycle [8]. Weft knitting action occurs in the course direction, as indicated by a solid dark line in Figure 3.2a. Several types of knitting stitches are used in weft knit fabrics including plain, tuck, purl (reverse), and float (miss). The plain stitch fabric has all of its loops drawn through the same side of the fabric. The plain fabric has a smooth face and a rough back. These fabrics have good stretchability especially in the course direction [2]. Warp knit fabrics are produced by using a warp beam containing several hundred or thousand ends. Each end passes through its own needle and is formed into loops which intersect with adjacent loops. Thus, a flat looped fabric is knitted using only warp yarns without the necessity of weft yarns being interwoven. Warp knitting takes place in the wale direction of the fabric, as indicated by a solid dark line in Figure 3.2b.

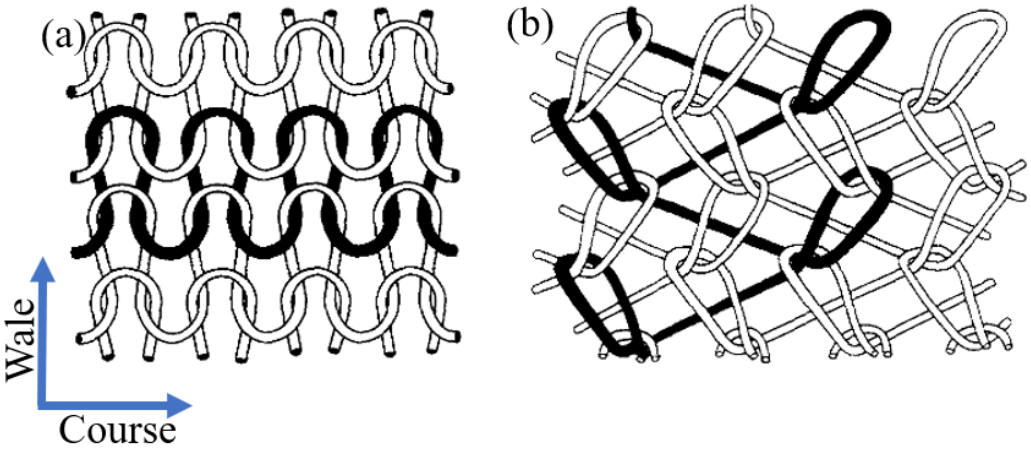

Figure 3.2. Schematic diagrams showing different types of knit fabric structures: (a) Weft knit, and (b) Warp knit [8].

A braid structure is formed by crossing a number of yarns diagonally so that each yarn passes alternately over and under one or more of the others. The most common designs of braids are diamond braid, regular braid, and Hercules braid. These braids are categorized as biaxial braids since the yarns are positioned in two different directions at certain angle (oriented at an angle in the $+\theta$ and $-\theta$ directions) [9]. A diamond braid has the intersection of yarns diagonally with a yarn over and under another yarn (1/1 repeating pattern). A regular braid has a repeating pattern of a yarn over and under two yarns (2/2 repeating pattern). Similarly, Hercules braid has 3/3 intersection repeating pattern [2]. Triaxial braided fabric has three different sets of yarns: ± braids (±bias) and warp (axial). Braided yarns intertwin with each other around the axial yarns at about 45° angle whereas the axial yarns do not interlace or intertwin with other yarns and are trapped between the two braided yarns in the structure. The schematic diagram showing the formation of biaxial and triaxial braid structures are presented in Figure 3.3a and b. Bifurcated braid structures have two divisions of braid structure at one end as shown in Figure 3.3c.

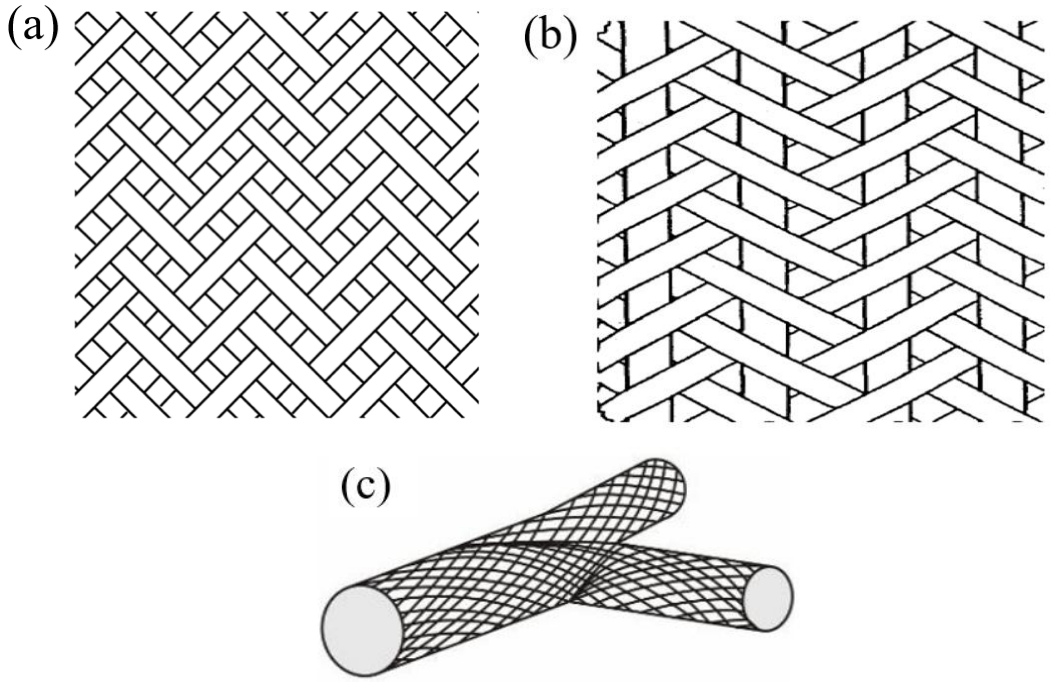

Figure 3.3. Schematic diagrams showing two-dimensional (2D) braids. (a) Regular braid representing biaxial braid, (b) Triaxial braid [9], and (c) Bifurcated braid [10].

The development of additive manufacturing (AM) methods has attracted the attention of several researchers on 3D printing of textile-based structures. The most common methods used for 3D printing of fabrics are fused deposition modeling (FDM), and selective laser sintering (SLS). Few materials explored are poly(lactic) acid (PLA), acrylonitrile butadiene styrene (ABS), thermoplastic polyurethane (TPU), and nylon. Melnikova et. al. explored several polymeric materials such as PLA, soft PLA, and BendLay and 3D printed weft knitted fabric structures using FDM method. They found that FDM is not suitable for 3D printing of fine models, and soft PLA can be used for future production of textile-based structures [11]. Partsch et. al. 3D printed three different plain weave fabric structures using ABS and found that it is possible to print textile structures [12]. Lussenburg et. al. attempted to design a wearable garment using PLA with 3D printing and concluded that final product does not resemble all the fabric properties and needs further research to improve tear resistance and softness of the final structures [13]. Spahiu et. al. designed and 3D printed a wearable dress using the material, FilaFlex with a shore hardness of A82. They realized that further research is required to achieve the textile properties to replace the traditional way of garment manufacturing [14]. Kim et. al. used TPU filament and 3D printed unit cells inspired by spider web. All the unit cells were assembled, and the final 3D printed cloth was obtained [15]. Beecroft designed and 3D printed textile-based tubular weft knitted structures using SLS

method with nylon powder [16]. The details on the use of nylon powder in SLS method can be found in ref. [17]. The printed structures were inspected visually.

This chapter focuses mainly on the design and 3D printing of plain weave, twill weave, weft-knitted and braided fabric structures using PLA. Mechanical properties and microscopic structures are studied for the 3D printed samples. This work also shows the feasibility of 3D printed fabrics by presenting a comprehensive design and manufacturing methods using AM to replace the traditional fabric manufacturing methods.

3.2. Materials and methods

In this section, the design of fabrics structures, fabrication of samples using fused deposition modeling (FDM) additive manufacturing method, and experimental set up for the property analysis of the samples are described.

3.2.1. Material selection and 3D printing

PLA of diameter 1.75 mm and Dremel 3D45 machine was used to 3D print the plain weave and twill weave fabrics, whereas Polymaker PolyLite ^{TM} black PLA filament of diameter 2.85 mm and 3D printer, LulzBot Taz Pro was employed to fabricate the weft-knitted and braided fabric samples. PLA was chosen for this research because of its availability, biodegradable properties, and low cost. The filaments are used as received. The fabrics were designed in CAD software Solidworks® and exported as an STL document. The STL files of plain weave and twill weave fabrics were imported to an open-source 3D printing software Dremel Digilab 3D Slicer whereas these files of weft-knitted and braided structures were imported to an open-source 3D printing slicing software, Cura LulzBot Edition version 3.6.36 where all the printing commands were given and controlled. The 3D print settings used are the same for all the samples and are shown in Table 3.1.

Table 3.1. 3D printing settings for plain weave, twill weave, weft knitted and braided fabric structures.

Parameters	**Value**
PLA filament diameter	1.75 mm for plain weave and twill weave structures 2.85 mm for weft-knitted and braided structures
Layer Height	0.2 mm
Infill density	100 %
Printing Temperature	225 ℃

Build Plate Temperature	40 ℃
Print Speed	30 mm/s for plain weave and twill weave structures 10 mm/s for weft knitted and braided structures
Travel Speed	120 mm/s for plain weave and twill weave structures 70 mm/s for weft knitted and braided structures

3.2.2. Design and 3D printing of plain weave and twill weave fabrics

The yarns in printing direction are called warp yarns and the perpendicular yarns in cross-printing direction are termed as weft yarns. The nozzle moves in horizontal axis (X-axis) and prints the first layer in horizontal pattern and then moves upward (Z- axis) to print the next layer of the fabric. As a result, the warp yarns lie in X-axis (warp direction) and weft yarns in Z-axis (weft direction). Y-axis represents the thickness of the fabric structure as shown in Figure 3.4.

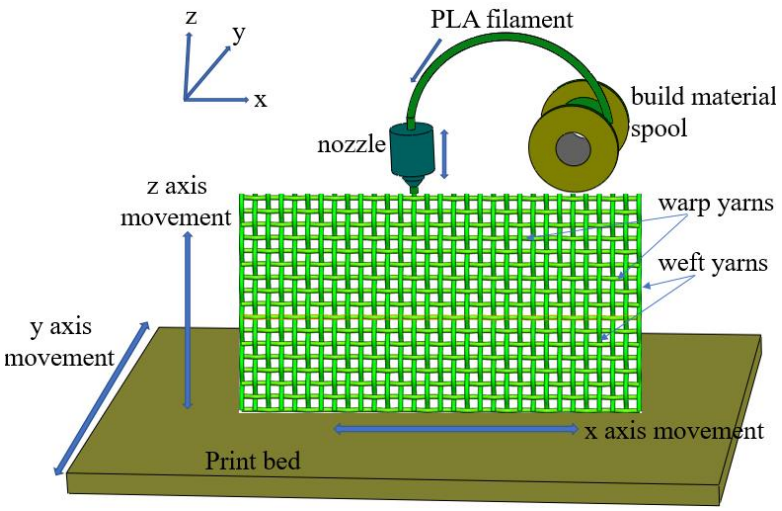

Figure 3.4. Schematic representation of the fused deposition modeling (FDM) setup for 3D printing of 2/1 twill weave fabric-like structures.

3.2.2.1. Plain Weave

Since 3D printing requires a CAD model, a plain weave design was modelled in Solidworks as shown in Figure 3.5. The designed structure had the dimensions of 83mm x 83mm having 17 warp and 17 weft yarns. A solid object made of PLA was 3D printed in a vertical orientation as shown in Figure 3.6. The diameter of each yarn was set to 3 mm and the spacing between two warp yarns as well as two weft yarns was Y = 5 mm (Figure 3.7).

However, all the yarns were fused together and could not be separated because no support material was used for this structure.

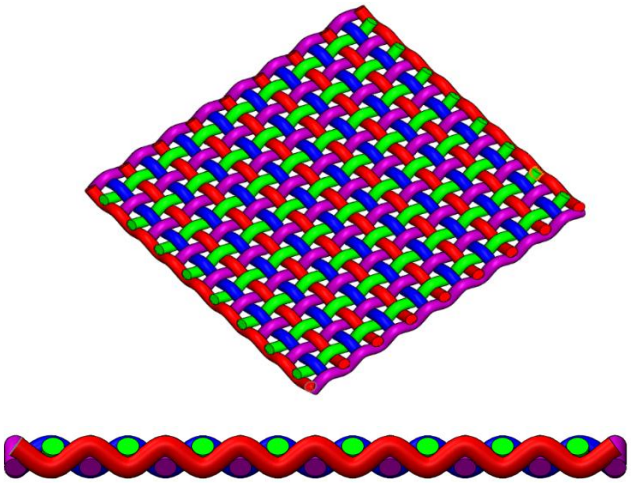

Figure 3.5. CAD model of plain weave fabric.

Figure 3.6. 3D printed plain weave with FDM and PLA.

The design was modified by increasing the spacing between warp yarns and between weft yarns to Y = 10mm with a gap of *h* = 1mm between their crossing points (Figure 3.7). Since all the yarns are supposed to be separate and independent of each other, a support material was necessary to complete the printing process using PLA in three different orientations: flat, vertical and 45° inclination. Since Dremel 3D45 machine does not use material other than PLA for support, it was a challenging task to print the fabric. The support was fused together with the fabric structure and therefore could not be removed. The CAD model was again changed by decreasing the gap from *h* = 1mm to *h* = 0.25mm, keeping other values the same. Support was not provided for the yarns printed which again caused the fibers to be fused. At some

points, fine fibers could be seen clearly and the surface was not smooth. This might have happened due to printing defects.

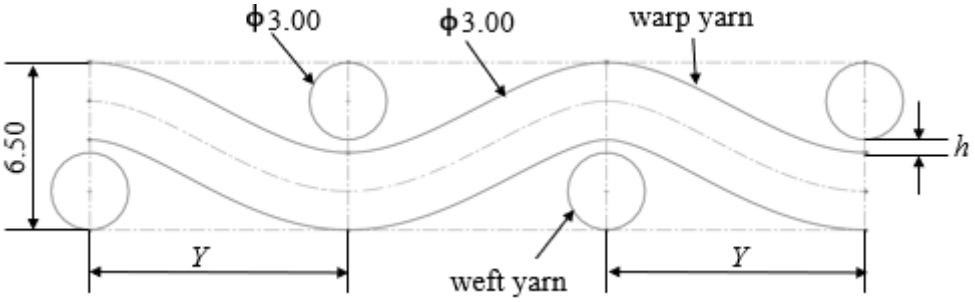

Figure 3.7. Detail view of plain weave fabric (dimensions, in mm).

After a series of modifications in CAD drawing and 3D printing, a flexible and compact woven structure made of PLA with separated yarns was obtained. It was a plain woven fabric-like structure printed in vertical orientation. The yarn diameter was 3mm and the spacing between two warp yarns and two weft yarns was Y = 10mm. The thickness of the structure was 6.5mm which allows to maintain a gap of h = 0.5mm between the yarns at the interlacing point. Figure 3.8 and Figure 3.9 represent the final CAD design of plain weave fabric and 3D printed fabric using PLA, respectively. The support material of PLA was applied only at the crossing points in minimal amount and was removed manually after fabric formation to allow the yarns to move freely. However, the warp yarns in plain weave design were not printed uniformly; the fibers were not fused together well, and the nozzle also failed to extrude the molten polymer which caused diameter variations. This may have happened because the nozzle had to extrude the molten PLA over a long spacing (Y = 10mm) between the yarns without the support in overhanging position. As a result, the 3D printer failed to print uniform warp yarns. Considering all these challenges, it was decided to move forward with a gap of h = 0.5mm at the interlacing points.

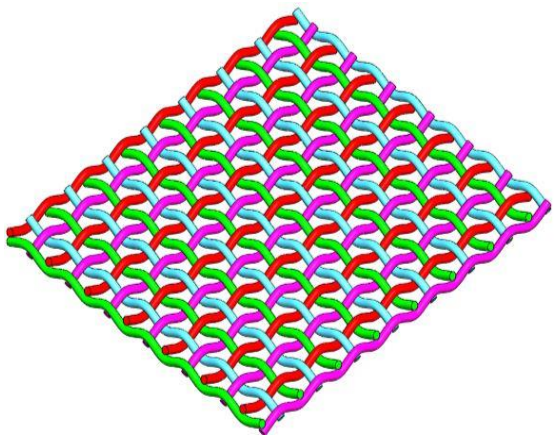

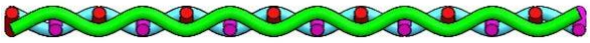

Figure 3.8. Final CAD design of plain weave fabric.

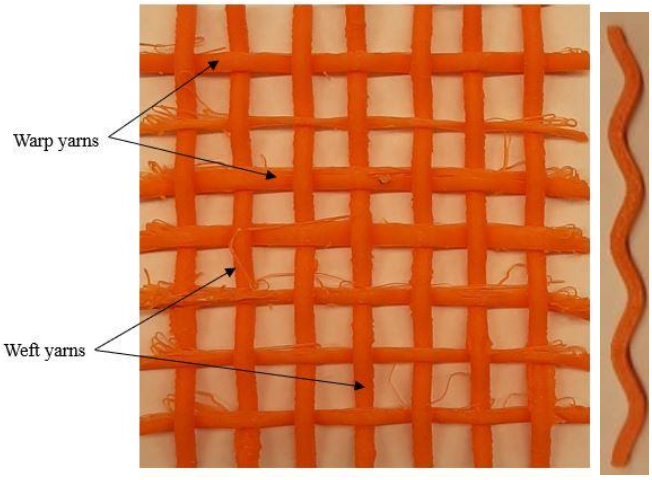

Figure 3.9. FDM PLA plain woven structure 3D printed in vertical orientation (left) and an individual yarn separated from fabric (right).

3.2.2.2. Twill Weave

Next, fabrication of 2/1 twill weave fabric was attempted which was designed by fixing the diameter of each yarn at 1 mm. The spacing between the warp and weft yarns was kept at h = 0.5 mm. The distance between the two weft yarns under warp was 3 mm. The designed fabric was 3D printed with PLA as the main material; however, the printed part had attached yarns that could not be separated. The close observation revealed that the weft yarns under warp were sticking to warp yarns since the spacing was not enough. The warp yarn was passing under one and over two weft yarns such that its bending with different radius of curvatures at different locations caused a difference in the spacing between them. When a warp yarn passes over two weft yarns, some of their parts bulges outside. Figure 3.10 shows 2/1 twill weave fabric design.

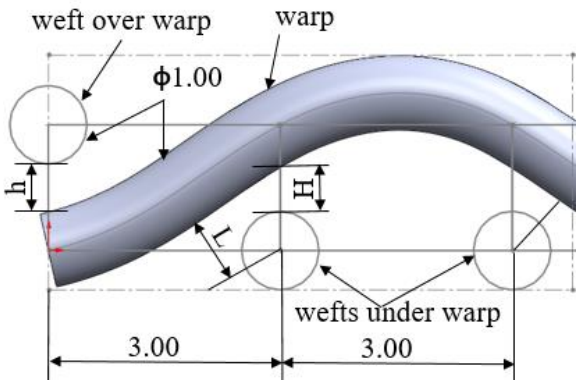

Figure 3.10. 2/1 Twill design (dimensions in mm).

The design was again revised by increasing the value of h from 0.5mm to 0.65mm keeping all the other values the same. This increment resulted in H = 0.59 mm and L = 0.90 mm. After printing, it was observed that the weft yarns under warp were barely touching the surface of the warp yarns and they could be easily separated manually. This structure was flexible, compact and had load bearing strength which was later determined by different tests.

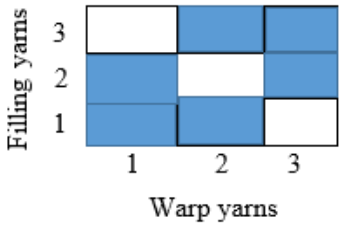

Figure 3.11. Schematic of 2/1 left-hand twill weave.

Figure 3.11 represents the unit cell of 2/1 left hand twill weave design. The columns and rows stand for warp and weft (filling) yarn, respectively. Each warp yarn passes over two and under one filling yarns. While designing this fabric, three different types of warp yarns and filling yarns were used and then assembled appropriately to obtain the shape of the twill fabric.

A detailed explanation with schematic diagram is necessary to better understand the implementation of this design for FDM method. The first warp is running over the first two weft yarns and then under the third weft yarn, over fourth and fifth, under sixth and so on. The second warp is over the first weft, under the second weft, over third and fourth weft, under fifth weft and so on. The third warp is under the first weft, over the second and the third weft, under fourth, over fifth and sixth and so on. Figure 3.12 shows the three successive warp yarns used in the design of 2/1 twill weave fabric. Similarly, the first weft is running under the first two warp yarns and then over the third warp, under fourth and fifth, over sixth and so on. The

second weft is under the first warp, over the second, under the third and the fourth, over fifth, under sixth and so on. The third weft is over the first warp, under the second and the third, over fourth, under fifth and sixth and so on. Figure 3.13 shows the three successive weft yarns used in the design of 2/1 twill weave fabric. The warp and weft yarns were assembled to get the final design. The final CAD design and the 3D printed product are shown in Figure 3.14.

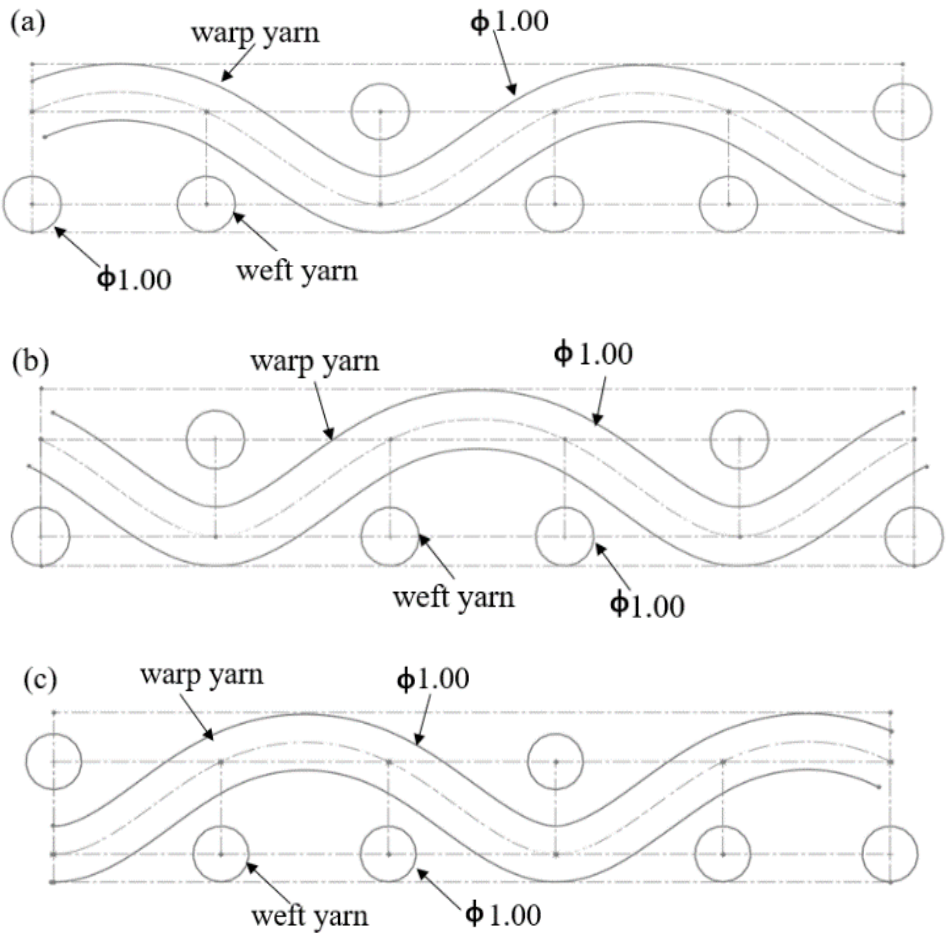

Figure 3.12. Warp profiles of 2/1 twill design: (a) first warp yarn, (b) second warp yarn and (c) third warp yarn.

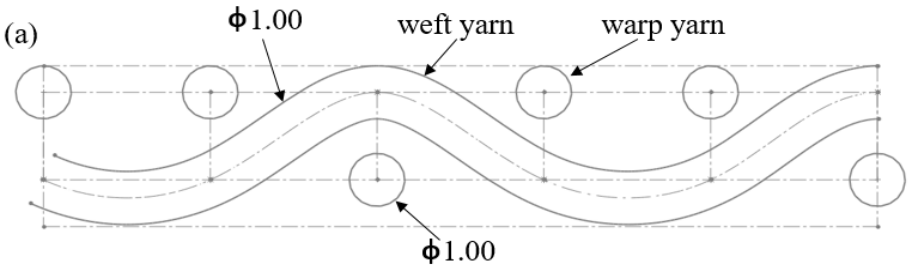

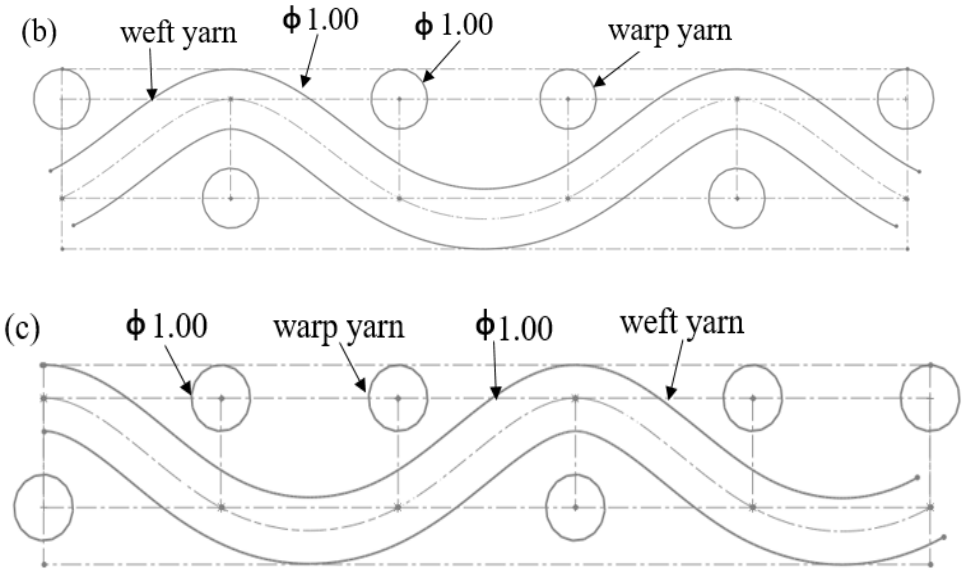

Figure 3.13. Weft profiles of 2/1 twill design: (a) first weft yarn, (b) second weft yarn and (c) third weft yarn.

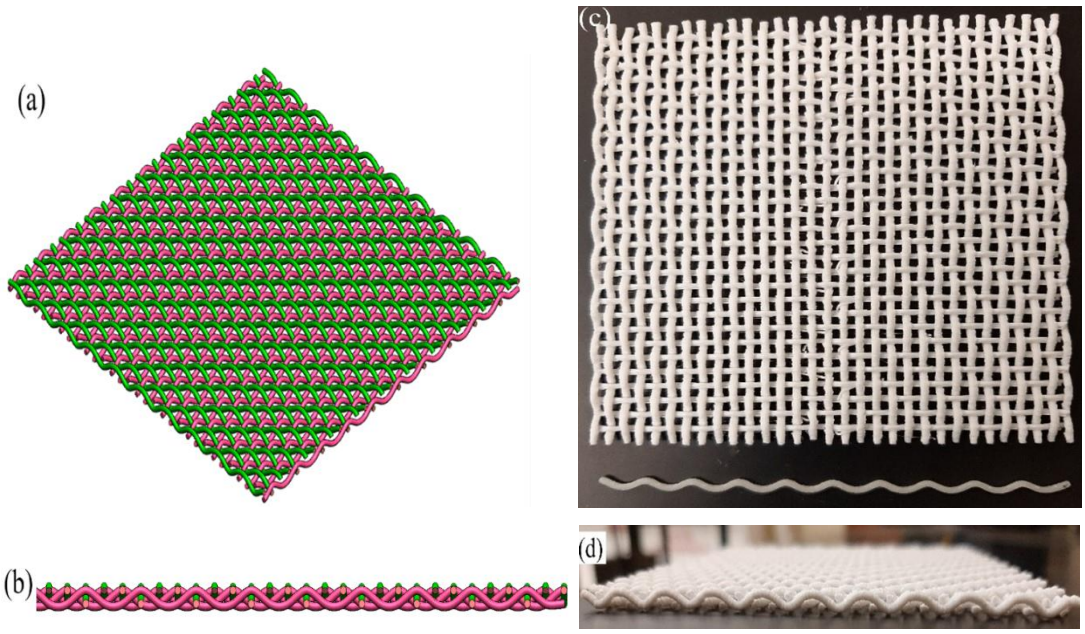

Figure 3.14. CAD model and 3D printed 2/1 twill weave fabric. (a) and (b) CAD design, (c) and (d) 3D printed fabric and a separated yarn.

3.2.3. Design and 3D printing of weft-knitted fabrics

The diameter of each yarn considered was 2.54 mm and the height of each loop was 27.14 mm. The design parameters and the related dimensions are shown in Figure 3.15a. A CAD model of a single loop is shown in Figure 3.15b. Using the linear pattern command in Solidworks® (Version 2021, Education Edition), a yarn was generated. The yarns were then

used to model the entire weft knitted fabric. The vertical columns are known as wales and horizontal rows as courses (Figure 3.15d).

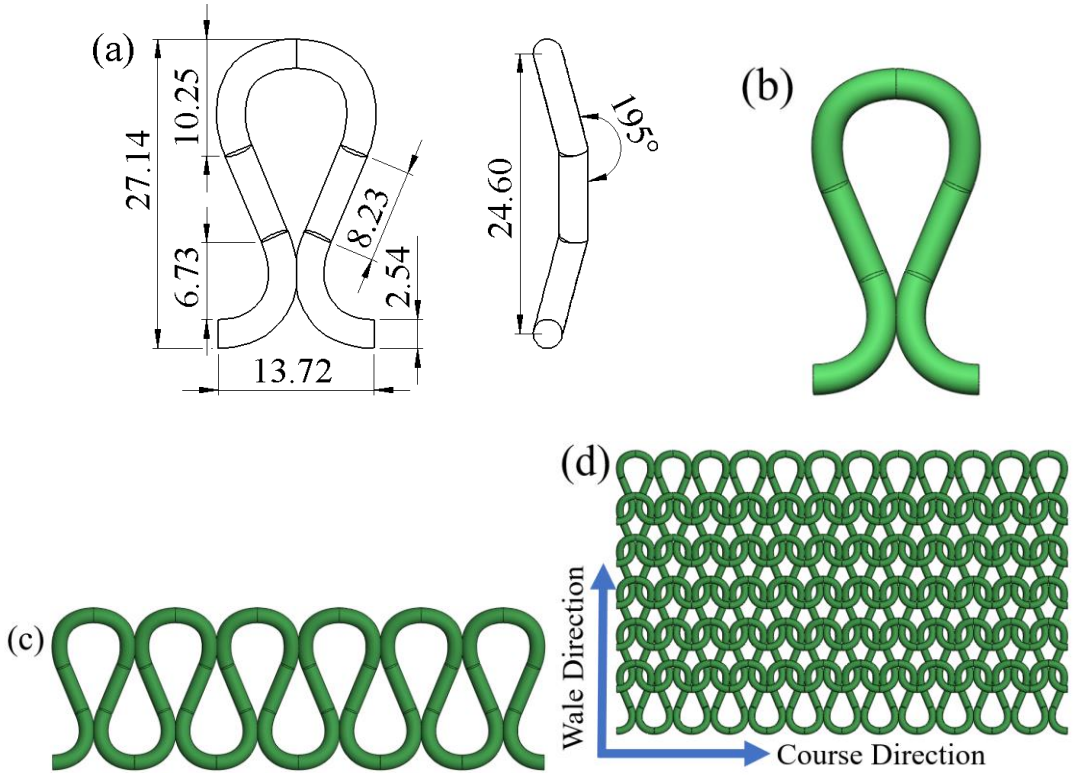

Figure 3.15. Computer-aided design (CAD) modeling of weft knitted fabrics. (a) Design of a single loop, (b) 3D model of a loop, (c) 3D model of a yarn, and (d) 3D model of an entire fabric. The dimensions are given in millimeters (mm).

The 3D printed individual yarn and weft knitted fabric are shown in Figure 3.16. These parts were 3D printed in horizontal (flat) orientation. PLA was used for support structure, and later after the completion of the task, it was removed manually. The printed yarns were initially inspected by stretching, bending, and shearing. The initial observations showed that the yarns were flexible and can be stretched, bent, and sheared to some extent (Figure 3.16 a-e). The tensile and flexural test results of the weft knitted fabrics are presented in Section 3.3.2.

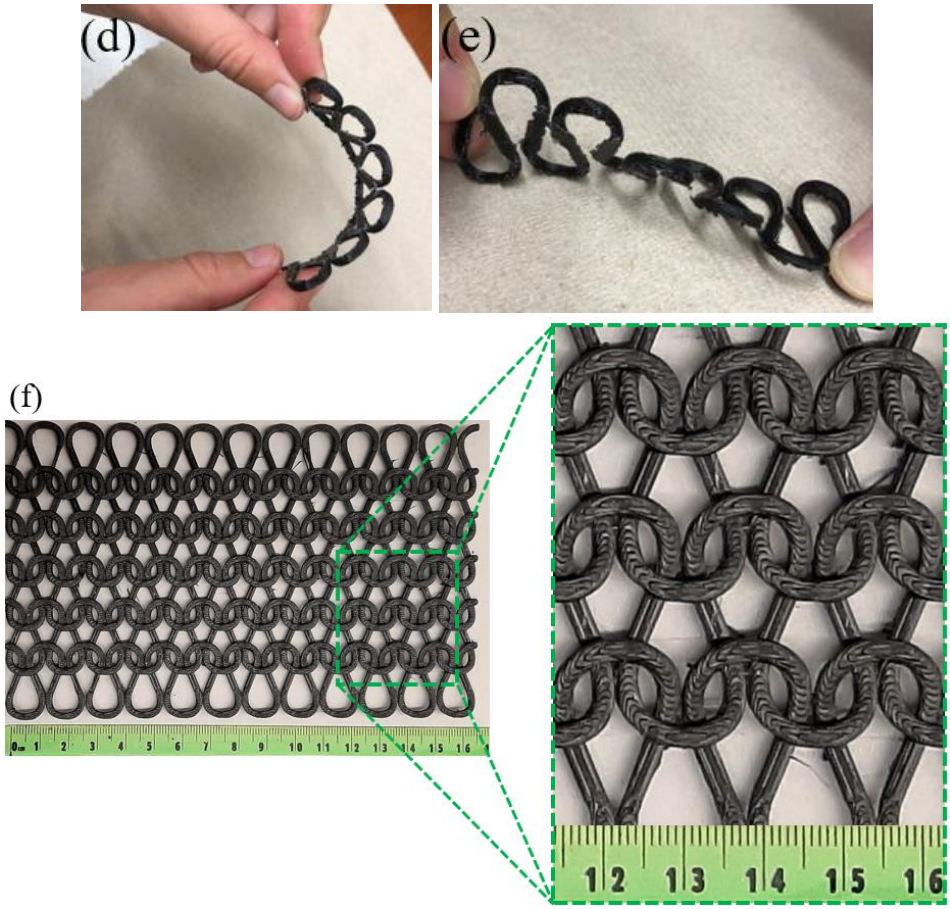

Figure 3.16. Additive manufacturing of weft knitted fabrics. (a) 3D printed single yarn, (b) In-plane stretching of the yarn, (c) In-plane bending of the yarn, (d) Out-of-plane bending of the yarn, (e) Twisting of the yarn, and (f) Weft knitted fabric structure with its magnified view.

3.2.4. Design and 3D printing of braided structures

All the braids were designed to have a yarn of circular cross-section of 2 mm in diameter. A cylindrical structure was generated having a height of 50 mm and outside diameter of 54.55 mm. The CAD modeling was done using SolidWorks® (Version 2021, Education Edition). The design and CAD model of a diamond braid is shown in Figure 3.17. The design and CAD model of regular, Hercules, triaxial and bifurcated braids are included in the Appendix A.

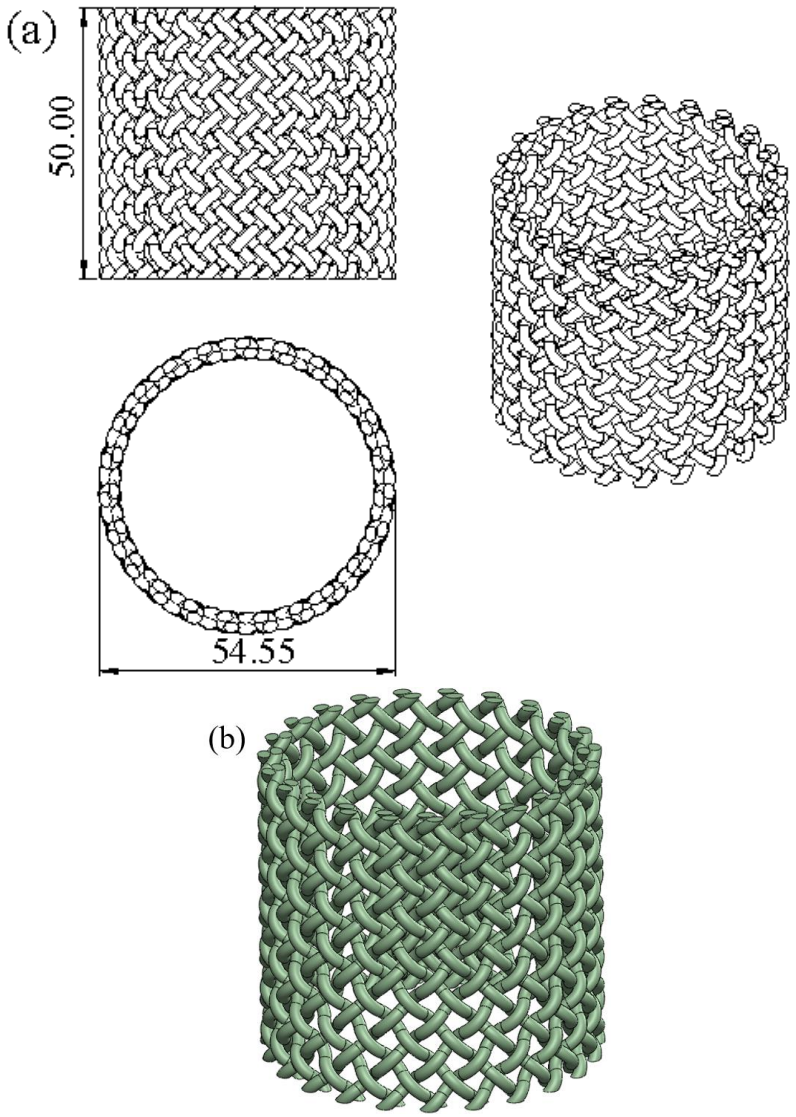

Figure 3.17. Design and CAD modeling of diamond braid fabric structure. (a) Design of a braid, and (b) 3D model of braid. The dimensions are given in millimeters (mm).

Different designs of braiding such as diamond, regular, Hercules, triaxial and bifurcated were 3D printed using PLA filaments as base material. These samples were printed in vertical orientation. The support material was used to print the bifurcated braid and after the completion of the print, it was removed manually. Figure 3.18 shows the printed samples made with PLA.

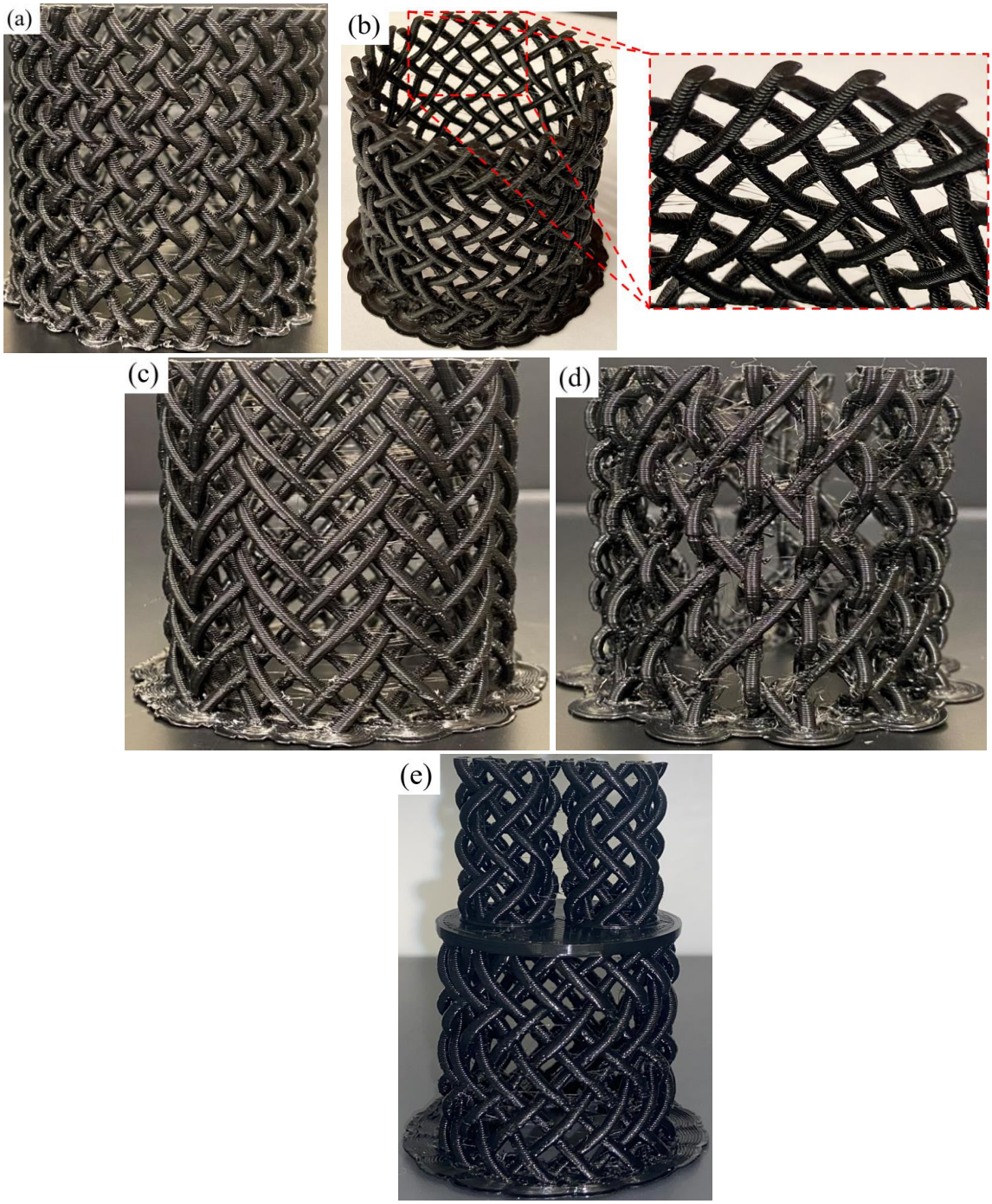

Figure 3.18. 3D printing of different designs of braided structures made of PLA. (a) Diamond braid, (b) Regular braid, (c) Hercules braid, (d) Triaxial braid, and (e) Bifurcated braid.

3.2.5. Mechanical testing of 3D printed twill weave structures

A PLA specimen was dismantled manually to remove its warp yarns and weft yarns for testing. Ten yarns were tested for tensile strength in each direction. ASTM D3822-01 standard test method was used to test the tensile strength of the printed specimens. The diameter of each printed yarn was 1.0 mm. Uniaxial tensile tests of single yarns were performed with 25 mm gauge length and 1 kN load cell at a fixed loading rate of 10 mm/min using Instron 5565

universal testing machine and the corresponding strain was measured. The experimental data were processed to determine the tensile stress at maximum load (σ_t) and the tensile Young's modulus (E_t). Tensile stress at maximum load was calculated using the following equation:

$$\sigma_t = \frac{F_{max}}{A} \tag{3.1}$$

where, F_{max} is the force at maximum load and *A* is the cross-sectional area of the yarn.

For tensile and three-point bending tests of the printed twill structures, samples in warp and weft directions were cut from the printed structures; each set contained 10 specimens with a total of 40 specimens. The dimensions of the specimens were 92 mm (length) x 46 mm (width) x 3.15 mm (thickness). The uniaxial tensile tests for printed twill fabrics were performed by maintaining the same test conditions as single yarns. Tensile stress at maximum load was calculated using the following equation:

$$\sigma_t = \frac{F_{max}}{n * A} \tag{3.2}$$

where, *n* is the number of yarns (warps or wefts).

For 3-point bending tests of the 3D printed fabrics, ASTM D790-17 standard test method was followed using Instron 5565 testing machine with a loading speed of 10 mm/min, and support span of 40 mm; the structure is assumed as a rectangular object. The maximum normal flexural stress in 3-point bending test can be written as:

$$\sigma_f = \frac{3F_{max}L}{2wt^2} \tag{3.3}$$

where, F_{max} is the force at maximum flexural load, *L* is the length of support span, *w* is the width of specimen, and *t* is the thickness of the specimen. The maximum strain ϵ_f of the outer surface at mid-span was calculated using the following relation:

$$\epsilon_f = \frac{6\delta t}{L^2} \tag{3.4}$$

where, δ is the flexural displacement at maximum flexural load. The flexural modulus of elasticity E_f is the ratio of flexural stress to the corresponding flexural strain at a given point on the stress-strain curve, which can be calculated as:

$$E_f = \frac{L^3 m}{4wt^3} \tag{3.5}$$

where, *m* is the gradient (i.e., slope) of the initial straight-line portion of the load deflection curve.

3.2.6. Mechanical testing of 3D printed weft knitted structures

The 3D printed weft knitted fabric structure was considered as a rectangular specimen. The dimensions of the specimens were 160 mm (length), 51 mm (width) and 4.50 mm (thickness). Tensile tests were performed with a gauge length of 25 mm and a fixed loading rate of 3 mm/min using Instron 5565 universal testing machine with 5 kN load cell following the ASTM D5035-11 Standard Test Method for Breaking Force and Elongation of Textile Fabrics (Strip Method) [18]. The force-displacement graphs were obtained. The experimental set up of the tensile test is shown in Figure 3.19a. The tensile test in the wale direction is not performed because the length of the fabric in this direction is not sufficient enough. The length of sample is 51 mm in this direction. After fixing the sample in tensile testing fixtures, the gage length was less than 8 mm, which is not considered good for this type of sample.

The flexural (3-point bending) tests were performed in both course and wale directions using Instron 5565 universal testing machine with a loading rate of 1.27 mm/min (0.05 in/min), and a support span of 51.05 mm (2.01 in) following the ASTM D790-17 Standard Test Methods for Flexural Properties of Unreinforced and Reinforced Plastics and Electrical Insulating Materials [19]. The experimental set up of the flexural ensile test is shown in Figure 3.19b.

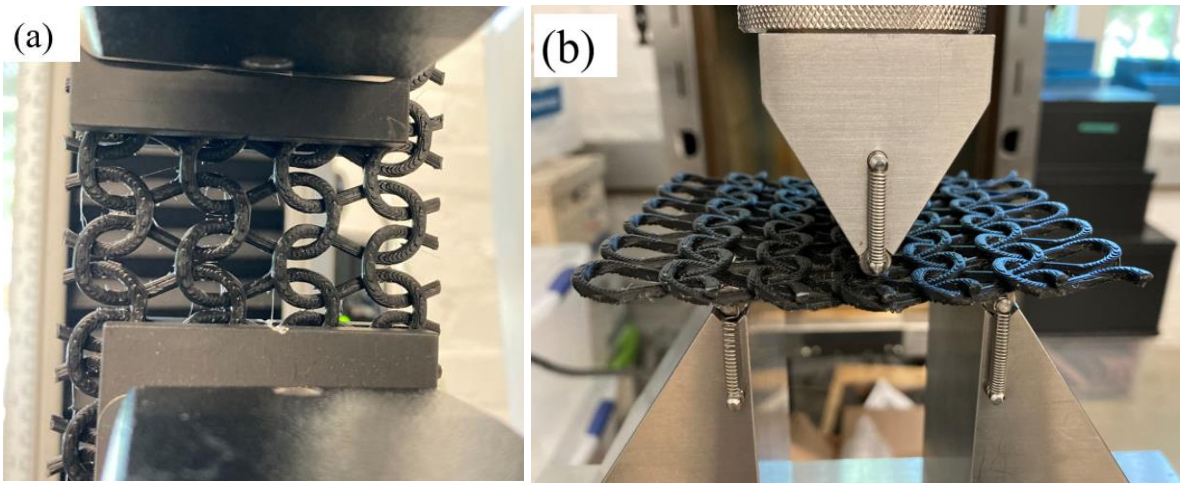

Figure 3.19. Representative mechanical test set up of knitted fabric structures. (a) Tensile test set up, and (b) Flexural (3-point bending) set up.

3.2.7. Mechanical testing of 3D printed braided structures

The 3D printed braided structures were considered as a cylinder having a circular cross-section. The height of the structures was 50 mm with an outer diameter of 54.55 mm for diamond, regular, Hercules, and triaxial braids. The diameter of individual yarns was 2 mm. The height of bifurcated braid was 62.50 mm, outer diameter 40 mm and diameter of individual yarns was 2 mm. Compression test was performed using Instron 5565 universal testing machine with a compressive load rate of 2 mm/min following the ASTM D695-15 Standard Test Method for Compressive Properties of Rigid Plastics [20]. This test method is suitable for testing unreinforced cellular materials. The braids bulged outside somewhere halfway of their height. A representative compression test on diamond braid is shown in Figure 3.20.

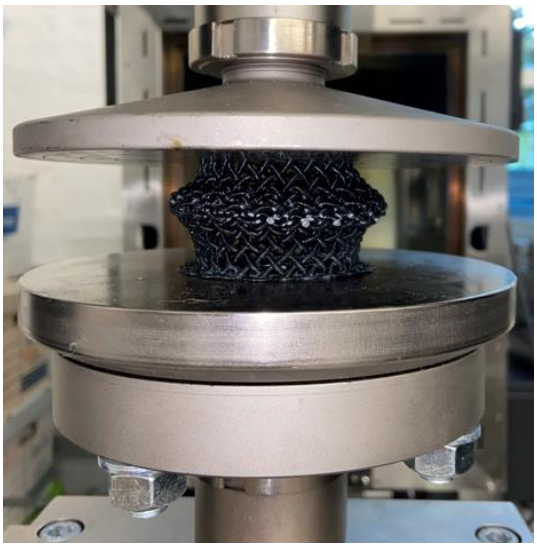

Figure 3.20. Representative compression test on diamond braid.

3.2.8. Optical microscope analysis

The cross-sections and longitudinal surfaces of yarns fractured during tensile testing were studied using an optical microscope (Olympus SZX7, Japan).

3.3. Results and discussion

3.3.1. Microscopic Analysis

The microscopic structures of warp yarns and weft yarns were analyzed using an optical microscope. It was found that the yarns are printed like continuous filaments in printing direction and like short fibers in cross-printing direction. This contrast in structure caused the warp yarns to be stronger than the weft yarns, which can be classified as an orthotropic material. The weft yarns are formed by addition of small cross-sectional materials layer upon layer, which resulted in non-uniform and rough surfaces that contain peaks and valleys, causing weaker interlayer bonding, which increases the chances to develop cracks and ultimately failure even under small loads applied. The warp yarns are formed by the fusion of long fibers extruded through the nozzle resulting in more smooth and uniform surfaces. The alignment of fiber material along the yarn axis makes the warp yarns stronger along the longitudinal direction under applied loads; however, fusion between the successive fibers is not very good. Two neighboring layers can be easily differentiated from each other, and the valleys formed at their fusion lines can be observed, which means that the inter-layer fusion would not be strong. Figure 3.21 shows optical microscope images at 500 µm resolution. It was also observed that few warp yarns had an additional polymeric material attached as shown in Figure 3.21 (c) and (d), which may be due to the printing defects.

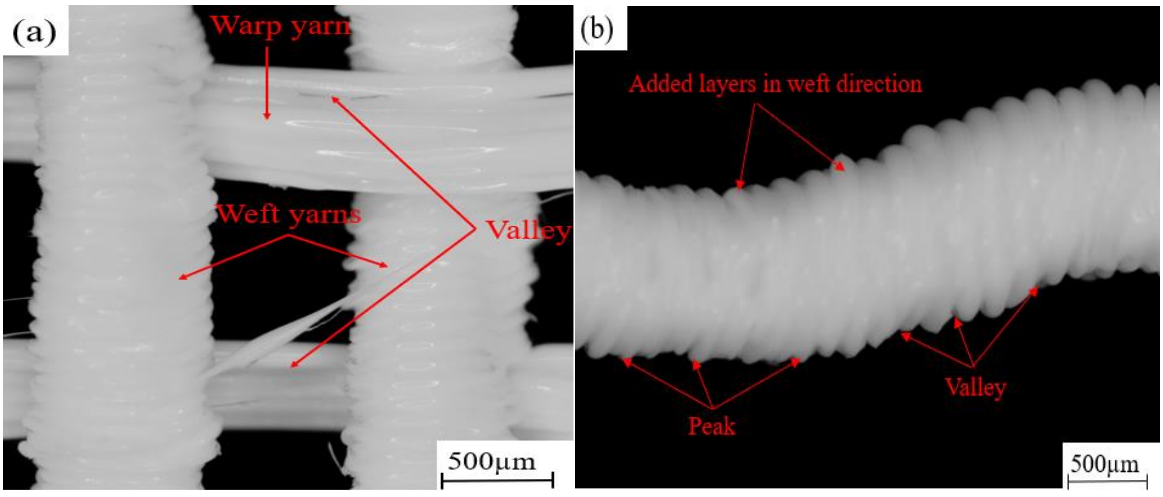

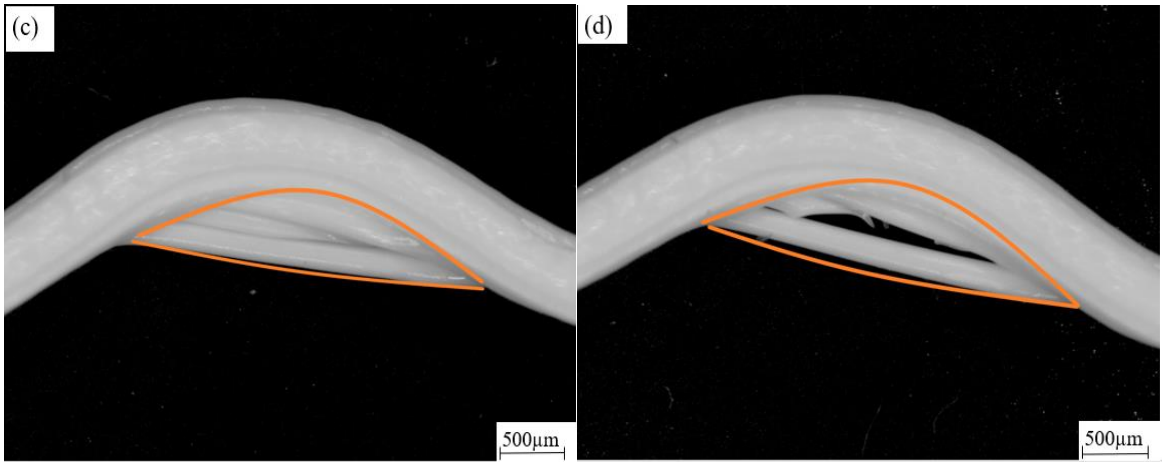

Figure 3.21. Optical microscope images showing the details of the surfaces of 3D printed 2/1 twill structures. (a) Top view of the printed twill structure showing the continuous and short fibers in warp and weft yarns, respectively, (b) Weft yarn profile showing each added layer in weft direction, (c) and (d) Printing defects in some warp yarns.

The microscopic examinations of the printed twill fabrics also revealed that the yarns contain voids in the cross-sections as well as on the surfaces. Voids in FDM are caused by many factors such as nozzle size and shape, layer orientations, cooling rate, melt flow pressure and velocity gradients [20]. The voids play a major role in weakening the structure and develop crack initiation due to stress concentrations. The bonding of a layer with its neghbouring layer is highly dependent on the energy of semi-molten polymer and thus, the temperature of successive layers is important to achieve a good quality of bond. Figure 3.22 shows inter-layer bonding and voids in 3D printed warp and weft yarns at their cross-sections and surfaces. In warp yarns, the voids look like channels between the layers and a number of voids are present at their cross-sections. However, the overall volume of voids in warp yarns is less in comparison with the weft yarns. In weft yarns, more uniform fusion of extruded polymer is observed at the cross-sections but the voids are spotted as holes on their surfaces. The sizes of the voids are inconsistent and ramdomly spread. The deposition of each layer and bonding between them is also not uniform, especially in the curved regions. The number of voids and their sizes must be reduced to improve the mechanical strength of the structure.

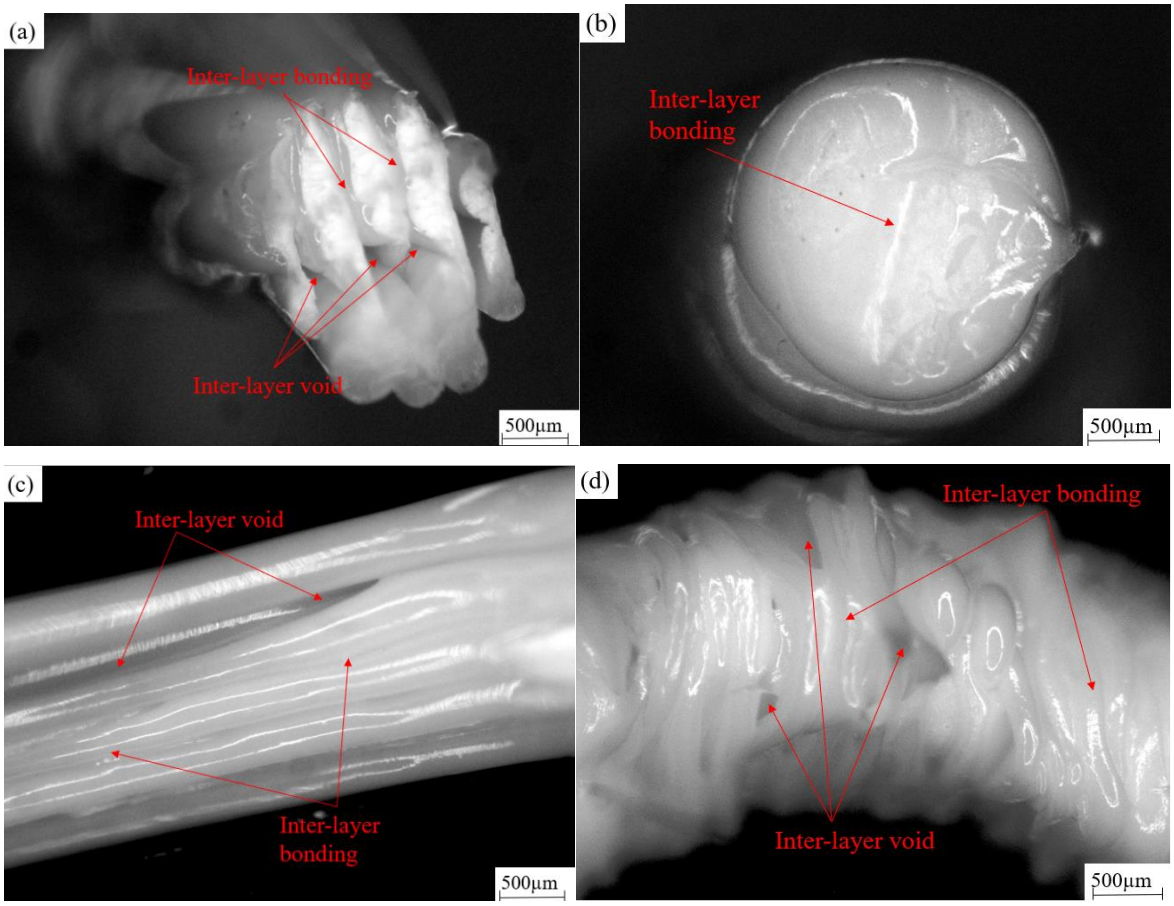

Figure 3.22. Optical microscope images showing the inter-layer bonding and voids at longitudinal direction and cross-sections of warp and weft yarns. (a) inter-layer bonding and voids in cross-section of warp yarns, (b) inter-layer bonding in cross-section of weft yarns, (c) inter-layer bonding and voids on the surface of warp yarns, (d) inter-layer bonding and voids on the surface of weft yarns.

The microscopic analysis of the yarns of weft knitted and braided structures were performed using optical microscope (OM). The yarns were printed with a mixed form of filament deposition: continuous filament deposition in printing direction and short fibers deposition in cross-printing direction. It can be seen in Figure 3.23a that the cross-section of the yarn contains voids as indicated by the arrows. It can also be seen (Figure 3.23b) that the deposited neighboring layers can be easily differentiated due to peaks and valleys at their infusion lines. All these surface roughness, peaks, valleys, and voids contribute to lower inter-layer fusion and hence increase the chances of generating cracks and ultimately failure under relatively small loads applied.

Voids in FDM are caused by many factors such as nozzle size and shape, layer orientations, cooling rate, melt flow pressure and velocity gradients [20]. The voids play a

major role in weakening the structure and develop crack initiation because of stress concentrations. The bonding of a layer with its neighboring layer is highly dependent on the energy of semi-molten polymer and, thus, the temperature of successive layers is important to achieve a good quality of bond. The number of voids and their sizes must be reduced to improve the mechanical strength of the structure.

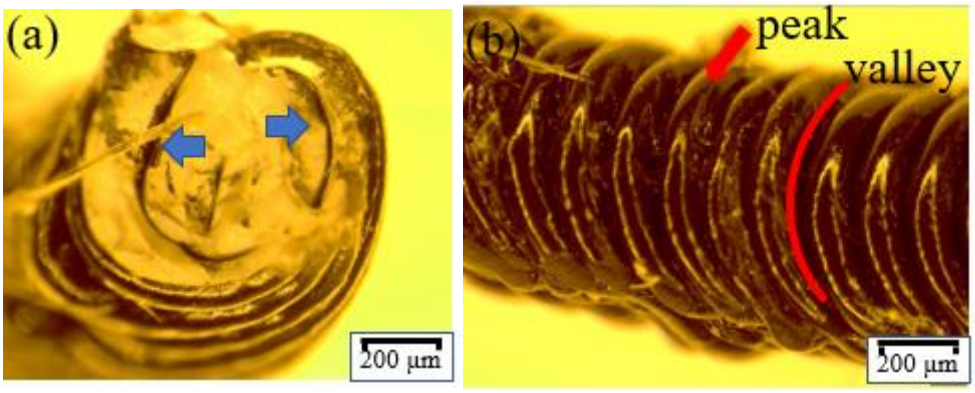

Figure 3.23. Representative optical microscopic images. (a) Cross-section of a yarn, and (b) longitudinal surface of a yarn.

3.3.2. Mechanical Test Results

The stress-strain (for uniaxial tensile tests) and force-displacement (for flexural tests) curves of the 3D printed twill fabrics and yarns (after separating from the fabric) are shown in Figure 3.24 for print and cross-print directions. The shape of the curves varies from nearly linear elastic behavior at first followed by non-linear response due to plastic behavior in both warp and weft directions. The warp yarns showed elastic-plastic behavior with significant ductility and strength compared to the weft yarns. The elastic modulus and the tangent modulus are almost the same during elastic stretch of the yarns; then, the yarns undergo plastic deformation where the tangent modulus starts decreasing. The weft yarns show elastic-plastic deformation with limited ductility. They exhibit permanent deformation under the influence of small strains in a relatively small plastic region where the tangent modulus decreases. The decrease of tangent modulus is due to geometric change of woven fabrics (i.e., decrease of undulation). Microscopic damages are induced in the curved regions of yarns, which is commonly observed in fabric structures [21].

Due to weaker inter-layer bonding, the failure strains for the 3D printed weft yarns and twill fabric structures in weft direction are less than 5% under uniaxial tensile loading and less than 5 mm in flexural displacement. In contrast, the 3D printed warp yarns and fabrics in warp

direction exhibit more strength and break at an elongation between 10% - 30% under tensile loading and between 8 mm -12 mm under flexural displacement. This is because the warp yarns are made of long and continuous bundles of fine layers, called fibers, which stick to each other better. As a result, when a tensile load is applied along the yarn axis, the fibers resist the load together which increases the total load bearing strength in the warp direction, while increasing the breaking elongation as well.

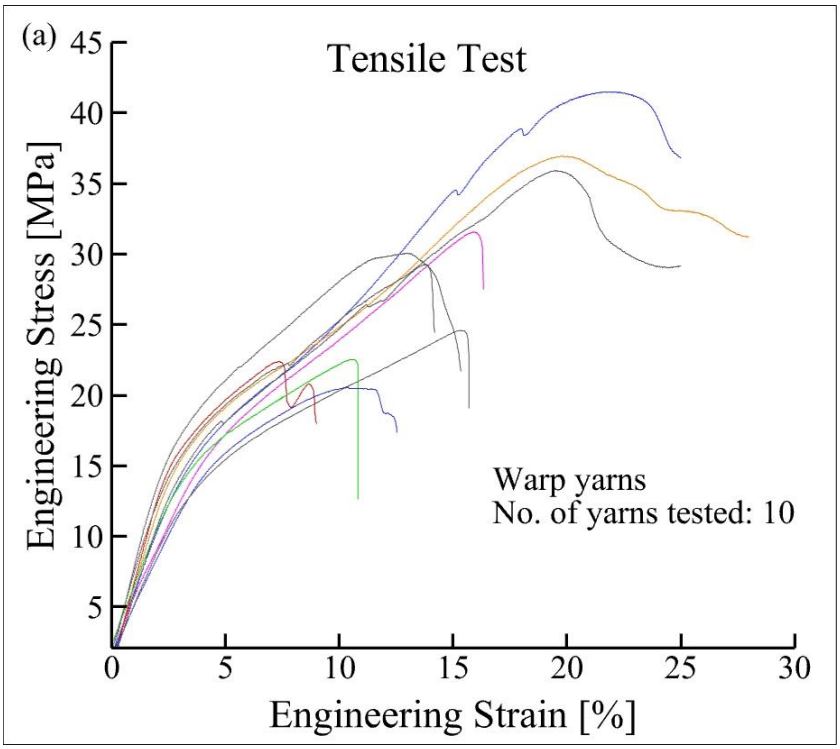

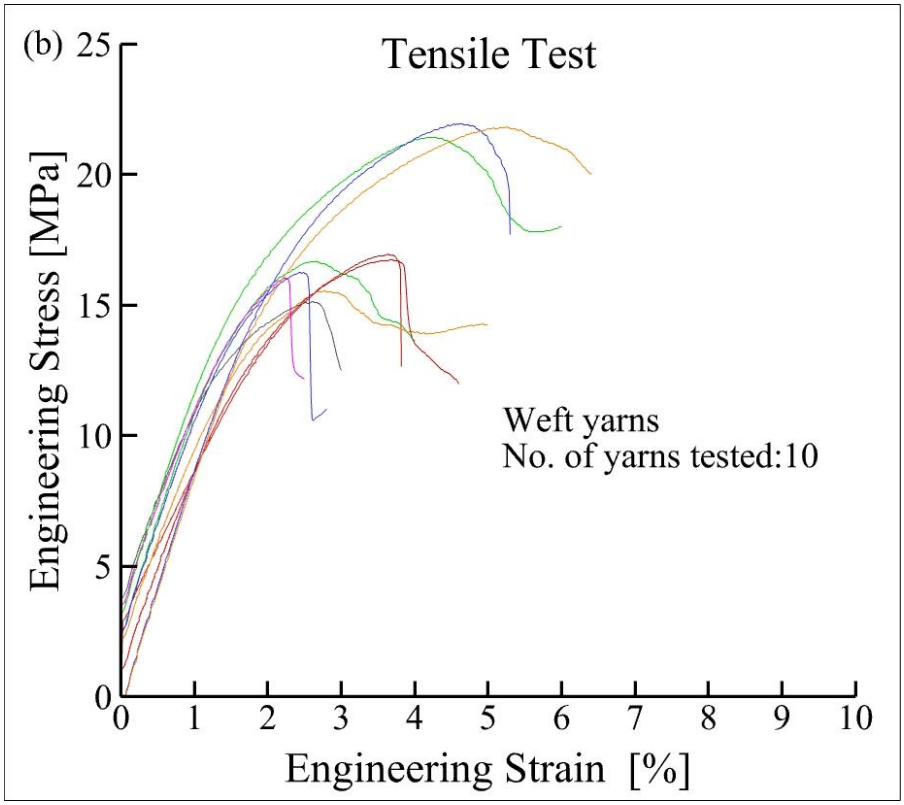
(b)
Tensile Test
Engineering Stress [MPa]
Engineering Strain [%]
Weft yarns
No. of yarns tested:10
0
5
10
15
20
25
0
1
2
3
4
5
6
7
8
9
10

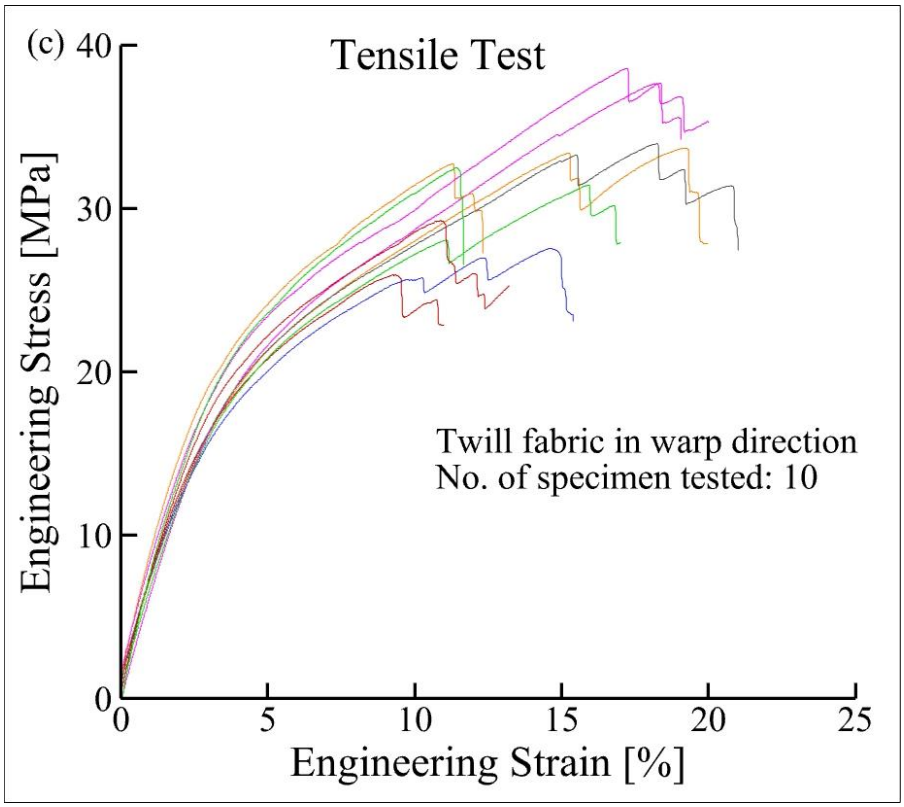
(c)
Tensile Test
Engineering Stress [MPa]
Engineering Strain [%]
Twill fabric in warp direction
No. of specimen tested: 10
0
10
20
30
40
0
5
10
15
20
25

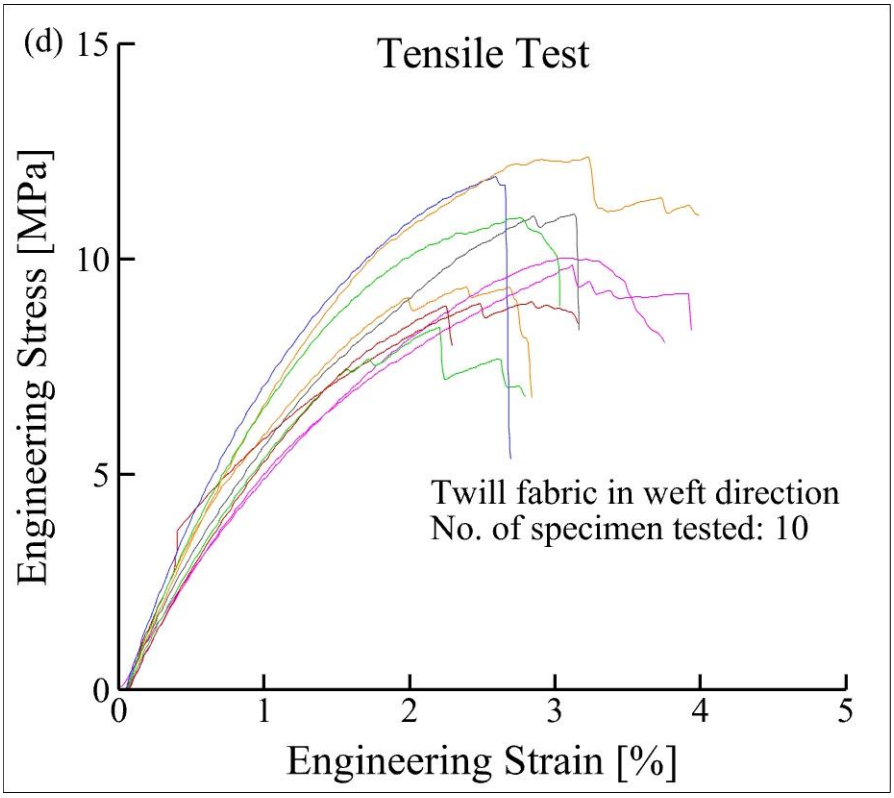
(d)
Tensile Test
Engineering Stress [MPa]
Engineering Strain [%]
Twill fabric in weft direction
No. of specimen tested: 10
0
5
10
15
0
1
2
3
4
5

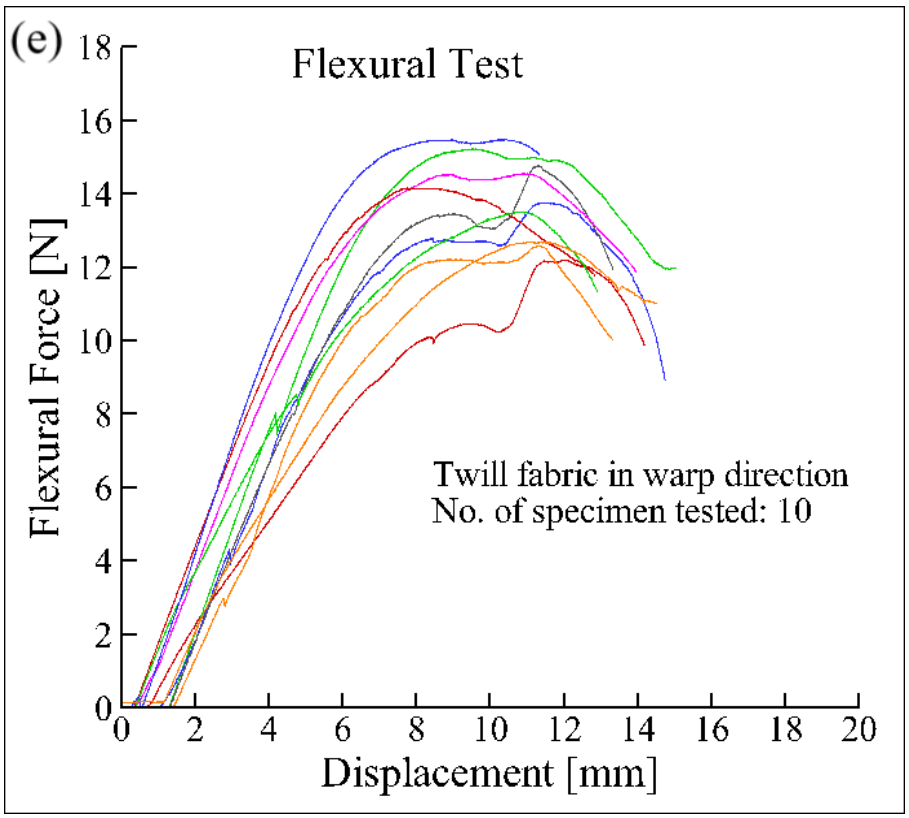
(e)
Flexural Test
Flexural Force [N]
Displacement [mm]
Twill fabric in warp direction
No. of specimen tested: 10
0
2
4
6
8
10
12
14
16
18
0
2
4
6
8
10
12
14
16
18
20

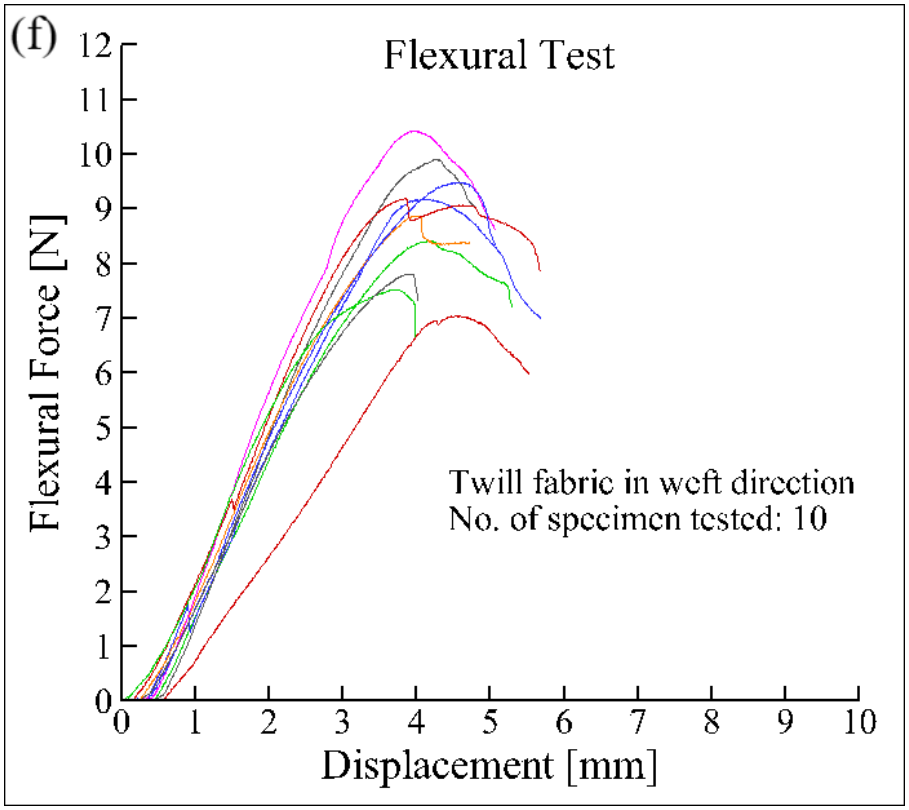

Figure 3.24. Mechanical property testing of 3D printed twill fabric structures: (a) Stress-strain curves for individual warp yarns, (b) Stress-strain curves for individual weft yarns, (c) Stress-strain curves for twill fabric in warp direction, (d) Stress-strain curves for twill fabric in weft direction, (e) Force-displacement curves for flexural tests in warp direction, (f) Force-displacement curves for flexural tests in weft direction.

The average values of the test results of the maximum strengths (σ_t, σ_f) and stiffnesses (E_t, E_f) for the printed yarns and twill fabric structures from PLA are tabulated in Table 3.2 for tensile tests and in Table 3.3 for flexural tests. The warp yarns showed higher tensile strength than the weft yarns. The mean tensile stress at maximum load is 29.54 MPa and 17.86 MPa for warp and weft yarns, respectively. The maximum load applied for a single warp yarn and twill fabric with 15 warp yarns are 23.20 N and 381.02 N respectively, which indicates that the load bearing capacity of the fabric is roughly equal to the number of warp yarns times the load bearing capacity of a single yarn. The maximum forces applied on a single weft yarn and twill fabric having 15 weft yarns are 14.03 N and 120.03 N, respectively, i.e., the load bearing capacity of the fabric in weft direction is only 8.5 times the single weft yarn before being permanently deformed. It was also observed that the flexural strength for twill fabric was smaller than the fabric tensile strength; hence, this twill structure could fail under bending force easier than under tensile load.

Table 3.2. Average tensile test results of the 3D printed warp yarns and 2/1 twill fabrics

Sample	Number of yarns	$F_{max}(N)$	$\sigma_t(MPa)$	$E_t(MPa)$
Warp yarn	1	23.20	29.54	415.12
Weft yarn	1	14.03	17.86	628.32
Fabric (warp direction)	15	381.02	32.34	609.07
Fabric (weft direction)	15	120.03	10.19	532.28

Table 3.3. Average 3-point bending flexural test results of 3D printed 2/1 twill fabrics

Sample	Number of yarns	$F_{max}(N)$	$\sigma_f(MPa)$	$E_f(MPa)$
Fabric (warp direction)	15	14.165	1.842	28.520
Fabric (weft direction)	15	8.785	1.147	35.196

During tensile testing, the yarns of weft knitted fabrics are stretched, and the stress concentration occurs at the curves of each yarn. On further extension, the yarns break at curves as shown in Figure 3.25, which is commonly observed in fabric structures [21]. The force-displacement graphs of 3D printed weft knitted fabrics are shown in Figure 3.26. The shape of the curves varies from nearly linear elastic behavior at first followed by nonlinear response because of plastic behavior in the yarns. The yarn reaches the peak force and on further loading the fracture occurs in the course direction, specifically at the head of the knitted loop. The head expands elasto-plastically first, then fractures. After that the other yarns bear the load and reach the peak force and then fracture in randomly sequential fashion. This process continues until the complete failure of the sample happens. This type of behavior of the fabric structure is shown in Figure 3.26a.

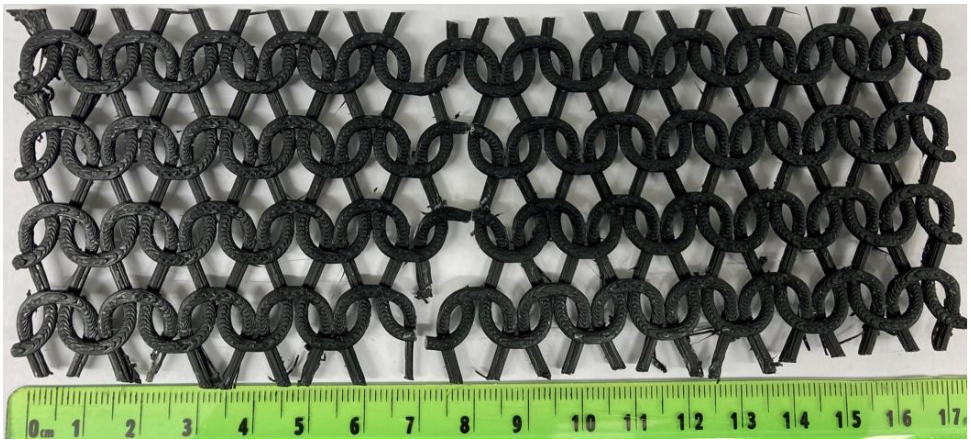

Figure 3.25. Fractured weft knitted fabric specimen during tensile test.

The tensile displacement can be observed in the range of 12 – 15 mm. This result also revealed that the fabric possesses ductile behavior and can withstand significant load in the course direction before failure. The maximum force applied on the knitted fabric is nearly 250 N. On the other hand, the flexural tests show that the maximum load applied is in the range of 15 – 22 N in the course direction, and 85 – 95 N in the wale direction. The lower amount of flexural force compared to tensile load demonstrated that the fabrics could experience failure easier in flexing. They provide less strength in out-of-plane direction and can be said that they are more brittle against flex loading. The maximum flexural displacement is close to 10 mm. It should be noted that this is sufficient for enough flex and bending for several applications such as filtration, artificial knee joints and geotextiles. The weaker inter-layer bonding and voids are the reasons for lower mechanical strength in the specimens.

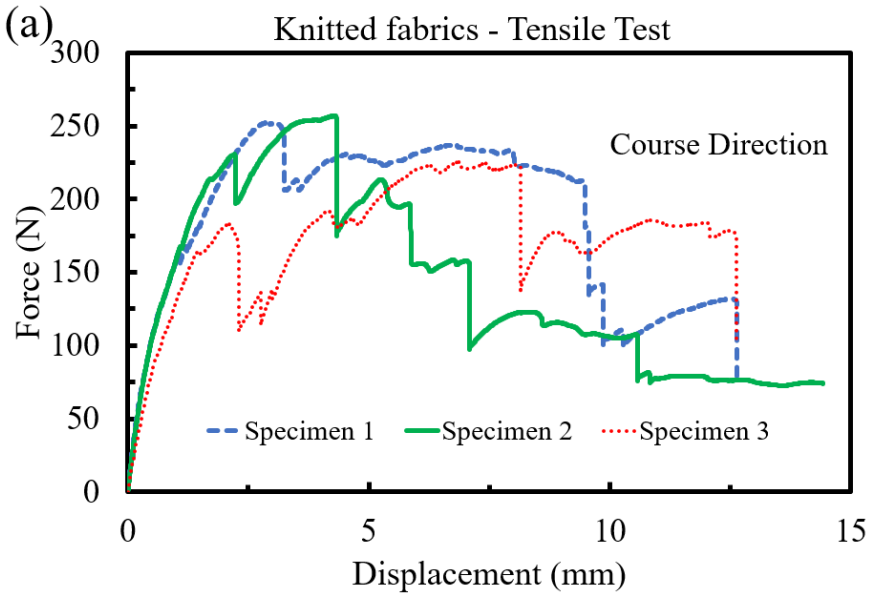

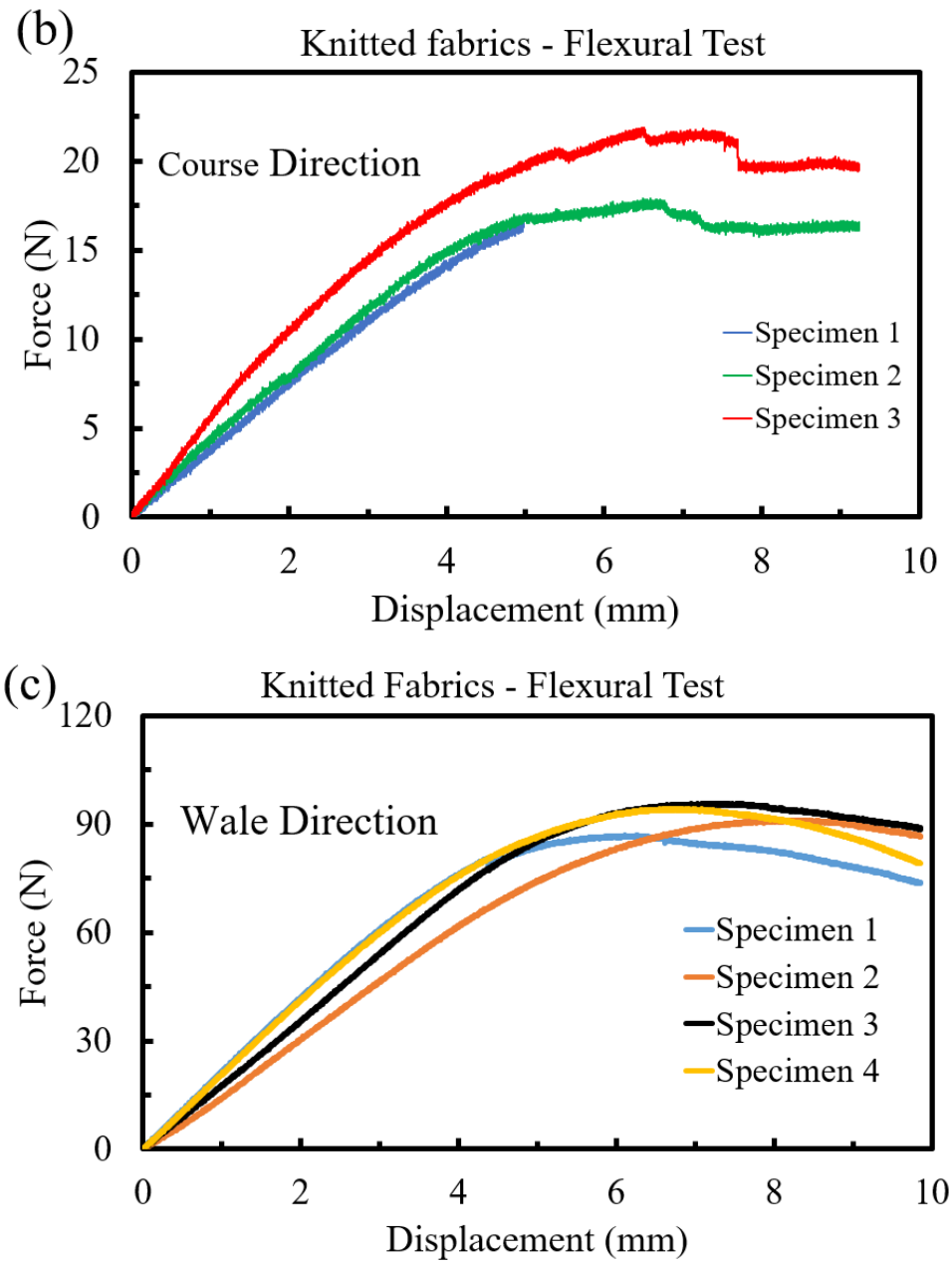

Figure 3.26. Mechanical test results of 3D printed weft knitted fabric structures.

The samples for compression testing were 3D printed using PLA as a base material. Three specimens were tested for each braid design; the compressive force-displacement graphs of 3D printed braids are shown in Figure 3.27. The average maximum compressive force is 1234.62 N for diamond braids, 915.16 N for regular braids, 1056.88 N for Hercules braids, 440.21 N for triaxial braids and 658.76 N for bifurcated braids. The displacement at maximum load is 5.04 mm for diamond braids, 3.75 mm for regular braids, 3.89 mm for Hercules braids, 3.05 mm for triaxial braids and 4.39 mm for bifurcated braids. The displacement at failure is 25 mm for diamond braids, 35 mm for regular braids, 30 mm for Hercules braids, 25 mm for triaxial braids, and 40 mm for bifurcated braids. The compression test results showed that these

structures can bear a significant amount of load before complete failure and can be used for shock absorption applications.

Braid structures have several yarns arranged in a circular and helical pattern. When the compressive load is applied, the sample withstands a force up to its proportional limit value. When the load exceeds the limit, a permanent deformation occurs in the structures. Here, when the permanent deformation occurs, a yarn fractures and as a result, a drop in compressive force is observed. Again, the other yarns bears the load until they fracture. This is the reason for increasing of the force after dropping when the yarns fracture. This scenario is seen during the compressive loading as shown in Figure 3.27.

Diamond braid has a pattern of 1/1 in the unit cell. Therefore, if one yarn breaks, then the whole structure collapses as shown in Figure 3.27(a). Regular braid has a pattern of 2/2 in the unit cell. Therefore, it is possible that each of the two yarns does not fail at the same time as shown in Figure 3.27(b). The same is true for Hercules braid, which is 3/3 (Figure 3.27(c)). Triaxial braid has yarns in the loading direction which are brittle; therefore, their failure causes a rather sudden drop in force (Figure 3.27(d)). The bifurcated braid has also 2/2 pattern like regular braid; that's why its curve (Figure 3.27(e)) is similar to that of regular braid.

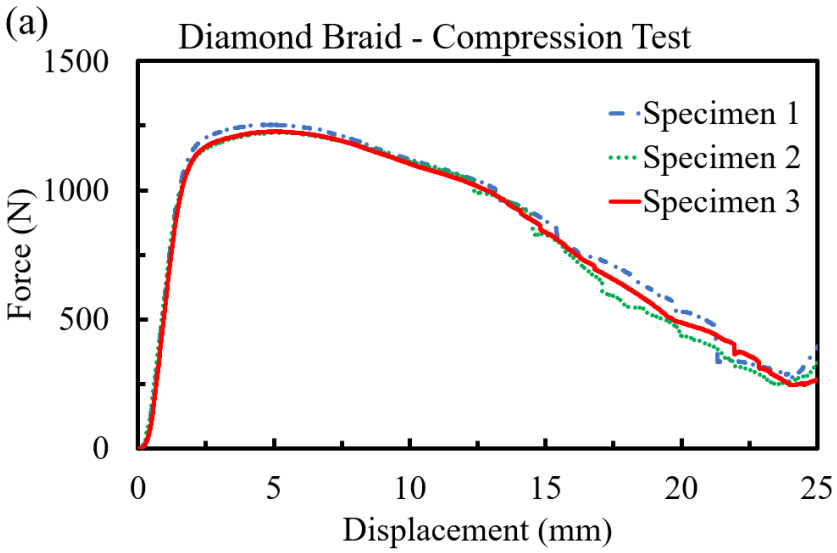

(b)

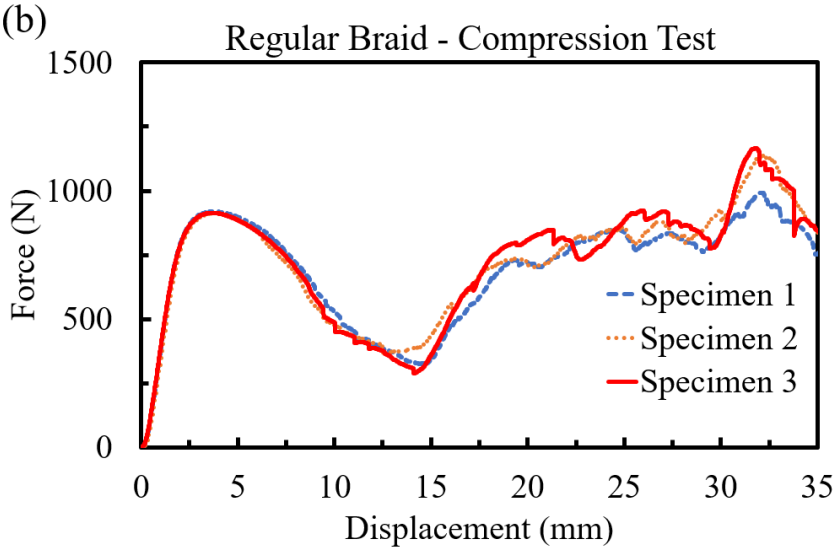
Regular Braid - Compression Test
Force (N)
1500
1000
500
0
0
5
10
15
20
25
30
35
Displacement (mm)
Specimen 1
Specimen 2
Specimen 3

(c)

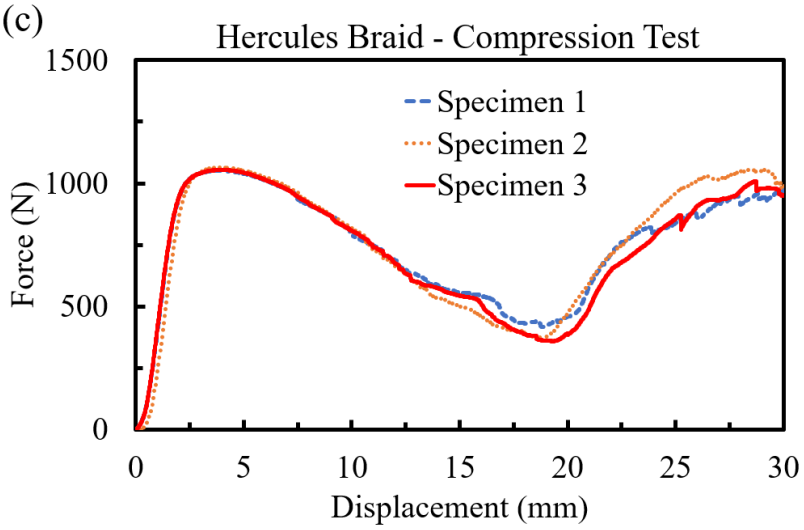
Hercules Braid - Compression Test
Force (N)
1500
1000
500
0
0
5
10
15
20
25
30
Displacement (mm)
Specimen 1
Specimen 2
Specimen 3

(d)

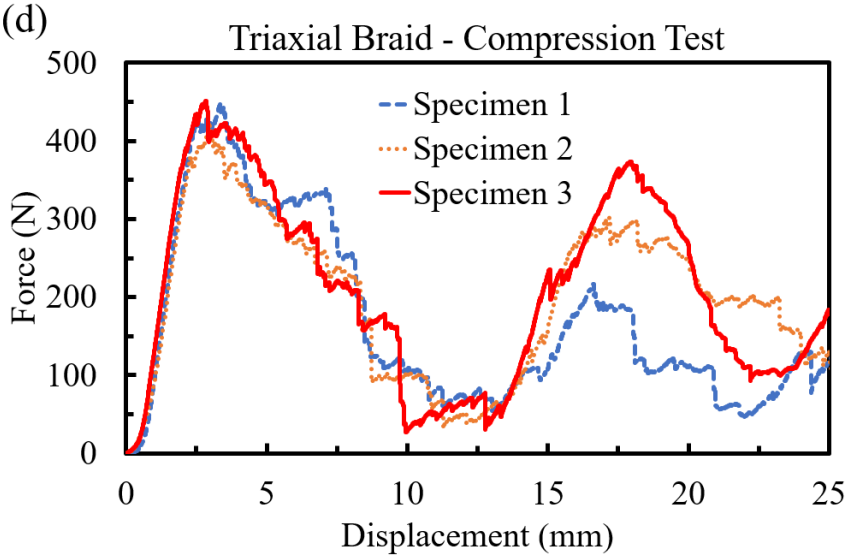
Triaxial Braid - Compression Test
Force (N)
500
400
300
200
100
0
0
5
10
15
20
25
Displacement (mm)
Specimen 1
Specimen 2
Specimen 3

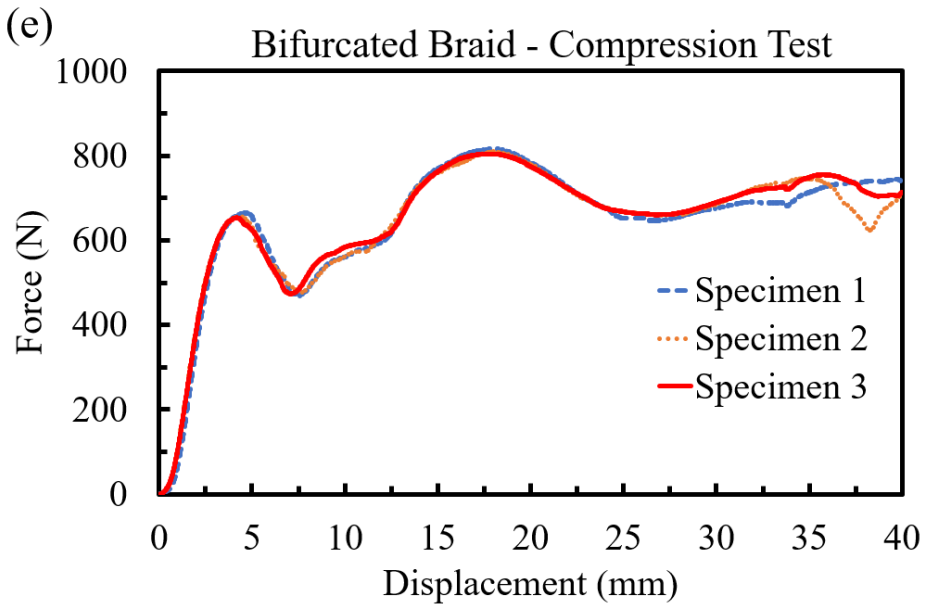

Figure 3.27. Compression test results of 3D printed braid structures, (a) Diamond braid, (b) Regular braid, (c) Hercules braid, (d) Triaxial braid, and (e) Bifurcated braid.

3.4. Conclusions

This work was performed to explore the application of fused deposition modeling (FDM) method to fabricate complex structures such as plain weave, twill weave, weft-knitted fabrics, and braid structures. Poly(lactic) acid (PLA) filaments were used in this research to fabricate the samples. The weft knitted fabrics were 3D printed in horizontal orientation whereas the plain weave, twill weave and braid designs were 3D printed in vertical orientation. The mechanical properties of the printed samples were studied using tensile, flexural, and compression test methods. The microscopic structures were analyzed using optical microscope (OM). The results showed that the warp yarns are stronger than the weft yarns, which results in a stronger fabric in warp direction. It was also found that the knitted fabrics had good flexibility in both course and wale directions, but the flexural strength in course direction is significantly lower than in wale direction. The maximum tensile force of knitted fabrics in course direction is almost 250 N. The compression tests on braids revealed that they are capable of holding failure displacement of more than 25 mm. However, the fabric structures still need improvements to increase the tensile, bending, and other strengths to make the printed fabrics more flexible and stronger. The performance of these structures can also be improved by using a combination of different materials to increase the mechanical properties.

3.5. References

[1] S. Adanur, *Handbook of Weaving*, First Edit. Boca Raton: CRC Press, 2001.

[2] S. Adanur, "Wellington Sears Handbook of Industrial Textiles," Technomic Publishing Co. Inc., 1995, pp. 273–294.

[3] S. Luo and W. Ooij, "Surface modification of textile fibers for improvement of adhesion to polymeric matrices: a review," *J. Adhes. Sci. Technol.*, vol. 16, no. 13, pp. 1715–1735, 2002, doi: https://doi.org/10.1163/156856102320396102.

[4] S. Adanur and T. Liao, "3D modeling of textile composite preforms," *Compos. Part B Eng.*, vol. 29, no. 6, pp. 787–793, Nov. 1998, doi: 10.1016/S1359-8368(98)00036-5.

[5] S. Vassiliadis, A. Kallivretaki, D. Domvoglou, and C. Provatidis, "Mechanical Analysis of Woven Fabrics:The State of the Art," in *Advances in Modern Woven Fabrics Technology*, InTech, 2011.

[6] S. Adanur and J. S. Vakalapudi, "Woven fabric design and analysis in 3D virtual reality. Part 1: computer aided design and modeling of interlaced structures," *J. Text. Inst.*, vol. 104, no. 7, pp. 715–723, 2013, doi: 10.1080/00405000.2012.753698.

[7] T. Campbell, C. Williams, O. Ivanova, and B. Garrett, "Could 3D Printing Change the World? Technologies, Potential, and Implications of Additive Manufacturing," *Atl. Counc.*, pp. 1–14, 2011.

[8] S. Ramakrishna, "Characterization and modeling of the tensile properties of plain weft-knit fabric-reinforced composites," *Compos. Sci. Technol.*, vol. 57, no. 1, pp. 1–22, 1997, doi: 10.1016/S0266-3538(96)00098-X.

[9] K. Bilisik, "Three-dimensional braiding for composites: A review," *Text. Res. J.*, vol. 83, no. 13, pp. 1414–1436, 2013, doi: 10.1177/0040517512450766.

[10] F. Schreiber, F. K. Ko, H. J. Yang, E. Amalric, and T. Gries, "Novel three-dimensional braiding approach and its products," *ICCM Int. Conf. Compos. Mater.*, 2009.

[11] R. Melnikova, A. Ehrmann, and K. Finsterbusch, "3D printing of textile-based structures by Fused Deposition Modelling (FDM) with different polymer materials," *IOP Conf. Ser. Mater. Sci. Eng.*, vol. 62, no. 1, pp. 1–6, 2014, doi: 10.1088/1757-899X/62/1/012018.

[12] L. Partsch, S. Vassiliadis, and P. Papageorgas, "3D Printed Textile Fabrics Structures," *5th Int. Istanbul Text. Congr. 2015 Innov. Technol. "Inspire to Innov.*, no. September, pp. 3–10, 2015.

[13] K. Lussenburg, N. Van Der Velden, Z. Doubrovski, J. Geraedts, and E. Karana, "Designing with 3D Printed Textiles," *Proc. 5th Int. Conf. Addit. Technol.*, pp. 74–81,

2003.

[14] T. Spahiu, E. Canaj, and E. Shehi, “3D printing for clothing production,” *J. Eng. Fiber. Fabr.*, vol. 15, pp. 1–8, 2020, doi: 10.1177/1558925020948216.

[15] S. Kim, H. Seong, Y. Her, and J. Chun, “A study of the development and improvement of fashion products using a FDM type 3D printer,” *Fash. Text.*, vol. 6, no. 9, pp. 1–24, 2019, doi: 10.1186/s40691-018-0162-0.

[16] M. Beecroft, “Digital interlooping: 3D printing of weft-knitted textile-based tubular structures using selective laser sintering of nylon powder,” *Int. J. Fash. Des. Technol. Educ.*, vol. 12, no. 2, pp. 218–224, 2019, doi: 10.1080/17543266.2019.1573269.

[17] A. Jayswal and S. Adanur, “An overview of additive manufacturing methods, materials, and applications for flexible structures,” *J. Ind. Text.*, vol. 52, pp. 1–42, 2022, doi: 10.1177/15280837221114638.

[18] ASTM International, “ASTM D5035-11: Standard Test Method for Breaking Force and Elongation of Textile Fabrics (Strip Method),” West Conshohocken, PA, 2019.

[19] ASTM International, “ASTM D790-17: Standard Test Methods for Flexural Properties of Unreinforced and Reinforced Plastics and Electrical Insulating Materials,” West Conshohocken, PA, 2017.

[20] ASTM International, “ASTM D695-15: Standard Test Method for Compressive Properties of Rigid Plastics,” West Conshohocken, PA, 2015. doi: 10.1520/D0695-15.2.

[21] E. A. Papon and A. Haque, “Tensile properties, void contents, dispersion and fracture behaviour of 3D printed carbon nanofiber reinforced composites,” *J. Reinf. Plast. Compos.*, vol. 37, no. 6, pp. 381–395, 2018, doi: 10.1177/0731684417750477.

[22] T. Yokozeki, S. ichi Takeda, T. Ogasawara, and T. Ishikawa, “Mechanical properties of corrugated composites for candidate materials of flexible wing structures,” *Compos. Part A Appl. Sci. Manuf.*, vol. 37, no. 10, pp. 1578–1586, 2006, doi: 10.1016/j.compositesa.2005.10.015.

Chapter 4

Effect of heat treatment on crystallinity and mechanical properties of 3D printed twill weave fabric structure

(Jayswal, A., and Adanur, S., *"Effect of heat treatment on crystallinity and mechanical properties of flexible structures 3D printed with fused deposition modeling",* Journal of Industrial Textiles, vol. 51, No. 2S, pp. 2616S–2641S, 2021)

Abstract

Fused Deposition Modeling (FDM) is a widely used 3D printing technique, which works based on the principle of melted polymer extrusion through nozzle(s) and depositing them on a build plate layer by layer. However, products manufactured with this method lack proper mechanical strength. In this work, 2/1 twill weave fabric structures are 3D printed using poly (lactic) acid (PLA). The ultimate tensile strength in the warp and weft directions and the modulus (stiffnesses) are measured for non-heat-treated (NHT) samples. The printed samples were heat-treated (HT) to improve the strength and stiffness. The variation in ultimate tensile strength is statistically insignificant in warp direction at all temperatures; however, the tensile strength in weft direction decreased after heat treatment. The modulus in warp direction increased by 31% after heat treatment while in the weft direction it decreased after heat treatment. Differential scanning calorimetry (DSC) tests showed the highest crystallinity at 125°C. The properties of the twill fabrics were compared with a standard dog-bone (DB) specimen using uniaxial tensile tests, Differential scanning calorimetry tests, and optical microscope (OM). For dog-bone specimens, the maximum values of crystallinity, ultimate tensile strength, and modulus were found to be at 125°C. The maximum crystallinity percentages are higher than that of the NHT samples. The ultimate tensile strength of NHT DB specimen 3D printed in horizontal orientation improved after heat treatment. The ultimate tensile strength of DB samples in vertical directions increased after heat treatment as well. The stiffness increased in both directions for DB samples.

4.1. Introduction

Additive manufacturing (AM) is a revolutionary manufacturing technology which has the potential to build almost any complex product within a reasonably short time with minimal waste [1]. This technology is classified into seven categories by The American Society for Testing and Materials (ASTM): material extrusion, material jetting, binder jetting, sheet lamination, vat photopolymerization, powder bed fusion, and directed energy deposition [2].

Fused deposition modelling (FDM) works on the material extrusion principle and utilizes thermoplastic materials such as poly(lactic) acid (PLA), acrylonitrile butadiene styrene (ABS), polyether ether ketone (PEEK), nylon, Poly(methyl methacrylate) (PMMA) and poly(carbonate) (PC). The polymer is melted and extruded through a nozzle and deposited on a build plate layer by layer forming a solid object [3]. However, the mechanical strength of FDM 3D printed parts is lower compared to those obtained from injection molding or other manufacturing methods due to the presence of voids and weaker bonding between layers and rasters [4]. Therefore, different methods have been proposed to increase the strength which includes parameter optimization, addition of filler materials and post curing with heat treatment (HT).

Akhoundi and Behravesh [5] investigated the effect of filling patterns and infill density on the mechanical properties of 3D printed parts and concluded that concentric fill at all infill densities and Hilbert curve pattern (named after the German mathematician David Hilbert which is a continuous space-filling curve) at 100 % infill density show increase in mechanical strength of the products. However, a study of these parameters on non-standard materials such as 3D printed fabrics would be required to truly compare their effects on non-standard materials. Chacón, et. al. [6] studied several process parameters such as build orientation, layer thickness and feed rate and their effects on final strength of 3D printed products and found that upright orientation exhibited the lowest mechanical properties whereas on-edge and flat orientations the highest. They also observed an increase in mechanical properties with increasing layer thickness and decrease with increasing feed rate for upright orientation whereas the layer thickness and feed rate play insignificant role for on-edge and flat orientations. However, it should be mentioned that all non-standard materials may not be possible to print in flat or on-edge orientations. Chacón et al. [7] worked on continuous fiber reinforced thermoplastic composites and demonstrated that the carbon fiber reinforced samples developed the highest strength and stiffness than all other samples. Heat treatment increases the crystallinity of samples and hence improves the mechanical properties in comparison with the non-heat-treated (NHT) samples [8]. This method increases the bonding between the layers and rasters. Avila et. al. [9] investigated the effect of heat treatment at 90% of glass-transition temperature (T_g) on mechanical properties of FDM printed products using PC, PMMA and PEEK. They found an increase in tensile strength of about 10 MPa for PC, 20 MPa for PMMA and a slight change for PEEK. Akhoundi et. al. [10] studied the effect of heat treatment on mechanical properties of high-temperature polylactic acid (HTPLA) printed at 250°C and

found that the tensile strength and modulus increased by 2.5% and 15.31%, respectively. Yang et al. [11] studied various thermal processing conditions in 3D printing of PEEK materials and found that different degrees of crystallinity and mechanical properties can be found. However, it would be highly recommended to study the effect of heat treatment at various temperatures on non-standard samples such as 3D printed fabrics and compare it with the ASTM standard dog-bone samples to derive any conclusion about this method, which is the main objective of this paper.

Recently, FDM has been used in fashion and textile industries to produce bikinis [12], gowns [13] and shoes [14]. Melnikova et al. [15] 3D printed textile based structures using different polymers. They studied PLA, soft PLA, Lay Tekkks and BendLay and demonstrated that soft PLA is the potential candidate to be used to print textile-like structures. Partsch et al. [16] used ABS to insert textile properties in 3D printed objects. They designed, printed, and evaluated three different plain weaves. Quan et al. [17] 3D printed multidirectional preforms using ABS and showed the feasibility of 3D printing of multi-directional textile based preforms. Lussenburg et al. [18] designed a wearable garment using PLA and concluded that final product does not resemble all the fabric properties and needs further research to improve tear resistance and softness of the structures. Although several researchers attempted to 3D print fabric structures, the evaluation of mechanical properties of 3D printed fabric structures is lacking in the literature except as indicated in our previous work [4]. We evaluated the tensile and flexural properties of 3D printed twill weave fabric structures and found that the fabrics in weft direction fail at less than 5 % of strain under uniaxial tensile loading and less than 5 mm in flexural displacement. Fabrics in warp direction exhibited more strength and broke at an elongation between 10 % and 30% under tensile loading and between 8 mm and 12 mm under flexural displacement. The average ultimate tensile strengths were 32 MPa and 10 MPa in warp and weft directions, respectively.

PLA is one of the most common materials used in 3D printing with FDM. It is bio-degradable, recyclable and renewable thermoplastic material synthesized from starch obtained from corn, wheat, rice, etc. [19] [20]. It is produced by processing and polymerization of lactic acid monomer and it exists in two optically active configurations, the L(+) and D(-) isomers as shown in Figure 4.1 [21] [22] [23]. The content of L, D and D-L type of lactides in the blend influences crystallinity, mechanical properties and degradation characteristics of PLA [8]. A highly crystalline PLA can be produced by decreasing the D content (< 2%) whereas a totally amorphous PLA can be obtained by increasing the D content (>20%) [22] [24]. Hence, to produce the PLA material for commercial use, generally a higher amount of L type lactides

and lower content of D type lactides are used [8] [24]. These lactides are blended in a required amount to produce either semi-crystalline PLLA (poly-L-lactic acid) or amorphous PDLA (poly-D-lactic acid) by a ring opening polymerization process.

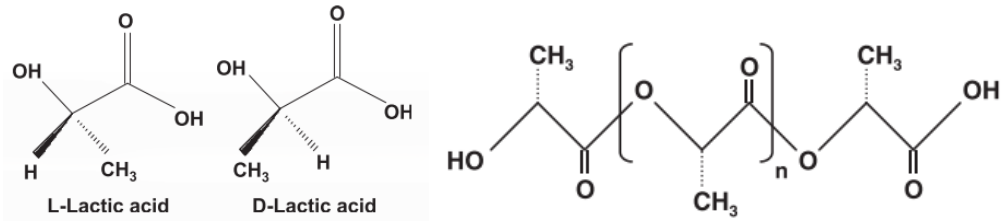

Figure 4.1. Chemical structure of L and D isomers of lactic acid (left) and high molecular weight PLA formed by ring opening polymerization (right) [22].

The arrangement of macromolecular polymer chains is an important factor related to mechanical strength. In crystalline regions, the macromolecular chains are arranged in a regular fashion and hence they contribute towards the higher intermolecular forces whereas in amorphous regions, the macromolecular chains have a random arrangement and therefore they are weaker in strength. Figure 4.2 shows a schematic diagram representing the arrangement of crystalline and amorphous regions of 3D printed PLA samples.

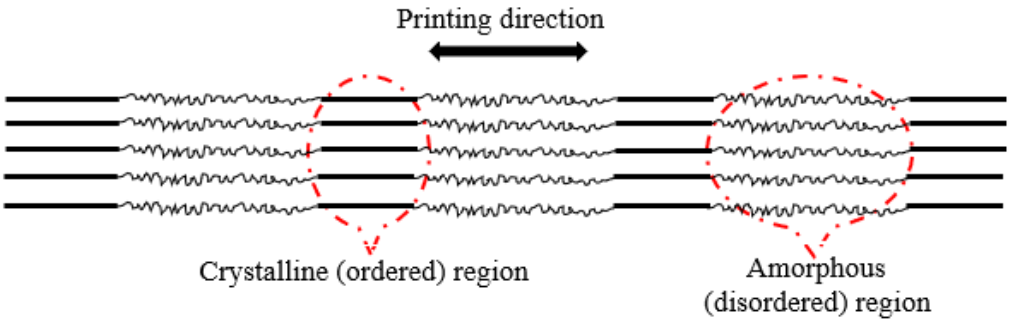

Figure 4.2. Schematic diagram showing the arrangement of crystalline and amorphous regions in 3D printed PLA samples.

This research focuses on 3D printing of twill weave structures for wearable fabrics which is a current development area. The effect of heat treatment at various temperatures on the mechanical properties and crystallization behavior of PLA is studied. The relationship between crystallinity and mechanical properties (e.g., modulus and ultimate tensile strength) is investigated. The properties of 3D woven fabric structures are compared with those of standard dog-bone samples.

4.2. Materials and methods

4.2.1. Materials and 3D print settings

PLA filaments (Hatchbox®, 3D printer filament, true black) were used for this project with a diameter of 1.75 ± 0.03 mm and recommended extrusion temperature of 180 ℃ − 210 ℃. The print settings used in this work were kept the same for all the specimens which is presented in Table 4.1.

Table 4.1. 3D print settings for 2/1 twill weave fabrics and dog-bone specimens [4].

Parameters	**Values**
PLA filament diameter	1.75 mm
Layer height	0.2 mm
Infill density	100 %
Printing temperature	225 ℃
Build Plate temperature	40 ℃
Print speed	30 mm/s
Travel speed	120 mm/s
Initial layer speed	25 mm/s

4.2.2. 3D printing of specimens

3D models of 2/1 twill weave fabrics and dog-bone specimens were prepared using computer aided design (CAD) software, Solidworks® and saved with .STL format. Dremel DigiLab 3D slicer 1.2.2 software was used to slice the 3D models, and the resulting gcode files were used for 3D printing using Dremel DigiLab® 3D45 3D printer (Dremel Manufacturing Company, Racine, Wisconsin, USA). The printer had a nozzle diameter of 0.4 mm.

The movement of the nozzle in x-direction is the print direction (PD, 0°) and the movement in z-direction is the cross-print direction (CD, 90°). The yarns in printing direction are called warp yarns and the perpendicular yarns in cross-printing direction are termed as weft yarns. Y-axis represents the thickness of the fabric structure. The fabrics were printed in a vertical orientation in a square shape. Figure 4.3 represents the schematic of FDM process used in the 3D printing of twill weave fabrics and Figure 4.4 shows the FDM 3D printed twill fabric structures. The dimensions of the 3D printed fabrics are 92 mm x 92 mm with 30 warp and 30 weft yarns; each yarn diameter is 1 mm. The spacing between the yarns is 3 mm in both directions. The areal density of the fabric is 1.018 mg/mm^2 and the average fabric cover is

4,684 mm^2 or 55.34%. For details about the construction and design of the 2/1 twill weave fabrics, one may refer to reference [4]. The dog-bone specimens were designed, and 3D printed in vertical and horizontal orientations having their width dimension parallel to the print bed (Figure 4.5 and Figure 4.6).

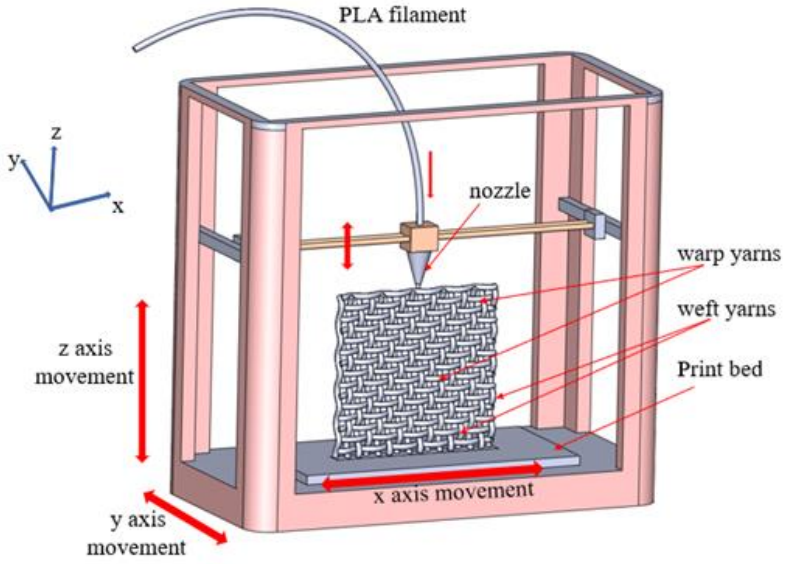

Figure 4.3. Schematic of FDM printing of 2/1 twill weave fabric structures (not to scale).

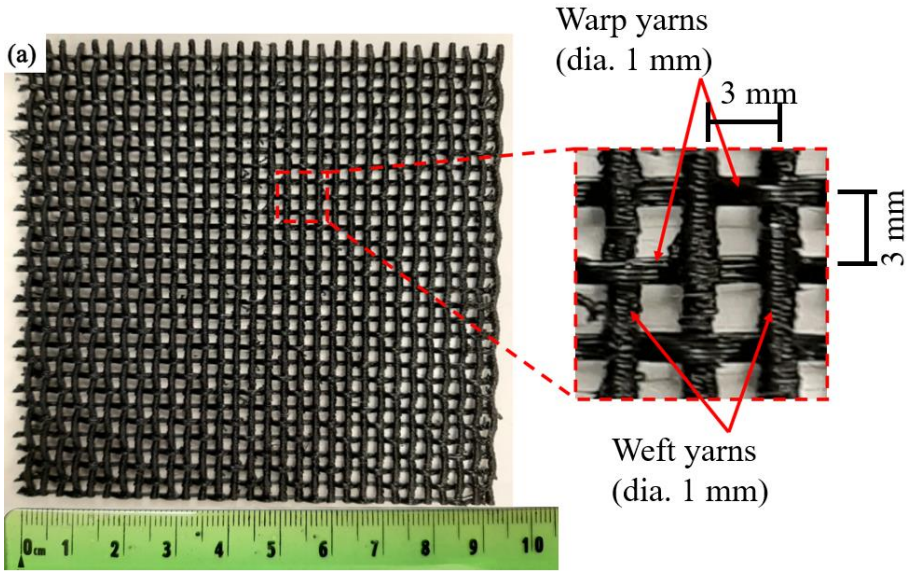

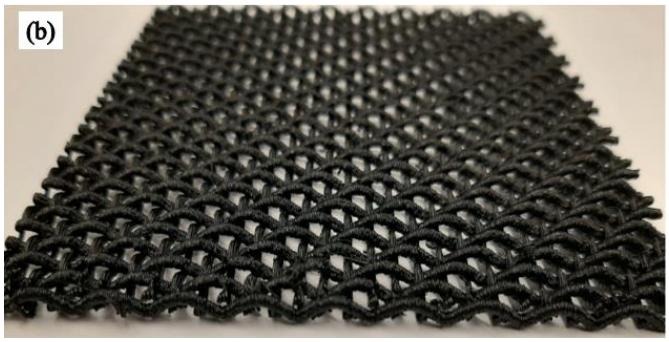

Figure 4.4. FDM 3D printed 2/1 twill weave fabric structure: (a) Front view of the fabric along with its unit cell, and (b) Side view of the 3D printed fabric.

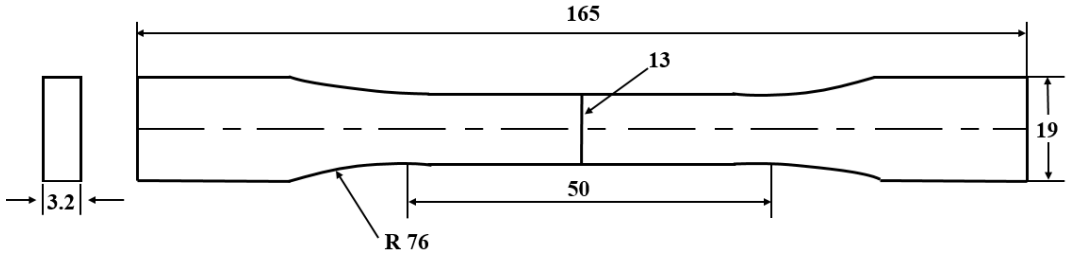

Figure 4.5. Dog-bone specimen geometry and dimensions for uniaxial tensile tests according to ASTM D638-14, Type I standard (dimensions in mm) [25].

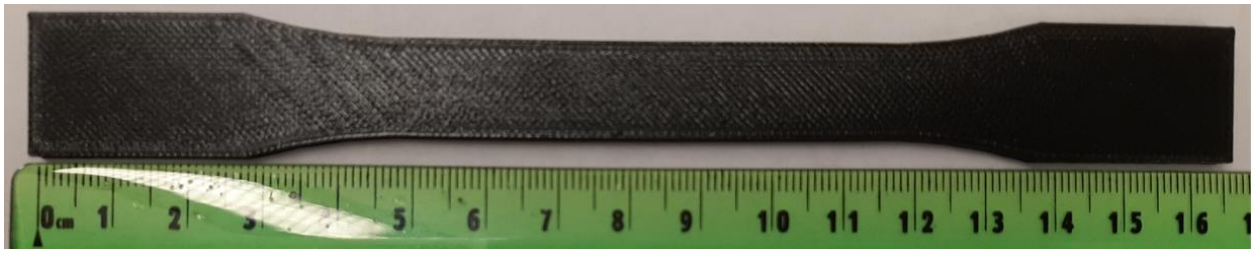

Figure 4.6. 3D printed and non-heat-treated dog-bone specimen.

4.2.3. Heat treatment of samples

The printed samples were heated in a temperature-controlled lab oven at different temperatures for 1 hour and then allowed to cool slowly in the oven, a process called furnace cooling. The samples were heat-treated at 50 ℃, 75 ℃, 100 ℃, and 125 ℃ for 1 hour and were termed as HT50, HT75, HT100, and HT125, respectively. The nomenclature of the samples used in this study is shown in Figure 4.7.

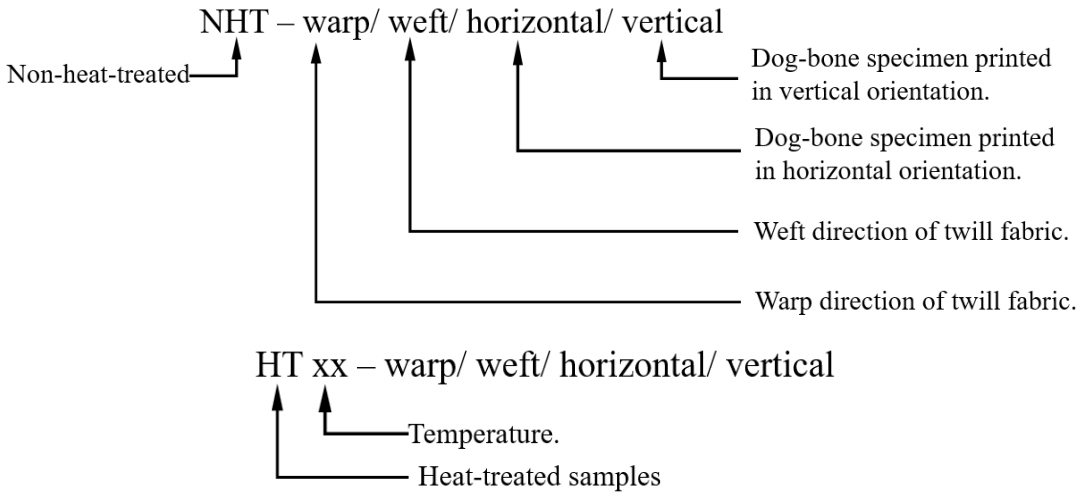

Figure 4.7. Nomenclature of the samples used in this study.

4.2.4. Uniaxial tensile testing

The tensile test samples were cut from the printed twill fabric structures in warp and weft directions having dimensions of 92 mm (length) x 46 mm (width) x 3.15 mm (thickness) in such a way that each test specimen contained 15 yarns. Mechanical properties of 3D printed, heat- treated (HT) and non-heat-treated (NHT) twill weave fabric structures were measured using an Instron 5565 universal testing machine (Norwood, MA, USA) with a load cell of 1 kN following the ASTM D5035 standard [26], with a gage length of 25 mm, and crosshead speed of 3 mm/min. The breakage of the first yarn is considered as the failure of the fabric structure. The experimental data were processed to determine the ultimate tensile strength and Young's modulus. Tensile stress (σ_t) of the 3D printed fabric structures was calculated using the following equation:

$$\sigma_t = \frac{F}{n * A} \tag{4.1}$$

where, F is the force applied during the tests, n (=15) is the number of yarns (both for warps or wefts) in each fabric sample, and A (= $\pi d^2/4$, where d = 1 mm is the yarn diameter) is the initial cross-sectional area of each yarn.

Similarly, the mechanical properties of 3D printed, heat-treated and non-heat-treated rectangular dog-bone specimens were measured using the same equipment with a load cell of 5 kN, a gage length of 50 mm and thickness of 3.2 mm (Figure 4.5) following ASTM D638-14, Type I standard [25]. The tensile test was carried out on 5 specimens for each structure at room temperature, and the average values were reported. Tensile stress (σ_t) of the 3D printed dog-bone samples was calculated using the following equation:

$$\sigma_t = \frac{F}{width \times thickness} \tag{4.2}$$

where, *F* is the force applied during the tests; initial width and thickness of the dog-bone samples are 13 mm and 3.2 mm respectively.

Young's modulus (E) was measured in linear region by using the following equation:

$$\sigma_t = \text{E. } \varepsilon \tag{4.3}$$

where, ε is the elongation (or strain) of the samples.

4.2.5. Differential scanning calorimetry (DSC)

DSC test was conducted using a Q 2000 (TA instruments, USA) maintaining a nitrogen atmosphere with a supply rate of 50 mL/min. The samples used weighs in the range of 4 to 8 mg. They were first heated from 40 ℃ to 200 ℃ and then were cooled back to 40 ℃ at a heating and cooling rate of 10 ℃/min. The measurements such as glass transition temperature (T_g), cold crystallization temperature (T_{cc}), cold crystallization enthalpy (ΔH_{cc}), melting temperature (T_m), and melting enthalpy (ΔH_m) were measured. The enthalpy of fusion of a 100% crystalline PLA sample (ΔH_m^0) is 93.6 J/g [27], [28]. Eq. (4.4) was used to determine the crystallinity of the samples.

$$\chi_c = \frac{\Delta H_m - \Delta H_{cc}}{\Delta H_m^0} \times 100\% \tag{4.4}$$

4.2.6. Optical Microscope Images

The cross-sections and longitudinal surfaces of warp yarns, weft yarns, and dog-bone specimens fractured during tensile testing were studied using an optical microscope (Olympus SZX7, Japan). The optical microscope was used to measure the area of voids on each image and percent void content relative to the total area, as shown in Figure 4.8. The void content is calculated as the ratio of void area to total cross-sectional area or surface area. Mathematically, it can be expressed as:

$$\text{void content} = \frac{\Sigma \text{ Area of each void}}{\text{Total cross} - \text{section area or surface area}} \times 100\% \tag{4.5}$$

The void content of HT125-warp sample is $\frac{139{,}752.01\ \mu m^2}{1{,}111{,}191.88\ \mu m^2} \times 100\% = 12.58\%$.

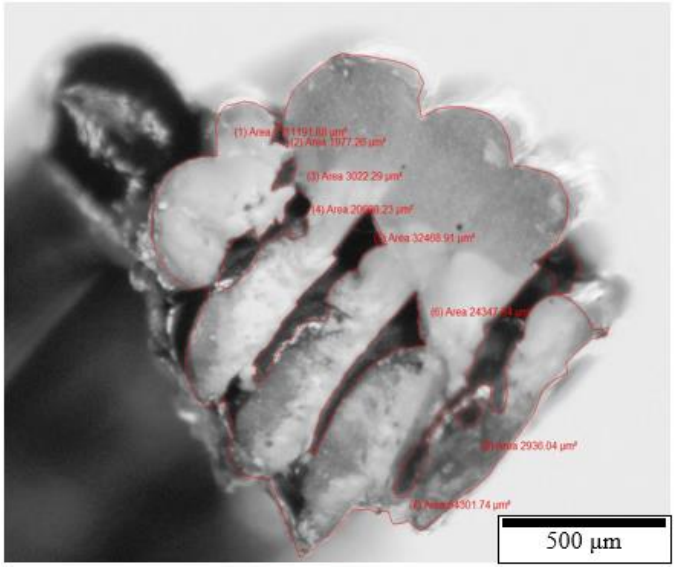

Figure 4.8. Example showing the measurement of void content on the cross-section of HT125-warp sample.

4.2.7. Statistical Analysis

Analysis of variance (ANOVA) test was done for tensile test results by using Microsoft Excel to evaluate the effect of heat treatment on the 3D printed fabrics and dog-bone samples. All analyses were carried out at 0.05 significance level (i.e., $\alpha = 0.05$). To determine exactly which group means are significantly different, a Tukey-Kramer post hoc test was performed.

4.3. Results and discussion

4.3.1. Optical Microscope (OM) Analysis

The OM images of the cross-sections of fractured NHT and HT twill fabric samples are presented in Figure 4.9. The cross-section of NHT-warp shows uniform fusion of fibers having smaller pores, whereas the HT125-warp has separated fibers having a large volume of voids, as indicated by dotted circles. Although each fiber is separated, the breaking of individual fibers is not seen. Since all the fibers are positioned parallel to each other, they are united under tensile loading and contribute equally to mechanical strength. The NHT-weft yarn has proper fusion of fibers on its cross-section, but it contains crack growth lines extending from the circumference towards the center with a void content of 1.82% of its total cross-sectional area.

After heat treatment at 125 ℃, the crack propagated causing each deposited layer to be fractured and the void content increased to 6.78% of the total cross-sectional area. The fractured layer contributes to strength reduction and ultimately failure.

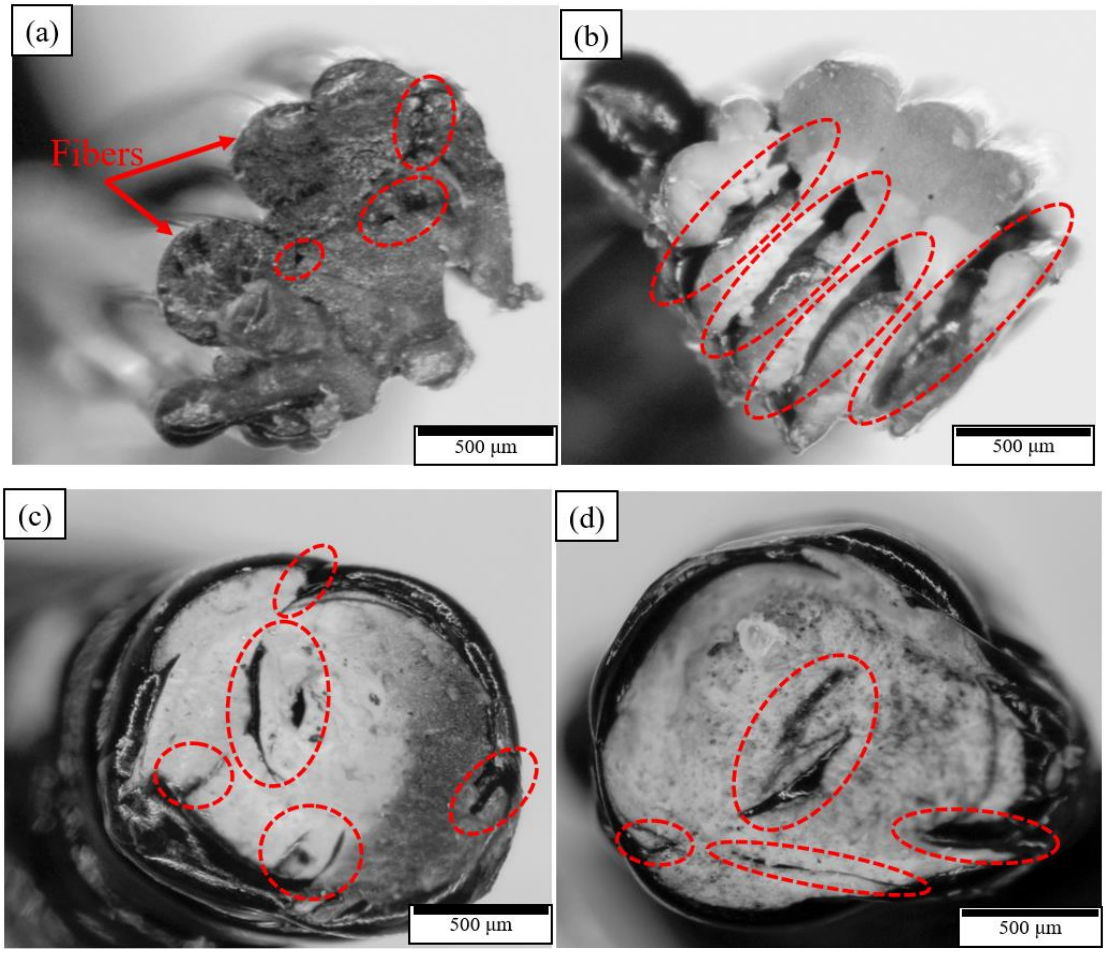

Figure 4.9 Optical microscope images showing the cross-sections of non-heat-treated and heat-treated warp and weft yarns separated from 3D printed 2/1 twill fabric structures after tensile testing: (a) NHT-warp, (b) HT125-warp, (c) NHT-weft, and (d) HT125-weft.

The longitudinal surfaces of warp and weft yarns are shown in Figure 4.10. The surface of NHT-warp is observed to be intact and voids are hard to find, whereas in the HT125-warp yarn, the broken fibers can be easily observed. However, most of the fibers are still intact and continuous; as a result, the change in tensile strength was statistically insignificant. In case of weft yarns, the NHT-weft yarn contained proper fusion of deposited layers except few voids, which is only 0.69% of the total surface area. As a result of heat treatment at 125 ℃, the layers are broken multiple times as shown by dotted circles (Figure 4.10 d) and the void content became 1.17% of total surface area. Since the tensile force is applied perpendicular to these

deposited layers, they got detached from each other under relatively small loads, which contributed towards the reduction in mechanical properties.

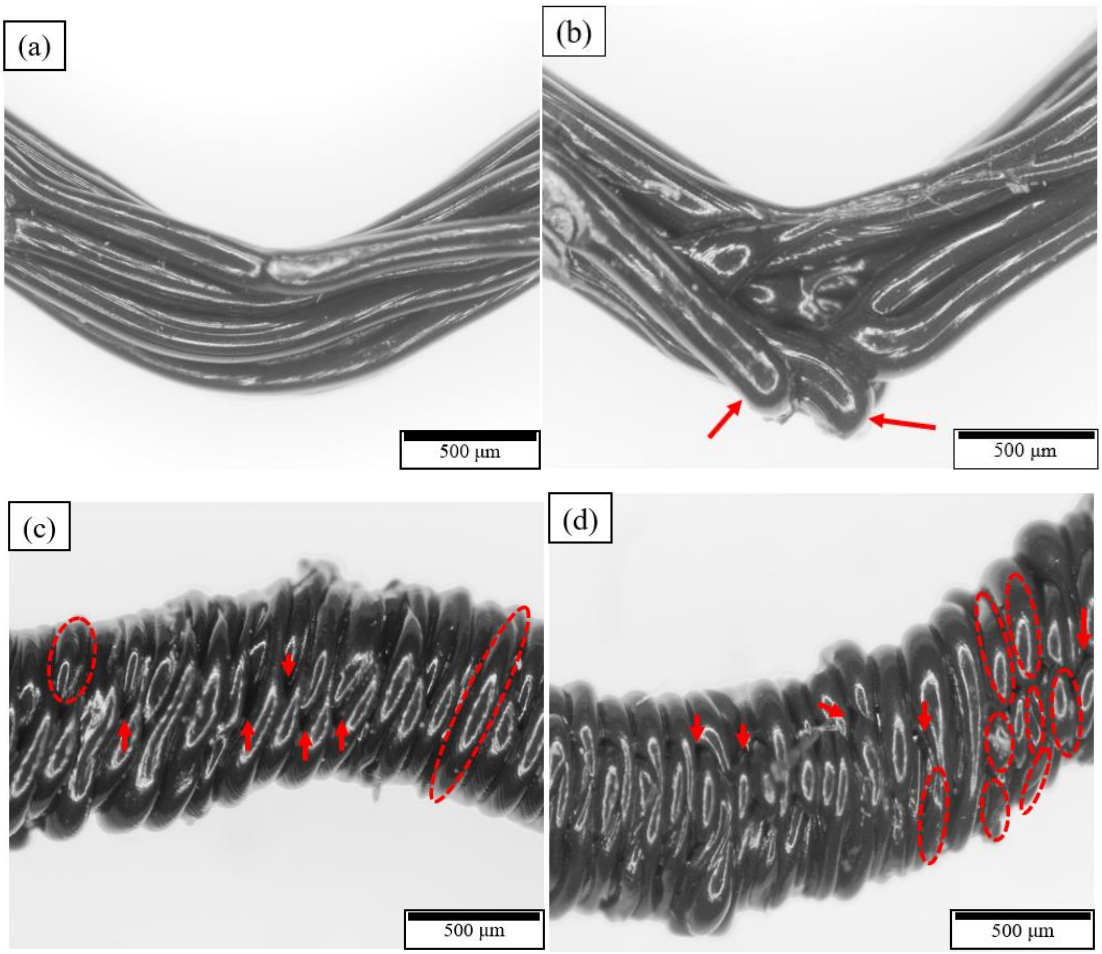

Figure 4.10. Optical microscope images showing the longitudinal surfaces of heat-treated and non-heat-treated warp and weft yarns separated from 3D printed 2/1 twill fabric structures after tensile testing: (a) NHT-warp, (b) HT125-warp, (c) NHT-weft, and (d) HT125-weft.

Figure 4.11 represents the microscopic images of cross-sections for heat-treated (at 125 ℃) and non-heat-treated dog-bone specimens. The cross-section of NHT-horizontal specimen shows the fusion of the deposited layers; after heating at 125℃, the layers are arranged in a sequence. The HT125-horizontal specimen undergoes brittle failure showing higher mechanical strength and lower elongation at maximum load. In vertical specimens, a void content of 26.70% of the total cross-sectional area between the layers can be seen as shown by the arrows. Those voids are filled up by the respective layers at 125 ℃ and reduced to 5.65%. This might have happened due to heating above glass transition temperature at which the polymer chain got chance to reinfuse together. It is believed that his reinfusion of layers improved the mechanical properties.

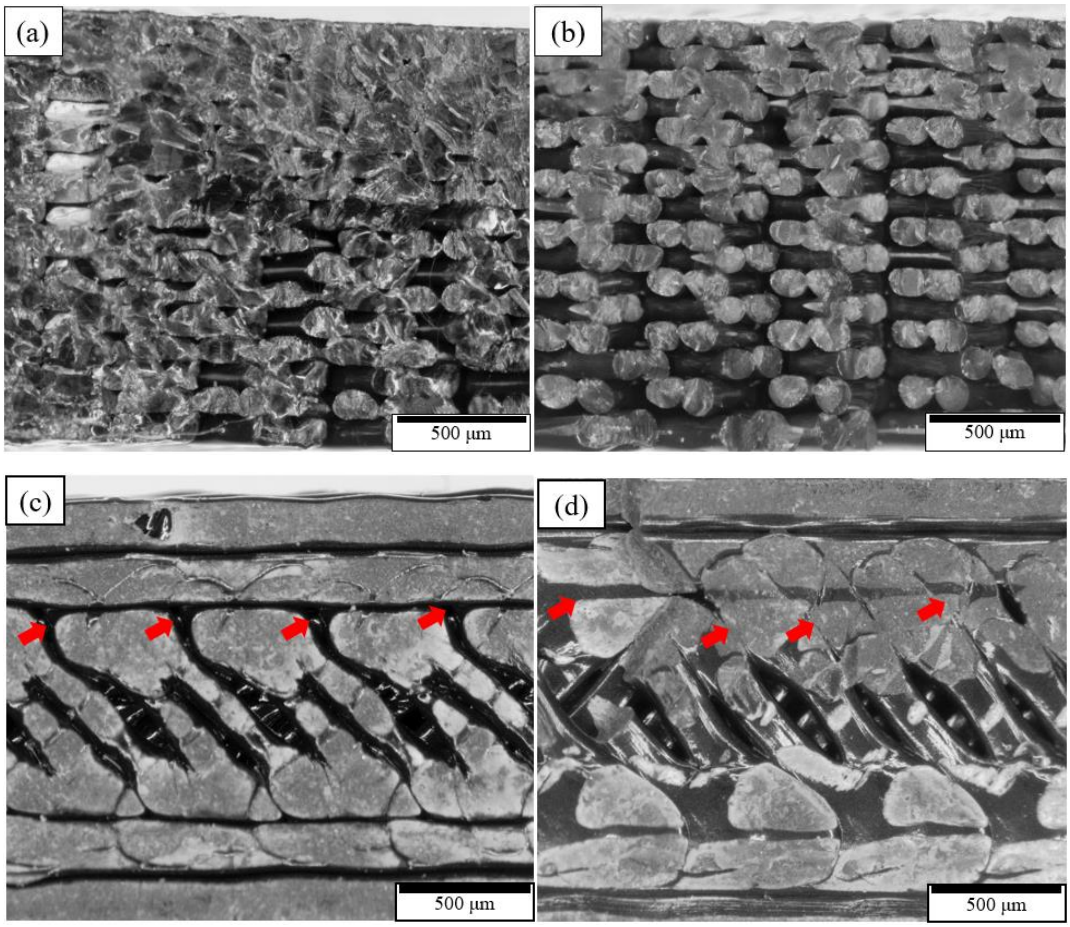

Figure 4.11. Optical microscope images showing the cross-sections of heat-treated and non-heat-treated horizontal and vertical dog-bone specimens after tensile testing: (a) NHT-horizontal, (b) HT125-horizontal, (c) NHT-vertical, and (d) HT125-vertical.

The longitudinal surfaces of dog-bones samples are shown in Figure 4.12. The surface of NHT-horizontal sample showed separation between the deposited layers as shown in the figure by rectangular boxes. These layers became attached after heating at 125 ℃ as shown by arrows. The layers of dog-bone samples printed in vertical orientation has higher void content as indicated in the figure. After heating at 125 ℃, void content was reduced to 0.75% of the total surface area. The reduction in void content improved the mechanical properties.

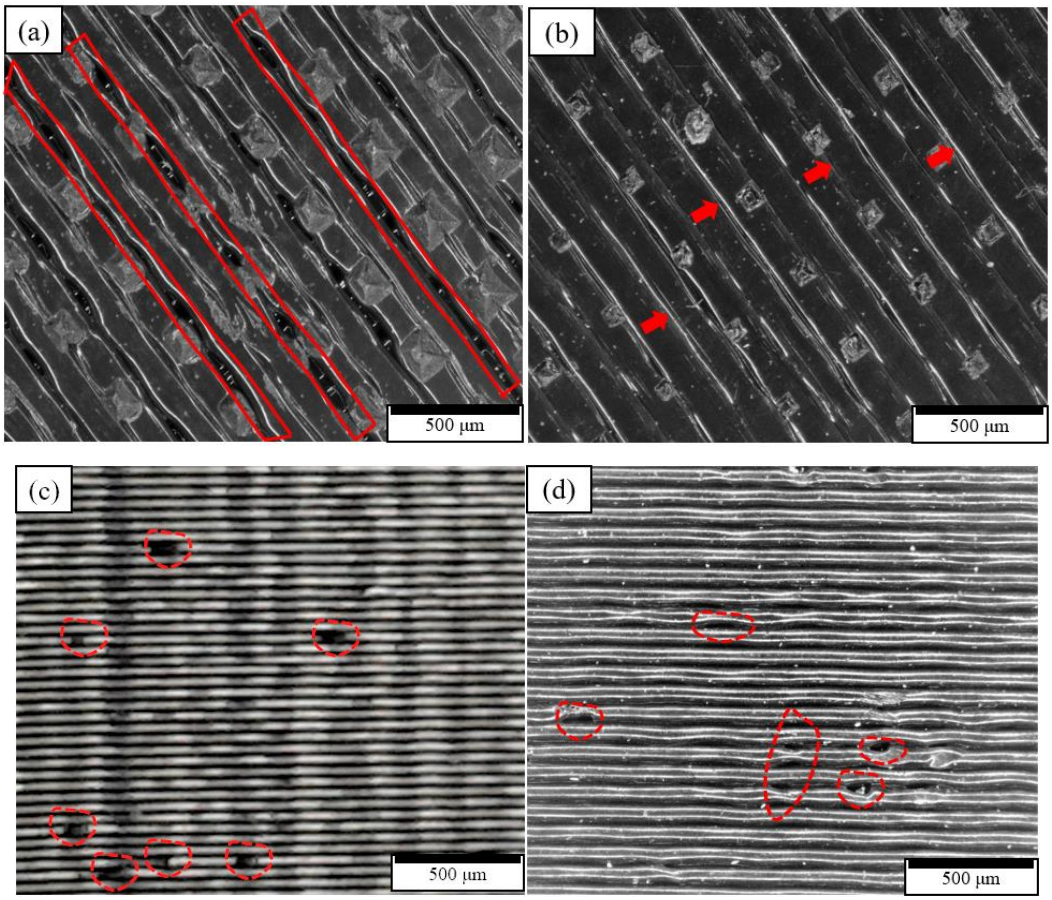

Figure 4.12. Optical microscope images showing the longitudinal surfaces of heat-treated and non-heat-treated horizontal and vertical dog-bone specimens after tensile testing. (a) NHT-horizontal, (b) HT125-horizontal, (c) NHT- vertical, and (d) HT125- vertical.

4.3.2. Uniaxial tensile test results

The uniaxial tensile test results of NHT and HT samples of twill fabrics and dog-bone specimens are presented in Figure 4.13 and Figure 4.14, respectively. In case of twill fabrics, the statistical analysis shows that there is no significant difference in ultimate tensile strength with the increasing temperature in warp direction ($p > 0.05$), whereas it decreases at 100 ℃ and 125 ℃ in weft direction ($p < 0.05$). The ultimate tensile strengths for fabric in warp direction are 29.85 ± 4.05 MPa, 28.60 ± 4.20 MPa, 27.70 ± 2.90 MPa, 26.30 ± 1.95 MPa, 25.80 ± 1.85 MPa for NHT, HT50, HT75, HT100, and HT125 samples, respectively. Similarly, on applying Tukey-Kramer post hoc test on multiple comparisons, it was found that the stiffnesses of fabrics in warp direction are significantly different ($p < 0.05$) except for NHT-warp vs HT50-warp. The stiffness of HT100-warp samples is 651.15 ± 36.50 MPa and that of NHT-warp samples is 497.30 ± 50 MPa, which shows an increment of 31 %, whereas the stiffness of HT125-warp samples is 578.07 ± 85.80 MPa, which shows an increment of 16.25 %. The ultimate tensile

strengths of the fabrics in weft direction are 15.70 ± 1.15 MPa, 16.65 ± 1.15 MPa, 14.08 ± 1.10 MPa, 7.73 ± 2.12 MPa, 12.54 ± 1.05 MPa for NHT, HT50, HT75, HT100, and HT125 samples, respectively. The tensile strength of HT125-weft samples is 20.13 % less than that of NHT-weft samples. The stiffness of HT100-weft samples is 463.70 ± 69.60 MPa and that of NHT-weft samples is 539.30 ± 38.30 MPa, which shows a decrease of 14 %, whereas the stiffness of HT125-weft samples is 431.65 ± 90.63 MPa, which shows a decrease of 20 %. As a result of applying Tukey-Kramer post hoc test on multiple comparisons, it was found that the elongations at maximum load are significantly different in warp and weft directions for HT75 and HT100 samples as compared to NHT samples. The elongation at maximum load decreases from 17.90 % ± 6.55 % for NHT-warp samples to 10.64 % ± 0.88 % for HT75-warp samples and to 10.20 % ± 2.03 % for HT100-warp samples. Similarly, the elongations decrease from 4.30% ± 0.55% for NHT-weft samples to 2.92 % ± 0.45 % for HT75-weft samples and to 3.09 % ± 0.72 % for HT100-weft samples**.**

In this study, the improvement in fabric stiffness in warp direction, unchanged tensile strength in warp direction, and decrease in tensile strength and modulus in weft direction are observed. The mechanical properties of fabrics in warp direction are satisfactory since the fibers are continuous and aligned parallel to each other in warp direction. Although some separation between the fibers can be seen in the cross-section (shown in Figure 4.9 a and b), nevertheless all the fibers are grouped together providing the strength. As shown in Figure 4.10 a and b, the breakage of a fiber is visible; however, most of the fibers are still intact which tend to preserve the strength of the fabric. On the other hand, the fabric mechanical properties are not satisfactory in weft direction. This is because the weft yarns are formed by deposition of staple-like fibers on top of each other on the cross-section (as shown in Figure 4.10 c and d), which results in fibers being discontinuous along the weft direction. As stated earlier, a single deposited layer is broken multiple times as shown by dotted circles since the void content increased from 1.82% in non-heat-treated state to 6.78% of the total cross-sectional area and the void content on the surface of weft yarns increased from 0.69% to 1.17% of the total surface area. As a result, stress concentration increased at cross-over points during tensile loading making them easier to break.

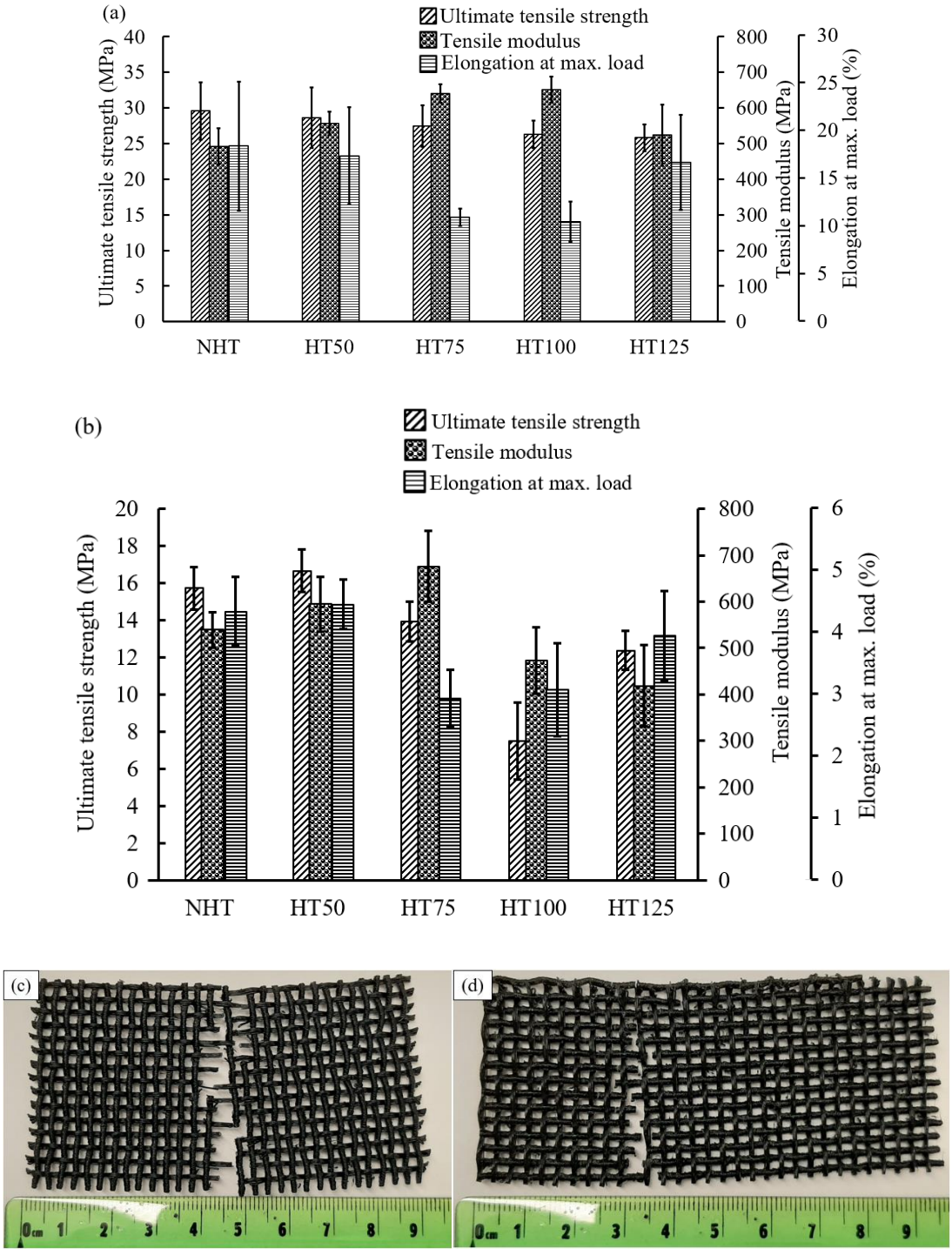

Figure 4.13. Uniaxial tensile test results of the fabrics: (a) Twill fabric in warp direction, (b) Twill fabric in weft direction, (c) Failure of HT125-warp sample, and (d) Failure of HT125-weft sample.

After performing Tukey-Kramer post hoc test on multiple comparisons, the ultimate tensile strength increased for dog-bone samples heat-treated at 100 ℃ and 125 ℃ in both horizontal and vertical directions. The ultimate tensile strengths of dog-bone samples in

horizontal direction are 37.80 ± 3.60 MPa, 40.30 ± 3.10 MPa, 40.30 ± 7.55 MPa, 45.20 ± 1.40 MPa and 47.70 ± 3.15 MPa for NHT, HT50, HT75, HT100, and HT125 samples, respectively. There is 20% and 26% increase in ultimate tensile strength after heat treatment at 100 ℃ and 125 ℃ respectively. The ultimate tensile strengths of dog-bone samples in vertical directions are 22.75 ± 1.75 MPa, 23.05 ± 4.0 MPa, 25.05 ± 1.70 MPa, 26.60 ± 1.5 MPa and 28.0 ± 1.40 MPa for NHT, HT50, HT75, HT100, and HT125 samples, respectively. There is a 17% and 23% increase in ultimate tensile strength after heat treatment at 100 ℃ and 125 ℃, respectively. This is because higher temperature might have made the polymer rubbery in nature, enhancing the polymer chain mobility and hence allowing the deposited layers to glue better with each other as shown in Figure 4.11 and Figure 4.12. The stiffness also increased due to heat treatment in both directions at 100 ℃ and 125℃. It increased from 1.49 ± 0.18 GPa for NHT-horizontal to 1.79 ± 0.03 GPa for HT100-horizontal samples (20% increment) and to 2.07 ± 0.41 GPa for HT125-horizontal samples (39% increment). In vertical orientation, the stiffness increased from 1.63 ± 0.07 GPa of NHT to 1.80 ± 0.05 GPa of HT100 samples (10% increment) and to 2.15 ± 0.07 GPa of HT125 samples (32% increment). The elongation at maximum load decreased for HT125-horizontal samples (30% less); however, there is no statistically significant difference in elongation for dog-bone samples 3D printed in vertical orientation. The thermal processing might have enhanced the polymer chain mobility and provided enough time to recrystallize which improved the crystallinity of polymer. In addition, it also provided an opportunity for reinfusion between the deposited layers and hence increased the bonding between the layers and rasters (Figure 4.11 and Figure 4.12). As a result, improvement in mechanical properties has been observed.

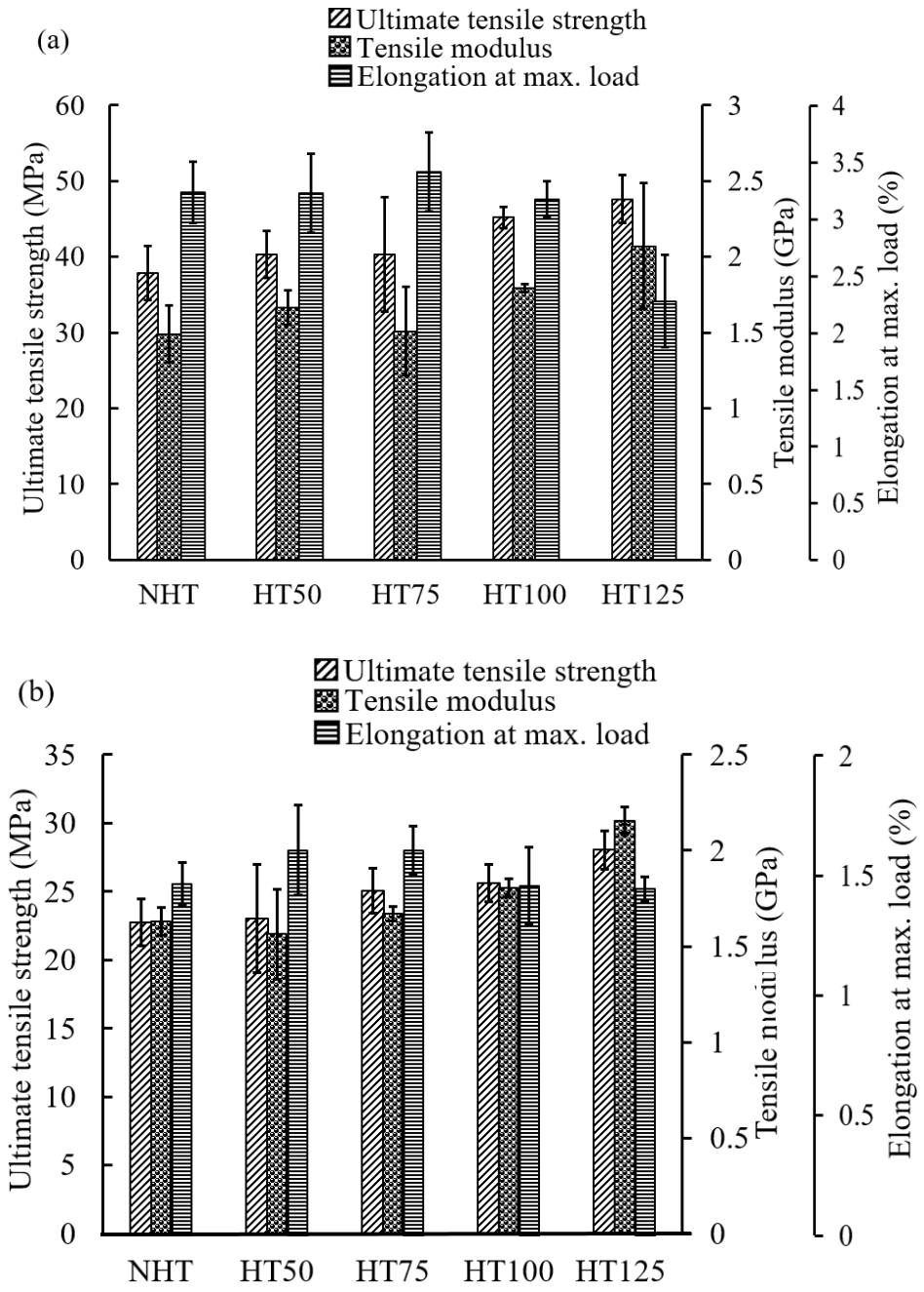

Figure 4.14. Uniaxial tensile test results of DB samples: (a) Dog-bone specimen in horizontal orientation, and (b) Dog-bone specimen in vertical orientation.

Different behavior of 3D printed twill fabrics was observed after heat treatment in comparison with the dog-bone samples, which can be attributed to the yarns in the fabric structure having crimps. Stress concentration at cross-over points of fabrics plays a significant role in fabric failure, which causes them to break easier. In addition, deposited layers or fibers on the surfaces were broken which affected the mechanical strength.

4.3.3. DSC Results

The DSC curves showing the first heating and cooling cycles of NHT and HT twill fabric and dog-bone specimens are presented in Figure 4.15 and Figure 4.16 and the properties obtained from the tests are tabulated in Table 4.2 and Table 4.3, respectively. The important phases such as glass transition (T_g), cold crystallization and melting point (T_m) are critically analyzed to determine the polymer crystallinity. The heating cycle shows the glass transition temperature at about 60℃ and melting temperature in the range of 165-175℃ for all the samples.

In case of twill fabrics, the cold crystallization point is observed only for NHT and HT50 samples at about 103℃. A peak of small area is observed for HT75 sample showing the cold crystallization temperature at 152℃ and average enthalpy of 4.4 J/g in both directions. Since the NHT and HT50 samples are below T_g, it is expected to have cold crystallization peaks which causes the reduction in percent crystallinity. HT75-warp and HT75-weft samples were heat-treated close to their T_g; therefore, the appearance of cold crystallization peaks of smaller area before melting point is expected. The heat treatment at higher temperatures (100℃ and 125℃) slightly enhances the crystallinity behavior of PLA and hence the cold crystallization points disappear. The higher temperature allows better mobility of polymer chains to align properly, increasing the crystallinity.

In case of dog-bone specimens, two cold crystallization peaks are seen at about 85℃ and 153℃ for NHT-horizontal and HT50-horizontal samples, similar to observations in ref. [29], whereas these peaks appear at 103℃ and at 152℃ for NHT-vertical and HT50-vertical samples. This type of cold crystallization is caused by rapid cooling of the melt during the extrusion process. Similar to the fabric samples, the heat-treated dog-bone samples show a cold crystallization peak having enthalpy of about 5 J/g at 154℃ for HT75-horizontal samples and at 144℃ for HT75-vertical samples. Again, crystallization is improved with increasing temperatures, caused by better mobility of polymer chains.

During the first heating cycle, HT125-warp and HT125-weft samples exhibited two endothermic melting peaks at ~160℃ and ~170℃, similar to observations in ref. [30], which has been formed due to the presence of multiple crystalline states (α′ and α) of PLA [8], [31], [32]. The first peak present at lower temperature is associated with the melting of the α′ crystalline state and its recrystallization into the α form, whereas the second peak at higher

temperature is related to the melting of the α state. The transition of α′ form after melting and into α form due to its recrystallization is called α′– α phase transition [8]. The cooling cycle gives the melt crystallization peak in each sample. The values of enthalpies obtained from melting peak during heating cycle and melt crystallization peak during cooling cycle are almost equal in each sample. This peak indicates the crystalline nature of the polymer.

The factors such as spatial confinement, nucleation on sample boundaries, temperature gradient, and melt flow play a vital role in crystallization of polymers [33]. Similarly, the addition of foreign substances in the pure PLA matrix affects the crystallization of PLA either by assisting or hindering the chain mobility [34]. The PLA filament used in this study has a crystallinity of 14.74%, T_g of 62℃, T_{cc} of 88℃ with ΔH_{cc} of 16.24 J/g and T_m of 165℃ with ΔH_m of 30.04 J/g. The crystallinity percentages of NHT twill fabrics are 2.82% and 1.94% in warp and weft directions, respectively. After heat-treatment at 50℃, the values increased to 4.58% and 2.67% in warp and weft directions, respectively. This indicates that thermal processing increases the crystallinity of polymer. The crystallinity of NHT and HT50 twill fabrics in both warp and weft directions are very low, which indicates that the material is amorphous. The heat-treatment at 75℃, 100℃, and 125 ℃ for 1 hour increased the percent crystallinity showing the semi-crystalline behavior of PLA. The maximum crystallinity is reached at 125℃ with 31.28% and 30.22% in warp and weft directions, respectively.

The crystallinity percentage of NHT-horizontal dog-bone specimen is 11%, which indicates more amorphous and less crystalline behavior. The NHT-vertical specimen has a lower crystallinity, about 4% because of fast extrusion over adjacent layers and rapid cooling. With the increasing temperature, the crystallinity increases until 125℃, with the maximum values of 38.28% and 28.96% in horizontal and vertical orientations, respectively. Higher temperature might have assisted in recrystallization.

The lower crystallinity in non-heat-treated samples might have happened due to melting, and extrusion through nozzle at higher temperature and rapid cooling of the polymer during 3D printing. During 3D printing, a high temperature difference between nozzle and print-bed occurs that provides a short period of time to crystallize which results in lower crystallinity.

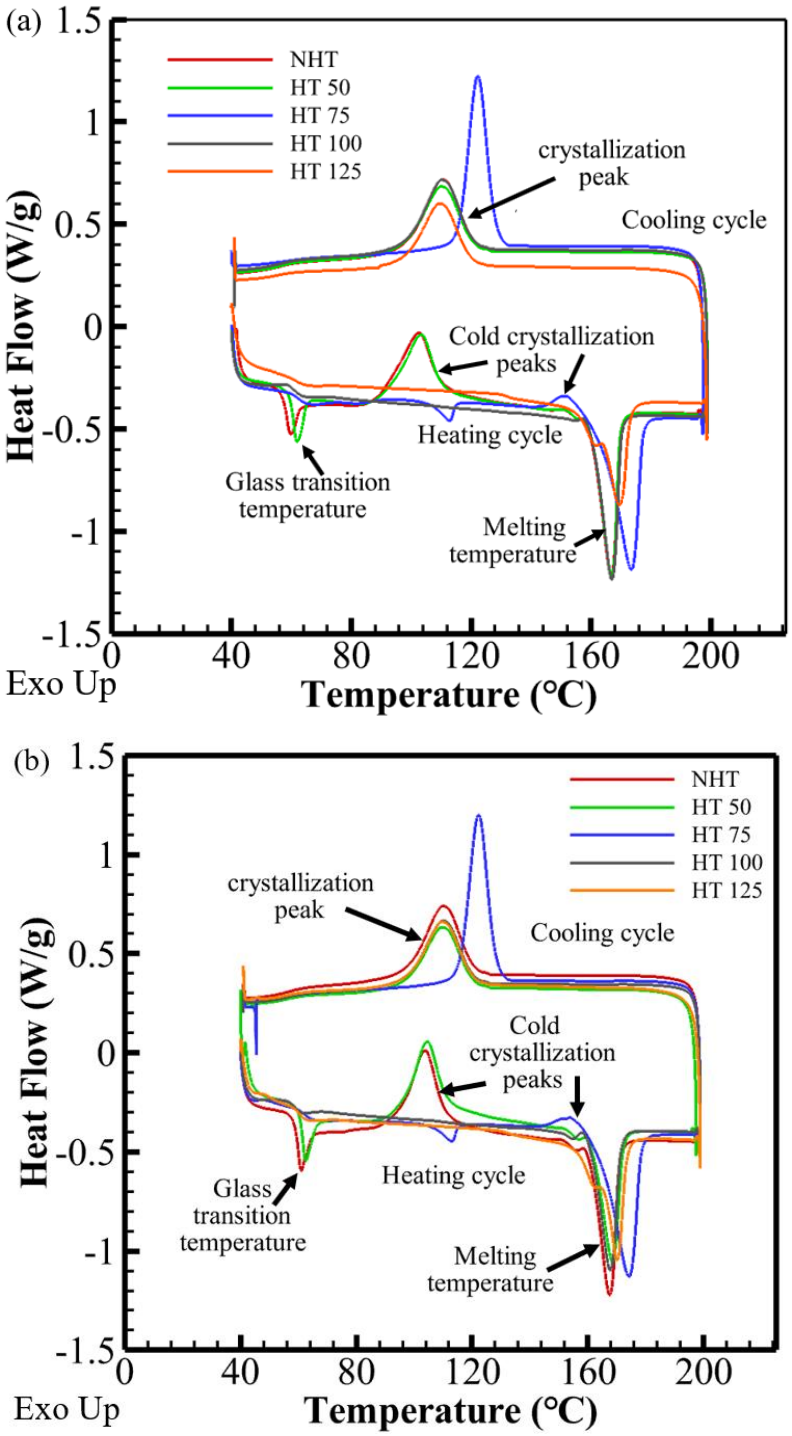

Figure 4.15. DSC graphs of heat-treated (HT) and non-heat treated (NHT) specimens: (a) Twill fabric in warp direction, (b) Twill fabric in weft direction.

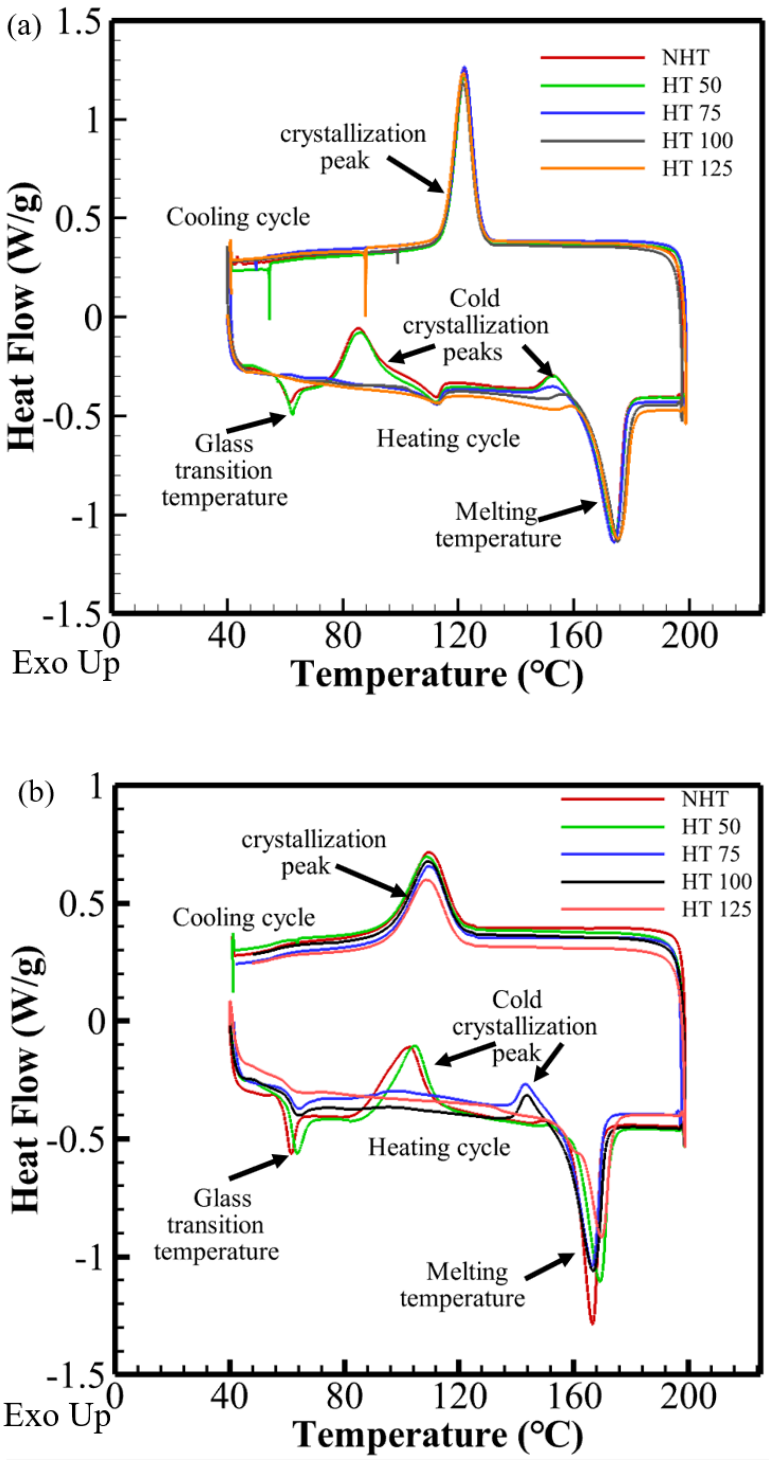

Figure 4.16. DSC graphs of heat-treated (HT) and non-heat-treated (NHT) specimens: (a) Dog-bone specimen printed in horizontal orientation, and (b) Dog-bone specimen printed in vertical orientation.

Table 4.2. DSC results of 2/1 PLA twill fabric samples obtained from the first heating cycle.

Sample	T_g (℃)	T_{cc_1} (℃)	ΔH_{cc_1} (J/g)	T_{cc_2} (℃)	ΔH_{cc_2} (J/g)	T_m (℃)	ΔH_m (J/g)	Crystallinity [%]
PLA filament	62.02	88.58	16.24	*	*	165.72	30.04	14.74
NHT–warp	58.57	102.42	26.42	*	*	166.78	29.06	2.82
NHT–weft	59.84	103.70	27.15	*	*	167.54	28.97	1.94
HT50–warp	60.88	103.29	23.67	*	*	166.94	27.96	4.58
HT50–weft	61.66	104.61	22.68	*	*	168.64	25.18	2.67
HT75–warp	59.92	*	*	147.74	3.705	169.24	30.75	28.90
HT75–weft	59.73	*	*	148.83	4.701	169.78	31.68	28.82
HT100–warp	60.07	*	*	*	*	167.07	29.15	31.14
HT100–weft	58.84	*	*	*	*	167.71	27.82	29.72
HT125–warp	59.72	*	*	*	*	168.61	29.28	31.28
HT125–weft	60.14	*	*	*	*	168.53	28.29	30.22

Note 4.1: * sign indicates the disappearance of cold crystallization peak. For NHT and HT50 samples, the cold crystallization peak appears around 100℃ and for HT75 samples, it is seen around 150℃ whereas it vanishes when the samples are heat-treated at higher temperatures which proves that the specimens are more crystalline.

Table 4.3. DSC results of dog-bone specimens obtained from the first heating cycle.

Sample	T_g (℃)	T_{cc} (℃)	ΔH_{cc_1} (J/g)	T_{cc_2} (℃)	ΔH_{cc_2} (J/g)	T_m (℃)	ΔH_m (J/g)	Crystallinity [%]
NHT–horizontal	59.93	85.46	23.01	153.52	5.96	173.73	39.27	11
NHT–vertical	60.26	102.71	25.79	150.86	1.154	166.49	30.62	3.93
HT50–horizontal	61.68	85.59	18.72	153.56	7.60	173.97	39.00	13.55
HT50–vertical	61.57	104.53	25.48	153.32	0.993	169.25	27.62	1.23
HT75–horizontal	60.75	*	*	154.42	5.026	173.94	35.09	32.12
HT75–vertical	62.13	*	*	143.75	5.874	166.50	30.83	26.67
HT100–horizontal	59.83	*	*	157.48	1.785	175	33.56	33.95
HT100–vertical	61.37	*	*	144.07	4.696	166.89	30.52	27.59
HT125–horizontal	59.72	*	*	*	*	175.11	35.83	38.28
HT125–vertical	60.19	*	*	*	*	169.81	27.11	28.96

Note 4.2: * sign indicates the disappearance of cold crystallization peak. For NHT and HT50 samples, two cold crystallization peaks are seen, whereas it vanishes when the samples are heat-treated at higher temperatures which proves that the specimens are more crystalline.

4.3.4. Relationship between crystallinity and mechanical strength

Figure 4.17 shows the effect of crystallinity on mechanical properties of the samples. As shown in the figure, the crystallinity increases slightly at 50℃, which indicates that the crystallinity can increase due to thermal processing after 3D printing. Further heat treatment at

75℃, 100 ℃, and 125 ℃ increased the average value of crystallinity to 28%, 30% and 31%, respectively. This improvement might have happened due to better chain mobility of polymers and enough time for crystallization. There is no significant difference between the modulus for NHT-warp and HT50-warp samples; however, a significant improvement in modulus can be observed for HT75-warp, HT100-warp, and HT125-warp samples. The stiffnesses was increased by 29%, 31%, and 16% after heat treatment at 75 ℃, 100 ℃, and 125 ℃, respectively. This shows that the increase in crystallinity might have increased the stiffness of the structure. However, the ultimate tensile strength remains statistically insignificant in warp direction. The stiffnesses of fabrics in weft direction decreased by 14% at 100 ℃ and 20% at 125 ℃. Likewise, the strength also decreased by 50%, and 20% at 100 ℃, and 125 ℃, respectively.

It has been reported that increase in crystallinity should increase tensile strength and stiffness of the PLA material [22], [23] , [35]. However, in this study, improvement in stiffness for fabrics in warp directions, unaffected tensile strength in warp direction, and decrease in strength and modulus in weft direction have been observed. This may have happened due to the interlacing nature of the fabrics made of brittle materials like PLA, which develops stress concentration making them easier to break at the cross-over points of yarns. Also, the slower cooling method could have caused shrinkage distortion leading to internal defects and residual stress affecting the mechanical strength of 3D printed PLA fabric samples [11].

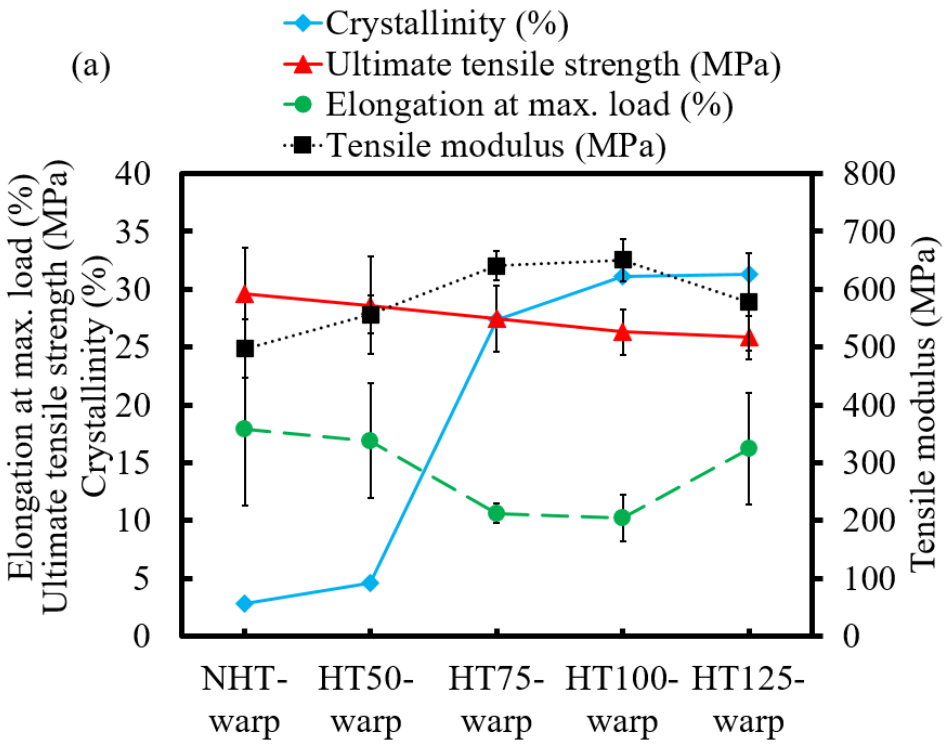

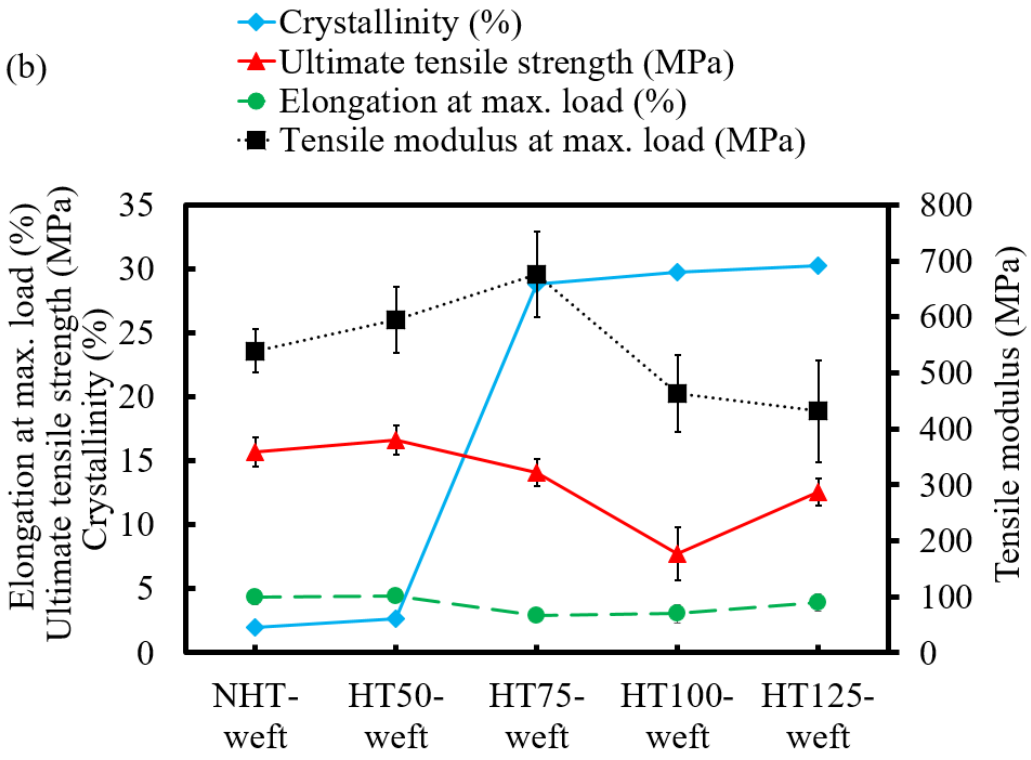

Figure 4.17. Relationship between crystallinity and mechanical properties of 3D printed parts using PLA for heat-treated (HT) and non-heat-treated (NHT) samples: (a) Twill fabric in warp direction, (b) Twill fabric in weft direction.

Figure 4.18 shows the relationship between crystallinity and mechanical properties of HT and NHT DB samples. The thermal processing lower than glass transition temperature did not have significant effect on crystallinity. However, heat treatment at 75°C, 100°C, and 125°C caused an improvement up to 32%, 34%, and 38% for HT75-horizontal, HT100-horizontal, and HT125-horizontal samples, respectively, and up to 27%, 28%, and 29% for HT75-vertical, HT100-vertical, and HT125-vertical samples, respectively. The ultimate tensile strength increased for dog-bone samples heat-treated at 100°C and 125°C in both horizontal and vertical directions. It increased by 20% and 26% for HT100-horizontal and HT125-horizontal samples, respectively. Similarly, in vertical direction, it is improved by 17% and 23% after heat treatment at 100°C and 125°C, respectively. The stiffness also increased due to heat treatment in both directions at 100°C and 125°C. It increased by 20% for HT100-horizontal samples and by 39% for HT125-horizontal samples. In vertical orientation, the stiffness increased by 10% at 100°C, and by 32% at 125°C.

From this analysis, it can be concluded that heat treatment increases the crystallinity of samples and also improves the mechanical properties in comparison with the NHT samples.

Hence, a direct relationship between crystallinity and mechanical properties (e.g., modulus and ultimate tensile strength) can be established for a standard sample but may not be true for non-standard samples such as woven fabrics. The heat treatment method enhanced the polymer chain mobility and provided enough time to recrystallize which improved polymer crystallinity. At the same time, it also provided an opportunity for reinfusing between the deposited layers and hence increased the bonding between the layers and rasters. As a result, an improvement in mechanical properties has been observed.

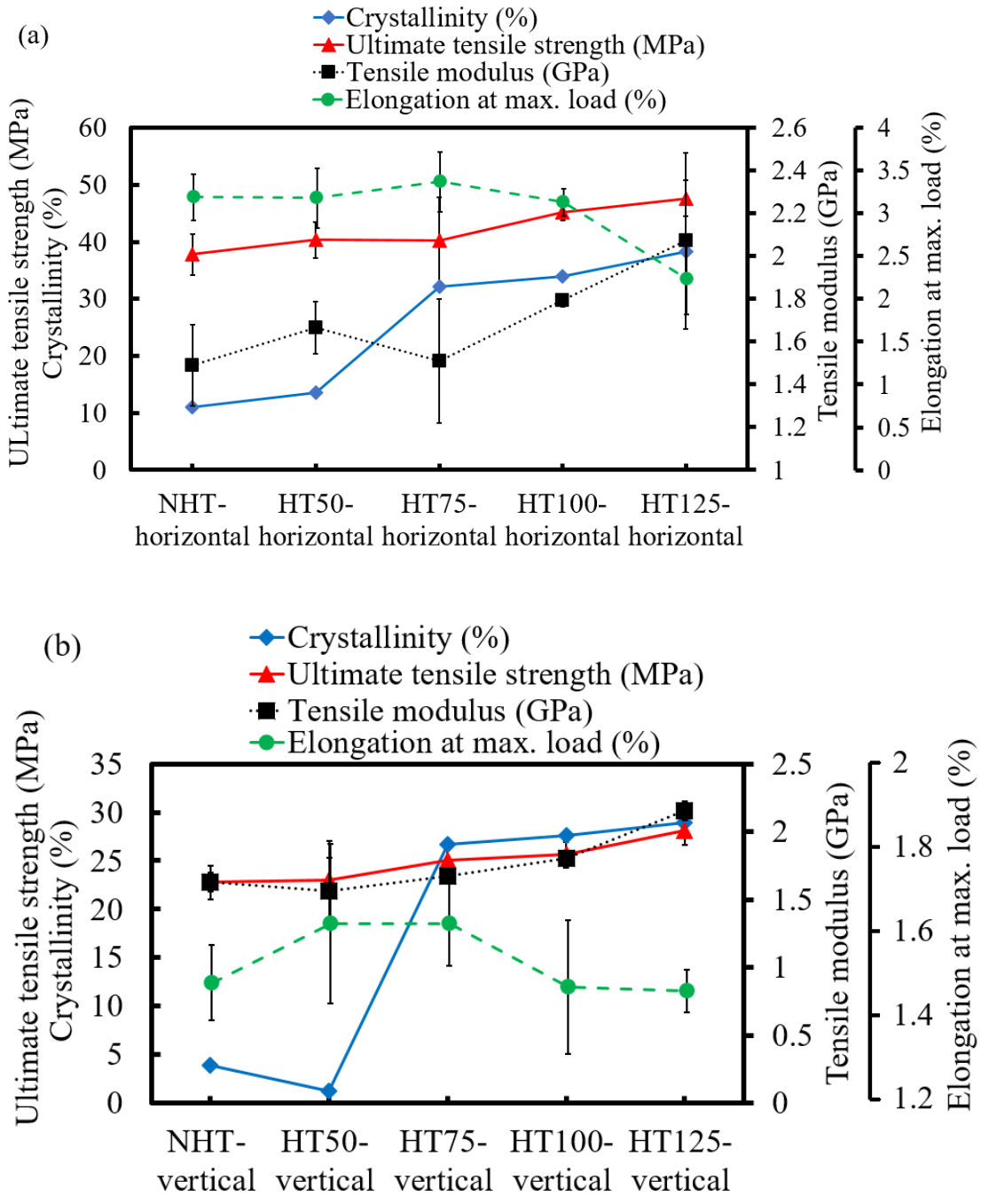

Figure 4.18. Relationship between crystallinity and mechanical properties of 3D printed parts using PLA for heat-treated (HT) and non-heat-treated (NHT) samples: (a) Dog-bone specimen in horizontal orientation, and (b) Dog-bone specimen in vertical orientation.

4.4. Conclusions

This study contributes to the research work related to wearable 3D printed fabrics. 2/1 twill fabric structures were designed, and 3D printed using FDM technology. As a post-processing method to improve the mechanical performance, heat treatment at different temperatures for 1 hour was adopted. This research investigated the effects of heat treatment on mechanical properties and crystallinity for 3D printed samples. The following conclusions can be drawn from this work:

- The tensile test results showed that the mechanical properties of 3D printed samples depend on heat treatment at various temperatures and the geometry of the structure. This method improved fabric stiffness in warp direction; however, the difference in ultimate tensile strength in warp direction is statistically insignificant. Unlike warp direction, both the strength and stiffness decreased in weft direction after heat treatment. However, the tensile strength and stiffness were improved for dog-bone samples 3D printed in both horizontal and vertical directions.
- The crystallinity of all the studied samples increased when heated above the glass transition temperature. This might have happened due to increased polymeric chain mobility and sufficient time to recrystallize, which lacks during 3D printing. During 3D printing, there is a significant difference in nozzle and bed temperature and less time to crystallize resulting in lower crystallinity.
- Although crystallinity increased for fabric samples, a significant improvement in mechanical properties was not noted. The interlacing nature of the fabrics may be the reason behind it, which develops stress concentration at cross-over points, causing breakage of deposited layers. This research shows that relationships between crystallinity and mechanical properties may not be established for non-standard 3D printed fabric samples. In the case of dog-bone samples, the mechanical properties improved with increasing polymer crystallinity. This indicates that a direct relationship between crystallinity and mechanical properties can be established for an ASTM standard dog-bone samples.

This research presents results for 3D printing of 2/1 twill weave fabrics and dog-bone samples. 2/1 twill design is more complicated than the plain weave design which was the subject of our earlier work (Ref. 4). Other types of fabric designs such as basket, satin, and knitted structures will be studied in future work. Various other polymers and polymer composites can be used for 3D printing of fabrics to achieve improved fabric properties such as tear resistance, flexibility, smoothness, and mechanical strength. The effects of various heat treatment times will be the subject of future work.

4.5. References

[1] T. Campbell, C. Williams, O. Ivanova, and B. Garrett, "Could 3D Printing Change the World? Technologies, Potential, and Implications of Additive Manufacturing," *Atl. Counc.*, pp. 1–14, 2011.

[2] ASTM F2792-12a, "Standard Terminology for Additive Manufacturing Technologies," West Conshohocken (PA): ASTM International, 2012.

[3] T. R. Giri and R. Mailen, "Controlled snapping sequence and energy absorption in multistable mechanical metamaterial cylinders," *International Journal of Mechanical Sciences*, vol. 204. 2021, doi: 10.1016/j.ijmecsci.2021.106541.

[4] S. Adanur and A. Jayswal, "Additive manufacturing of interlaced fibrous structures," *Rapid Prototyp. J.*, vol. 27, no. 4, pp. 671–681, 2021, doi: 10.1108/RPJ-05-2020-0095.

[5] B. Akhoundi and A. H. Behravesh, "Effect of Filling Pattern on the Tensile and Flexural Mechanical Properties of FDM 3D Printed Products," *Exp. Mech.*, vol. 59, no. 6, pp. 883–897, 2019, doi: 10.1007/s11340-018-00467-y.

[6] J. M. Chacón, M. A. Caminero, E. García-Plaza, and P. J. Núñez, "Additive manufacturing of PLA structures using fused deposition modelling: Effect of process parameters on mechanical properties and their optimal selection," *Mater. Des.*, vol. 124, pp. 143–157, Jun. 2017, doi: 10.1016/J.MATDES.2017.03.065.

[7] J. M. Chacón, M. A. Caminero, P. J. Núñez, E. García-Plaza, I. García-Moreno, and J. M. Reverte, "Additive manufacturing of continuous fibre reinforced thermoplastic composites using fused deposition modelling: Effect of process parameters on mechanical properties," *Compos. Sci. Technol.*, vol. 181, pp. 1–18, 2019, doi: 10.1016/j.compscitech.2019.107688.

[8] T. Tábi, I. E. Sajó, F. Szabó, A. S. Luyt, and J. G. Kovács, “Crystalline structure of annealed polylactic acid and its relation to processing,” *EXPRESS Polym. Lett.*, vol. 4, no. 10, pp. 659–668, 2010, doi: 10.3144/expresspolymlett.2010.80.

[9] E. de Avila, J. Eo, J. Kim, and N. P. Kim, “Heat Treatment Effect on Mechanical Properties of 3D Printed Polymers,” in *MATEC Web of Conferences*, 2019, vol. 264, pp. 1–5, doi: https://doi.org/10.1051/matecconf/201926402001.

[10] B. Akhoundi, M. Nabipour, F. Hajami, and D. Shakoori, “An Experimental Study of Nozzle Temperature and Heat Treatment (Annealing) Effects on Mechanical Properties of High-Temperature Polylactic Acid in Fused Deposition Modeling,” *Polym. Eng. Sci.*, vol. 60, no. 5, pp. 979–987, 2020, doi: 10.1002/pen.25353.

[11] C. Yang, X. Tian, D. Li, Y. Cao, F. Zhao, and C. Shi, “Influence of thermal processing conditions in 3D printing on the crystallinity and mechanical properties of PEEK material,” *J. Mater. Process. Technol.*, vol. 248, no. April, pp. 1–7, 2017, doi: 10.1016/j.jmatprotec.2017.04.027.

[12] “Magazine, D. . N12 3D-printed bikini by Continuum Fashion and Shapeways. https://www.dezeen.com/2011/06/07/ n12-3d-printed-bikini-by-continuumfashion\ -and-shapeways/, 2011 (accessed on 22 Jan., 2020).” .

[13] “Studio, F. Dita’s Gown: A 3D Printed Dress. https: //www.francisbitonti.com/ditas-gown/, 2014 (accessed on 22 Jan., 2020).” .

[14] “All3DP. (2017). 3D Printed Shoes: An Overview. https://all3dp.com/3dprinted-shoes/ (accessed on 22 Jan., 2020).” .

[15] “Melnikova, R., Ehrmann, A., & Finsterbusch, K. 3D printing of textile-based structures by Fused Deposition Modelling (FDM) with different polymer materials. IOP Conference Series: Materials Science and Engineering. 62. IOP Publishing Ltd. 2014.”

[16] L. Partsch, S. Vassiliadis, and P. Papageorgas, “3D Printed Textile Fabrics Structures,” *5th Int. Istanbul Text. Congr. 2015 Innov. Technol. “Inspire to Innov.*, no. September, pp. 3–10, 2015.

[17] Z. Quan *et al.*, “Additive manufacturing of multi-directional preforms for composites: Opportunities and challenges,” *Mater. Today*, vol. 18, no. 9, pp. 503–512, 2015, doi: 10.1016/j.mattod.2015.05.001.

[18] “Lussenburg, K., Velden, N., Doubrovski, Z., Karana, E., & Geraedts, J. Designing with 3D Printed Textiles. 2014.”

[19] J. R. Dorgan, H. J. Lehermeier, L. Palade, and J. Cicero, “Polylactides: properties and prospects of an environmentally benign plastic from renewable resources,” *Macromol. Symp.*, vol. 175, no. 1, pp. 55–66, 2001.

[20] R. E. Drumright, P. R. Gruber, and D. E. Henton, “Polylactic acid technology,” *Adv. Mater.*, vol. 12, no. 23, pp. 1841–1846, 2000.

[21] R. Auras, B. Harte, and S. Selke, “An overview of polylactides as packaging materials,” *Macromol. Biosci.*, vol. 4, no. 9, pp. 835–864, 2004, doi: 10.1002/mabi.200400043.

[22] B. Gupta, N. Revagade, and J. Hilborn, “Poly(lactic acid) fiber: An overview,” *Prog. Polym. Sci.*, vol. 32, no. 4, pp. 455–482, 2007, doi: 10.1016/j.progpolymsci.2007.01.005.

[23] A. Sodergard and M. Stolt, “Properties of polylactic acid fiber based polymers and their correlation with composition,” *Prog. Polym. Sci.*, vol. 27, no. 6, pp. 1123–1163, 2002, doi: 10.1016/S0079-6700(02)00012-6.

[24] J. A. Cicero, J. R. Dorgan, J. Garrett, J. Runt, and J. S. Lin, “Effects of molecular architecture on two-step, melt-spun poly(lactic acid) fibers,” *J. Appl. Polym. Sci.*, vol. 86, no. 11, pp. 2839–2846, 2002, doi: 10.1002/app.11268.

[25] ASTM D638-14, “Standard Test Method for Tensile Properties of Plastics,” *ASTM Int. West Conshohocken, PA*, no. December, 2014, doi: 10.1520/D0638-14.

[26] ASTM D5035-11, “Standard Test Method for Breaking Force and Elongation of Textile Fabrics (Strip Method),” *ASTM Int. West Conshohocken, PA*, 2019.

[27] Z. Quan *et al.*, “Additive manufacturing of multi-directional preforms for composites: Opportunities and challenges,” *Materials Today*. 2015, doi: 10.1016/j.mattod.2015.05.001.

[28] C. Zhang *et al.*, “Thermal, mechanical and rheological properties of polylactide toughened by expoxidized natural rubber,” *Mater. Des.*, vol. 45, pp. 198–205, 2013, doi: 10.1016/j.matdes.2012.09.024.

[29] L. Běhálek, M. Maršálková, P. Lenfeld, J. Habr, J. Bobek, and M. Seidl, “Study of

crystallization of polylactic acid composites and nanocomposites with natural fibres by DSC method," *Nanocon*, 2013, Accessed: Dec. 14, 2020. [Online]. Available: http://konsys-t.tanger.cz/files/proceedings/14/reports/1959.pdf.

[30] M. A. Abdelwahab, A. Flynn, B.-S. Chiou, S. Imam, W. Orts, and E. Chiellini, "Thermal, mechanical and morphological characterization of plasticized PLA-PHB blends," *Polym. Degrad. Stab.*, vol. 97, pp. 1822–1828, 2012, doi: 10.1016/j.polymdegradstab.2012.05.036.

[31] M. A. Cuiffo, J. Snyder, A. M. Elliott, N. Romero, S. Kannan, and G. P. Halada, "Impact of the Fused Deposition (FDM) Printing Process on Polylactic Acid (PLA) Chemistry and Structure," *Appl. Sci.*, vol. 7, no. 6, p. 579, Jun. 2017, doi: 10.3390/app7060579.

[32] A. Jalali, M. A. Huneault, and S. Elkoun, "Effect of thermal history on nucleation and crystallization of poly(lactic acid)," *J. Mater. Sci.*, vol. 51, no. 16, pp. 7768–7779, 2016, doi: 10.1007/s10853-016-0059-5.

[33] S. Wasti *et al.*, "Influence of plasticizers on thermal and mechanical properties of biocomposite filaments made from lignin and polylactic acid for 3D printing," *Compos. Part B Eng.*, vol. 205, 2021, doi: 10.1016/j.compositesb.2020.108483.

[34] V. Mimini *et al.*, "Compatibility of Kraft Lignin, Organosolv Lignin and Lignosulfonate With PLA in 3D Printing," *J. Wood Chem. Technol.*, vol. 39, no. 1, pp. 14–30, Jan. 2019, doi: 10.1080/02773813.2018.1488875.

[35] W. Zhai, Y. Ko, W. Zhu, A. Wong, and C. B. Park, "A study of the crystallization, melting, and foaming behaviors of polylactic acid in compressed CO2," *Int. J. Mol. Sci.*, vol. 10, no. 12, pp. 5381–5397, 2009, doi: 10.3390/ijms10125381.

Chapter 5

Multiphysics computational analysis of 3D printed fabric structures

(Jayswal, A., Mailen, R. W., Liu, J. P., Harris, G., Siwakoti, M., and Adanur, S., *"Thermomechanical behavior of three dimensionally printed fabric structures",* Polymer Engineering & Science, 2023)

Abstract

Additive manufacturing of fabrics is an emerging research topic with potential applications in several industries including high performance wearable products and high-temperature textiles. Therefore, thermal, mechanical, and viscoelastic properties of such fabrics need to be determined. In this research, the thermo-mechanical behavior of additively manufactured plain weave fabrics at and above glass transition temperature (T_g) is studied. The time-dependent mechanical response using a viscoelastic material model is represented by a Prony series as a function of frequency (*f*). Unit cells of plain weave fabrics are additively manufactured using poly(lactic) acid (PLA). Tensile and compression tests were performed on unit cells in a thermal environment using dynamic mechanical analysis (DMA). A multi-physics finite element model is implemented to duplicate the experimental setup. The experimental results are compared with that of computational results. The relative error percentages in the peak forces at each temperature are 23.60% at 60 ℃, −8.85% at 65 ℃, and –6.25% at 70 ℃. A better agreement in peak forces is seen for unit cells above T_g. The computational model developed for unit cells is used to predict the thermo-mechanical-viscoelastic response of large additively manufactured fabric structures which is difficult to evaluate experimentally.

5.1. Introduction

A wide variety of methods have been used to manufacture fabrics with high strength, high flexibility and good tear resistance [1] [2]. Depending on the method adopted, a definite fabric design and structure is obtained which is used in several industries such as composites [3], filtration [4], fashion [5], safety and protection [6], and sports [7]. Although the traditional fabric manufacturing technologies have fulfilled the demands of fabric consumption [8], the whole manufacturing processes generate millions of tons of textile solid waste [9], contributes to almost 20 % of industrial water pollution and is also a major source of air pollution [10]. In addition, with the increasing population and sophisticated life standards, the demand for fabrics is ever increasing, especially the single-use or short-term-use fabrics which end up in landfills.

This makes the textile industry one of the major sources of pollution on our planet. It should also be kept in mind that soon the globe will not be able to handle additional solid waste anymore. Furthermore, the fabric production process passes through different phases such as fiber production, yarn production and many inter processes, and thus it consumes a lot of time, energy, and human resources to manufacture fabrics. Hence, a scientific selection of materials, and manufacturing processes comes into play. For these reasons, research on the additive manufacturing of fabrics has attracted the attention of researchers and scientists.

Several researchers have worked on producing the prototypes of additively manufactured fabric structures using fused deposition modeling (FDM) and Selective Laser Sintering (SLS) methods. However, FDM is the most used 3D printing technology in textiles and fashion industries. Melnikova et. al. used PLA, soft PLA, Lay Tekkks and BendLay and 3D printed textile-based structures [11]. Partsch et. al. designed, 3D printed and evaluated three different plain weaves using ABS polymer [12]. Lussenburg et. al. 3D printed a wearable garment using PLA and demonstrated that the final product does not contain fabric properties [13]. Spahiu et al. 3D printed several lattice auxetic structures having arrowhead shape with negative Poisson's ratio using a flexible material and then joined all the parts in a definite pattern to produce a wearable dress [14]. Kim et al. 3D printed several lattice structures of triangular shapes using thermoplastic polyurethane (TPU) and assembled them together producing the final 3D printed cloth [15]. Uysal and Stubbs 3D printed patterns and later sewn them together to obtain a final 3D printed glove [16]. Several other researchers used selective laser sintering (SLS) method to 3D print flexible weft knitted structures [17], and other structures such as skirts, blouses, belts, and jewelry using nylon powder as a feed material [18]. Although all these researchers attempted to 3D print fabric structures, the evaluation of mechanical properties of 3D printed fabric structures was not performed. The reasons include the complexity of lattice structures and the loading on the testing fixture. In our previous studies, we designed, 3D printed and evaluated the mechanical properties of plain weave, twill weave, weft knitted and braided fabric structures [8] [19] [20] [21]. Considering the difficulties in measuring and predicting the mechanical properties of 3D printed fabric structures, this study is conducted to propose a computational method to predict a coupled thermo-mechanical-viscoelastic behavior of large 3D printed fabric structures. The material is prone to creep and stress relaxation at service temperatures. One goal of this study is to investigate the critical temperature region near Tg.

The experimental evaluation of the properties of such complex structures is challenging due to the constraints in boundary conditions. To address this issue, analytical and numerical analysis has been adopted by different researchers [22] [23] [24].Dixit et. al. developed a finite element modeling of 5-harness satin weave composite unit cell and estimated its in-plane elastic properties [25]. Lin et. al. investigated the mechanical behavior of plain weave and satin weave fabrics using 3D finite element analysis in conjunction with a nonlinear mechanical model for the yarn [26]. Daelemans et. al. utilized a simulation methodology based on the concept of virtual fibers and digital elements and determined the mechanical behavior of 3D woven fabrics. In this method, the fibrous nature of the fabric is considered by modeling a yarn as a bundle of virtual fibers [27]. The fabrics considered for the studies are made of natural and/or synthetic fibers and yarns. Several researchers have worked on finite element modeling and simulation of fabric structures [28] [29] [30] [31] [32] but no work on the numerical analysis of 3D printed fabrics can be found in the literature to our knowledge.

The additively manufactured fabrics can be exposed to different temperatures according to the requirement. The mechanical properties of polymers are affected by temperature, especially at and above the glass transition temperature (T_g). In the present work, the thermomechanical behavior of additively manufactured plain weave fabric structures under tensile and compression loading is studied via experiments and finite element analysis (FEA). While the FEA has been widely used to study the thermomechanical, and viscoelastic behavior of various lattice structures [33], the multiphysics computational analysis of additively manufactured plain weave fabric structures is conducted for the first time in this study. The FEA model utilized in this study is based on linear elastic, and linear viscoelastic properties of the polymer. This model provides a basis for predicting the deformation of the material at and above glass transition temperature. Additionally, it helps to predict the behavior of larger additively manufactured fabric structures based on the behavior of the unit cells.

This chapter is organized into different sections. In the materials and methods section, the fabrication process explaining the 3D print settings used, thermal, viscoelastic, and mechanical property characterization of base material is explained. In addition, the design and 3D CAD model of plain weave fabric structures, and unit cells for experimental and computational analysis are described as well. In the results and discussion section, the thermomechanical behavior of the unit cell, its comparison with the computational model and

application to large fabric structures are explained. Finally, the associated challenges and limitations related to this work are mentioned.

5.2. Materials and methods

5.2.1. Material Selection and 3D printing

For fabrication purposes of the samples throughout this study, as-purchased black PolyLite ™ PLA 3D printing filament having a diameter of 2.85 mm is used. PLA is chosen for this study because it is biodegradable and renewable thermoplastic polymer which is derived from starch that is obtained from renewable sources such as corn, wheat, rice and sugarcane [20][34]. The properties such as relatively low glass transition temperature (T_g = 55–65°C), melting temperature (T_m = 170–180°C), low coefficient of thermal expansion [35] and non-adherence to the printing surface makes it a suitable candidate for 3D printing purposes [36] [37].

The samples are additively manufactured using a Lulzbot Taz Pro 3D printer, which has a nozzle diameter of 0.50 mm. Print settings include a printing temperature of 225 ℃, build plate temperature of 45 ℃, print speed of 10 mm/s, infill density of 100 %, and the infill pattern followed is "Lines". All the samples used in this work are 3D printed in horizontal (flat) orientation.

5.2.2. Thermal properties

Differential scanning calorimetry (DSC) test was performed to determine the thermal properties such as glass transition temperature (T_g), and specific heat capacity (C_p) of the as-purchased PLA filament using the TA instrument DSC25. The samples were subjected to heat-cool-heat (HCH) cycle between 20 ℃ to 100 ℃ with a linear heating and cooling rate of 5 ℃/min. The second heating cycle, shown in Figure 5.1, is used to determine the T_g and found to be approximately 60 ℃. It is important to study the behavior of polymers near T_g as the findings are transferable to other polymers with similar T_g. The specific heat capacity of the base material is found to be $C_p = 1410$ J/kg.K.

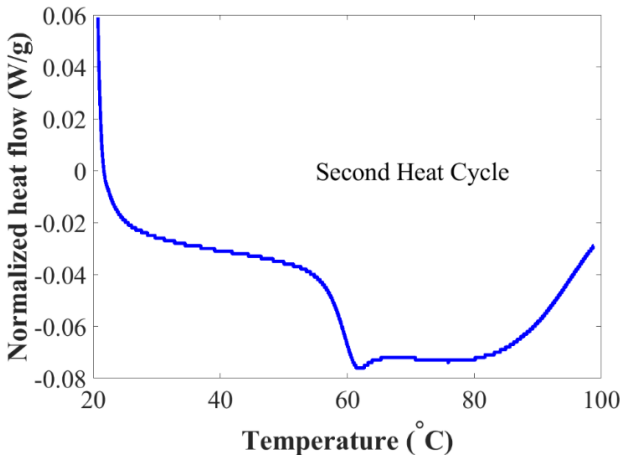

Figure 5.1. DSC results of PLA filament showing the second heating cycle.

5.2.3. Thermomechanical properties

To determine the thermomechanical properties of PLA, the dynamic mechanical analysis (DMA) test was performed using a TA instrument HR-20 Hybrid Rheometer. Before conducting this test, specimens with dimensions of 40 mm × 10 mm × 1 mm were 3D printed using Lulzbot Taz Pro 3D printer with the settings as explained in Section 5.2.1. The temperature sweep test was conducted using a torsion fixture from 30 °C to 75 °C in 3 °C increments for frequencies from 0.1 Hz to 10 Hz with 10 points per decade, and strain of 0.1%.

The time-dependent mechanical response using a viscoelastic material model [38] is represented by a Prony series, given by equations *(5.1)*, *(5.2)*, and *(5.3)*, as a function of frequency (*f*), which utilizes linear elastic and linear viscoelastic material models.

$$G'(f) = G_0\left[1 - \sum_{i=1}^{n} g_i\right] + G_0\left[\sum_{i=1}^{n} \frac{g_i(2\pi f\tau_i)^2}{1 + (2\pi f\tau_i)^2}\right] \quad (5.1)$$

$$G''(f) = G_0\left[\sum_{i=1}^{n} \frac{g_i(2\pi f\tau_i)}{1 + (2\pi f\tau_i)^2}\right] \quad (5.2)$$

$$\tan\delta = \frac{G''(f)}{G'(f)} \quad (5.3)$$

where, G_0 is the instantaneous shear modulus, g_i is the increment in storage modulus related to the relaxation time τ_i and tan δ is the phase angle. The fit of the Prony series to experimental viscoelastic material data has been verified by comparison to tan δ experimental results. The solid lines demonstrate the curve fitting of a Prony series with 2 relaxation times per decade in

Figure 5.2. The time-temperature superposition principle (TTSP) was applied to shift the individual curves and obtain the viscoelastic master curves as shown in Figure 5.2. TA Instruments Trios software was used for this purpose. The reference temperature considered was T_g = 60 °C. In this plot, the storage modulus (G'), loss modulus (G'') and tanδ are shown by blue, red and green curves, respectively. The discrete data represent the experimental results obtained from DMA analysis whereas the solid curves demonstrate the curve fitting of a Prony series with 2 relaxation times per decade.

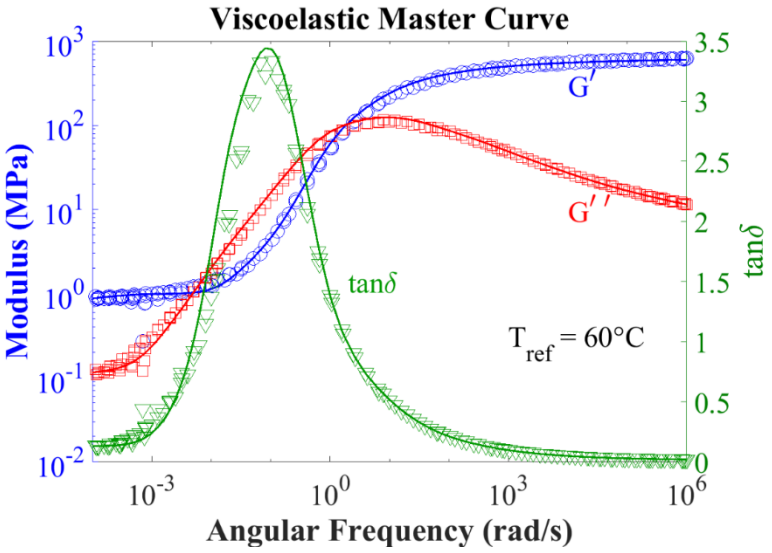

Figure 5.2. Viscoelastic master curve obtained from the temperature sweep DMA tests. $\boldsymbol{G'}$ is the storage modulus, $\boldsymbol{G''}$ is the loss modulus and tanδ is the phase angle.

The viscoelastic relaxation times τ_i are affected by the temperature and hence it is updated according to the time-temperature superposition principle (TTSP) by using the Williams-Landel-Ferry (WLF) equation [39]:

$$\log(a_t) = \frac{-C_1(T - T_{ref})}{C_2 + (T - T_{ref})} \tag{5.4}$$

where, a_t is the shift factor, C_1 and C_2 are the empirical constants which are experimentally determined for our material (C_1 = 13.65 and C_2 = 42.87), T is the instantaneous local temperature in degree Celsius, and T_{ref} is the reference temperature in degree Celsius which is typically taken to be T_g, which is 60 °C. The comparison between the experimentally obtained shift factors from DMA test and WLF model as a function of temperature is shown in

Figure 5.3. It is observed that the model fitted very well with the experimental results only above the glass transition temperature, which is to be expected for the WLF model. Because of the discrepancy in shift factors resulting from application of WLF, only the performance of the printed fabrics at or above T_g is considered.

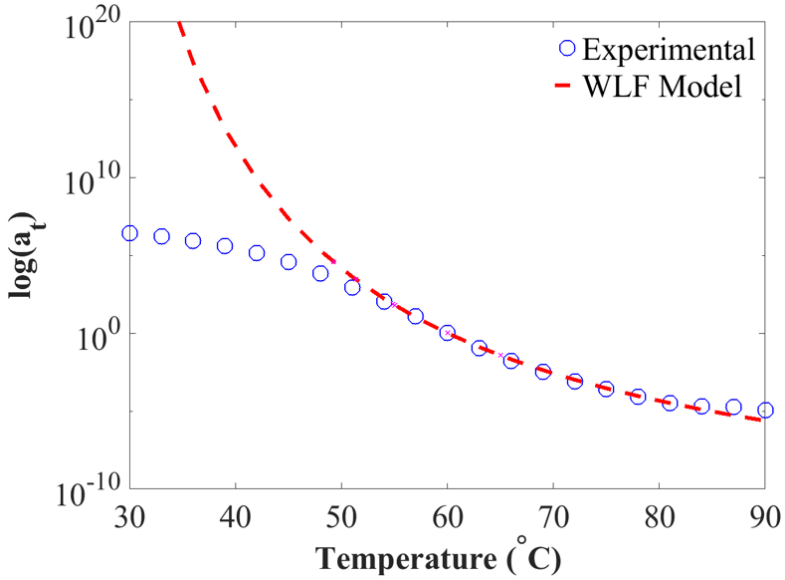

Figure 5.3. Shift factors of time-temperature superposition principle (TTSP). The discrete points show the experimental results, and the dashed line represents the WLF model.

5.2.4. Mechanical properties

The uniaxial tensile test was performed on 3D printed rectangular dog-bone specimens fabricated in horizontal direction using an Instron 5565 universal testing machine (Norwood, MA, USA) with a load cell of 5 kN, a gage length of 50 mm and thickness of 3.2 mm following the ASTM D638-14 Standard Test Method for Tensile Properties of Plastics, Type I standard [40]. The tensile test was carried out on five specimens at room temperature, and the average value is reported. The Young's modulus is evaluated in the linear region and found to be 1.496 GPa (Figure 5.4), and the Poisson's ratio is considered to be 0.33 as suggested in reference [41].

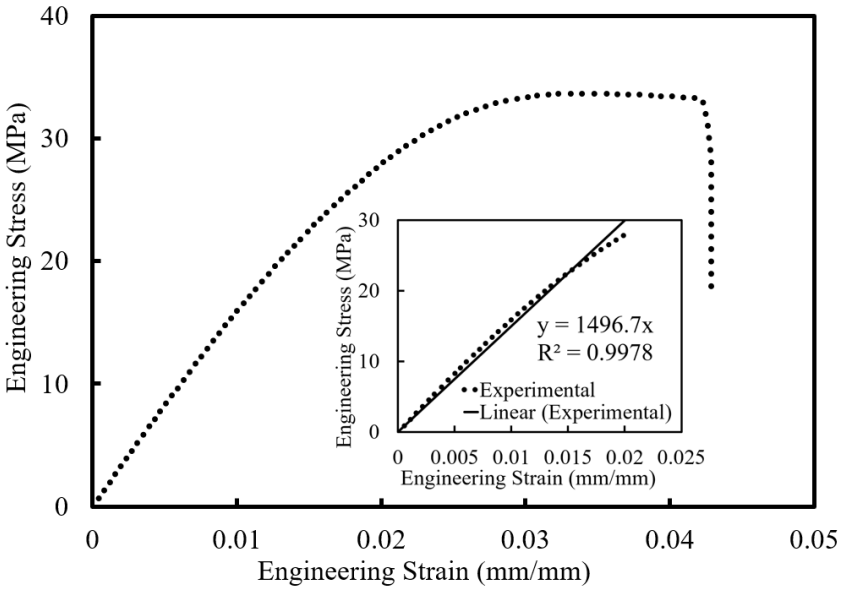

Figure 5.4. Average engineering stress-strain behavior for FDM 3D printed dog-bone specimens fabricated in horizontal direction.

5.2.5. Design and 3D model of plain weave fabric structures

Plain weave fabrics are formed by the interlacing (weaving) of two sets of orthogonal yarns. The yarns in the longitudinal direction (or machine direction) are known as warp yarns whereas the yarns in the transverse direction (or cross-machine direction) are known as weft or filling yarns [8][42][20].

In this study, a yarn of circular cross-section is considered. The diameter of each yarn is 1.70 mm, the spacing between yarns (warp and weft) is 8.0 mm and the thickness of fabric structure is 3.00 mm (Figure 5.5). Figure 5.5 d and e represent the 3D CAD model of the plain weave fabric. Computer aided design (CAD) software, Solidworks® was used to model the structures. It consists of 6 warp and 6 weft yarns constituting the overall dimensions of 48.00 mm × 48.00 mm × 3.00 mm.

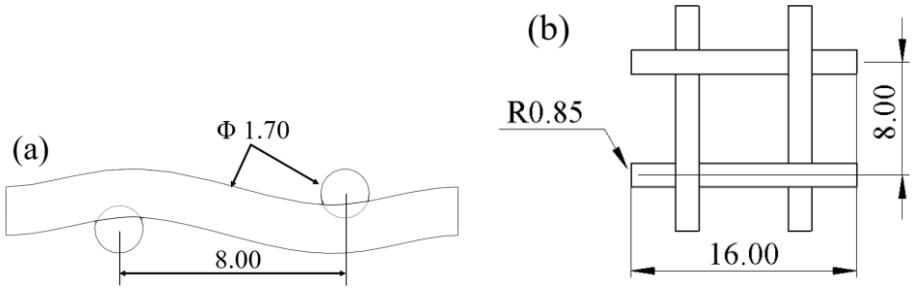

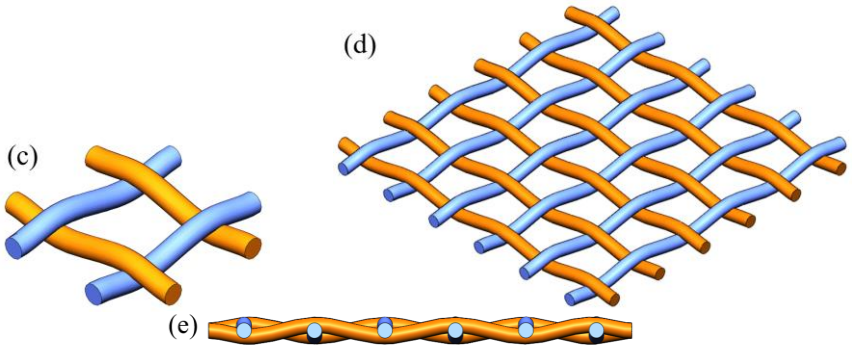

Figure 5.5. Design of plain weave fabric: (a) Schematic front view of the unit cell, (b) Schematic top view of the unit cell. 3D CAD model: (c) Isometric view of the unit cell, (d) Isometric view of the fabric with 6 warp yarns and 6 weft yarns, and (e) Front view of the fabric. The dimensions are in millimeters (mm).

5.2.6. Design of unit cell

The fabric structures consist of a finite number of building blocks, which are the repetitive elements of the same volume and material. This repeating block of identical weaving pattern is called representative volume element (RVE) or unit cell [43]. Unit cell is the smallest component of the fabric that exhibits the same material properties. Since the experimental and computational analysis of a large fabric structure is complicated and cumbersome, it is useful to model and analyze its unit cell of a plain weave fabric. For finite element modeling and to replicate the experimental set-up, the tabs are attached on both ends (Figure 5.6). These tabs are used to hold the testing specimen in the equipment.

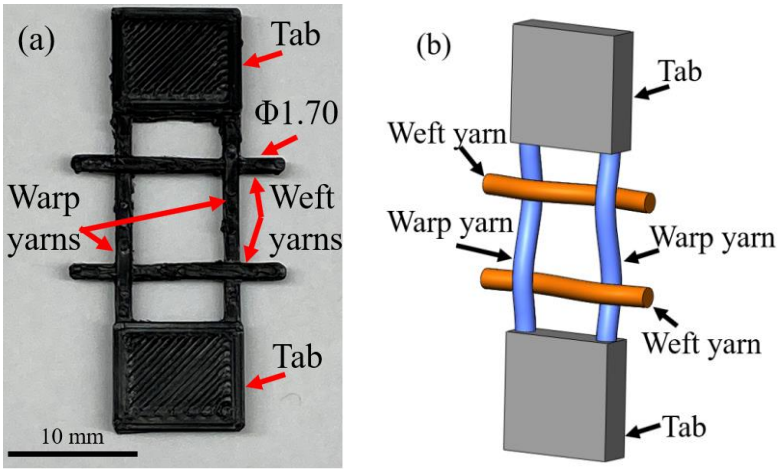

Figure 5.6. Unit cell of plain weave fabric structure. This cell incorporates tabs for loading into test fixture. (a) 3D printed unit cell, and (b) 3D CAD model of the unit cell used in the computational analysis.

5.2.7. Finite element model (FEM)

A multiphysics finite element framework is used in this study developed for large deformations of viscoelastic materials [33],[44],[45]. A uniaxial tensile and compression test was performed for 3D printed plain weave unit cell using the DMA equipment. In the test, the specimen was considered as a rectangular object having dimensions of 15 mm (length), 9.70 mm (width) and 3.00 mm (thickness). For the sake of holding the specimen and performing the test on the unit cell, tabs were connected on either end. Finite element modeling was performed to replicate the experimental setup that predicts the deformation of the specimen under the mechanical loading in an isothermal environment along with the incorporation of viscoelastic properties of the material. A fixed displacement was applied to one tab and a linear displacement boundary condition was applied to the other tab at a displacement rate of 0.01 mm/s. The boundary conditions applied on the specimen during the experiment and simulation are shown in Figure 5.7. The analysis was conducted at different temperatures at and above glass transition temperatures namely 60 ℃, 65 ℃, and 70 ℃. The main purpose of selecting this temperature range is to study the deformation behavior for potentially higher temperature applications. PLA is a relevant material for additive manufacturing, and it is anticipated that other polymeric fabrics operating near their T_g will behave in a similar manner.

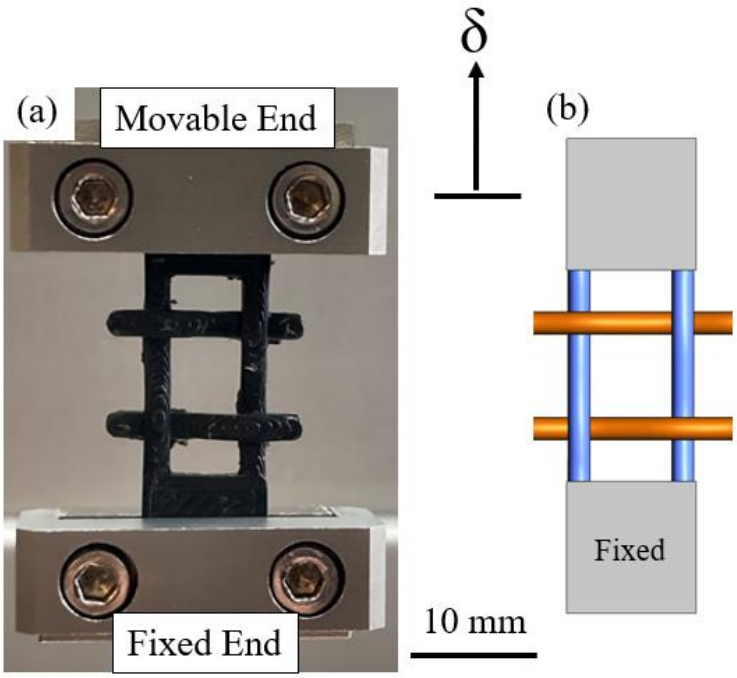

Figure 5.7. Boundary conditions applied to the unit cell: (a) Experimental setup, and (b) Model.

The unit cell was discretized by using C3D4T element type with linear geometric order in ABAQUS/CAE 2019. This element type is a 4-node thermally coupled tetrahedron, linear displacement and temperature. A mesh convergence test was performed to evaluate the optimum mesh density which can provide results with minimum error. Figure 5.8 demonstrates the mesh densities used for this study containing 2789, 3648, 9307 and 41261 elements. The corresponding force-displacement graph was obtained for the specimen at 60 ℃ as shown in Figure 5.9. Generally, fine mesh produces more accurate results but causes high computational cost and while coarse mesh produces sacrificed results with low computational cost. It is quite evident from Figure 5.9 that the force-displacement graph shows the convergence when the number of elements in the mesh is equal to or greater than 3648, i.e., Figure 8b, Model 2. The difference of 0.76% is found in the peak force for Model 2 as compared to Model 3. Therefore, in subsequent simulations, Model 2 having 3648 elements is used.

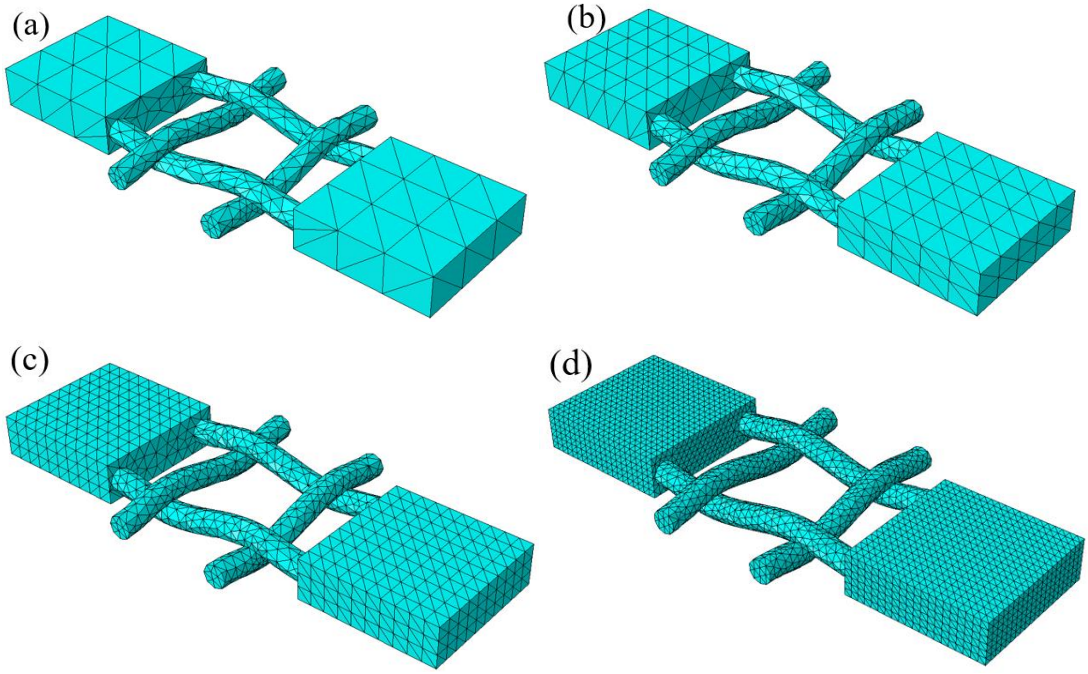

Figure 5.8. Different mesh densities are utilized to discretize the 3D printed plain weave fabric unit cell: (a) Model 1: 2789 elements, (b) Model 2: 3648 elements, (c) Model 3: 9307 elements, and (d) Model 4: 41261 elements.

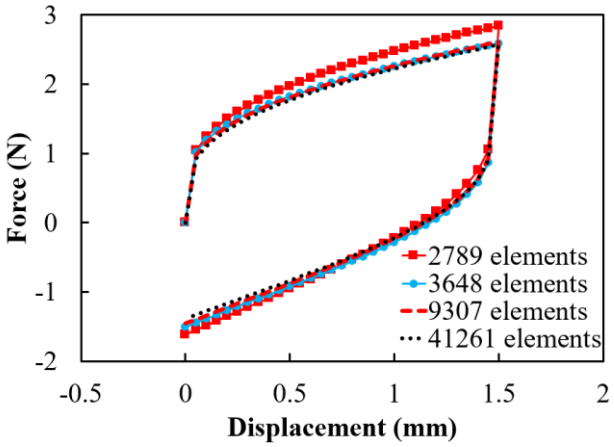

Figure 5.9. Mesh convergence test results for the sample at 60 ℃.

5.3. Results and discussion

5.3.1. Thermo-mechanical behavior of the unit cell

A tensile load followed by compression load is applied on the unit cell of plain weave fabric structure at varying temperatures. The contour plots showing the Von-Mises stress of unit cells under tensile and compression load at various temperatures are shown in Figure 5.10. The maximum stresses can be seen on the unit cells at 60 ℃ since this is the transition phase from glassy state to rubbery state of the polymer. The specimen at T_g holds higher stress than those at higher temperatures. As the polymer enters the rubbery state, it undergoes softening and hence leads to decrease in the load bearing capability. Further, these maximum stresses occur in the warp yarns, halfway between the weft yarns.

The results of force versus displacement for the unit cells at 60 ℃, 65 ℃, and 70 ℃ are shown in Figure 5.11. The experimental results are shown by the dotted line and computational results are shown by the solid line. A hysteresis loop is seen throughout the loading and unloading conditions due to the viscoelastic properties of the material. The computational results correlate well with the experimental results. The results are compared in terms of maximum tensile force at each temperature. Since the glass transition temperature of the polymer used is 60 ℃, the material is transitioning from glassy to rubbery state. With the phase transition of the polymer, the material becomes soft and hence the load bearing strength decreases. For the unit cell at 60 ℃, the maximum force obtained experimentally is about 3.40 N, which decreases to 1.13 N at 65 ℃, and to 0.97 N at 70 ℃. The decrease in the magnitude of tensile force is expected at higher temperatures for a viscoelastic material. It should be noted that the exact same material model is used in all computations, and the varying mechanical

response results from changes to the relaxation times, which are related to temperature via the WLF equation (Equation 4).

The peak forces and the error percentage between the experimental and computational results are presented in Figure 5.12. The peak forces obtained from the computational analysis are 2.60 N at 60 ℃, 1.23 N at 65 ℃, and 1.02 N at 70 ℃. Therefore, the relative error percentages at each temperature are 23.60% at 60 ℃, −8.85 % at 65 ℃, and –6.25 % at 70 ℃. The error percentage is higher at T_g, which was also observed in ref. [33]. However, the magnitude of difference is lower as the temperature increases, and this error level is considered to be satisfactory for a computational analysis. A better agreement in peak forces is seen for unit cells above T_g.

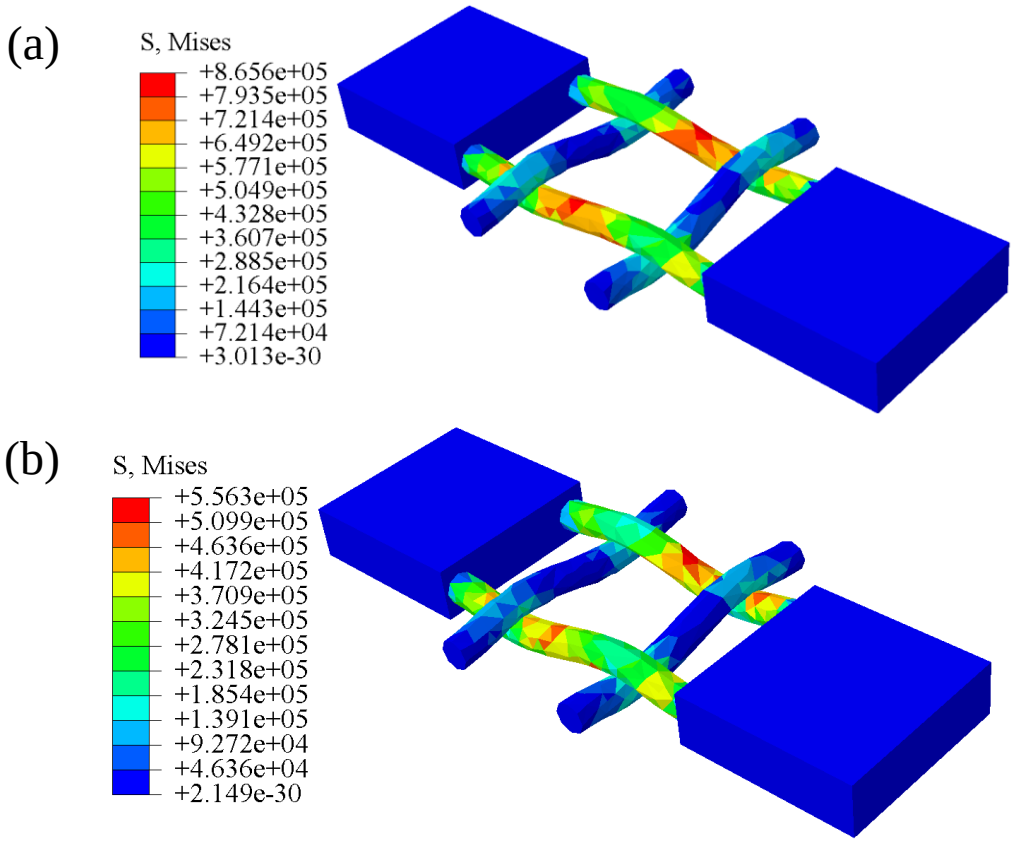

(c)

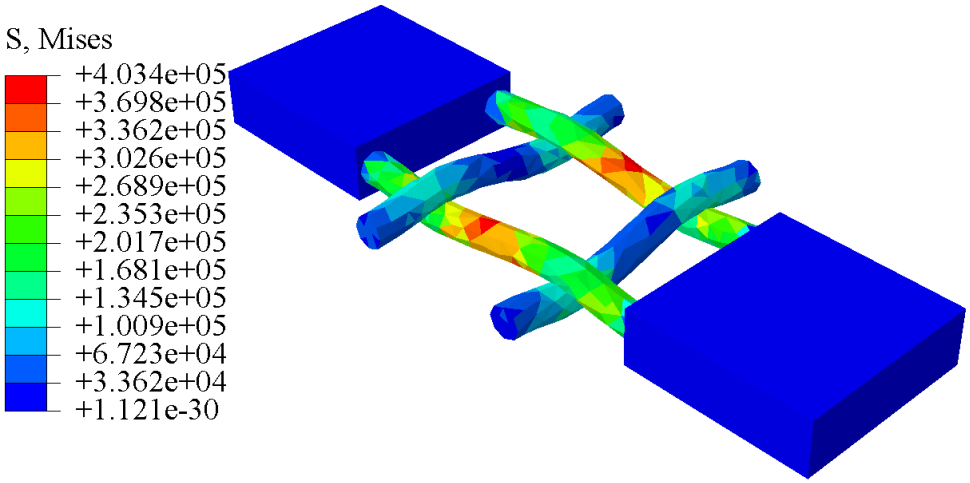
S, Mises
+4.034e+05
+3.698e+05
+3.362e+05
+3.026e+05
+2.689e+05
+2.353e+05
+2.017e+05
+1.681e+05
+1.345e+05
+1.009e+05
+6.723e+04
+3.362e+04
+1.121e-30

(d)

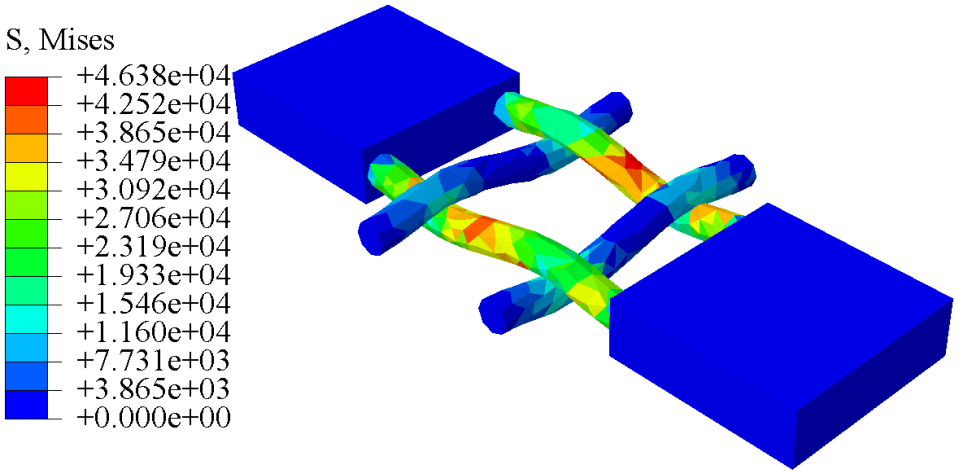
S, Mises
+4.638e+04
+4.252e+04
+3.865e+04
+3.479e+04
+3.092e+04
+2.706e+04
+2.319e+04
+1.933e+04
+1.546e+04
+1.160e+04
+7.731e+03
+3.865e+03
+0.000e+00

(e)

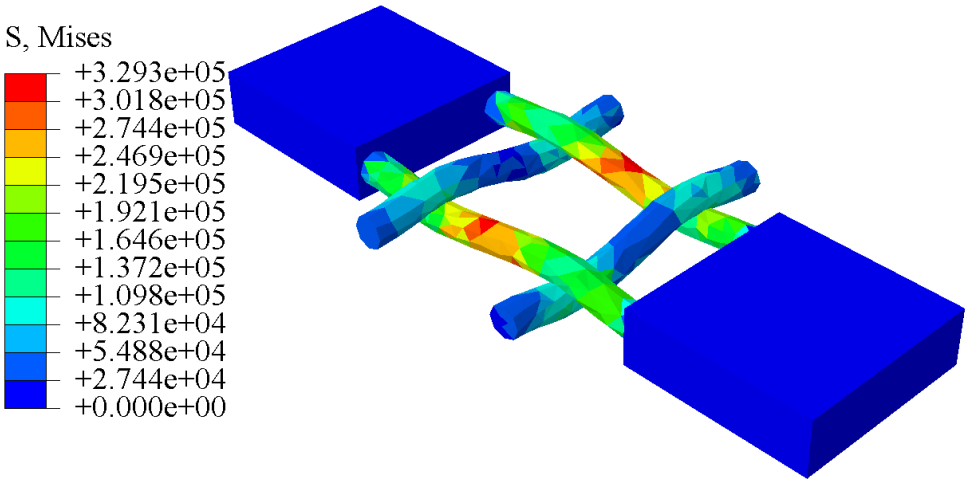
S, Mises
+3.293e+05
+3.018e+05
+2.744e+05
+2.469e+05
+2.195e+05
+1.921e+05
+1.646e+05
+1.372e+05
+1.098e+05
+8.231e+04
+5.488e+04
+2.744e+04
+0.000e+00

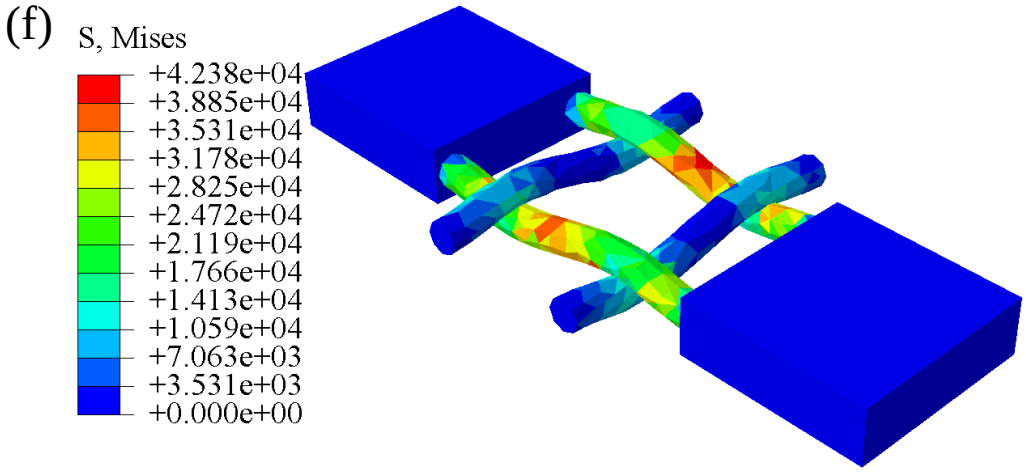

Figure 5.10. Computational stress contour results for unit cell at different temperatures (units in Pa). (a) Maximum tension at 60 ℃, (b) Maximum compression at 60 ℃, (c) Maximum tension at 65 ℃, (d) Maximum compression at 65 ℃, (e) Maximum tension at 70 ℃, and (f) Maximum compression at 70 ℃.

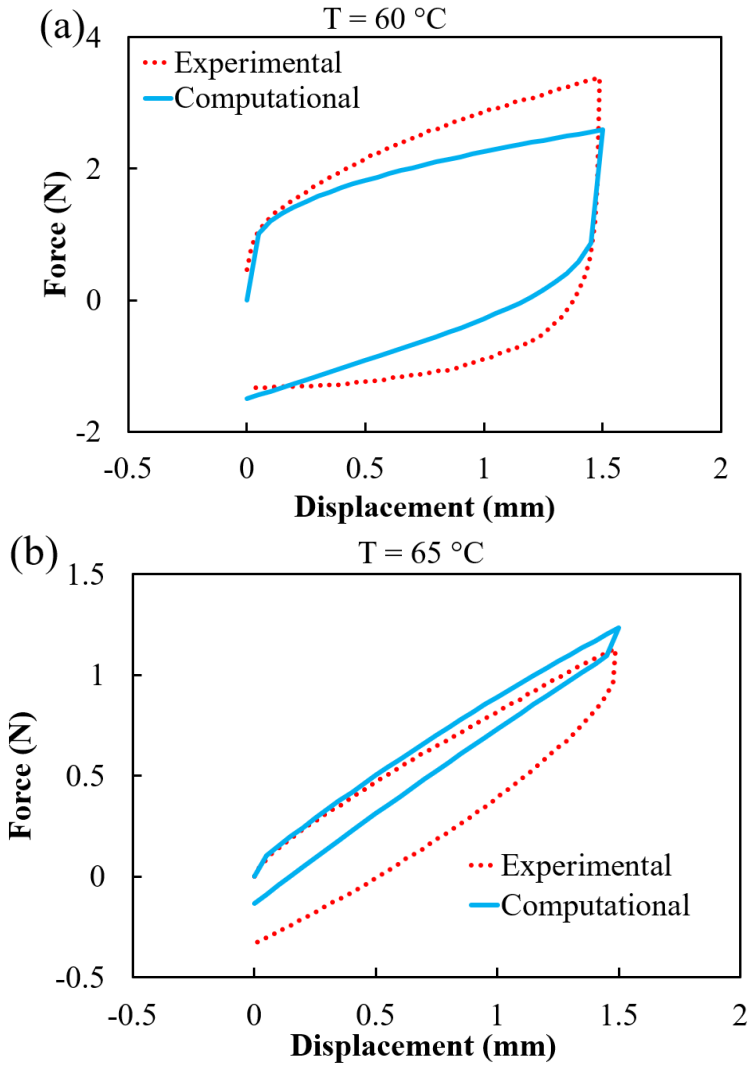

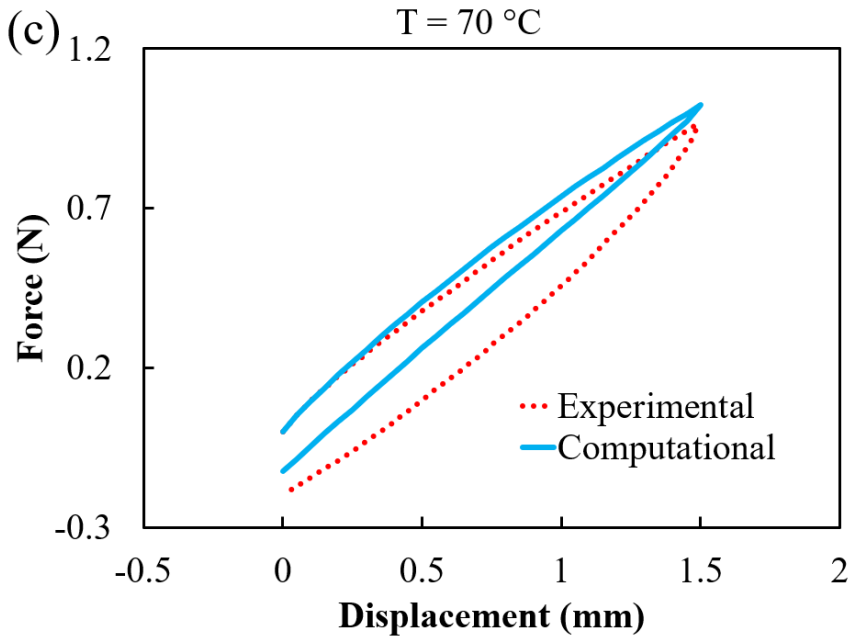

Figure 5.11. Force-displacement graphs of the unit cell of plain weave fabric structure showing the comparison of the experimental results and computational results at (a) 60 ℃, (b) 65 ℃, and (c) 70 ℃.

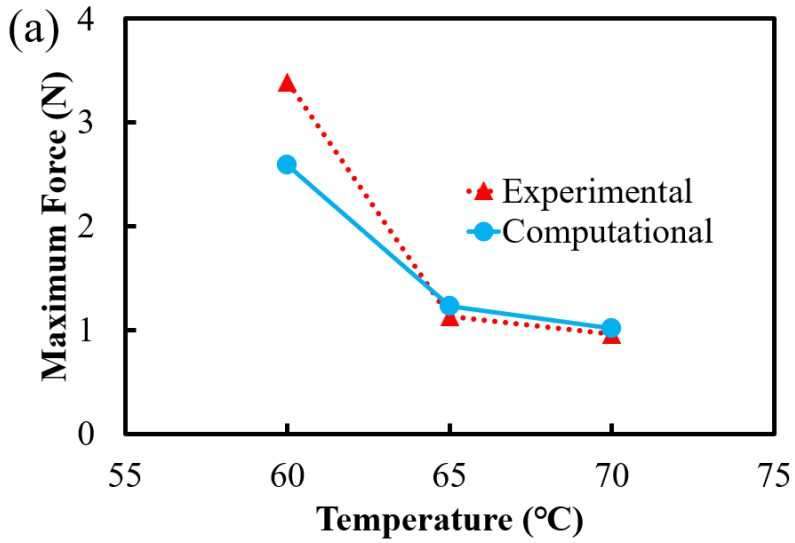

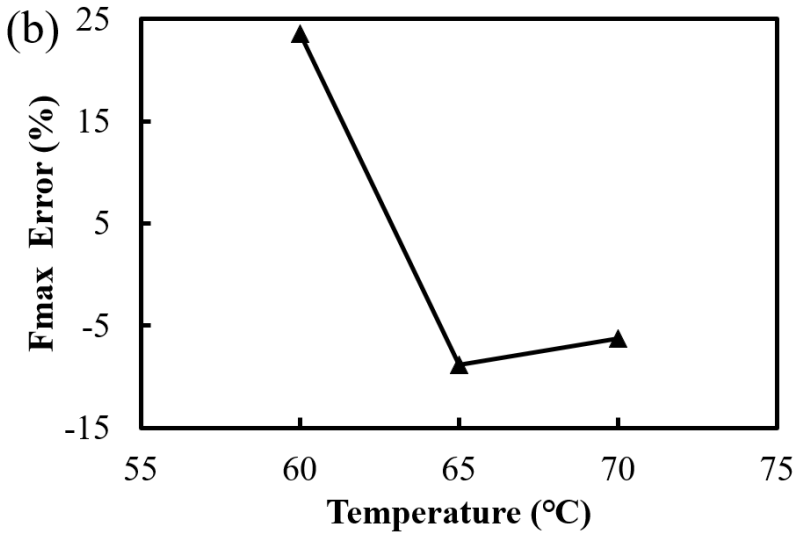

Figure 5.12. (a) Comparison of maximum forces obtained from the experimental results and computational analysis, and (b) Relative error in maximum forces obtained from the experiments and computational analysis.

5.3.2. Thermo-mechanical behavior of fabric structures

The computational model developed for the unit cell is employed to predict the thermo-mechanical behavior of a large fabric structure. The fabric structure considered has 6 warp yarns and 6 weft yarns with overall dimensions of 48.00 mm × 48.00 mm × 3.00 mm. One end of the fabric structure is fully constrained, and the other end is given a displacement of 4.8 mm to reach the maximum tension and then the compression loading is applied to reach the original point. The displacement on the fabric structure remained vertical throughout the tension and compression loading as shown in

Figure 5.13.

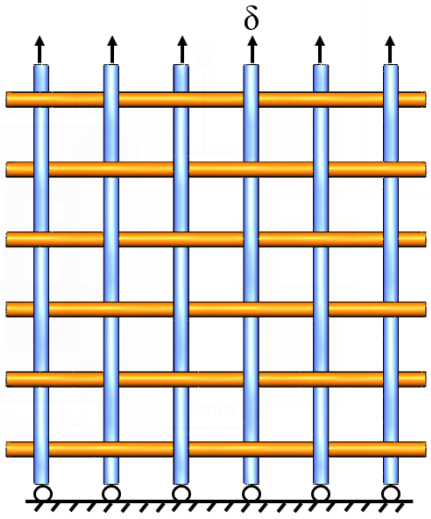

Figure 5.13. Boundary conditions on a fabric structure having 6 warp and 6 weft yarns.

This model is useful because it is difficult to evaluate the mechanical behavior of a large fabric structure experimentally due to the difficulties in loading the sample in the test fixtures. This model provides a platform to evaluate thermo-mechanical properties computationally and quickly iterate on design parameters, such as number of warp and weft yarns, weave type, yarn diameter, and yarn spacing. Figure 5.14 presents the computational results of the plain weave fabric structure at various temperatures. It shows the deformation at maximum tension (loaded) and maximum compression (unloaded) conditions at all the temperatures considered. Different color represents the magnitude of the Von Mises stresses (in Pa) at different locations on the yarns. The force versus displacement graphs for the fabric structure obtained computationally are shown in Figure 5.14 (g).

It is observed that the fabric at 60 ℃ exhibits maximum stiffness compared to the other temperatures, similar to the single unit cell. At the loaded condition, the maximum force predicted is 12.70 N. The curves of the yarns experience the maximum stress. At the unloaded condition, the force is −1.70 N. This shows that while unloading, the fabric does not follow the same path and formed a hysteresis loop, as expected for a viscoelastic polymer. The fabric structures are also loaded and unloaded in the rubbery phase, i.e., above T_g. That's why they experienced lower stiffness.

The computational model developed in this study can be used for fabrics having any number of yarns, and dimensions to study their mechanical performances at T_g and temperatures above it. For this purpose, the number of warp and weft yarns of the fabrics or the overall dimensions can be changed according to the requirement. To precisely predict the performance of the fabric, the dimensions of the unit cell should also be changed. The finite element model developed from the unit cell can then be used to study the behavior of the fabrics.

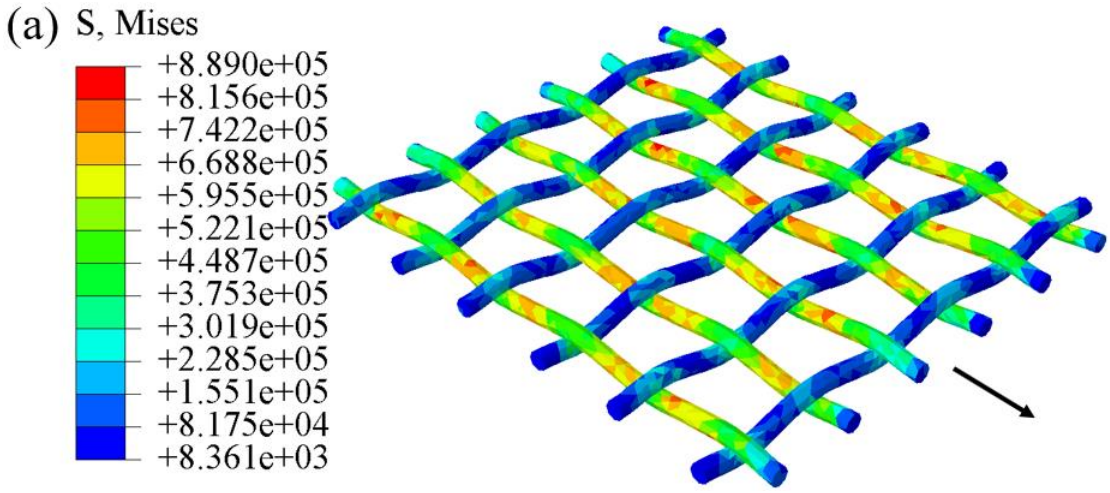
(a) S, Mises
+8.890e+05
+8.156e+05
+7.422e+05
+6.688e+05
+5.955e+05
+5.221e+05
+4.487e+05
+3.753e+05
+3.019e+05
+2.285e+05
+1.551e+05
+8.175e+04
+8.361e+03

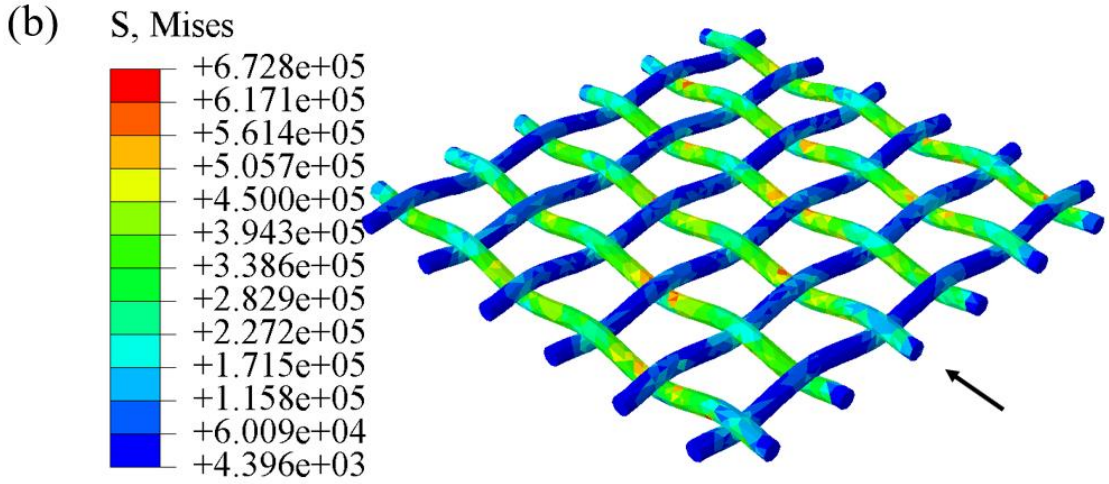
(b) S, Mises
+6.728e+05
+6.171e+05
+5.614e+05
+5.057e+05
+4.500e+05
+3.943e+05
+3.386e+05
+2.829e+05
+2.272e+05
+1.715e+05
+1.158e+05
+6.009e+04
+4.396e+03

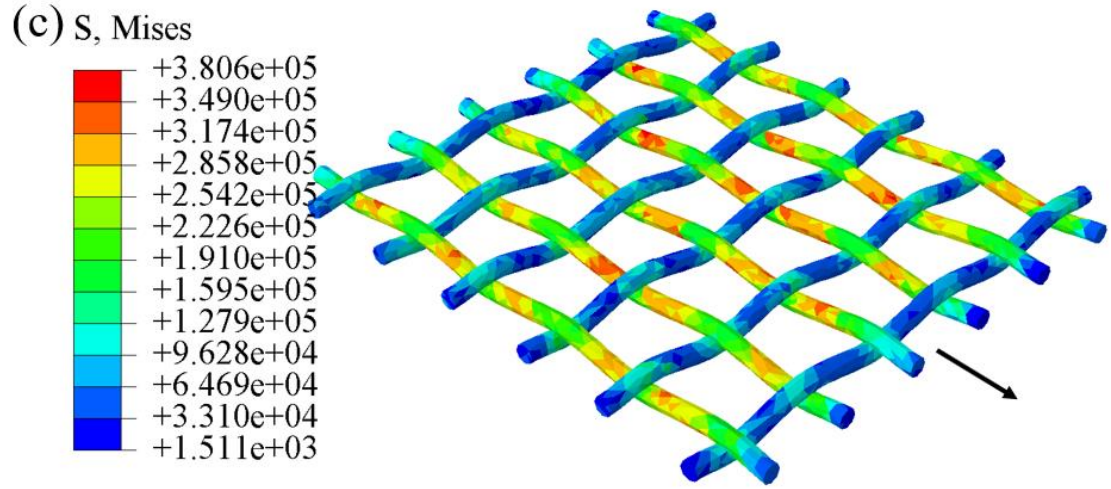
(c) S, Mises
+3.806e+05
+3.490e+05
+3.174e+05
+2.858e+05
+2.542e+05
+2.226e+05
+1.910e+05
+1.595e+05
+1.279e+05
+9.628e+04
+6.469e+04
+3.310e+04
+1.511e+03

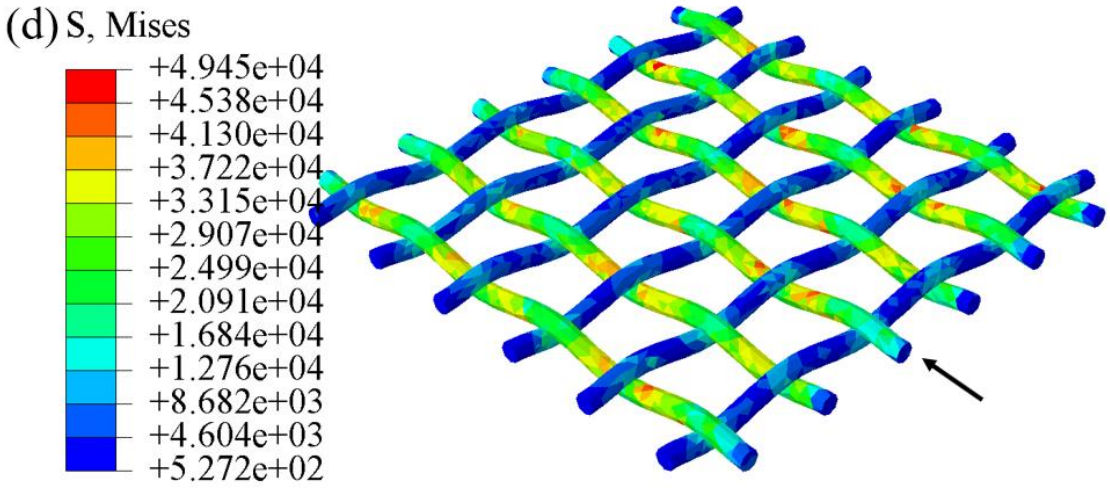
(d) S, Mises
+4.945e+04
+4.538e+04
+4.130e+04
+3.722e+04
+3.315e+04
+2.907e+04
+2.499e+04
+2.091e+04
+1.684e+04
+1.276e+04
+8.682e+03
+4.604e+03
+5.272e+02

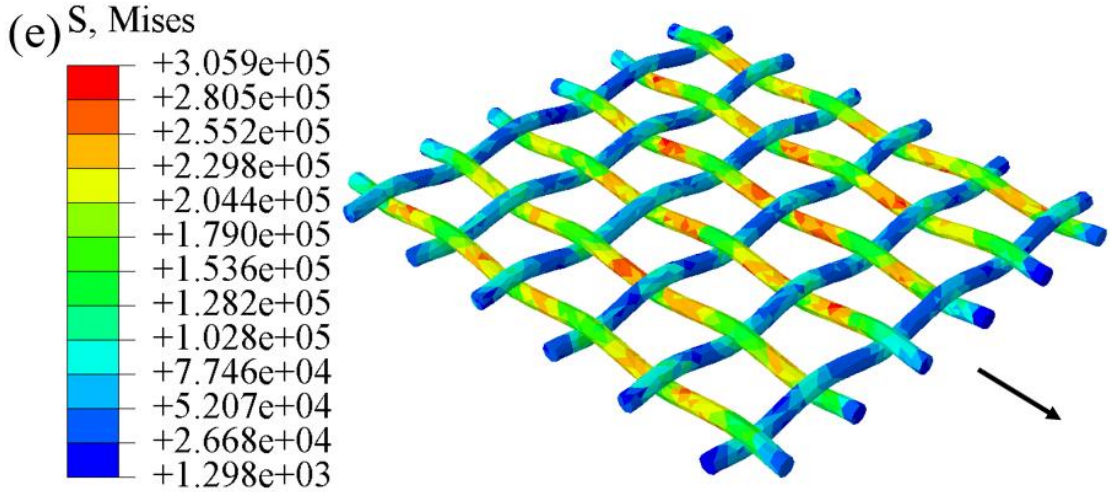
(e) S, Mises
+3.059e+05
+2.805e+05
+2.552e+05
+2.298e+05
+2.044e+05
+1.790e+05
+1.536e+05
+1.282e+05
+1.028e+05
+7.746e+04
+5.207e+04
+2.668e+04
+1.298e+03

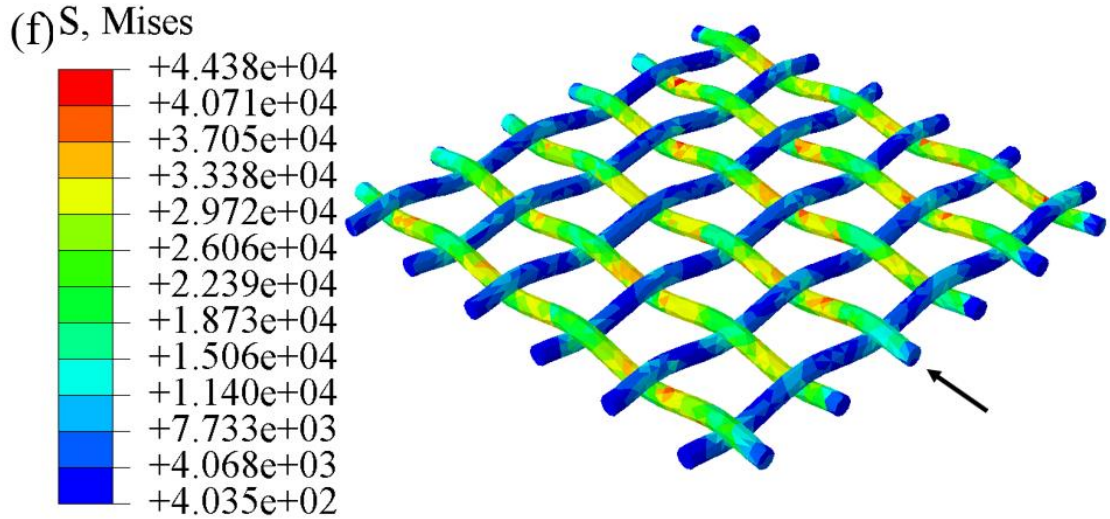
(f) S, Mises
+4.438e+04
+4.071e+04
+3.705e+04
+3.338e+04
+2.972e+04
+2.606e+04
+2.239e+04
+1.873e+04
+1.506e+04
+1.140e+04
+7.733e+03
+4.068e+03
+4.035e+02

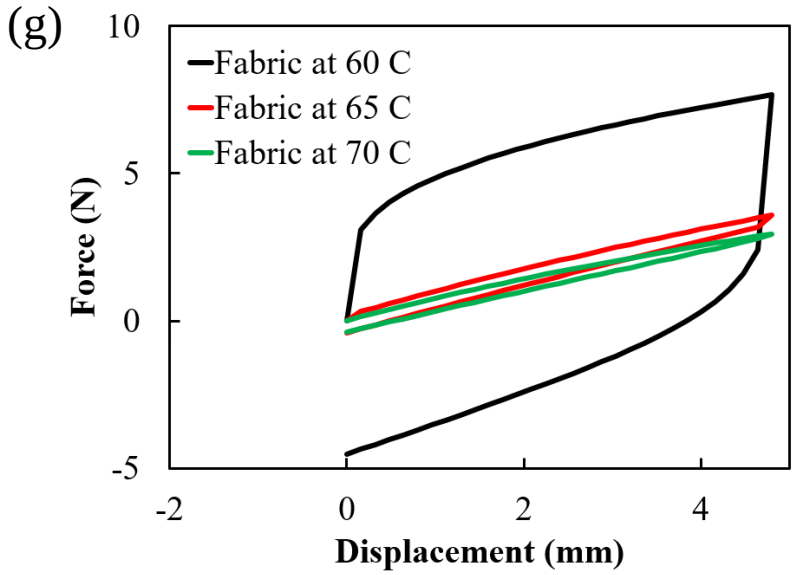

Figure 5.14. Simulation results of a plain weave fabric structure at different temperatures. (a) Maximum tension at 60 ℃, (b) Maximum compression at 60 ℃, (c) Maximum tension at 65 ℃, (d) Maximum compression at 65 ℃, (e) Maximum tension at 70 ℃, (f) Maximum compression at 70 ℃, and (g) Computational force-displacement results of a plain weave fabric structure having 6 warp yarns and 6 weft yarns at different temperatures.

5.4. Challenges and limitations

The multiphysics computational model developed is useful to study the thermo-mechanical behavior of a plain weave structure comprising viscoelastic materials. The computational results agree well with the experimental results. However, one needs to overcome the following challenges and limitations to resolve the discrepancies seen between them.

(a) Although polymer additive manufacturing method allows a rapid prototyping of complex structures, including non-planar weaves, depending on the CAD model, the parts produced do not have high mechanical strength. The voids between the deposited layers and beads can be seen [46]. They lack homogenization between the deposited layers and do not have continuum in the materials. As a result, the accurate measurements of mechanical properties becomes challenging [8]. However, many studies related to post-processing techniques such as thermal annealing to improve the mechanical strength and surface finish of FDM parts have been conducted [19] [47].

(b) The additive manufacturing of unit cells of fabric structures with smaller diameters, e.g., 1.70 mm, is challenging because of the weaving patterns [8]. Hence, the unit cells are simplified by keeping the yarns fused to each other and to keep the weft yarns in

place while loading in a tensile fixture. However, future work should focus on 3D printing of separate yarns, use of a friction model between them and use of multiple warp and weft yarns instead of two as used in this study to hold the weft yarns in place while loading.

5.5. Conclusions

A unit cell of plain weave fabric structure is additively manufactured using PLA as a base material. Fused deposition modeling (FDM) method is used to 3D print the samples. Tensile and compression loading is applied on the unit cell in a closed thermal chamber maintaining the temperatures of 60 ℃, 65 ℃, and 70 ℃ using DMA instrument. This temperature range is selected to study the behavior of polymers near T_g as the findings are transferable to other polymers operating similarly close to their T_g. PLA is a relevant material for additive manufacturing, and it is anticipated that other polymer fabrics operating near their T_g will behave in a similar manner. The force-displacement graphs are obtained experimentally. A multi-physics computational finite element model is developed incorporating the thermal, mechanical, and viscoelastic properties of the polymer. The force-displacement graphs are obtained computationally and are compared with the experimental results. The error percentages in the peak forces are 23.60% at 60 ℃, −8.85 % at 65 ℃, and –6.25 % at 70 ℃. A better agreement in peak forces is seen for unit cells above T_g. The computational model developed is applied to predict the behavior of a larger fabric structure having 6 warp yarns and 6 weft yarns. This model becomes useful since it is difficult to evaluate the behavior of larger fabric structures due to boundary conditions imposed by the test fixtures.

A limitation to this model is that the yarns are modeled to slightly touch each other. One of the reasons is that the unit cells are to be tested in tensile fixture. Hence, the yarns are made to touch each other, otherwise the weft yarns could not be held in place. The second reason is the 3D printing process itself, where the 3D printing of separate yarns in a unit cell is a challenging task. Future works should be done to 3D print separate yarns by considering bigger unit cells containing three or more warp and weft yarns, which could help to hold the weft yarns in place.

5.6. References

[1] S. Adanur, *Wellington Sears Handbook of Industrial Textiles*. Lancester, Pennsylvania: Technomic Publishing Co. Inc., 1995.

[2] S. Adanur, *Handbook of Weaving*, First Edit. Boca Raton: CRC Press, 2001.

[3] Y. Shen, D. Branscomb, and K. (Kelvin) Fu, "Core-shell hybrid pre-preg tow for lightweight composite truss," *Compos. Part B Eng.*, vol. 223, no. 109093, pp. 1–8, 2021, doi: 10.1016/j.compositesb.2021.109093.

[4] S. Adanur and A. Jayswal, "Filtration mechanisms and manufacturing methods of face masks: An overview," *J. Ind. Text.*, vol. 51, no. 3S, pp. 3683S-3717S, 2020, doi: 10.1177/1528083720980169.

[5] P. Bertola and J. Teunissen, "Fashion 4.0. Innovating fashion industry through digital transformation," *Res. J. Text. Appar.*, vol. 22, no. 4, pp. 352–369, 2018, doi: 10.1108/RJTA-03-2018-0023.

[6] B. Wang, X. Lai, H. Li, C. Jiang, J. Gao, and X. Zeng, "Multifunctional MXene/Chitosan-Coated Cotton Fabric for Intelligent Fire Protection," *ACS Appl. Mater. Interfaces*, vol. 13, no. 19, pp. 23020–23029, 2021, doi: 10.1021/acsami.1c05222.

[7] M. Senthilkumar and N. Anbumani, "Dynamics of elastic knitted fabrics for sports wear," *J. Ind. Text.*, vol. 41, no. 1, pp. 13–24, 2011, doi: 10.1177/1528083710387175.

[8] S. Adanur and A. Jayswal, "Additive manufacturing of interlaced fibrous structures," *Rapid Prototyp. J.*, vol. 27, no. 4, pp. 671–681, 2021, doi: 10.1108/RPJ-05-2020-0095.

[9] United States Environmental Protection Agency, "Facts and Figures about Materials, Waste and Recycling," 2022. https://www.epa.gov/facts-and-figures-about-materials-waste-and-recycling/national-overview-facts-and-figures-materials#Landfilling (accessed Sep. 03, 2022).

[10] NRDC, "Encourage Textile Manufacturers to Reduce Pollution." https://www.nrdc.org/issues/encourage-textile-manufacturers-reduce-pollution#:~:text=Textile mills generate one-fifth,by burning coal for energy (accessed Sep. 05, 2022).

[11] R. Melnikova, A. Ehrmann, and K. Finsterbusch, "3D printing of textile-based structures by Fused Deposition Modelling (FDM) with different polymer materials," *IOP Conf. Ser. Mater. Sci. Eng.*, vol. 62, no. 1, pp. 1–6, 2014, doi: 10.1088/1757-899X/62/1/012018.

[12] L. Partsch, S. Vassiliadis, and P. Papageorgas, “3D Printed Textile Fabrics Structures,” *5th Int. Istanbul Text. Congr. 2015 Innov. Technol. “Inspire to Innov.*, no. September, pp. 3–10, 2015.

[13] K. Lussenburg, N. Van Der Velden, Z. Doubrovski, J. Geraedts, and E. Karana, “Designing with 3D Printed Textiles,” *Proc. 5th Int. Conf. Addit. Technol.*, pp. 74–81, 2003.

[14] T. Spahiu, E. Canaj, and E. Shehi, “3D printing for clothing production,” *J. Eng. Fiber. Fabr.*, vol. 15, pp. 1–8, 2020, doi: 10.1177/1558925020948216.

[15] S. Kim, H. Seong, Y. Her, and J. Chun, “A study of the development and improvement of fashion products using a FDM type 3D printer,” *Fash. Text.*, vol. 6, no. 9, pp. 1–24, 2019, doi: 10.1186/s40691-018-0162-0.

[16] R. Uysal and J. B. Stubbs, “A new method of printing multi-material textiles by fused deposition modelling (FDM),” *Tekstilec*, vol. 62, no. 4, pp. 248–257, 2019, doi: 10.14502/Tekstilec2019.62.248-257.

[17] M. Beecroft, “Digital interlooping: 3D printing of weft-knitted textile-based tubular structures using selective laser sintering of nylon powder,” *Int. J. Fash. Des. Technol. Educ.*, vol. 12, no. 2, pp. 218–224, 2019, doi: 10.1080/17543266.2019.1573269.

[18] Nervous System, “Kinematics Bodice,” 2014. https://n-e-r-v-o-u-s.com/projects/tags/3dprint/albums/kinematics-clothing/ (accessed Nov. 03, 2021).

[19] A. Jayswal and S. Adanur, “Effect of heat treatment on crystallinity and mechanical properties of flexible structures 3D printed with fused deposition modeling,” *J. Ind. Text.*, vol. 51, no. 2S, pp. 2616S-2641S, 2021, doi: 10.1177/15280837211064937.

[20] A. Jayswal and S. Adanur, “An overview of additive manufacturing methods, materials, and applications for flexible structures,” *J. Ind. Text.*, vol. 52, pp. 1–42, 2022, doi: 10.1177/15280837221114638.

[21] S. Adanur, A. Jayswal, K. O. Griffin, and J. L. Hancock, “Additive Manufacturing of Weft Knitted and Braided Fabric Structures with Fused Deposition Modeling,” *J. Text. Inst.*, 2022.

[22] A. Vigliotti and D. Pasini, “Linear multiscale analysis and finite element validation of stretching and bending dominated lattice materials,” *Mech. Mater.*, vol. 46, pp. 57–68,

2012, doi: 10.1016/j.mechmat.2011.11.009.

[23] X. C. Zhang, H. M. Ding, L. Q. An, and X. L. Wang, “Numerical investigation on dynamic crushing behavior of auxetic honeycombs with various cell-wall angles,” *Adv. Mech. Eng.*, vol. 7, no. 2, 2015, doi: 10.1155/2014/679678.

[24] J. Zhang, G. Lu, Z. Wang, D. Ruan, A. Alomarah, and Y. Durandet, “Large deformation of an auxetic structure in tension: Experiments and finite element analysis,” *Compos. Struct.*, vol. 184, no. May 2017, pp. 92–101, 2018, doi: 10.1016/j.compstruct.2017.09.076.

[25] A. Dixit, H. S. Mali, and R. K. Misra, “Unit cell model of woven fabric textile composite for multiscale analysis,” *Procedia Eng.*, vol. 68, pp. 352–358, 2013, doi: 10.1016/j.proeng.2013.12.191.

[26] H. Lin, M. Sherburn, J. Crookston, A. C. Long, M. J. Clifford, and I. A. Jones, “Finite element modelling of fabric compression,” *Model. Simul. Mater. Sci. Eng.*, vol. 16, no. 3, 2008, doi: 10.1088/0965-0393/16/3/035010.

[27] L. Daelemans *et al.*, “Finite element simulation of the woven geometry and mechanical behaviour of a 3D woven dry fabric under tensile and shear loading using the digital element method,” *Compos. Sci. Technol.*, vol. 137, pp. 177–187, 2016, doi: 10.1016/j.compscitech.2016.11.003.

[28] G. Hivet, A. Wendling, B. Laine, and P. Boisse, “Modeling Strategies for Fabrics Unit Cell Geometry- Application To Permeability Simulations . Fabrics Modelling,” *Int J Mater Form*, vol. 3, pp. 727–730, 2010, doi: 10.1007/s12289-010-087.

[29] F. Desplentere, S. V. Lomov, D. L. Woerdeman, I. Verpoest, M. Wevers, and A. Bogdanovich, “Micro-CT characterization of variability in 3D textile architecture,” *Compos. Sci. Technol.*, vol. 65, no. 13, pp. 1920–1930, 2005, doi: 10.1016/j.compscitech.2005.04.008.

[30] J. Pazmino, S. Mathieu, V. Carvelli, P. Boisse, and S. V. Lomov, “Numerical modelling of forming of a non-crimp 3D orthogonal weave E-glass composite reinforcement,” *Compos. Part A Appl. Sci. Manuf.*, vol. 72, pp. 207–218, 2015, doi: 10.1016/j.compositesa.2015.02.013.

[31] B. Nadler, P. Papadopoulos, and D. J. Steigmann, “Multiscale constitutive modeling and

numerical simulation of fabric material," *Int. J. Solids Struct.*, vol. 43, no. 2, pp. 206–221, 2006, doi: 10.1016/j.ijsolstr.2005.05.020.

[32] Z. Zheng, N. Zhang, and X. Zhao, "Simulation of Heat Transfer through Woven Fabrics Based on the fabric geometry model," *Therm. Sci.*, vol. 22, no. 6B, pp. 2815–2825, 2018.

[33] T. R. Giri and R. W. Mailen, "Thermomechanical behavior of polymeric periodic structures," *Addit. Manuf.*, vol. 49, no. November 2021, p. 102512, 2022, doi: 10.1016/j.addma.2021.102512.

[34] R. C. Nonato *et al.*, "Nanocomposites of PLA/ZnO nanofibers for medical applications: Antimicrobial effect, thermal, and mechanical behavior under cyclic stress," *Polym. Eng. Sci.*, vol. 62, no. 4, pp. 1147–1155, 2022, doi: 10.1002/pen.25913.

[35] J. Domínguez-Robles *et al.*, "Antioxidant PLA composites containing lignin for 3D printing applications: A potential material for healthcare applications," *Pharmaceutics*, vol. 11, no. 165, pp. 1–14, 2019, doi: 10.3390/pharmaceutics11040165.

[36] M. A. Cuiffo, J. Snyder, A. M. Elliott, N. Romero, S. Kannan, and G. P. Halada, "Impact of the Fused Deposition (FDM) Printing Process on Polylactic Acid (PLA) Chemistry and Structure," *Appl. Sci.*, vol. 7, no. 6, p. 579, Jun. 2017, doi: 10.3390/app7060579.

[37] I. Chiulan, A. N. Frone, C. Brandabur, and D. M. Panaitescu, "Recent advances in 3D printing of aliphatic polyesters," *Bioengineering*, vol. 5, no. 2, pp. 2–18, 2018, doi: 10.3390/bioengineering5010002.

[38] N. Alizadeh, A.-D. N. Celestine, M. L. Auad, and V. Agrawal, "Mechanical characterization and modeling stress relaxation behavior of acrylic–polyurethane-based graft-interpenetrating polymer networks," *Polym. Eng. Sci. Sci.*, vol. 61, no. 5, pp. 1299–1309, 2021, doi: 10.1002/pen.25640.

[39] M. L. Williams, R. F. Landel, and J. D. Ferry, "The Temperature Dependence of Relaxation Mechanisms in Amorphous Polymers and Other Glass-forming Liquids," *Journal of the American Chemical Society*, vol. 77, no. 14. pp. 3701–3707, 1955, doi: 10.1021/ja01619a008.

[40] ASTM D638-14, "Standard Test Method for Tensile Properties of Plastics," *ASTM Int. West Conshohocken, PA*, no. December, 2014, doi: 10.1520/D0638-14.

[41] R. T. L. Ferreira, I. C. Amatte, T. A. Dutra, and D. Bürger, "Experimental

characterization and micrography of 3D printed PLA and PLA reinforced with short carbon fibers," *Compos. Part B Eng.*, 2017, doi: 10.1016/j.compositesb.2017.05.013.

[42] A. Jayswal and S. Adanur, "Characterization of polylactic acid/thermoplastic polyurethane composite filaments manufactured for additive manufacturing with fused deposition modeling," *J. Thermoplast. Compos. Mater.*, pp. 1–22, 2021, doi: 10.1177/08927057211062561.

[43] P. Sharma, P. Priyanka, H. S. Mali, and A. Dixit, "Geometric modeling and finite element analysis of kevlar monolithic and carbon-kevlar hybrid woven fabric unit cell," *Mater. Today Proc.*, vol. 26, pp. 766–774, 2019, doi: 10.1016/j.matpr.2020.01.023.

[44] R. W. Mailen, Y. Liu, M. D. Dickey, M. Zikry, and J. Genzer, "Modelling of shape memory polymer sheets that self-fold in response to localized heating," *Soft Matter*, vol. 11, no. 39, pp. 7827–7834, 2015, doi: 10.1039/c5sm01681a.

[45] R. W. Mailen, M. D. Dickey, J. Genzer, and M. A. Zikry, "A fully coupled thermo-viscoelastic finite element model for self-folding shape memory polymer sheets," *J. Polym. Sci. Part B Polym. Phys.*, vol. 55, no. 16, pp. 1207–1219, 2017, doi: 10.1002/polb.24372.

[46] C. Gupta, M. B. Pallavi, N. K. Shet, A. K. Ghosh, S. Bandyopadhyay, and P. Mukhopadhyay, "Microstructure and mechanical performance examination of 3D printed acrylonitrile butadiene styrene thermoplastic parts," *Polym. Eng. Sci.*, vol. 60, no. 11, pp. 2770–2781, 2020, doi: 10.1002/pen.25507.

[47] R. V. Pazhamannil, V. N. Jishnu Namboodiri, P. Govindan, and A. Edacherian, "Property enhancement approaches of fused filament fabrication technology: A review," *Polym. Eng. Sci.*, vol. 62, no. 5, pp. 1356–1376, 2022, doi: 10.1002/pen.25948.

Chapter 6

Manufacturing of PLA/TPU composite filaments for 3D printing

(Jayswal, A., and Adanur, S., *"Characterization of polylactic acid/thermoplastic polyurethane composite filaments manufactured for additive manufacturing with fused deposition modeling",* Journal of Thermoplastic Composite Materials, pp. 1-22, 2021)

Abstract

Polylactic acid (PLA) and thermoplastic polyurethane (TPU) were mixed in different proportions and extruded through twin-screw and single-screw extruders to obtain composite filaments to be used for 3D printing with fused deposition modeling (FDM) method. The properties of the filaments were characterized using uniaxial tensile tests, differential scanning calorimetry (DSC), thermogravimetric analysis (TGA), Fourier transform infrared spectroscopy (FTIR), rheology, polarized optical microscope (POM), and scanning electron microscope (SEM). 3D printed samples from composite filaments were tested using dynamic mechanical analysis (DMA). It was found that the tensile strength and modulus of the filaments decrease while elongation at break increases with the increasing TPU content in the composite. The analysis also showed a partial miscibility of the polymer constituents in the solution of composite filaments. Finally, a flexible structure, plain weave fabric, was designed and 3D printed using the composite filaments developed which proved that the filaments are well suited for 3D printing.

6.1. Introduction

Additive manufacturing (or 3D printing) is a revolutionary technology which has the capability of building complex geometrical parts/objects following a CAD design. Fused deposition modeling (FDM) is one of the most widely used 3D printing methods for polymers, in which the melted polymer is extruded through a nozzle and deposited on a platform layer by layer to form the product. It allows the fabrication of durable components made of high-strength thermoplastics such as polylactic acid (PLA), acrylonitrile butadiene styrene (ABS), thermoplastic polyurethane (TPU), poly(ether ether ketone) (PEEK), polycarbonate (PC), polyphenylsulfonate [1]. With FDM, various products can be manufactured within a limited time frame with minimal waste. This technology has been used in many industries including aerospace, automotive, composites, fabrics, and fashion.

Polylactic acid (PLA) is one of the most commonly used polymers in 3D printing because of its easy availability, low cost and non-toxicity. It is biodegradable, renewable, recyclable and compostable thermoplastic polymer derived from corn, wheat, rice [2]. It has high strength and high modulus which is an important property for 3D printed products [3]. The glass transition and melting temperatures are in the range of 45 – 60 ℃ and 150 – 165 ℃, respectively [3]. It can be used to make dimensionally accurate parts. However, PLA is very brittle with less than 10% elongation at break [4]. Hence, the blending of PLA with other polymers has been attempted by several researchers to achieve better toughness and elongation. Soft PLA (PLA + softener) has elongation at break up to 200 % [5]. Some researchers blended PLA and low density poly(ethylene) to improve toughness [6][7].

Thermoplastic Polyurethane (TPU) is a biocompatible and biodegradable polymer [8], [9], which can be used in several applications such as textile, footwear industry, tubings, biomaterials, and adhesives. Its properties vary from being a high performance elastomer to tough thermoplastic polymer [10], [11]. It is used for high tensile strength, abrasion resistance, tear resistance, low temperature flexibility and high versatility in chemical structures [12]. It is a linear segmented block copolymer and is made of hard segments (HS) (made from diisocyanate, e.g. diphenylmethane-4.4-diisocyanate (MDI), by addition of a chain extender, e.g. butanediol) and soft segments (SS) (e.g. polyester, polyether). The soft segment interconnects two hard segments and the hard segments are bonded together with the presence of hydrogen bonds and form physical crosslinks [12], [13]. It gets its rigidity and hardness from HS domains whereas the flexibility and elastomeric behavior is gained from SS domains [14]. TPU has been used for various material property profiles, which can be achieved by reinforcing the polymer with fillers. Nanoparticles (e.g., nanoclay, silica) [15], [16] and fibers (e.g. aramid, carbon, glass) [17], [18], [19] have been used as a reinforcement material to improve the mechanical properties of TPU.

Although FDM 3D printing offers several advantages, the parts produced do not have high mechanical strength in comparison to traditional manufacturing methods such as injection molding, due to the presence of voids and weaker bonding between layers [2]. Hence, several theories have been proposed to increase the strength which include parameter optimization [20], addition of filler materials in polymers to make a composite filament as a pre-processing method [21] and heat treatment (HT) as post-processing method [22]. The addition of filler

materials in the polymer matrix helps to improve the toughness, compatibility, thermal and mechanical properties depending on the filler content.

Zhou et. al. [23] investigated the effect of addition of thermoplastic polyurethane (TPU) in the blend of PC/PLA and found significant improvement in toughness of the composite material, increase in elongation at break, first increase and then decrease in impact strength, significant decrease in tensile strength and plastic fracture behavior of the composite. Jaso et. al. [24] added varying weight percentages (wt%) of poly(lactic) acid (PLA) in TPU matrix and found that the composite fibers had improved tensile strength and high elongation but decreased in elastic recovery. Mi et. al. [8] fabricated scaffolds using the blends of PLA/TPU and achieved large tensile and compressive strength, improvement in elongation-at-break and relatively larger pores with the increasing TPU content in the blends, which may be suitable for various medical and tissue engineering applications. Feng and Ye [25] fabricated the PLA/TPU blended tensile and impact specimens by using hot-press-molding process and observed yield and neck formation for the blends, which indicated the transition of brittle fracture of PLA to ductile fracture. They found partial miscibility of the polymers due to the formation of hydrogen bonding between the molecules as shown in Figure 6.1 Xu et. al. [26] studied the effects of TPU on the crystallization and melt strength of PLA. They found out that the crystallinity and melt strength increased and they confirmed the immiscibility of these polymers. Kaynak et. al. [27] studied the mechanical performance of neat PLA, glass fiber (GF)-reinforced PLA, and TPU-blended PLA composites using injection molding and 3D printing methods. They used twin-screw extruders and obtained the filaments for 3D printing using 10 wt% of TPU and 15 wt% of GF. Using the filaments obtained, they 3D printed dog-bone specimens and compared their performance with the dog-bone samples obtained from injection molding.

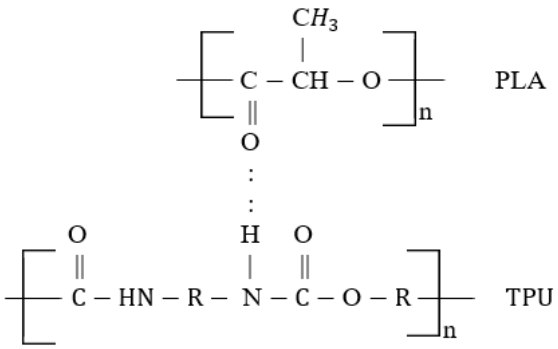

Figure 6.1. Hydrogen bonding between PLA and TPU molecules [25].

It should be noted that no information related to manufacturing of PLA/TPU composite filaments mixed in different proportions has been found in the literature. The mechanical, thermal, and rheological characterization of these filaments are missing in the literature as well. In the present work, PLA is blended with TPU in varying weights to obtain composite filaments with optimal strength and flexibility which can be used for 3D printing of flexible structures. The mechanical and thermal properties of the composite filaments are characterized, which showed that the filament experiences lower tensile strength but higher elongation at break with the increasing content of TPU.

6.2. Materials and methods

PLA pellets of commercial grade, Natureworks Ingeo 4043D were purchased from 3DX Tech (Grand Rapids, MI, USA) having a number average molecular weight (M_n) of 67 kDa, polymer dispersity index (PDI) of 2.2 [28], density of 1.24 g/cm^3, and the glass transition temperature (T_g) of 55 – 60 ℃. Thermoplastic polyurethane elastomer (Pellethane 2363-90AE TPU) pellets were supplied by LNS Technologies (Scotts Valley, CA, USA) with the properties such as density of 1.14 g/cm^3, T_g of – 33 ℃, melt flow index of 32 g/10 min (224 ℃, 1.2 kg load), shore hardness of 90 A and ultimate elongation of 550%.

The raw PLA and TPU pellets were dried in oven at 60 ℃ for 12 hours and then mixed manually in a required proportion as shown in Table 6.1 along with the sample code. The mixture of the pellets was fed into twin-screw extruder (Leistritz Mic 18/GL 40D, Nuremberg, Germany) and a composite filament was obtained. The twin-screw extruder has seven different temperature zones, namely 1 to 7, and the temperatures were fixed in the respective order: 155 ℃, 165 ℃, 165 ℃, 175 ℃, 180 ℃, 180 ℃, 170 ℃. The screw speed was set at 35 rpm. The filaments produced were again pelletized and kept in oven at 60 ℃ for 12 hours before processing in single-screw extruder (Automatik, Machinery Corporation, Charlotte, NC, USA). As a result, final filaments were obtained as shown in Figure 6.2. The single screw extruder had two temperature zones which were set in the range of 145 – 160 ℃ and 155 – 170 ℃ for zone 1 and 2, respectively, depending on the composition. The screw speed of the single-screw extruder was set in the range of 7 – 12 rpm depending on the amount of TPU. The composite filaments manufactured had diameters in the range of 1.2 mm to 2.3 mm; however, the filaments having diameters in the range of 1.56 mm to 1.86 mm were used for the analyses.

This range is a comparable to the ranges reported in the literature [29] which is 1.6 mm to 1.9 mm.

Table 6.1. Samples prepared for filament manufacturing.

Sample code	PLA (wt %)	TPU (wt %)
PLA	100	0
TPU_10	90	10
TPU_20	80	20
TPU_30	70	30
TPU_40	60	40
TPU	0	100

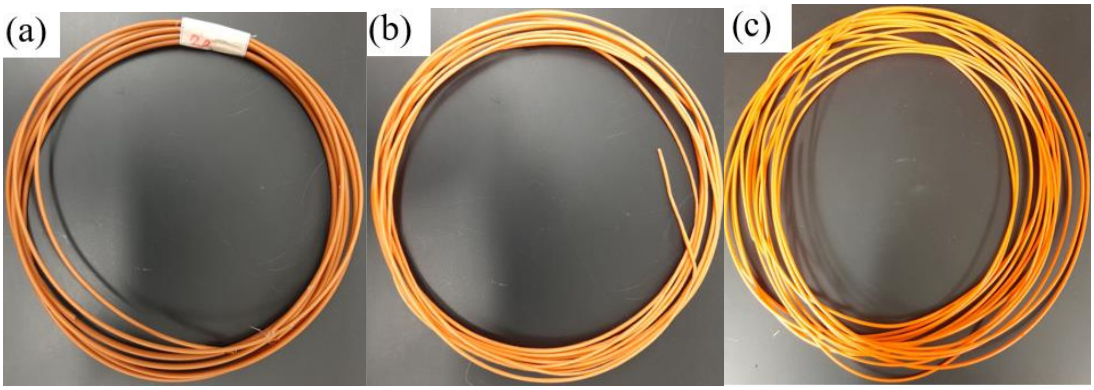

Figure 6.2. Examples of composite filaments manufactured. (a) TPU_20, (b) TPU_30, and (d) TPU_40.

The composite filaments of diameter in the range of 1.55 mm – 2.0 mm were selected for tensile testing using Instron 5565 (Norwood, MA, USA) with a load cell of 1 kN. The gage length was fixed at 50 mm and the crosshead movement was set at 25 mm/min. Ten specimens were tested for each composition and the average value was reported. The average diameters for PLA, TPU_10, TPU_20, TPU_30, and TPU_40 samples are 1.56 mm, 1.79 mm, 1.86 mm, 1.64 mm, and 1.74 mm, respectively.

Differential scanning calorimetry (DSC) was performed using a Q 2000 (TA instruments, New Castle, DE, USA), operated under a nitrogen atmosphere at the flow rate of 50 mL/min. The samples, weighing from 5 to 8 mg, were first heated from -80 ℃ to 250 ℃ and then were cooled from 250 ℃ to -80 ℃ and again heated to 250 ℃ at a heating and cooling rates of 10 ℃/min. The measurements such as glass transition temperature (T_g), cold crystallization temperature (T_{cc}), cold crystallization enthalpy (ΔH_{cc}), melting temperature (T_m), and melting enthalpy (ΔH_m) were measured. The enthalpy of fusion of a 100% crystalline PLA sample (ΔH_m^0) is 93.6 J/g. Eq. (6.1) was used to determine the crystallinity (χ_c) of the samples.

$$\chi_c = \frac{\Delta H_m - \Delta H_{cc}}{w_{PLA} \times \Delta H_m^0} \times 100\% \tag{6.1}$$

where, w_{PLA} is wt% of PLA in the blend.

The crystalline morphology of PLA and composite filaments was studied using a polarized optical microscope (Olympus BH-2, Tokyo, Japan) and the images were recorded using a digital camera FMA050. The samples were placed between two micro slides and heated to 200 ℃, then allowed to cool down to room temperature keeping the samples inside the oven.

Thermogravimetric analysis (TGA) was performed using Q500 (TA Instruments, New Castle, DE, USA), operated under a nitrogen atmosphere at the flow rate of 60 mL/min. The samples, weighing from 6 to 10 mg were kept in the platinum pan and were heated from 50 ℃ to 700 ℃ at a heating rate of 10 ℃/min.

For Dynamic Mechanical Analysis (DMA), specimens with dimensions 35 mm × 10 mm × 2 mm were 3D printed for each composition using the Original Prusa i3 MK3S 3D printer. The printer has a nozzle diameter of 0.4 mm. The printing temperature was set at 225 ℃, bed temperature at 50 ℃, print speed at 15 mm/s and infill density at 100%. The viscoelastic properties of the specimens were examined using an RSA 3 (TA instruments, New Castle, DE, USA) under flexural (three-point bending) mode having a span of 25 mm. The dynamic temperature ramp test was conducted from −60 ℃ to 120 ℃ at a ramp rate of 3 ℃/min, frequency of 1 Hz, and strain of 0.5%. Liquid nitrogen was used during the tests to regulate the heating and cooling process.

Fourier Transform Infrared Spectroscopy (FTIR) analysis of the filaments was performed using a Nicolet 6700 FTIR (ThermoFisher Scientific, Madison, WI, USA). The analysis was run for a total of 64 scans with a resolution of 4 cm^{-1}. Two spectra were recorded having the wavenumbers in the range of 400 to 4000 cm^{-1} for each sample, and the average spectrum was reported.

Specimens with diameter of 25 mm and thickness of 1 mm were 3D printed using the Original Prusa i3 MK3S 3D printer. The rheology test was performed using a rheometer (DHR-20 Hybrid Rheometer, TA instruments) by using a parallel-plate geometry at 200 ℃ to study the complex viscosity of PLA and composite filaments with angular frequencies from 100 to 0.1 rad/s at a constant strain rate of 1.0 s^{-1}. The soak time was 3 minutes at 200 ℃.

The specimens were cryogenically fractured by immersing them in liquid nitrogen to prevent the alteration of surface morphology, and then the fractured cross-sections were studied under a Zeiss EVO50 scanning electron microscope. They were gold-sputtered using an EMS Q150R sputter coating device. The cross-section was studied at a magnification of 2000X at an accelerating voltage of 15 kV and a working distance of approximately 10 mm – 15 mm.

Computer aided design (CAD) software, Solidworks® was used to design the 3D model of plain weave fabric structure as shown in Figure 6.3. For details about construction and design of fabric structures, one may refer to the references [2]. The filaments with diameter in the range of 1.70 – 1.80 mm was used to 3D print the structure. The Original Prusa i3 MK3S 3D printer having a nozzle diameter of 0.4 mm was used. The print settings used are given in Table 6.2.

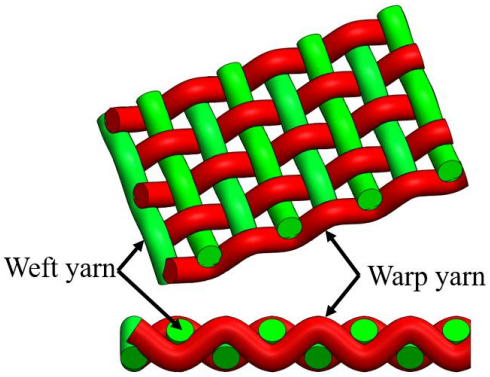

Figure 6.3. 3D design of plain weave fabric structure. The diameter of each yarn is 3 mm and the spacing between the yarns is 5 mm. Red (dark) and green (light) colors represent warp and weft yarns, respectively.

Table 6.2. Print settings for plain weave fabrics.

Parameters	Values
Layer height	0.20 mm
Infill density	100 %
Printing temperature	225 ℃
Build plate temperature	50 ℃
Print speed	15 mm/s
Travel speed	30 mm/s
Initial layer speed	15 mm/s

6.3. Results and discussion

6.3.1. Mechanical test results

The tensile test results of PLA and the composite filaments are given in Table 6.3 and Figure 6.4. The tensile strength and stiffness of TPU_10 samples is 37 % and 26 % less than that of the pure PLA filaments, respectively. The elongation at break of TPU_10 samples is 13 times higher than that of PLA. This result was attributed to the effect of soft segment of TPU blended together with PLA matrix. With the increasing content of TPU fillers in the PLA matrix, the strength and stiffness continue to decrease but the elongation at break increases for all composite filaments. The flexibility obtained with the compromised but optimal strength is the main goal of this research. The maximum elongation at break is obtained for TPU_40 samples having almost 50% reduction in stiffness and 62% reduction in stress as compared with the PLA filaments. The decrease in tensile strength of the composite filaments might be due to the increase in elastomeric properties inhibited by TPU, which could be attributed to a decrease in the effective load-bearing cross-section of the filament in the presence of TPU fillers; however, it stretched up to 535% of its initial gage length without breaking. The increase in the TPU filler amount causes the size of TPU aggregates to be larger due to the coalescence of the TPU particles as seen in the SEM images (Figure 6.11 e). Hence, due to the larger filler size, the surface area to volume ratio becomes smaller and this results in lower interfacial area and stress transfer at the matrix-filler interface. Apart from this, the phase separation between PLA and TPU and their partial miscibility as demonstrated by DMA might have affected the stress transfer between the PLA matrix and TPU fillers. Several researchers including Mi. et. al. [8] and Jaso et. al. [24] observed a decrease in tensile stress with the increasing content of TPU fillers in PLA matrix. Similarly, Feng and Ye [25] found strains up to 350% for 20 wt%

TPU and 375% for 30 wt% of TPU in PLA matrix. They also observed a tensile stress of 40 MPa for 20 wt% TPU in the PLA matrix, which is similar to our findings.

Table 6.3. Mechanical properties of the filaments manufactured (mean ± standard deviation).

Sample	Ultimate Tensile stress (MPa)	Young's Modulus (GPa)	Elongation at break (%)
PLA	64.87 ± 5.45	2.314 ± 0.183	16.26 ± 3.97
TPU_10	40.64 ± 4.96	1.702 ± 0.368	215.30 ± 35.76
TPU_20	38.97 ± 7.58	1.633 ± 0.203	227.21 ± 64.05
TPU_30	35.61 ± 4.35	1.417 ± 0.137	447.87 ± 33.32
TPU_40	24.55 ± 4.08	1.262 ± 0.217	535.33 ± 55.41

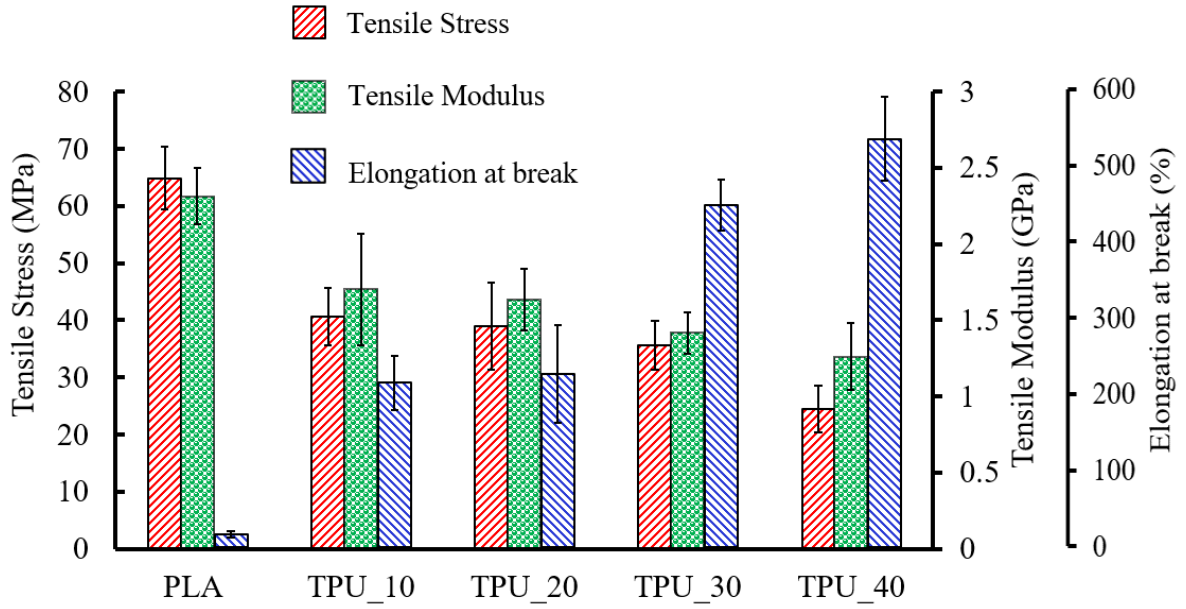

Figure 6.4. Mechanical properties of PLA and PLA/TPU composite filaments.

6.3.2. DSC results

The DSC thermograms for the first heating cycle, cooling cycle and second heating cycle are shown in Figure 6.5 and the results obtained are tabulated in Table 6.4 and Table 6.5, which give an insightful view about the interaction of PLA and TPU in the mixture. From the first heating curves, it is observed that the glass transition temperature of PLA is around 60 °C whereas pure TPU has a T_g around –45 °C. The T_g of TPU in the mixture is quite difficult to observe for the samples except for TPU_40, whose T_g is observed to be –43 °C in the first heating cycle and –35 °C during second heating cycle. The cold crystallization peaks appeared

at 127 ℃, and 123 ℃ for pure PLA and TPU_10 samples, respectively, whereas it is at around 110 ℃ for all the other composite filaments. Melting temperatures are at around 153 ℃ for all the samples. The cooling cycle shows similar crystallization behavior for all the samples. From the second heating curves, it is found that T_g is around 61 ℃ for PLA in all the samples and that of TPU in TPU_40 sample is at –35 ℃. The crystallization peaks appear at around 128 ℃ showing an increment over first heating cycle, followed by melting temperatures at around 152 ℃ with slight decrease in value for TPU_40. This observation indicates that the polymers show a partial miscibility between them by using twin-screw and then single-screw extruders for producing the composite filaments.

The addition of TPU has increased the crystallinity of PLA in the blends. Pure PLA is amorphous in nature having a crystallinity of 2.8 %, which increases with the increasing amount of TPU. Jaso et. al. [24] and Xu et. al. [26] observed an increase in crystallinity percent of PLA with the increasing amount of TPU in the blends. It can be said that TPU might have accelerated the crystallization by acting as a crystallization nucleating agent that highly affects the crystallinity [26].

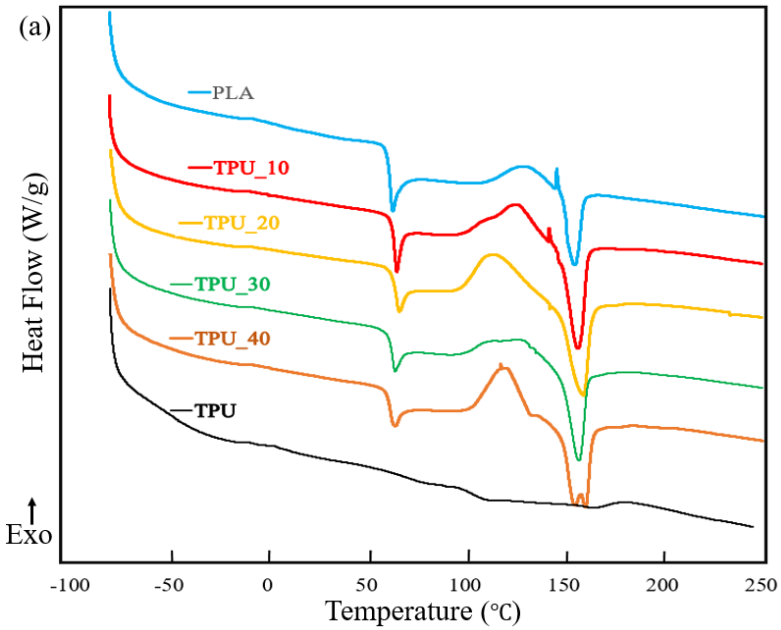

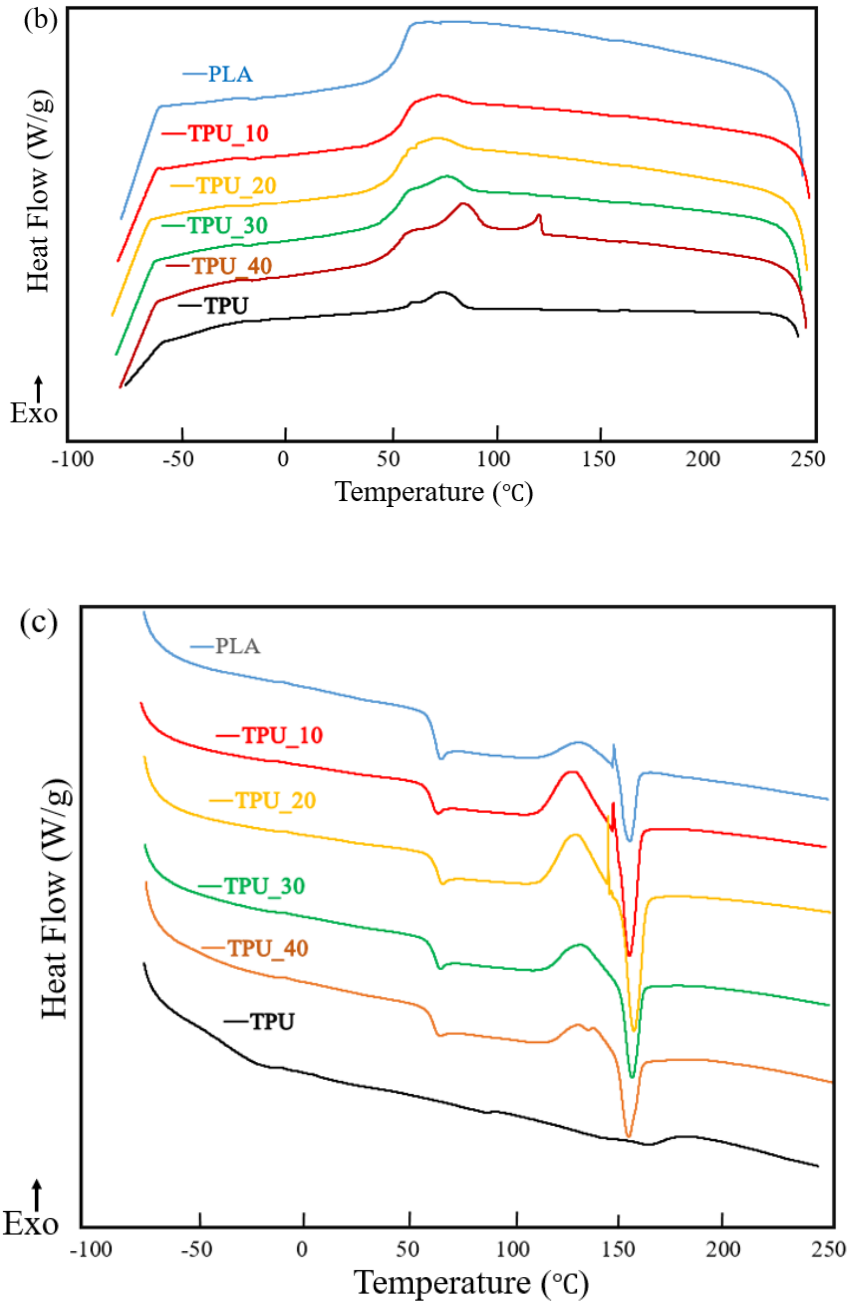

Figure 6.5. DSC thermograms of PLA filament, TPU pellets and their composite filaments: (a) First heating cycle, (b) Cooling cycle, and (c) Second heating cycle. The numbers in each sample code indicates the wt% of TPU in PLA/TPU composite filaments.

Table 6.4. DSC results of the composite filaments obtained from the first heating cycle.

Sample code	T_g (℃), TPU	T_g (℃), PLA	T_{cc} (℃)	ΔH_{cc} (J/g)	T_m (℃)	ΔH_m (J/g)	Crystallinity (%), PLA
PLA	-	60.14	127.24	6.05	151.57	8.68	2.81
TPU_10	*	62.36	123.21	15.78	153.75	17.49	2.03
TPU_20	*	63.04	110.82	13.90	155.82	18.52	6.17
TPU_30	*	60.88	110.28	5.575	153.65	13.42	11.97
TPU_40	−43.62	59.44	114.69	8.102	151.55	17.73	17.14
TPU	−45.91	ψ	ψ	ψ	ψ	ψ	ψ

Table 6.5. DSC results of the composite filaments obtained from the second heating cycle.

Sample code	T_g (℃), TPU	T_g (℃), PLA	T_{cc} (℃)	ΔH_{cc} (J/g)	T_m (℃)	ΔH_m (J/g)
PLA	-	61.60	12.88	3.99	151.83	6.29
TPU_10	*	61.37	127.23	15.43	152.98	16.27
TPU_20	*	61.74	126.36	10.78	152.82	16.39
TPU_30	*	60.73	129.33	9.19	152.78	10.08
TPU_40	−35.23	59.39	126.76	4.95	149.73	7.186
TPU	−36.61	ψ	ψ	ψ	ψ	ψ

Notes:

(i) T_g : Glass transition temperature, T_{cc} : Cold crystallization temperature, ΔH_{cc} : Cold crystallization enthalpy, T_m : Melting temperature, and ΔH_m : Melting enthalpy.

(ii) *: T_g of TPU in the respective samples were hardly observed during DSC tests.

(iii) Ψ: TPU samples do not show any significant peaks.

6.3.3. POM results

Figure 6.6 shows the crystalline morphology of PLA and composite filament observed under polarized optical microscope. The crystalline structures can be seen as a group of four crystallites in a circular pattern and this arrangement is called spherulite, similar to observation in ref. [30]. The shapes of the crystallites are supposed to define the structure and properties of the spherulites, which are known as crudely oriented spheroidal aggregates of crystallites and their attached amorphous regions [31]. From these figures, it is evident that the PLA and other composite filaments exhibit similar spherulitic structures which shows that the crystalline structure of PLA does not change in the composite material. The number of PLA crystals is increasing with the increasing content of TPU in the blend. This fact implies that the crystallinity percentage is increased which is also seen during the DSC tests. It is expected that with the increase of crystallinity percentage, the mechanical properties of the materials would improve. However, due to the presence of TPU, the strength of composite filament decreased. With the increasing amount of TPU, the amount of soft segments in the mixture increases, which are connected to the hard segments. Those soft segments play a role in increasing flexibility and hence the composite filament stretches very easily. This might be the reason behind the reduction of mechanical strength which is observed by mechanical tensile tests.

It should also be noted that the spherulite size has been increased in the composite filaments. This can be interpreted as the bonding of PLA and TPU crystallites due to the presence of hydrogen bonding and represents the compatibility between them to some extent. There are many smaller spherulites than the larger ones, which shows that most of the polymers did not blend well, which proves the presence of phase separation between them.

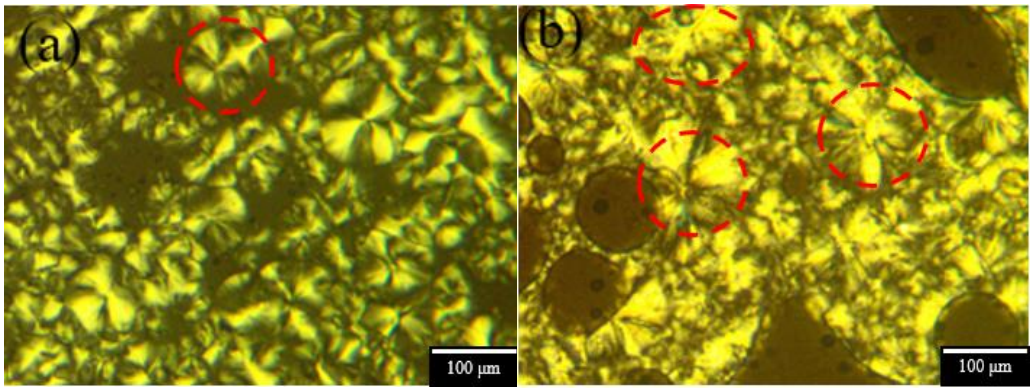

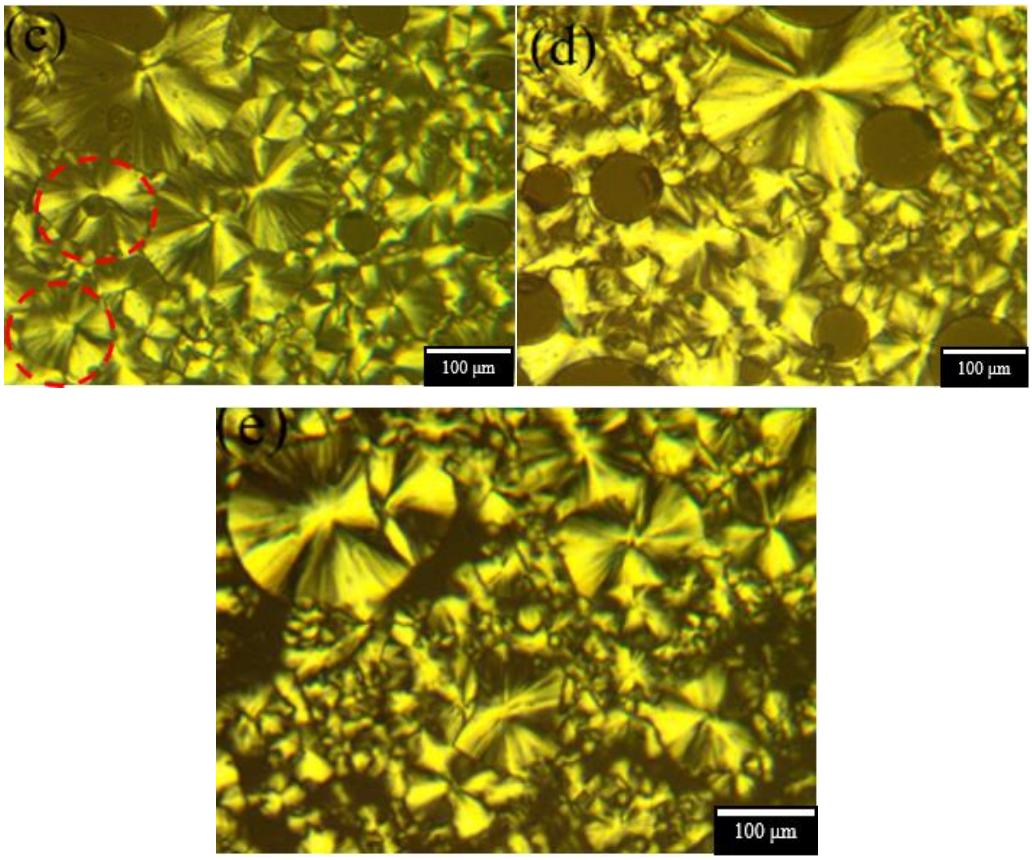

Figure 6.6. POM photographs of PLA and composite filaments: (a) PLA, (b) TPU_10, (c) TPU_20, (d) TPU_30, and (e) TPU_40.

6.3.4. DMA results

The thermo-mechanical properties of PLA and composite filaments were studied using dynamic mechanical analysis. The important dynamic parameters such as storage modulus (E′), loss modulus (E″), and damping factor (tan δ) are dependent on temperature and display the interlayer bonding between the polymers in composite materials. Figure 6.7a shows the storage modulus of the samples versus temperature. Storage modulus or dynamic modulus represents the stiffness of a material and its tendency to store energy applied to it [32]. The modulus of the samples depends on the quantity of polymers added, quality of interface between PLA and TPU, processing conditions, 3D printing setting and environmental conditions [12]. Pure PLA has modulus of 1.56 GPa at 30 ℃, which decreases with an increase in temperature because it approaches its glass transition temperature (~60 ℃). Other samples with higher percentage of TPU content have lower initial moduli than pure PLA, which is around 25 MPa at 60 ℃. The lower moduli might have happened due to increased flexibility of molecular chain because of the presence of soft segment of TPU. This graph also illustrates

two significant drops of storage moduli in composite samples that corresponds to the T_g of TPU and PLA phases.

Figure 6.7b shows the loss modulus (dynamic loss modulus) of the samples as a function of temperature, which represents the viscous behavior of a material and its tendency to dissipate energy applied to it [32]. The loss modulus curves exhibit a peak at 55 ℃ for PLA filament, which is associated with its T_g. Similarly, two peaks appeared for all other samples representing the T_g of TPU at lower temperature and PLA at higher temperatures (Table 6.6). This indicates two different phases in the blend at the microscopic level, which means that the polymers are immiscible in the blend.

Figure 6.7c denotes the tan δ curves of the samples as a function of temperatures. Tan δ is the damping factor or loss factor of the samples and is described as a ratio of loss modulus to storage modulus (Tan $\delta = \frac{E''}{E'}$). The PLA filament shows one peak in tan δ curves at 65.06 ℃, indicating its glass transition temperature; however, all other samples displayed two peaks representing T_g, which indicates the phase separation between TPU and PLA polymer constituents. The gap between the two peaks decreases (Table 6.6) with the higher content of TPU, which indicates improvement in compatibility between the two phases. This also means that these two polymers are partially miscible due to interaction between the molecules of PLA and TPU as expressed by Figure 6.1.

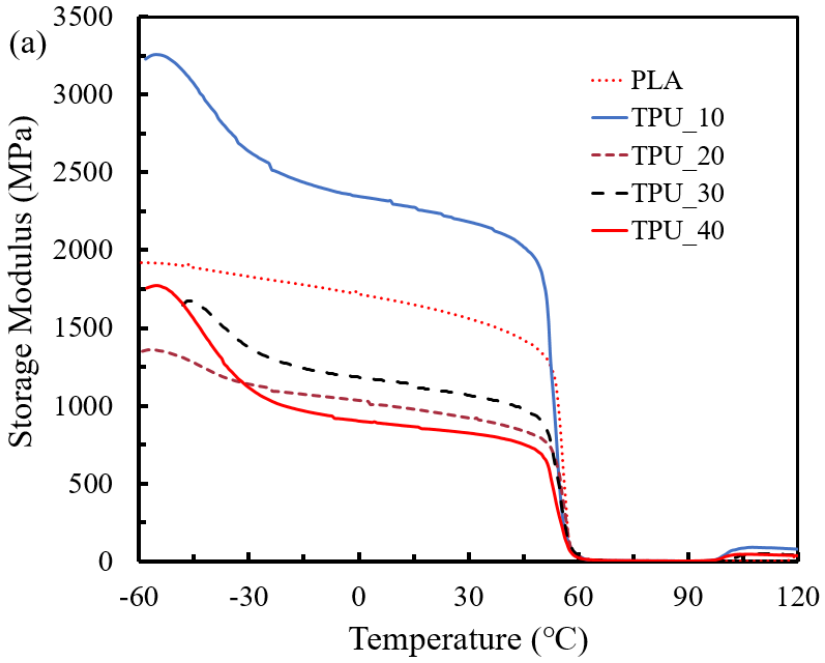

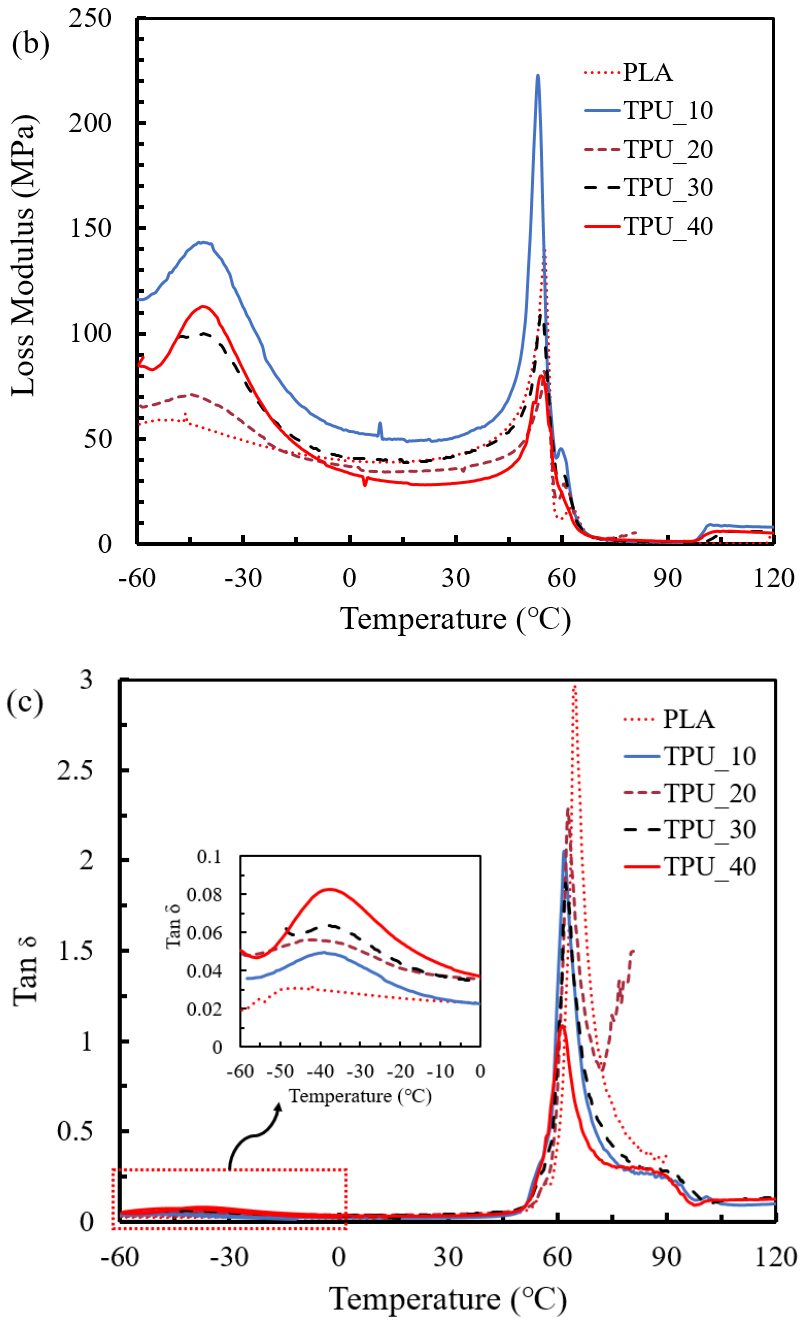

Figure 6.7. DMA graphs of PLA, and PLA/TPU composite filaments: (a) Storage Modulus, (b) Loss Modulus, and (c) Tan delta. The numbers in each sample code indicates the wt% of TPU in PLA/TPU composite filament.

Table 6.6. Glass transition temperatures of the samples obtained from Tan δ and Loss Modulus versus temperatures obtained from DMA.

Samples	Tan δ			Loss Modulus	
	T_g (℃), PLA	T_g (℃), TPU	ΔT_g $(\Delta T_{g(PLA)} - \Delta T_{g(TPU)})$	T_g (℃), PLA	T_g (℃), TPU
PLA	65.06	-	-	55.31	-
TPU_10	62.29	−39.09	101.38	53.31	−40.28
TPU_20	62.81	−43.07	105.88	54.70	−43.64
TPU_30	62.30	−39.74	102.04	54.81	−40.44
TPU_40	61.31	−37.44	98.75	53.88	−40.42

6.3.5. TGA results

The TGA curves of various samples showing the weight loss and rate of weight loss are given in Figure 6.8. The weight loss curve of PLA shows that the onset decomposition temperature is 367 ℃ and decomposes completely at 440 ℃. With the addition of TPU, the onset decomposition temperature of the blend decreases to 327 ℃, 326 ℃, 303 ℃, and 269 ℃ for TPU_10, TPU_20, TPU_30, and TPU_40 samples, respectively. This decrease might have happened due to earlier decomposition of TPU present in the PLA matrix. All the samples decomposed, and the masses left at 500 ℃ is less than 12% of its original mass and further keep decomposing. The derivative weight loss curves reveal that the weight loss of the blends have different stages, which can be seen in weight loss curves as well. TPU has different functional groups having different decomposition temperatures which leads to multi-stage degradation of the samples.

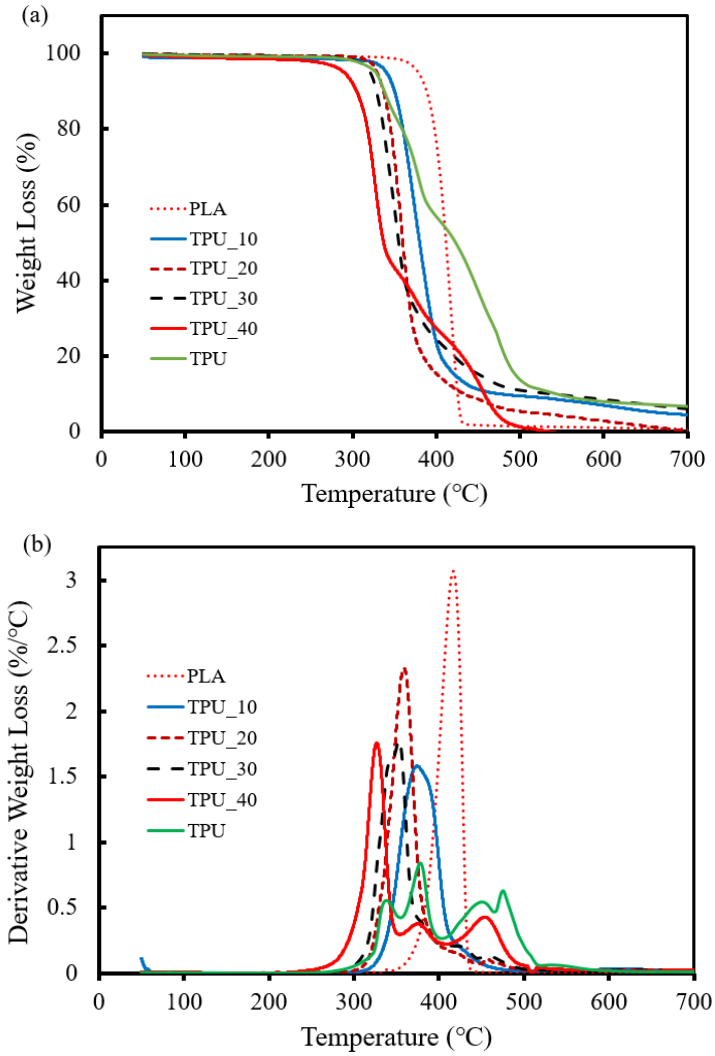

Figure 6.8. TGA thermograms of PLA filament, TPU pellets and their composite filament: (a) Percentage weight loss, and (b) Rate of weight loss. The numbers in each sample code indicates the wt% of TPU in PLA/TPU composite filament.

6.3.6. FTIR results

The FTIR spectra of PLA, TPU pellets, and their composite filaments are shown in Figure 6.9. PLA has medium and broad absorption band having 3 peaks in the range of 2815 – 3015 cm^{-1}. This attributed to the presence of alkane (C – H) bond, whose intensity increases with the increasing TPU content. The peaks of TPU appearing at 2916 and 2848 cm^{-1} are due to asymmetric and symmetric vibration of $-CH_2$ groups, respectively, and the medium intensity absorption peak at 3298 cm^{-1} indicates the presence of N – H groups [8]. The intensity of peak at 3298 cm^{-1} decreases with the decrease in TPU amount in the blends. Similarly, the strong intensity absorption peak is seen at 1745 cm^{-1} in PLA which suggests

the existence of C = O stretching of the carbonyl group whose intensity decreases with the increasing TPU content. From the spectra, it can be said that the composite samples contain both polymer properties since there are not any new chemical bonds present which advises the absence of any chemical reaction occurring during the extrusion processes [8].

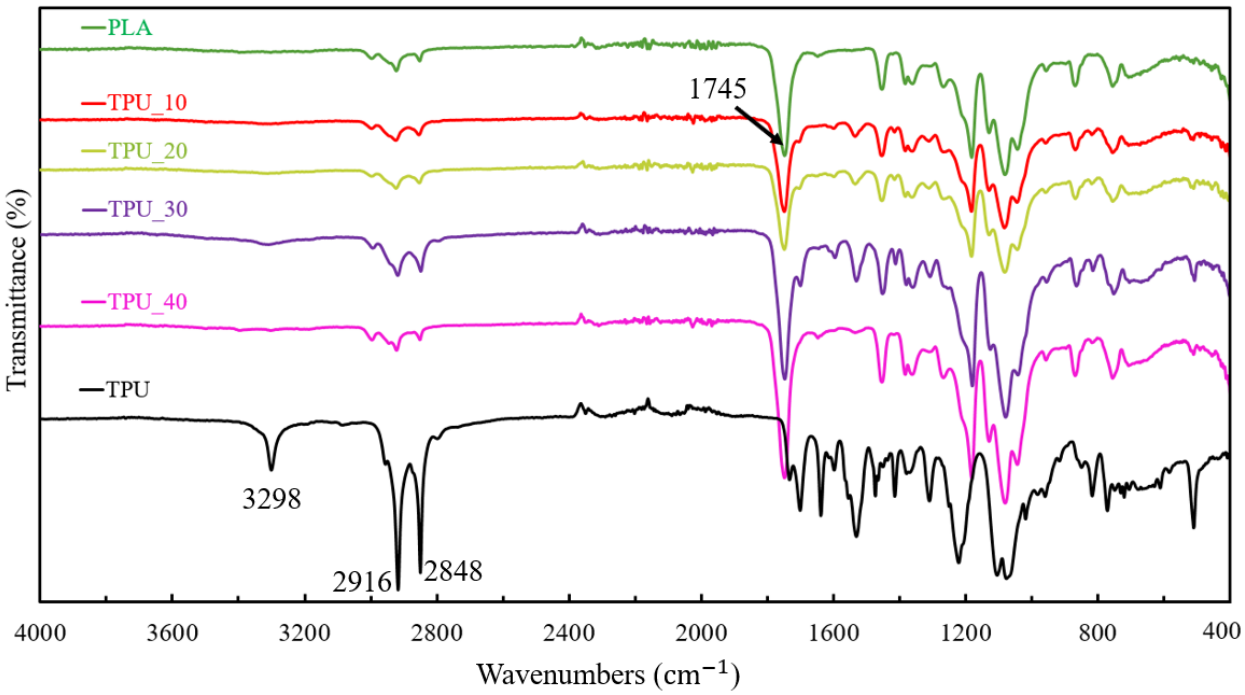

Figure 6.9. FTIR spectra of PLA filament, TPU pellets and their composite filaments. The numbers in each sample code indicates the wt% of TPU in PLA/TPU composite filament.

6.3.7. Rheology results

The rheological experiments were conducted to study the viscoelastic properties of PLA and the composite filaments for 3D printed structures. The complex viscosity (η^*) at various angular frequencies for the samples are summarized in Figure 6.10. The complex viscosity of PLA filament was higher than all the other samples below 0.5 rad/s. The complex viscosity of neat PLA filament starts around 475 Pa.s at 0.1 rad/s and decreases rapidly to 220 Pa.s at 0.6 rad/s. After this, it keeps decreasing slowly along with the frequencies. Besides this, the complex viscosity is increasing along with the TPU amount in the blend showing the highest value for TPU_40 with 340 Pa.s at 0.1 rad/s. The curves for TPU_30 and TPU_40 filaments tend to form a plateau after 2 rad/s. The reason behind the increased viscosity of the composite filaments may be that neat TPU has higher viscosity than neat PLA [8].

Mi et. al. [8] observed an increase in viscosity with the increasing TPU content in PLA/TPU composite samples. However, they found the viscosity of the polymer matrix to be in the range of 500 – 1300 Pa.s, which is higher than the viscosity of the polymer matrix examined in our work. Lower viscosity of matrix makes the manufacturing process of composites easier which is desirable [33]. Nofar et. al. [14] observed that the viscosity of PLA/TPU blend having 15 wt% of TPU had higher viscosity than the neat PLA samples. They found the values in the range of 10^3 - 10^5 Pa.s which also signifies the improvement in the properties for 3D printed structures.

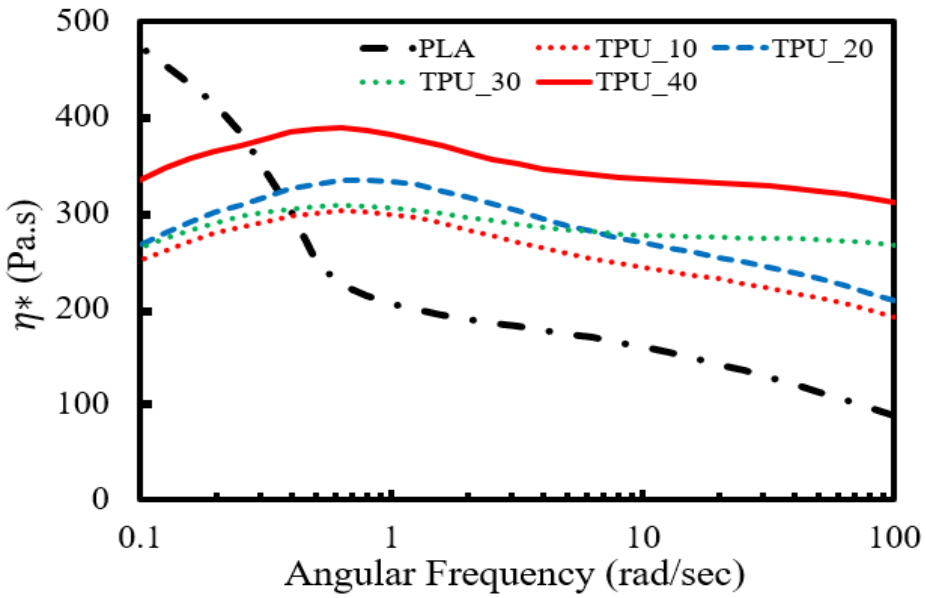

Figure 6.10. Rheology tests of 3D printed samples using the PLA and the composite filaments.

6.3.8. SEM

The SEM images of the cross-sections of cryogenically fractured PLA and their composite filaments are shown in Figure 6.11. The cross-section of PLA filament appears plain but with brittle failure (Figure 6.11 a). With the addition of TPU content, a ductile failure of the filament can be seen; few smaller spherical shaped TPU particles are dispersed in the PLA matrix (Figure 6.11 b, c, and d). Besides this, a good bonding between the PLA matrix and TPU fillers can be observed, similar to the observation in ref. [9]. Moreover, many larger spherical shaped TPU particles are dispersed homogeneously in the PLA matrix for 40 wt% of TPU in the blend (Figure 6.11 e). These larger particles might have formed due to the coalescence of TPU aggregates. Both polymers are fused together very well indicating a good

compatibility between them. Feng and Ye [25] also observed similar entanglement of TPU particles with the PLA. Increasing number of smaller ductile fibrils can be seen with the increasing TPU content in the blend, which causes the increase in elongation at break properties and making it more flexible but reduces the tensile strength.

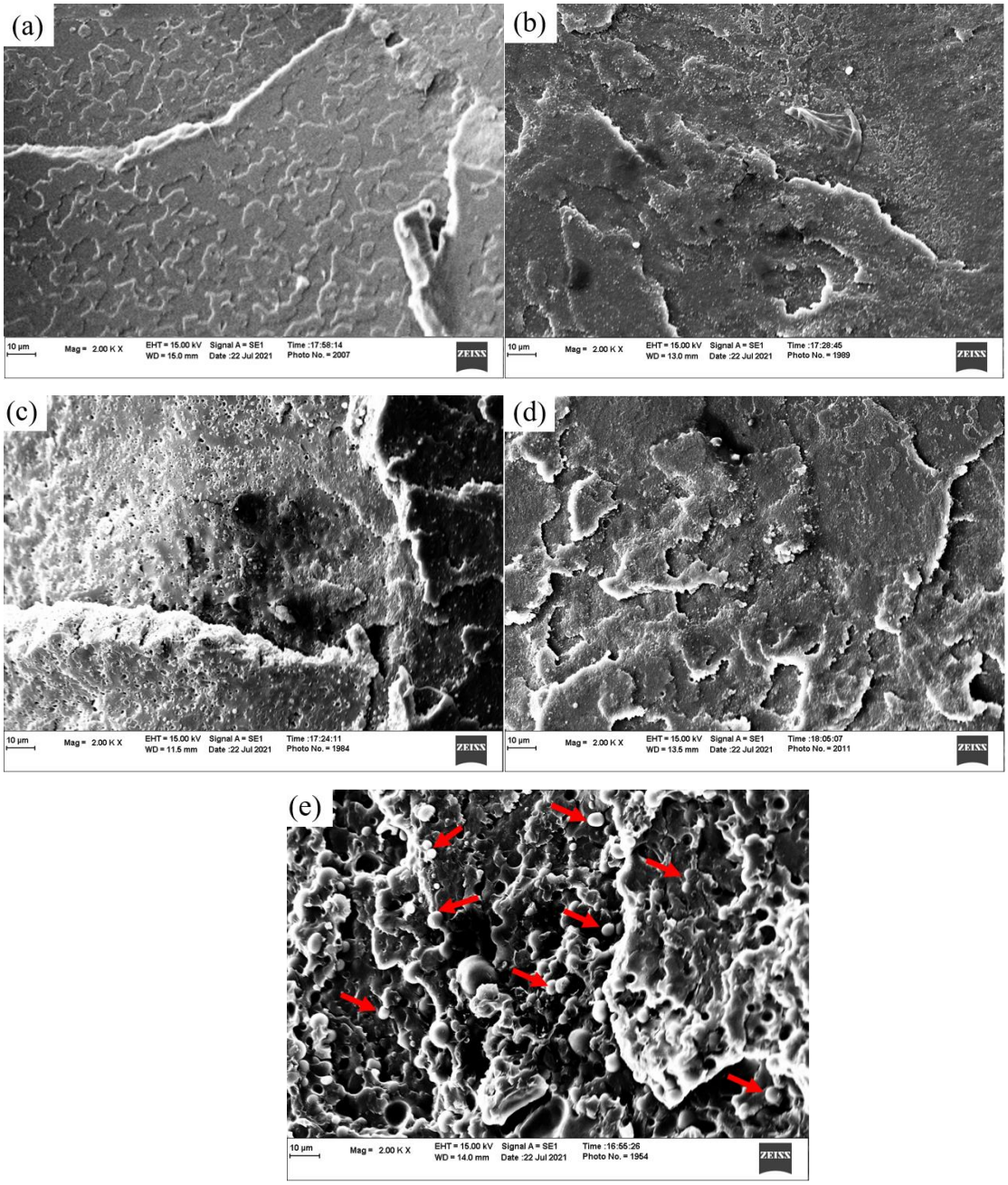

Figure 6.11. SEM images of cross-sections of cryogenically fractured PLA and their composite filaments. (a) PLA, (b) TPU_10, (c) TPU_20, (d) TPU_30, and (d) TPU_40.

6.3.9. 3D printing of fabric structures

A plain weave fabric structure was 3D printed using the TPU_30 composite filament to understand the printing ability of a complex structure of composite filaments. It is concluded that the composite filaments are suitable for 3D printing but non-uniformity in diameter affects the print quality and hence the overall properties. The work related to improving the print quality and fabric properties will be considered in our future research. Figure 6.12 shows the 3D printed fabric structure using the TPU_30 composite filament.

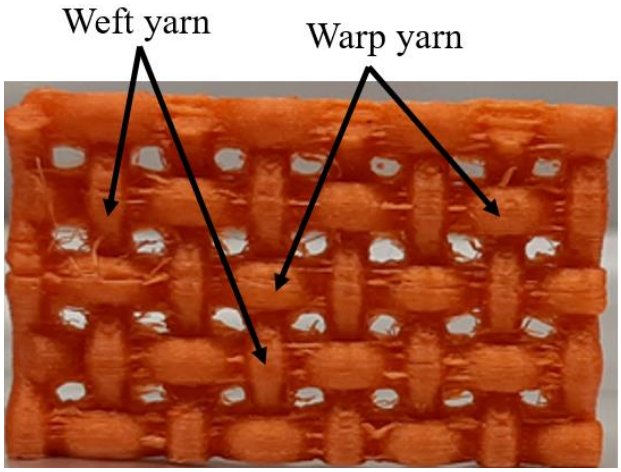

Figure 6.12. FDM 3D printed plain weave fabric using TPU_30 composite filament.

6.4. Conclusions

PLA and TPU pellets were blended using the twin–screw and single–screw extruders, and novel composite filaments have been obtained. The amounts of TPU polymer in the blend are 10 wt%, 20 wt%, 30 wt%, and 40 wt% of the total weight of the respective composition. The filaments manufactured have varying diameters but the filaments having diameter in the range of 1.56 mm to 1.86 mm were used for the analyses. The following conclusions can be drawn from this work:

The tensile test results showed that the tensile stress and stiffnesses of the filaments decrease with the increasing content of TPU fillers. However, the % elongation at break increases for each filament. This reveals the fact that the flexibility and ductility increase is due to the effect of soft segment contained in the TPU.

The DSC results showed that the crystallinity of PLA increases with the addition of TPU, which is verified by using the polarized optical microscope (POM).

The DMA tests demonstrated that there is a phase separation between the polymers, which is evidenced by two peaks representing the glass transition temperature of each polymer in storage modulus and loss modulus curves; this indicates their immiscibility. However, the Tanδ curves showed the decreasing phase difference between their glass transition temperatures which confirms improvement in their compatibility. Hence, it can be interpreted as partial immiscibility between them.

TGA analysis showed that PLA started decomposing at 367 ℃ and decomposed completely at 440 ℃. However, the increasing content of TPU reduced the onset decomposition temperature of the composite filaments and displayed multi-stage degradation of the samples due to various functional groups in it.

FTIR graphs suggested that there is not any new chemical reaction occurring during the melt blending process.

The SEM images of the filaments showed good compatibility between the polymers and increasing ductility of the filaments.

The 3D printed plain weave fabric structure using the fused deposition modeling (FDM) method with TPU_30 filament demonstrated the feasibility of these filaments to be used in 3D printing of fabrics having an optimized flexibility and strength. The print quality and other fabric properties, however, can be improved, which will be a recommended future work.

6.5. References

[1] J. C. Najmon, S. Raeisi, and A. Tovar, "Review of additive manufacturing technologies and applications in the aerospace industry," *Addit. Manuf. Aerosp. Ind.*, pp. 7–31, 2019, doi: 10.1016/B978-0-12-814062-8.00002-9.

[2] S. Adanur and A. Jayswal, "Additive manufacturing of interlaced fibrous structures," *Rapid Prototyp. J.*, vol. 27, no. 4, pp. 671–681, 2021, doi: 10.1108/RPJ-05-2020-0095.

[3] S. Farah, D. G. Anderson, and R. Langer, "Physical and mechanical properties of PLA, and their functions in widespread applications — A comprehensive review," *Adv. Drug Deliv. Rev.*, vol. 107, pp. 367–392, 2016, doi: 10.1016/j.addr.2016.06.012.

[4] R. M. Rasal and D. E. Hirt, "Toughness decrease of PLA-PHBHHx blend films upon surface-confined photopolymerization," *J. Biomed. Mater. Res. - Part A*, vol. 88, no. 4, pp. 1079–1086, 2009, doi: 10.1002/jbm.a.32009.

[5] T. Gérard, T. Noto, and T. Budtova, “Tensile Properties of Pla And Phbv Blends: Anomalous Elongation and Aging,” *11th Eur. Symp. Polym. Blends - Polyblends 2012*, 2012.

[6] Y. Wang and M. A. Hillmyer, “Polyethylene-Poly (L -lactide) Diblock Copolymers : Synthesis and Compatibilization of Poly (L -lactide)/ Polyethylene,” pp. 2755–2766, 2001.

[7] K. S. Anderson, S. H. Lim, and M. A. Hillmyer, “Toughening of polylactide by melt blending with linear low-density polyethylene,” *J. Appl. Polym. Sci.*, vol. 89, no. 14, pp. 3757–3768, 2003, doi: 10.1002/app.12462.

[8] H. Y. Mi *et al.*, “Characterization of thermoplastic polyurethane/polylactic acid (TPU/PLA) tissue engineering scaffolds fabricated by microcellular injection molding,” *Mater. Sci. Eng. C*, vol. 33, no. 8, pp. 4767–4776, 2013, doi: 10.1016/j.msec.2013.07.037.

[9] V. Jašo, M. Cvetinov, S. S. S. Rakič, and Z. S. Petrovič, “Bio-plastics and elastomers from polylactic acid/thermoplastic polyurethane blends,” *J. Appl. Polym. Sci.*, vol. 131, no. 22, pp. 1–8, 2014, doi: 10.1002/app.41104.

[10] N. Alizadeh *et al.*, “Synthesis and characterization of high performance interpenetrating polymer networks with polyurethane and poly(methyl methacrylate),” in *Unsaturated Polyester Resins*, Elsevier Inc., 2019, pp. 243–255.

[11] S. Jiang, G. Duan, H. Hou, A. Greiner, and S. Agarwal, “Novel Layer-by-Layer Procedure for Making Nylon-6 Nanofiber Reinforced High Strength, Tough, and Transparent Thermoplastic Polyurethane Composites,” *ACS Appl. Mater. Interfaces*, vol. 4, pp. 4366–4372, 2012.

[12] Q.-W. Lu and C. W. Macosko, “Comparing the compatibility of various functionalized polypropylenes with thermoplastic polyurethane (TPU),” *Polymer (Guildf).*, vol. 45, pp. 1981–1991, 2004, doi: 10.1016/j.polymer.2003.12.077.

[13] A. Frick and A. Rochman, “Characterization of TPU-elastomers by thermal analysis (DSC),” *Polym. Test.*, vol. 23, no. 4, pp. 413–417, 2004, doi: 10.1016/j.polymertesting.2003.09.013.

[14] M. Nofar, M. Mohammadi, and P. J. Carreau, “Effect of TPU hard segment content on the rheological and mechanical properties of PLA/TPU blends,” *Journal of Applied Polymer Science*, vol. 137, no. 45. 2020, doi: 10.1002/app.49387.

[15] A. Pattanayak and S. C. Jana, “Thermoplastic polyurethane nanocomposites of reactive silicate clays:effects of soft segments on properties,” *Polymer (Guildf).*, vol. 46, pp.

5183–5193, 2005, doi: 10.1016/j.polymer.2005.04.035.

[16] X. Zhanga, T.-T. Li, Z. Wang, H.-K. Peng, C.-W. Lou, and J.-H. Lin, “Facile fabrication and mass production of TPU/Silica/STF coated aramid fabric with excellent flexibility and quasi-static stab resistance for versatile protection,” *Prog. Org. Coatings*, vol. 151, 2021, doi: 10.1016/j.porgcoat.2020.106088.

[17] C. Vajrasthira, T. Amornsakchai, and S. Bualek-limcharoen, “Fiber – Matrix Interactions in Aramid-Short-Fiber- Reinforced Thermoplastic Polyurethane Composites,” *J. Appl. Polym. Sci.*, vol. 87, pp. 1059–1067, 2002.

[18] M.-C. Lin, J.-H. Lin, and L. Bao, “Applying TPU blends and composite carbonfibers toflexibleelectromagnetic-shielding fabrics: Long-fiber-reinforced thermoplasticstechnique,” *Compos. Part A*, vol. 138, 2020, doi: 10.1016/j.compositesa.2020.106022.

[19] M. He, D. Zhang, J. Guo, S. Qin, and X. Ming, “Mechanical, Thermal, and Dynamic Mechanical Properties of Long Glass Fiber-Reinforced Thermoplastic Polyurethane/Polyoxymethylene Composites,” *Polym. Compos.*, pp. 2067–2073, 2014, doi: 10.1002/pc.22868.

[20] B. Akhoundi and A. H. Behravesh, “Effect of Filling Pattern on the Tensile and Flexural Mechanical Properties of FDM 3D Printed Products,” *Exp. Mech.*, vol. 59, no. 6, pp. 883–897, 2019, doi: 10.1007/s11340-018-00467-y.

[21] J. M. Chacón, M. A. Caminero, E. García-Plaza, and P. J. Núñez, “Additive manufacturing of PLA structures using fused deposition modelling: Effect of process parameters on mechanical properties and their optimal selection,” *Mater. Des.*, vol. 124, pp. 143–157, Jun. 2017, doi: 10.1016/J.MATDES.2017.03.065.

[22] T. Tábi, I. E. Sajó, F. Szabó, A. S. Luyt, and J. G. Kovács, “Crystalline structure of annealed polylactic acid and its relation to processing,” *EXPRESS Polym. Lett.*, vol. 4, no. 10, pp. 659–668, 2010, doi: 10.3144/expresspolymlett.2010.80.

[23] Y. Zhou, L. Luo, W. Liu, G. Zeng, and Y. Chen, “Preparation and Characteristic of PC/PLA/TPU Blends by Reactive Extrusion,” *Adv. Mater. Sci. Eng.*, pp. 1–9, 2015, doi: 10.1155/2015/393582.

[24] V. Jašo, M. V. Rodić, and Z. S. Petrović, “Biocompatible fibers from thermoplastic polyurethane reinforced with polylactic acid microfibers,” *European Polymer Journal*, vol. 63. pp. 20–28, 2015, doi: 10.1016/j.eurpolymj.2014.11.041.

[25] F. Feng and L. Ye, “Morphologies and mechanical properties of polylactide/thermoplastic polyurethane elastomer blends,” *J. Appl. Polym. Sci.*, vol. 119,

no. 5, pp. 2778–2783, Mar. 2011, doi: 10.1002/app.32863.

[26] D. Xu, K. Yu, K. Qian, and C. B. Park, “Foaming behavior of microcellular poly(lactic acid)/TPU composites in supercritical CO2,” *J. Thermoplast. Compos. Mater.*, vol. 31, no. 1, pp. 61–78, 2018, doi: 10.1177/0892705716679480.

[27] C. Kaynak and S. D. Varsavas, “Performance comparison of the 3D-printed and injection-molded PLA and its elastomer blend and fiber composites,” *J. Thermoplast. Compos. Mater.*, vol. 32, no. 4, pp. 501–520, 2019, doi: 10.1177/0892705718772867.

[28] X. Meng, N. A. Nguyen, H. Tekinalp, E. Lara-Curzio, and S. Ozcan, “Supertough PLA-Silane Nanohybrids by in Situ Condensation andGrafting,” *ACS Sustain. Chem. Eng*, vol. 6, pp. 1289–1298, 2018, doi: 10.1021/acssuschemeng.7b03650.

[29] S. Wasti *et al.*, “Influence of plasticizers on thermal and mechanical properties of biocomposite filaments made from lignin and polylactic acid for 3D printing,” *Compos. Part B Eng.*, vol. 205, 2021, doi: 10.1016/j.compositesb.2020.108483.

[30] C. Zhang, Q. Lan, T. Zhai, S. Nie, J. Luo, and W. Yan, “Melt crystallization behavior and crystalline morphology of Polylactide/Poly(ε-caprolactone) blends compatibilized by lactide-caprolactone copolymer,” *Polymers (Basel).*, vol. 10, no. 11, pp. 1–12, 2018, doi: 10.3390/polym10111181.

[31] W. M. D. Bryant, R. H. H. Pierce, C. R. Lindegren, and R. Roberts, “Nucleation and growth of crystallites in high polymers. Formation of spherulites,” *J. Polym. Sci.*, vol. 16, no. 82, pp. 131–142, 1955, doi: 10.1002/pol.1955.120168204.

[32] N. Saba, M. Jawaid, O. Y. Alothman, and M. T. Paridah, “A review on dynamic mechanical properties of natural fibre reinforced polymer composites,” *Constr. Build. Mater.*, vol. 106, pp. 149–159, 2016, doi: 10.1016/j.conbuildmat.2015.12.075.

[33] N. Alizadeh, D. P. Thorne, M. L. Auad, and A. D. N. Celestine, “Mechanical performance of vinyl ester—polyurethane interpenetrating polymer network composites,” *J. Appl. Polym. Sci.*, vol. 138, no. 19, pp. 1–11, 2021, doi: 10.1002/app.50411.

Chapter 7

Effect of a plasticizer on PLA/TPU composite filaments

(Jayswal, A., Liu, J. P., Harris, G., and Adanur, S., "*Thermo-mechanical properties of composite filaments for 3D printing of fabrics*", Journal of Thermoplastic Composite Materials, 13 March 2023.)

Abstract

The objective of this study is to manufacture composite filaments to be used in 3D printing of fabrics using fused deposition modeling (FDM) method. The primary properties of a fabric are flexibility and strength which are lacking in the available 3D printed materials. Polylactic acid (PLA), thermoplastic polyurethane (TPU) and poly(ethylene) glycol (PEG) were blended in different proportions and extruded using twin-screw extruder to obtain composite filaments. The properties of the filaments were studied using various material characterization methods such as uniaxial tensile test, differential scanning calorimetry (DSC), thermogravimetric analysis (TGA), dynamic mechanical analysis (DMA), Fourier transform infrared spectroscopy (FTIR), and scanning electron microscope (SEM). With the addition of PEG in the PLA/TPU composition, it was found that the yield stress and Young's modulus of the composite filaments have significantly decreased compared to that of pure PLA filament. It was also noted that there was no significant difference in ultimate tensile strength whereas the elongation at break was increased by more than 500%. Using the composite filament, a plain weave fabric structure was 3D printed to investigate the printing ability of a complex structure. It is concluded that the composite filaments developed are suitable for 3D printing but non-uniformity in diameter affects the print quality and hence the overall properties of fabrics.

7.1. Introduction

Additive manufacturing (AM) (also known as 3D printing) is the process of producing three-dimensional (3D) objects by adding materials layer upon layer using the computer-aided design (CAD) models. The first patent related to additive manufacturing was granted in the United States in 1984 [1], entitled "Apparatus for production of three-dimensional objects by Stereolithography". However, this technology was commercialized after the expiration of the patent [2]. Hence this technology is quite new, but its use has skyrocketed in recent years. AM has been used in almost all industries including automotives, aerospace, defense, military, fashion, textiles, medicine, and many others.

The application of polymer-based additive manufacturing in fabric industry has fascinated the researchers [3] [4] [5] [6] [7] [8] [9] [10]. Different polymers such as polylactic acid (PLA), acrylonitrile butadiene styrene (ABS) and thermoplastic polyurethane (TPU) have been tried [11]. Among all the 3D printing methods, fused deposition modeling (FDM) is probably the most popular method. With the FDM method, various products can be manufactured within a limited time frame with minimal waste. It holds a potential to produce complex geometries [12] [13] [14]. Although it has several advantages, the parts produced with FDM do not have high mechanical strength, high flexibility, and tear resistance [15] . The reasons might be the presence of voids, weaker bonding between the layers, process parameters and the polymer used itself [16] [17]. Most of the polymers which are readily available for FDM 3D printing do not have high mechanical strength, and high flexibility together. To compensate for these drawbacks of the materials, a material having high mechanical strength (e.g., PLA) and another polymer having high flexibility (e.g., TPU) are blended together in different weight percentages (wt %) in this work. Poly(ethylene) glycol (PEG) is used as a plasticizer in varying proportions to enhance the properties of the composite filaments.

Composite materials affect the mechanical and chemical properties of the final product [17] [18][19]. They either improve or degrade the mechanical properties depending on the compatibility between the polymers [20] [21]. Depending on the quantity and type of materials used, the mechanical properties of the final product can be customized [22] [23] [24] [25]. PLA is a biodegradable and renewable thermoplastic polymer that is obtained from renewable resources such as corn, wheat, rice, and sugarcane [26] [27]. The properties such as low thermal stability, high degradation rate during processing, brittleness in nature with less than 10% elongation at break [28] [29], low toughness and moisture sensitivity limit its applications [30] [31]. TPU is a biocompatible, and linear segmented block copolymer [32] [33], and is synthesized by the reaction of polyols with aliphatic or aromatic diisocyanates. The polyols may be ether-, ester-, and carbonate-based diols. These polyols form the soft segments of the material whereas the diisocyanates such as diphenylmethane-4.4-diisocyanate (MDI) make the hard segments of TPU by addition of a chain extender such as butanediol. The soft segment (SS) interconnects two hard segments (HS) and the hard segments are bonded together with the presence of hydrogen bonds to form physical crosslinks [34] [35] [36]. PEG is biocompatible, yields non-immunogenicity, non-antigenicity, protein rejection, and non-toxic [37][38]. PEGs having molecular weight (MW) less than 1000 are viscous, colorless, water soluble and hygroscopic liquids at room temperature. The higher molecular weight PEGs are

waxy white solids. Its melting point is dependent on its molecular weight and exhibits a plateau at about 67 ℃ [39] [40].

Several researchers have worked on PLA/TPU composition for various applications, but the work related to FDM 3D printing of fabrics is not found in the literature. Zhou et. al., studied PC/PLA/TPU blend and found improvement in toughness, increase in flexibility, but decrease in tensile strength and fracture response of the composite [41]. Jaso et. al., investigated the PLA/TPU composition having varying weight percentages (wt%) of poly(lactic) acid (PLA) in TPU matrix and observed improvement in tensile strength, and elongation but decrease in elastic recovery [42]. Mi et. al., produced scaffolds for medical and tissue engineering applications using the PLA/TPU composition. They demonstrated increase in tensile and compressive strength, flexibility and larger pores with the addition of TPU content in the blends [33]. Feng and Ye fabricated tensile and impact specimens using hot-press-molding process with PLA/TPU polymers. They observed yield and neck formation which signifies the improvement of ductile behavior of the composite. They argued the presence of hydrogen bonding between PLA and TPU molecules which caused their partial miscibility [43]. Xu et. al., studied PLA/TPU composites and found the increase in crystallinity and melt strength and confirmed the immiscibility of these polymers [44]. Kaynak et. al., studied the mechanical performance of neat PLA, glass fiber (GF)-reinforced PLA, and TPU-blended PLA composites using injection molding and 3D printing methods. They used twin-screw extruders to obtain filaments for 3D printing using 10 wt% of TPU/ 15 wt% of GF, 3D printed dog-bone specimens and compared their performance with the dog-bone samples obtained from injection molding [45].

It should be noted that no information related to manufacturing of PLA/TPU/PEG composite filaments mixed in different proportions has been found in the literature. The mechanical, thermo-mechanical and morphological characterization of these filaments are missing in the literature as well. In the present work, PLA is blended with TPU and PEG in varying weights to obtain composite filaments with optimal strength and flexibility which can be used for 3D printing of flexible structures. The microstructure, mechanical and thermo-mechanical properties of the composite filaments obtained are investigated and used for 3D printing of plain weave fabric structures in this work.

7.2. Materials and methods

7.2.1. Materials

PLA pellets were purchased from Filabot (Barre VT, USA) having a melt flow index (MFI) of 3 g/10 min at 190℃, density of 1.24 g/cm^3, and the glass transition temperature (T_g) of 55 – 60 ℃ [46]. TPU pellets were supplied by LNS Technologies (Scotts Valley, CA, USA) with the properties such as shore hardness of 90A, density of 1.14 g/cm^3, T_g of – 33 ℃, and melt flow index of 32 g/10 min at 224 ℃ [47]. PEG powder was purchased from Acros Organics (New Jersey, USA) having an average molecular weight of 6000 Dalton.

7.2.2. Sample preparation and filament manufacturing

The pellets were dried in oven at 60 ℃ for 12 hours and then blended in a defined ratio as mentioned in Table 7.1. The polymer blend was fed into twin-screw extruder (Leistritz Mic 18/GL 40D, Nuremberg, Germany) and composite filaments were obtained as shown in Figure 7.1. Seven different temperature zones namely 1 to 7 were allocated on the twin-screw extruder and the temperatures were fixed in the respective order: 155 ℃, 165 ℃, 165 ℃, 175 ℃, 180 ℃, 180 ℃, 170 ℃. The screw speed was set at 30 rpm. The composite filaments produced had varying diameters as listed in Table 7.1.

Table 7.1. Composition and diameters of the filaments manufactured.

Samples	PLA (wt %)	TPU (wt %)	PEG (wt%)	Diameter (mm) (mean ± SD)
PLA	100	0	0	1.73 ± 0.073
PLA_TPU30_PEG0.5	69.5	30	0.5	1.73 ± 0.083
PLA_TPU30_PEG1	69	30	1	1.81 ± 0.070
PLA_TPU30_PEG2	68	30	2	1.80 ± 0.068
PLA_TPU30_PEG3	67	30	3	1.76 ± 0.057
PLA_TPU30_PEG4	66	30	4	1.75 ± 0.093
PLA_TPU30_PEG5	65	30	5	1.80 ± 0.082
PLA_TPU40_PEG0.5	59.5	40	0.5	1.79 ± 0.083
PLA_TPU40_PEG1	59	40	1	1.80 ± 0.066
PLA_TPU40_PEG2	58	40	2	1.78 ± 0.127
PLA_TPU40_PEG3	57	40	3	1.70 ± 0.082
PLA_TPU40_PEG4	56	40	4	1.79 ± 0.156

Note: 7.1. *PLA – Poly(lactic) acid, TPU – Thermoplastic polyurethane, PEG – Poly(ethylene) glycol, and SD – Standard Deviation.*

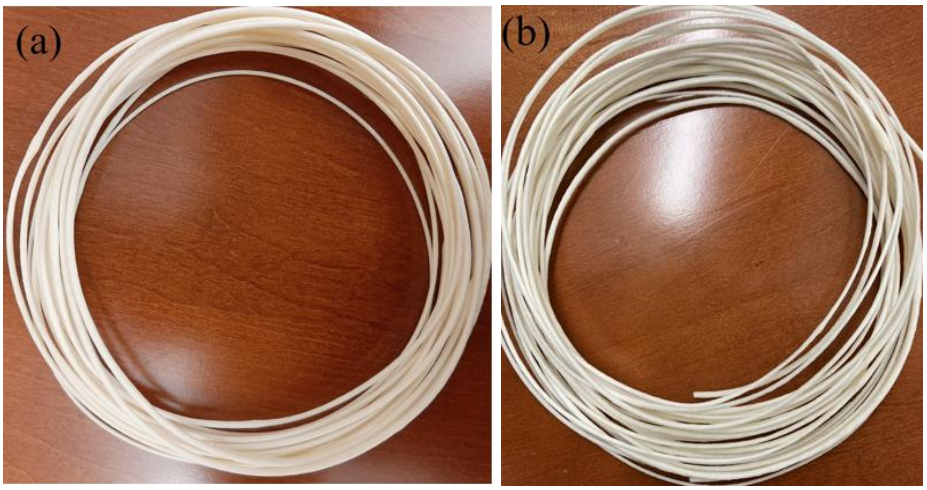

Figure 7.1. Representative composite filaments manufactured: (a) PLA_T40_P3, (b) PLA_T40_P0.5.

7.2.3. Material characterization methods

7.2.3.1. Uniaxial tensile tests of composite filaments

Proper selection of filaments is necessary to precisely predict the mechanical properties of the produced composite filaments. For this purpose, the filaments having diameter as shown in Table 7.1 were considered for the uniaxial tensile tests. Instron 5565 (Norwood, MA, USA) was employed to test the mechanical properties with a load cell of 1 kN, gage length of 50 mm, and crosshead speed of 25 mm/min (Figure 7.2). Five specimens were tested for each composition and the average values were reported.

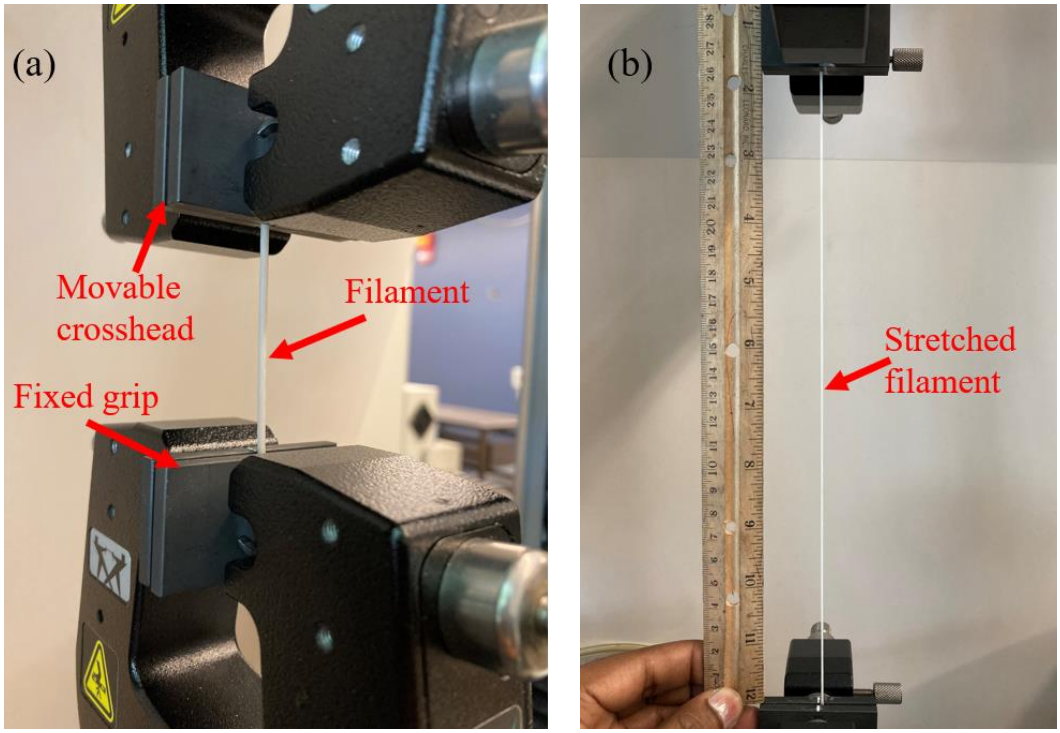

Figure 7.2. Uniaxial tensile testing of composite filaments manufactured. (a) Before extension on the Instron 5565 machine, and (b) After the extension.

7.2.3.2. Differential scanning calorimetry (DSC) analysis

Differential scanning calorimetry (DSC) analysis was conducted using a Q2000 TA instrument. All the experiments were operated under a nitrogen atmosphere at the flow rate of 50 mL/min. The samples, weighing from 5 to 10 mg, were first heated from −70°C to 220°C and then were cooled from 220°C to −70°C and again heated to 220°C at a heating and cooling rate of 10°C/min. The parameters such as glass transition temperature (T_g), melting temperature (T_m), crystallization point, and enthalpies were measured. The first heating cycle was performed to remove the thermal histories of the composite filaments and all data are collected from the second heating and cooling cycles.

7.2.3.3. Thermogravimetric analysis (TGA)

Thermogravimetric analysis (TGA) was conducted using Q500 TA instrument under a nitrogen atmosphere at a flow rate of 60 mL/min. The samples, weighing from 6 mg to 10 mg, were kept in the platinum pan and were heated from room temperature to 700 ℃ at a heating rate of 10 ℃/min.

7.2.3.4. Dynamic mechanical analysis (DMA)

The thermomechanical properties of the samples were evaluated by performing dynamic mechanical analysis (DMA) using an RSA3 TA instrument. The dynamic temperature ramp test was conducted from −50 ℃ to 80 ℃ using the three-point bending fixture (flexural mode) at a ramp rate of 3 ℃/min, frequency of 1 Hz, and strain of 0.5%. Liquid nitrogen was used during the tests to regulate the heating and cooling process. Before conducting the tests, specimens with dimensions 40 mm × 10 mm × 1 mm were manufactured for each composition using the hot press with the temperature set at 200 ℃.

7.2.3.5. Fourier transform infrared spectroscopy (FTIR)

Fourier transform infrared spectroscopy (FTIR) analysis of the composite filaments was performed using a Nicolet 6700 FTIR (ThermoFisher Scientific, Madison, WI, USA). It was conducted for a total of 64 scans with a resolution of 4 cm^{-1} and having the wavenumbers in the range of 400 to 4000 cm^{-1}.

7.2.3.6. Scanning electron microscope (SEM)

Scanning electron microscope (SEM) was used to study the cross-section and surfaces of the composite filaments. The filaments were cryogenically fractured by immersing them in liquid nitrogen to prevent any alteration in the surface morphology. The specimens were gold-sputtered using EMS Q150R sputter coating device since they were non-conductive. The study was performed at different magnifications at an accelerating voltage of 20 kV and a working distance of approximately 10 mm – 15 mm.

7.2.3.7. 3D printing of fabric using composite filament

A 3D model of plain weave fabric structure was constructed using computer aided design (CAD) software, Solidworks® as shown in Figure 7.3. The details of design and construction can be found in ref [12]. The print settings used were infill density of 100%, printing temperature of 225 ℃, and print speed of 10 mm/s.

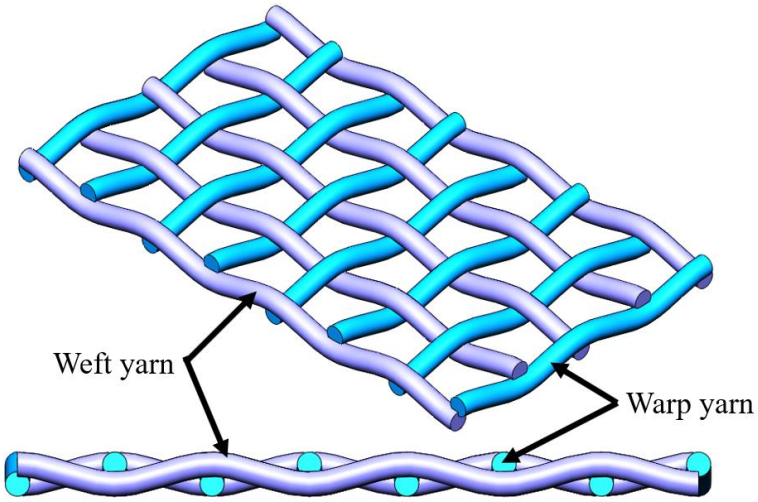

Figure 7.3. CAD model of plain weave fabric for 3D printing.

7.2.3.8. Statistical Analysis

Analysis of variance (ANOVA) test was done for tensile test results by using OriginPro Statistical Software to evaluate the effect of fillers and plasticizers on the composite filaments. All analyses were carried out at 0.05 significance level (i.e., $\alpha = 0.05$). To determine exactly *which* group means are significantly different, a Tukey test was performed.

7.3. Results and discussion

7.3.1. Tensile test results

The tensile tests on pure PLA filaments and composite filaments were conducted, and the results are presented in Figure 7.4, Table 7.2 and Table 7.3. This data show that the yield stress (σ_y) of the composite filaments decreased due to the addition of TPU and PEG. The yield stress of pure PLA filament was found to be 47.52 ± 2.37 MPa, whereas that of other composite filaments were in the range of 26 – 30 MPa. The reason behind the lower yield stress might be the presence of soft segment (SS) of TPU polymers which are elastomeric in nature. The ultimate tensile stress (UTS) of pure PLA filament was determined to be 49.83 ± 1.26 MPa. With the addition of 30 wt% TPU and the varying wt% of PEG, the UTS of composite filaments were in the range of 42 – 58 MPa. Similarly, with the addition of 40 wt% TPU and the varying wt% of PEG, the values of UTS were in the range of 51 – 56 MPa. However, the statistical analysis showed that there is no statistically significant difference in the values of composite filament UTS compared to the pure PLA filament ($p>0.05$). However, a significant drop in the Young's modulus (E) can be seen for all the composite filaments. For composite filaments having 30 wt% TPU and 0.5 wt% PEG, the modulus is decreased by 38.6% compared to that

of pure PLA ($p<0.05$). On applying for the Tukey test, it was found that there is no significant difference between the modulus of PLA_TPU30_PEG0.5 and PLA_TPU30_PEG1. With the addition of 2 and 3 wt % of PEG, the modulus has been increased by 15% and 28.5%, respectively compared to that of PLA_TPU30_PEG0.5, although all the modulus values are still lower than that of pure PLA. The modulus of PLA_TPU30_PEG4 is not significantly different than that of PLA_TPU30_PEG3. The modulus of PLA_TPU30_PEG5 decreased by 7.8% compared to PLA_TPU30_PEG4. The modulus of PLA_TPU40_PEG0.5 decreased by 39.5% compared to that of pure PLA. The statistical analysis showed that there is no significant difference between the modulus of PLA_TPU40_PEG0.5 and PLA_TPU40_PEG1. The modulus of PLA_TPU40_PEG3 and PLA_TPU40_PEG4 decreased by 28.5% and 34.5% respectively, compared to the modulus of pure PLA filament. On the other hand, the % elongation at break is increasing for all the composite filaments. The elongation at break of PLA filament is 4.64% whereas it is 386.75% for PLA_TPU30_PEG0.5 and 486.32% for PLA_TPU40_PEG0.5 filaments. There is no statistically significant difference between the % elongation at break for PLA_TPU30_PEG4 and PLA_TPU30_PEG5 samples ($p>0.05$). The elongation at break of PLA_TPU40_PEG4 filament is 512%. This analysis showed that the addition of 4 wt% PEG in both compositions (30 wt% TPU and 40 wt% TPU) exhibited the optimal mechanical properties. The mechanical properties of composites filaments along with the p-values obtained from multiple comparison using Tukey test is included in Appendix B.

.

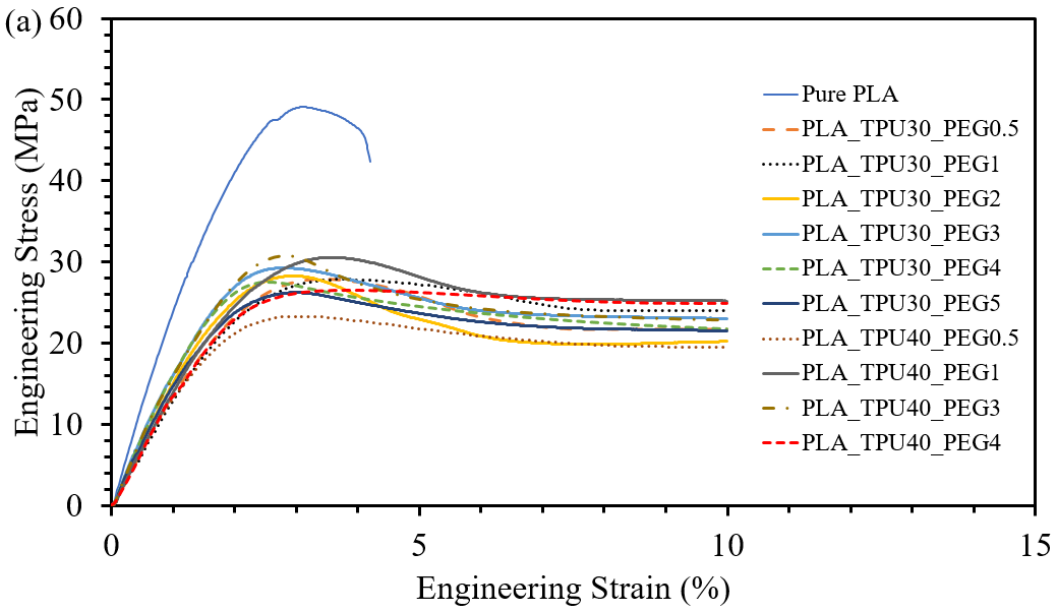

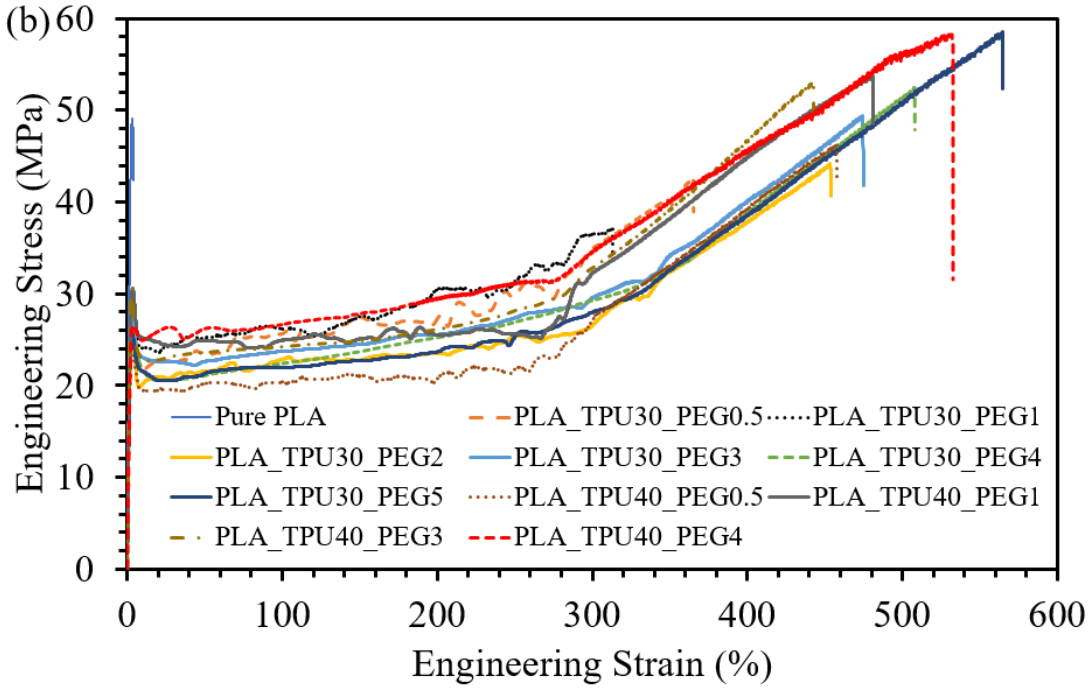

Figure 7.4. Engineering stress – strain curves of pure PLA filaments and composite filaments. (a) Stress-strain curves of PLA and composite filaments up to 10 % of their elongation, and (b) Stress-strain curves of PLA and composite filaments up to their elongation at break.

Table 7.2. Mechanical properties of the composite filaments manufactured with 30 wt% TPU and varying wt% PEG (mean ± standard error).

Samples	Yield Stress (σ_y) (MPa)	Ultimate Tensile Stress (UTS) (MPa)	Young's Modulus, E (MPa)	Elongation at break (%)
Pure PLA	47.52 ± 2.37	49.83 ± 1.26	2511.77 ± 115.50	4.64 ± 0.16
PLA_TPU30_PEG0.5	27.78 ± 1.45	45.20 ± 2.16	1541.71 ± 46.83	386.75 ± 8.55
PLA_TPU30_PEG1	27.74 ± 3.12	42.22 ± 2.80	1470.16 ± 129.68	350.61 ± 14.73
PLA_TPU30_PEG2	28.04 ± 2.15	47.16 ± 2.32	1773.04 ± 66.80	477.79 ± 13.00
PLA_TPU30_PEG3	29.10 ± 3.69	50.27 ± 3.47	1982.63 ± 73.71	477.74 ± 22.91
PLA_TPU30_PEG4	27.33 ± 1.25	55.36 ± 0.77	1849.22 ± 76.99	530.41 ± 6.40
PLA_TPU30_PEG5	26.10 ± 2.65	58.78 ± 2.73	1705.34 ± 41.89	562.07 ± 22.45

Table 7.3. Mechanical properties of the composite filaments manufactured with 40 wt% TPU and varying wt% PEG (mean ± standard error).

Samples	Yield Stress (σ_y) (MPa)	Ultimate Tensile Stress (UTS) (MPa)	Young's Modulus, E (MPa)	Elongation at break (%)
Pure PLA	47.52 ± 2.37	49.83 ± 1.26	2511.77 ± 115.50	4.64 ± 0.16
PLA_TPU40_PEG0.5	23.00 ± 4.36	51.63 ± 3.50	1518.85 ± 73.20	486.32 ± 10.94
PLA_TPU40_PEG1	30.44 ± 5.33	54.94 ± 2.01	1548.20 ± 80.48	495.82 ± 6.26
PLA_TPU40_PEG3	30.70 ± 3.75	55.90 ± 2.32	1796.84 ± 60.60	460.85 ± 7.71
PLA_TPU40_PEG4	26.05 ± 2.60	55.34 ± 1.28	1643.45 ± 128.80	512.79 ± 6.02

7.3.2. DSC results

The study of thermal properties of materials becomes crucial for applications in thermal environments and for this purpose, DSC was used in this research. The DSC curves showing the heat/cool/heat cycles of neat PLA is shown in Figure 7.5 and that for other polymer samples are presented in Appendix C. The properties obtained from the cooling and second heating cycle are presented in Table 7.4 and the properties obtained from the first heating cycle is presented in Appendix D. The important phases such as glass transition temperature (T_g), cold crystallization temperature (T_{cc}), cold crystallization enthalpy (ΔH_{cc}), melting temperature (T_m), and enthalpy of fusion (ΔH_m) are evaluated using the heating cycle whereas the crystallization temperature (T_c) and enthalpy of crystallization (ΔH_c) are obtained from the cooling cycle.

The T_g of neat PLA is 59 ℃, which remains almost the same for all the samples. This result implies that adding 30 wt% or 40 wt% TPU and varying wt% of PEG is not showing significant change in the T_g of the whole composition. This might have happened because the T_g of neat TPU is around –30 ℃, and that of PEG is around −15 ℃ [48]. Therefore, TPU and PEG are already in rubbery state and hence do not either assist or hinder the molecular chain mobility of PLA.

The cold crystallization peaks are visible for all the samples, and these are exothermic in nature. The T_{cc} and associated enthalpy for neat PLA are 134 ℃ and 6.8 J/g, respectively. With the addition of TPU and PEG, the T_{cc} has been decreased for all the samples whereas ΔH_{cc} found to be increased. For example, PLA_TPU30_PEG5 has a T_{cc} of 124 ℃ and ΔH_{cc} of

12.24 J/g. Similarly, PLA_TPU40_PEG4 has a T_{cc} of 120 ℃ and ΔH_{cc} of 13.12 J/g. Cold crystallization peaks are visible when the polymer chains do not get enough time to fully get ordered. It appears after the glass transition temperature when the chains get a chance to move and get ordered. Crystallization peak is visible during the cooling cycle which happens due to the polymer chain mobility and ordering in the material [49] [50]. The enthalpy of crystallization shows the energy used during crystallization by the polymer. This can be interpreted as a direct proportional relation with the number of crystalline structures. The higher the enthalpy, the higher the number of crystalline structures. From Table 7.4, it is evident that ΔH_c is quite low for all the composite filaments. It clearly indicates that the chains of the polymers in the composites are not getting enough time to get fully ordered and therefore experience low crystallization. That's why the exothermic cold crystallization peaks were visible. To solve this issue, lower cooling and heating rates may be applied.

The endothermic melting peaks appear after the exothermic cold crystallization peaks. The melting temperature of neat PLA is 154 ℃ and the enthalpy of fusion is 8.76 J/g. The melting temperatures found to be decreased slightly whereas the enthalpy of fusion (ΔH_m) increased for all the composites. For example, PLA_TPU30_PEG5 has T_m of 151.48 ℃ and ΔH_m of 13.78 J/g. Likewise, PLA_TPU40_PEG4 has T_m of 150.81 ℃ and ΔH_m of 14.01 J/g. The increase in enthalpy might have happened due to the alignment of chains during cold crystallization phase. An ordered polymeric chain will require higher energy to break down and melt than the unordered chains.

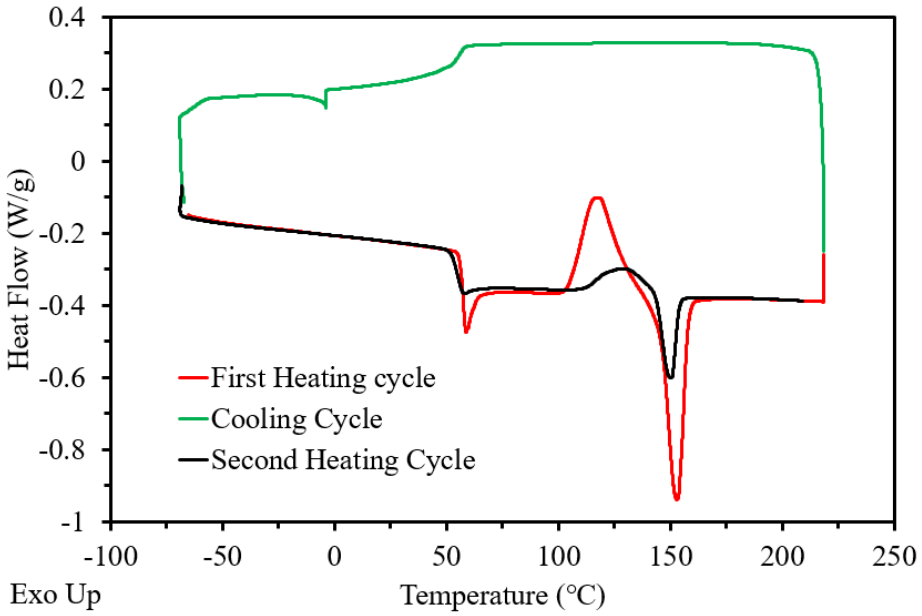

Figure 7.5. Heat/Cool/Heat Cycle of PLA.

Table 7.4. Summary of DSC results of the composite filaments**.**

Samples	T_g (℃), PLA	T_{cc} (℃)	ΔH_{cc} (J/g)	T_m (℃)	ΔH_m (J/g)	T_c (℃)	ΔH_c (J/g)
PLA	59.52	134.11	6.803	154.36	8.76	–	–
PLA_TPU30_PEG0.5	59.53	122.67	13.05	153.13	15.48	96.29	2.11
PLA_TPU30_PEG1	59.28	124.75	13.69	151.32	16.80	97.11	2.18
PLA_TPU30_PEG2	59.60	123.96	11.71	150.98	17.31	93.35	1.95
PLA_TPU30_PEG3	58.25	125.74	12.23	152.34	17.48	93.21	1.55
PLA_TPU30_PEG4	58.69	124.71	12.29	150.50	17.28	88.80	1.54
PLA_TPU30_PEG5	59.47	124.00	12.24	151.48	13.78	86.32	1.25
PLA_TPU40_PEG0.5	59.51	122.15	11.12	150.71	14.35	97.78	2.37
PLA_TPU40_PEG1	59.83	124.76	11.03	150.99	13.17	97.05	2.97
PLA_TPU40_PEG2	58.84	119.22	17.56	150.55	17.93	96.81	1.77
PLA_TPU40_PEG3	59.22	120.52	12.28	150.50	15.54	92.99	1.98
PLA_TPU40_PEG4	58.52	120.32	13.12	150.81	14.01	91.27	1.98

Note: 7.2. $\boldsymbol{T_g}$ – glass transition temperature; $\boldsymbol{T_{cc}}$ – cold crystallization temperature; $\Delta\boldsymbol{H_{cc}}$ – cold crystallization enthalpy; $\boldsymbol{T_m}$ – melting temperature; $\Delta\boldsymbol{H_m}$ – enthalpy of fusion; $\boldsymbol{T_c}$ – crystallization temperature; $\Delta\boldsymbol{H_c}$ – enthalpy of crystallization.

7.3.3. DMA results

The thermo-mechanical behavior of PLA and the composite filaments were studied using dynamic mechanical analysis (DMA) test method. The storage modulus (E'), loss modulus (E''), and *tanδ* curves as a function of temperature are shown in Figure 7.6. Storage modulus is related to the Young's modulus and indicates the stiffness of a material. It represents the tendency of a material to store energy applied on it [51]. The E' of PLA was higher than all other polymer compositions. It implies that PLA has a higher stiffness. With the addition of TPU and PEG in varying weight percentages, it was found that the storage modulus decreased for all the polymeric composite filaments. The decrease in rigidity and stiffness of composite filaments might have happened due to the presence of soft segments (SS) in TPU which caused increased flexibility of molecular chains. In addition, the plasticizing effect of PEG in the blend might have also contributed to decrease in modulus.

Loss modulus represents the viscous behavior of a material and its tendency to dissipate energy applied to it [51]. The initial loss modulus is lower for PLA filaments than other composites. This result represented that there was a change in polymer motion [52] and an increase in TPU and PEG content increased the molecular friction which might be the reason for higher loss modulus of the composite filaments. It should be noted that E'' depends on different molecular motions, transition, morphology and structural heterogeneities [51].

Tanδ denotes the damping factor of the materials and is defined as the ratio of loss modulus to storage modulus ($tan\delta = {}^{E''}/_{E'}$). Generally, the maximum value of the curve occurs at the glass transition temperature of the materials. It can be observed that PLA has only one peak near 60℃ which represents its T_g. Composites have two peaks indicating the presence of two glass transition temperatures. The lower temperature close to -40℃ indicates the T_g of TPU and the higher temperature at 60℃ indicates the T_g of PLA. The T_g of PEG is not observed clearly. The appearance of different peaks is an indication of phase separation between the polymers [53]. It can be said that all the materials showed a broad $tan\delta$ peak due to several relaxation mechanisms occurring in the system. This fact showed that these materials contain damping properties and the composition can also be used in shock absorbers and isolators [54].

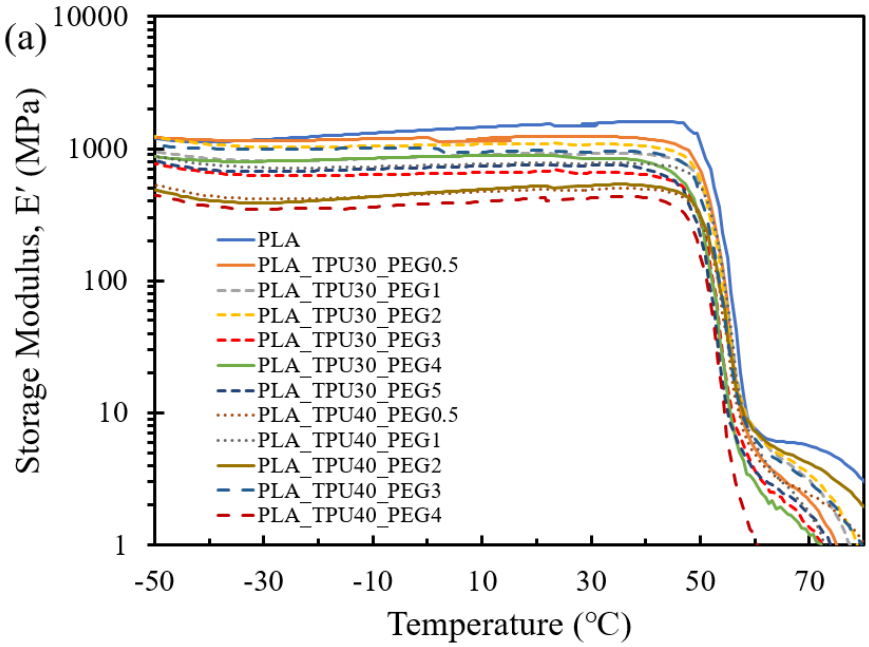

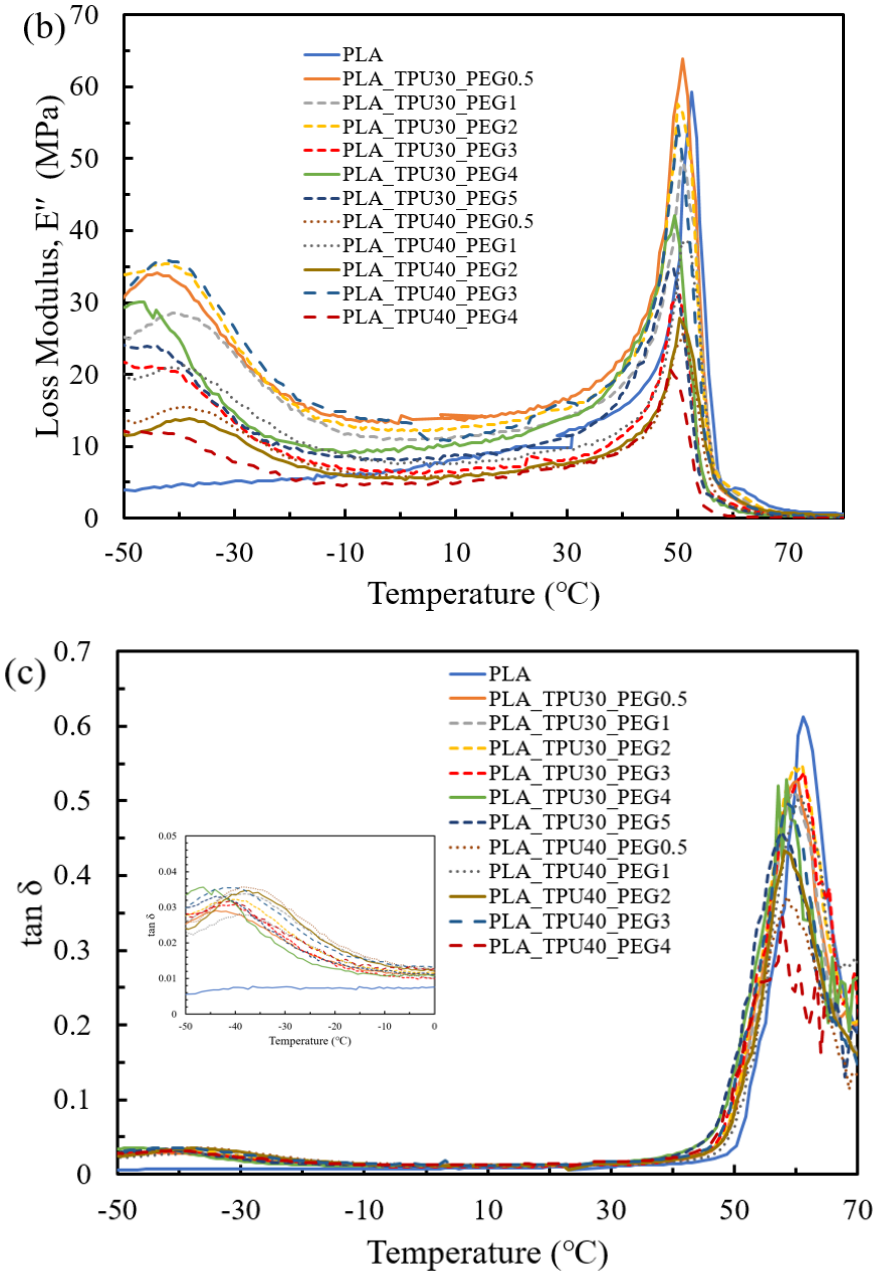

Figure 7.6. Thermo-mechanical analysis of composite filaments. (a) E' versus temperature, (b) E'' versus temperature, and (c) $tan\delta$ versus temperature.

7.3.4. TGA results

TGA is a useful method to understand the thermal degradation behavior of the substances [55]. The loss of mass and rate of loss at different temperatures help to determine the application of substances in thermal environments. The thermogravimetric (TG) and derivative thermogravimetric (DTG) curves of pure PLA filaments and composite filaments are shown in Figure 7.7. The effects of fillers and plasticizers in PLA matrix on thermal degradation was studied. Neat PLA is observed to be more stable than all the composite

materials. The onset thermal degradation temperature (T_{onset}) of neat PLA is 312 ℃. Similarly, the maximum thermal degradation temperature (T_{max}) is 363 ℃ at which about 96% of the weight is lost. The final thermal degradation temperature (FDT) is 380 ℃ and the char residues are only 3.13% of the initial weight (Table 7.5). With the addition of TPU and PEG, the onset temperature and maximum temperature decreased compared to pure PLA. This shows their rapid degradation behavior and lower thermal stability. The char residues of all the composites at 700 ℃ are almost negligible. This happened due to the lower decomposition temperature of TPU [41]. However, the final degradation temperatures of all the composites are higher than pure PLA. The DTG curves show multiple peaks which demonstrates that the TPU has different functional groups and structural elements having different decomposition temperatures. All the composites have similar thermal stability and degradation behavior. The composites followed similar residual weight plateau after 400 ℃. Hence, it can be said that these composites can be used in applications where the temperature does not rise over 285 ℃. In case of pure TPU filaments, it is suitable for applications below 270 ℃ around which its onset thermal degradation temperature lies.

Table 7.5. Characteristic temperatures of the composite filaments obtained from TGA.

Samples	T_{onset} (℃)	T_{max} (℃)	FDT (℃)	Char % at 700 ℃
PLA	312	363	380	3.13
PLA_TPU30_PEG0.5	290	323	610	0
PLA_TPU30_PEG1	290	327	525	0
PLA_TPU30_PEG2	290	327	580	0
PLA_TPU30_PEG3	293	328	390	0
PLA_TPU30_PEG4	290	325	560	0
PLA_TPU30_PEG5	285	325	400	0
PLA_TPU40_PEG0.5	290	327	538	7.91
PLA_TPU40_PEG1	293	323	580	0
PLA_TPU40_PEG2	300	330	600	0
PLA_TPU40_PEG3	295	323	620	0
PLA_TPU40_PEG4	300	326	600	1.45
TPU	273	280, 335, 420	450	4.42

Note: 7.3. $\boldsymbol{T_{onset}}$ is the onset thermal degradation temperature, $\boldsymbol{T_{max}}$ is the maximum thermal degradation temperature, and FDT is the final thermal degradation temperature.

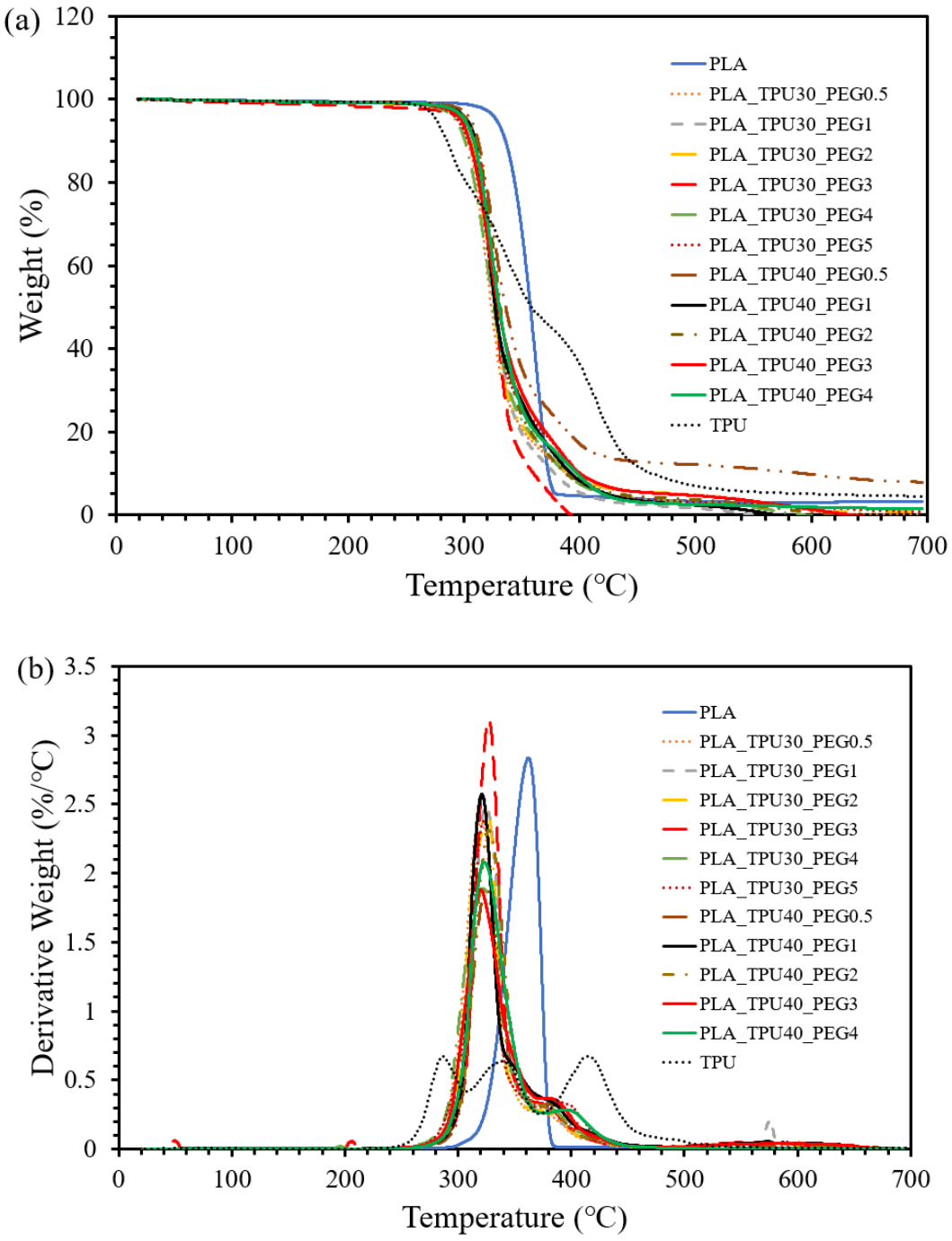

Figure 7.7. TGA thermograms of PLA filament, and the composite filaments manufactured. (a) TG curves showing the percentage weight loss of the composition at different temperatures, and (b) DTG curves showing the rate of weight loss.

7.3.5. FTIR results

To determine the functional groups of the polymers in the composites, FTIR spectroscopy was performed, and the results are shown in Figure 7.8. The spectra of the composite filaments having 30 wt% TPU, and varying wt% of PLA and PEG is shown in Figure 7.8a whereas the spectra of the composite filaments having 40 wt% TPU and varying wt% of PLA and PEG is shown in Figure 7.8b. The functional groups associated with their wavenumber and intensity of PLA and TPU are listed in Table 7.6.

For pure TPU, a medium peak at 3298 cm^{-1} corresponds to the stretching vibration of NH in urethane group. The spectrum also exhibits characteristic bands at 2848 cm^{-1} and 2921 cm^{-1}, attributed to the presence of Poly(tetramethylene glycol) (PTMG) [56]. PTMG forms the soft segment (SS) of the material. Soft segments provide flexibility and elastomeric behavior. They may be either polyester or polyether and interconnect two hard segments (HS) of the material. They are bonded together with the presence of hydrogen bonds and form physical crosslinks [34] [35] [57]. The bands at 1700 cm^{-1} and 1733 cm^{-1} are due to the stretching vibration (amide I band) of C=O carbonyl compound. The peak at 1637 cm^{-1} resembles the presence of stretching vibration of C=C bonds in the aromatic ring, whereas the peak at 815 cm^{-1} shows the presence of C–H out-of-plane bending in aromatic ring. The peaks at 1530 cm^{-1} and 1560 cm^{-1} show the N–H bending vibration (amide II band). The presence of peak at 1311 cm^{-1} was due to C–N (amide III band) stretching vibration. The bands at 1218 cm^{-1} and 1106 cm^{-1} were due to C−O−C stretching vibration in esters and ethers, respectively.

For neat PLA, two peaks of medium intensity at 2852 cm^{-1} and 2925 cm^{-1} can be seen which is due to the presence of asymmetric and symmetric stretching vibration of CH_3 whereas the peak at 1452 cm^{-1} was due to CH_3 antisymmetric bending vibration. A signal of strong intensity at 1750 cm^{-1} is attributed to the C=O stretching vibration. The peaks at 1359 cm^{-1} and 1382 cm^{-1} shows the deformation and symmetric mode of CH group. The peaks at 1043, 1080, 1128, and 1180 cm^{-1} are due to C−O−C stretching vibration.

In the composite filaments, the intensity of peaks in the range of 2850 to 2950 cm^{-1} has decreased. This might be because of the lower weight percentages of TPU in the composition. This is the range for PTMG which provides flexibility and elastomeric behavior to the materials. Due to lower weight percentages, the flexibility will be lower than that of pure

TPU. There are not any notable changes observed at around 3300 cm^{-1}. Almost similar intensity of peaks is seen at around 1750 cm^{-1}, which might be due to the presence of C=O stretching vibration in both TPU and PLA. Since the amount of PEG added is very low compared to the other two polymers, its effect has not been noted significantly on the spectra. From these spectra, it can be said that the composite samples contain all polymer properties.

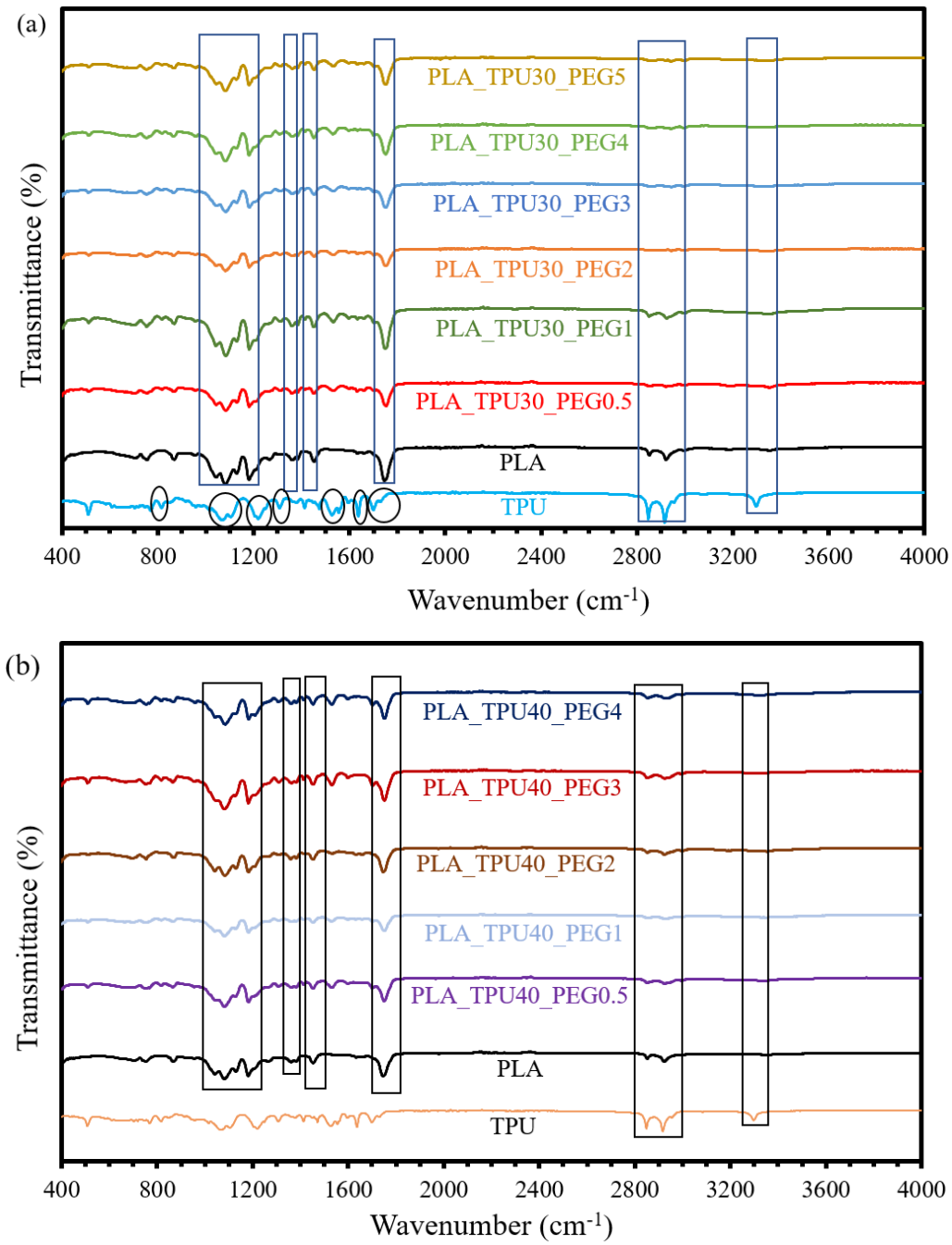

Figure 7.8. FTIR spectra of PLA, TPU and composite filaments. (a) The composite filaments have 30 wt% TPU and varying wt% of PLA and PEG, (b) The composite filaments have 40 wt% TPU and varying wt% of PLA and PEG.

Table 7.6. FTIR spectra of PLA, TPU and PEG polymers used in this study [55] [56].

Material	Wavenumber (cm^{-1})	Assignment
TPU	3298	Stretching vibration of NH in urethane group .
	2848 and 2921	Presence of Poly(tetramethylene glycol) (PTMG), known as Soft Segment (SS).
	1700 and 1733	C=O stretching vibration (amide I band).
	1637	C=C stretching vibration in the aromatic ring.
	1530 and 1560	N–H bending vibration (amide II band).
	1311	C–N (amide III band) stretching vibration.
	1218	C−O−C stretching vibration in esters.
	1106	C−O−C stretching vibration in ethers.
	815	C–H out-of-plane bending in aromatic ring.
PLA	2852 and 2925	Asymmetric and symmetric stretching vibration of CH_3.
	1750	C=O stretching vibration.
	1452	CH_3 antisymmetric bending vibration.
	1359 and 1382	Deformation and symmetric mode of CH group.
	1043, 1080, 1128, and 1180	C−O−C stretching vibration.

7.3.6. Scanning electron microscopy (SEM)

The SEM images of the cross-section of cryogenically fractured PLA and composite filaments are shown in Figure 7.9. The cross-section of PLA filaments appears flat with little roughness and showed brittle failure (Figure 7.9a). The addition of 30 wt% TPU and 2 wt% PEG caused an increase in spherical aggregates and voids in the cross-section (Figure 7.9b). Mi et. al., also observed similar surface morphology in the PLA/TPU blend [33]. The aggregates are shown by arrows and voids by dotted circles. The aggregates are uniformly distributed on the cross-section, which have been appeared due to the coalescence of TPU particles. The increase in TPU particles increases the flexibility of the filaments, which is seen in tensile tests. However, the formation of TPU aggregates is the indication of phase separation between PLA matrix and TPU additives, which is also seen in tan δ curves during DMA tests. The voids are present on the fractured surface, which might have occurred due to poor adhesion

between the PLA matrix, TPU additive and PEG plasticizer. This further provides evidence of phase separation and immiscibility of these polymers. On further increasing the PEG content to 5 wt%, the TPU aggregates and void formation was reduced (Figure 7.9c). This might have happened due to the bonding between the polymers. As a result, the elongation has increased during tensile tests. With the addition of 40 wt% TPU, the flexibility of the composite filaments increased. This is due to the hydrogen bond formation between PLA and TPU [43]. The uniform dispersion of TPU aggregates and voids are seen in Figure 7.9d, which are reduced with the addition of 4 wt % PEG.

Figure 7.10a shows a smooth surface with little roughness of PLA filament. The roughness might have occurred by stretching during the extrusion process. On the other hand, the composite filaments (Figure 7.10 b-e) exhibit rough surfaces and fine chiplets can be seen clearly. This happened due to the presence of PEG and TPU in the PLA matrix, which are immiscible. This also proves that they have poor compatibility and possess phase separation.

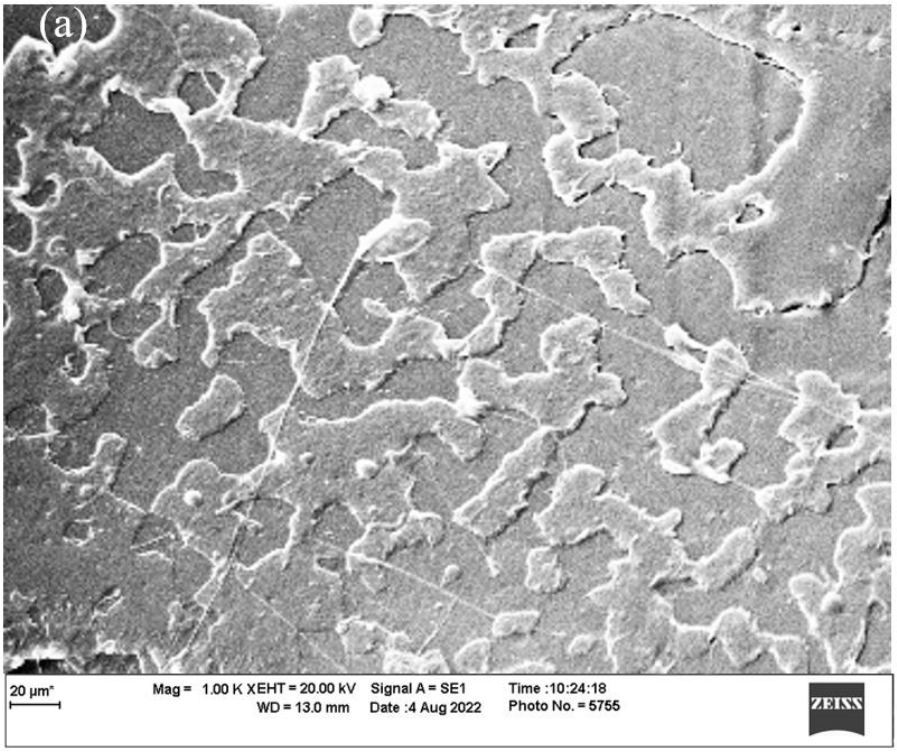

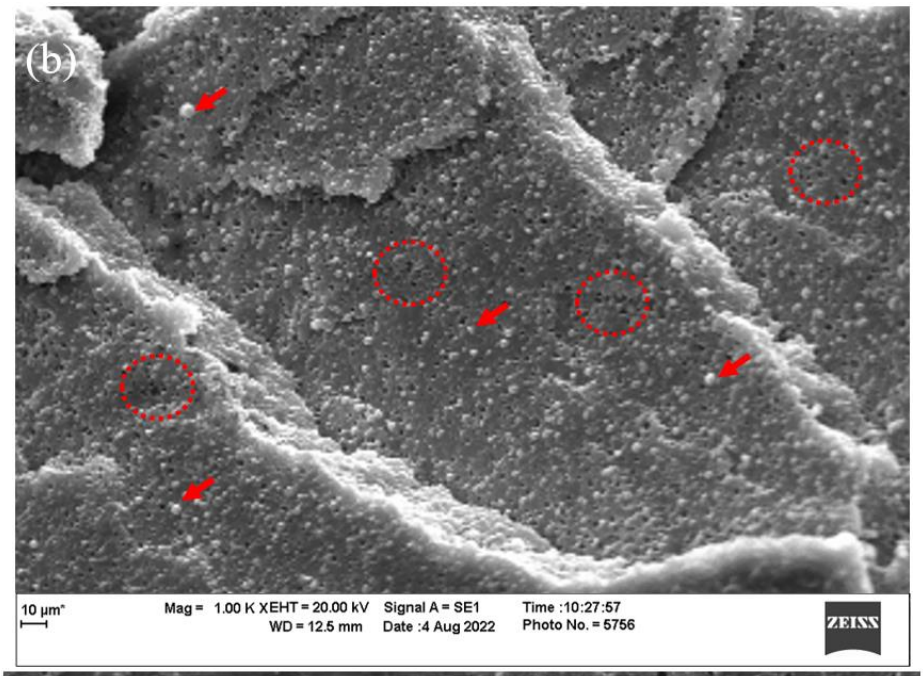
(b)
10 µm
Mag = 1.00 K XEHT = 20.00 kV
WD = 12.5 mm
Signal A = SE1
Date :4 Aug 2022
Time :10:27:57
Photo No. = 5756
ZEISS

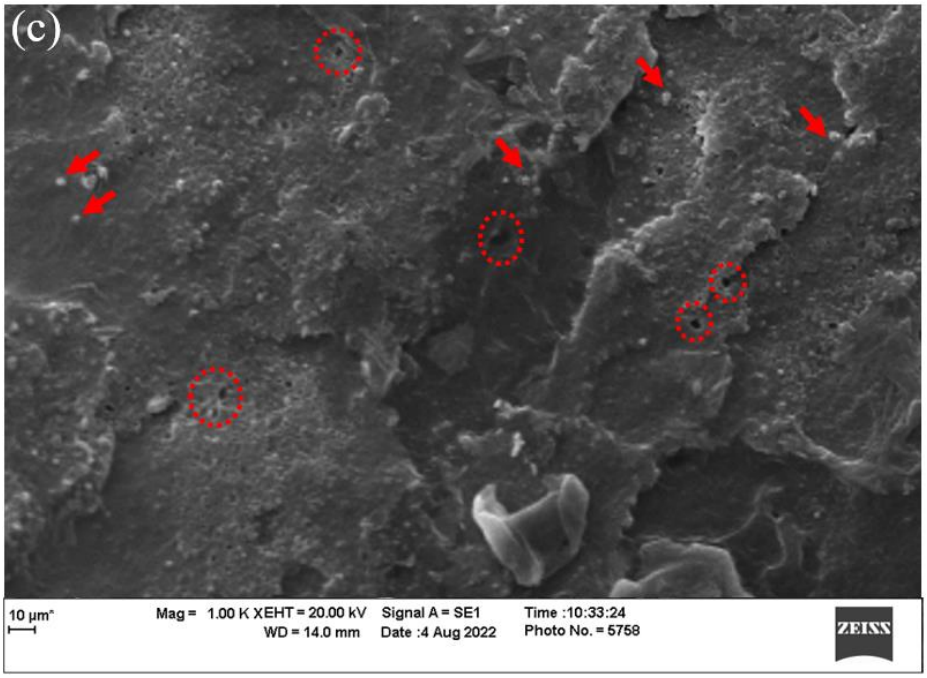
(c)
10 µm
Mag = 1.00 K XEHT = 20.00 kV
WD = 14.0 mm
Signal A = SE1
Date :4 Aug 2022
Time :10:33:24
Photo No. = 5758
ZEISS

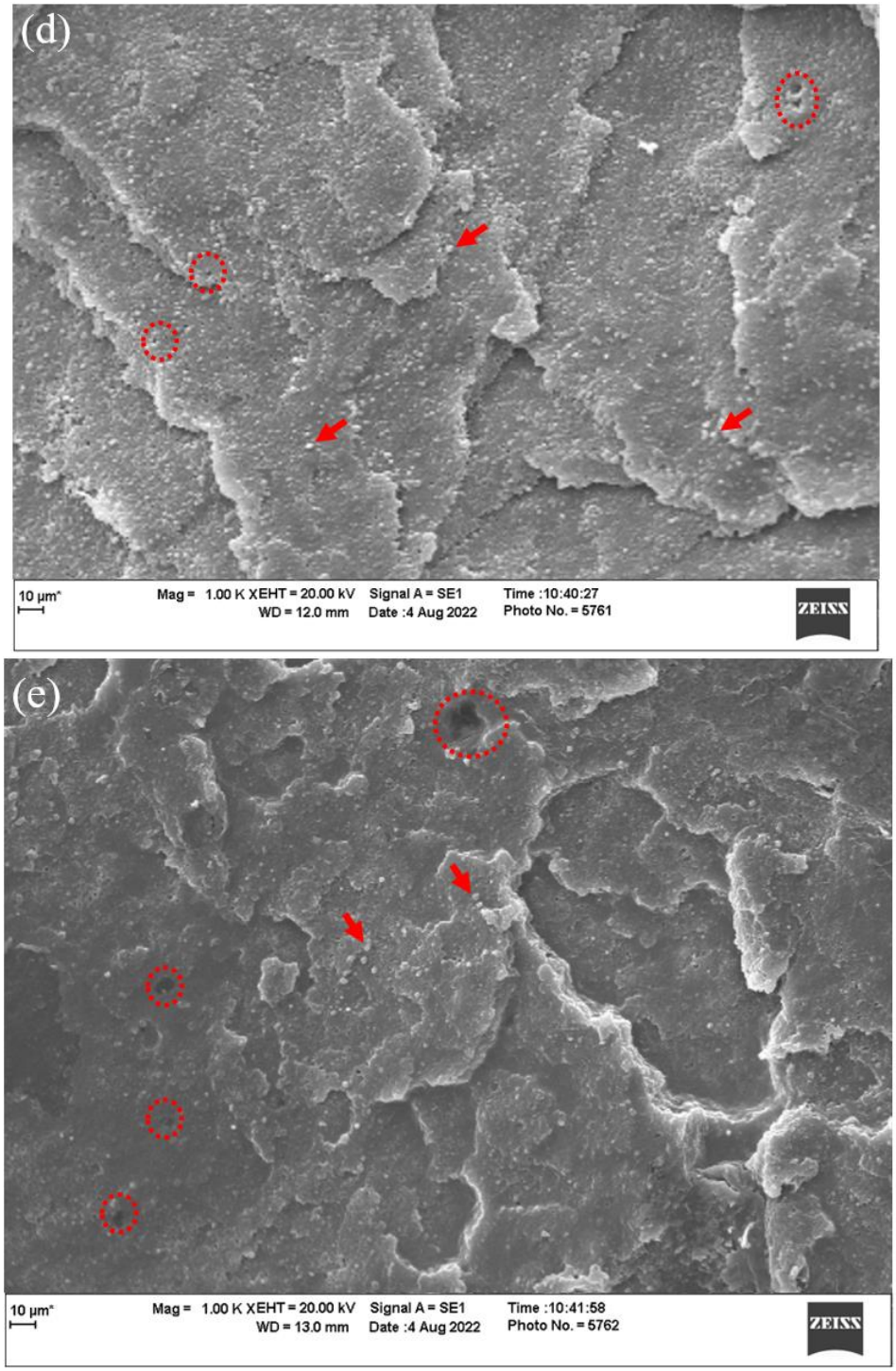

Figure 7.9. SEM images showing cross-sections of (a) PLA, (b) PLA_TPU30_PEG2, (c) PLA_TPU30_PEG5, (d) PLA_TPU40_PEG1, (e) PLA_TPU40_PEG4. The aggregates are shown by arrows and voids by dotted circles.

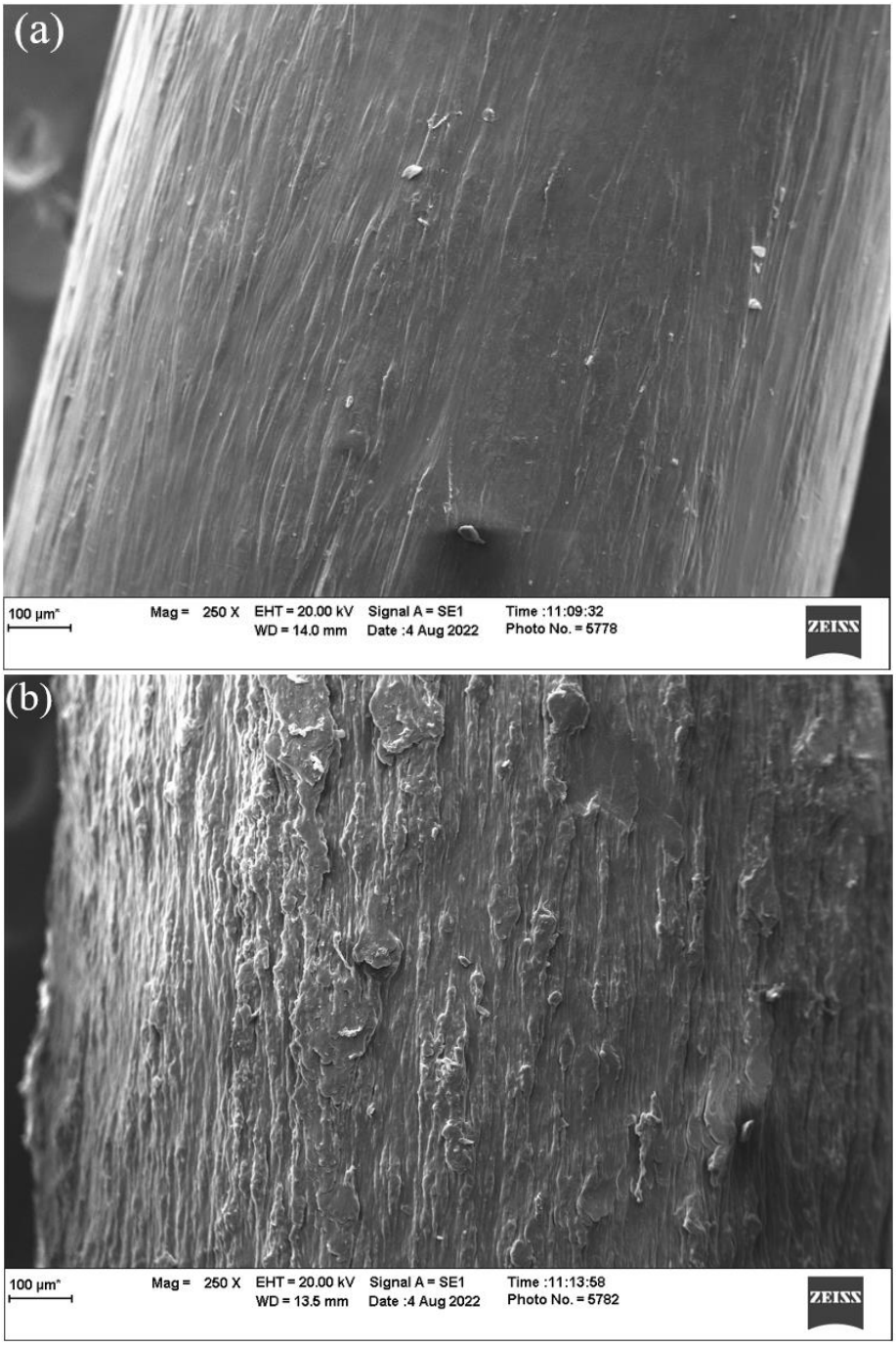
(a)
100 µm
Mag = 250 X
EHT = 20.00 kV
WD = 14.0 mm
Signal A = SE1
Date :4 Aug 2022
Time :11:09:32
Photo No. = 5778
ZEISS
(b)
100 µm
Mag = 250 X
EHT = 20.00 kV
WD = 13.5 mm
Signal A = SE1
Date :4 Aug 2022
Time :11:13:58
Photo No. = 5782
ZEISS

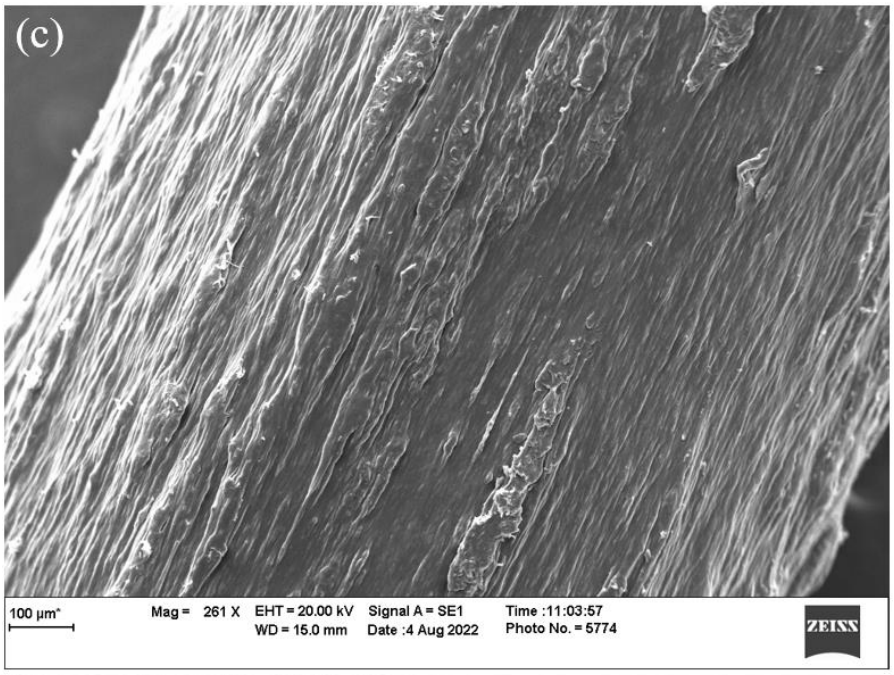
(c)
100 µm*
Mag = 261 X
EHT = 20.00 kV
WD = 15.0 mm
Signal A = SE1
Date :4 Aug 2022
Time :11:03:57
Photo No. = 5774
ZEISS

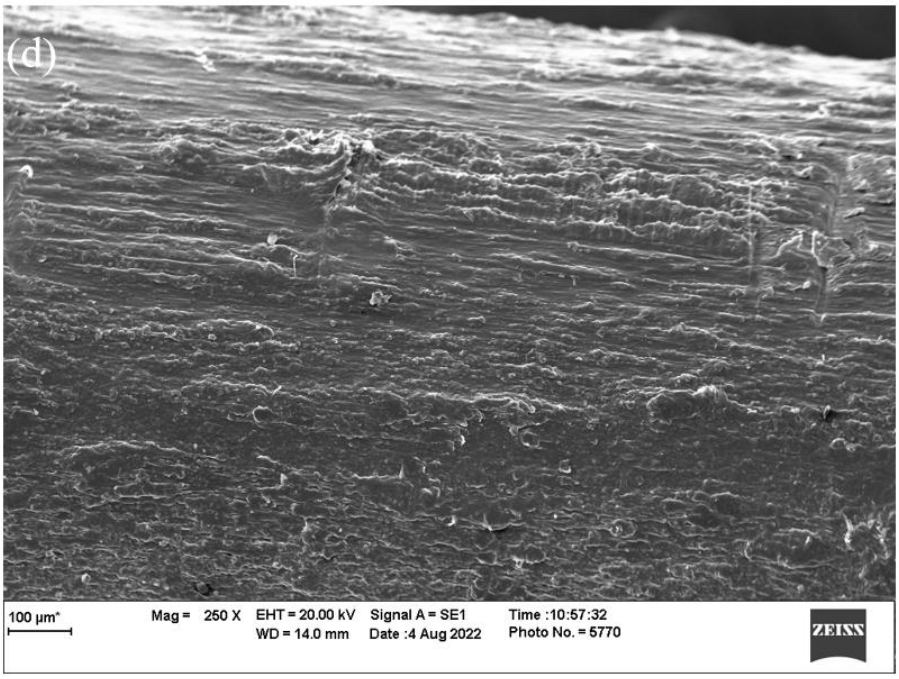
(d)
100 µm*
Mag = 250 X
EHT = 20.00 kV
WD = 14.0 mm
Signal A = SE1
Date :4 Aug 2022
Time :10:57:32
Photo No. = 5770
ZEISS

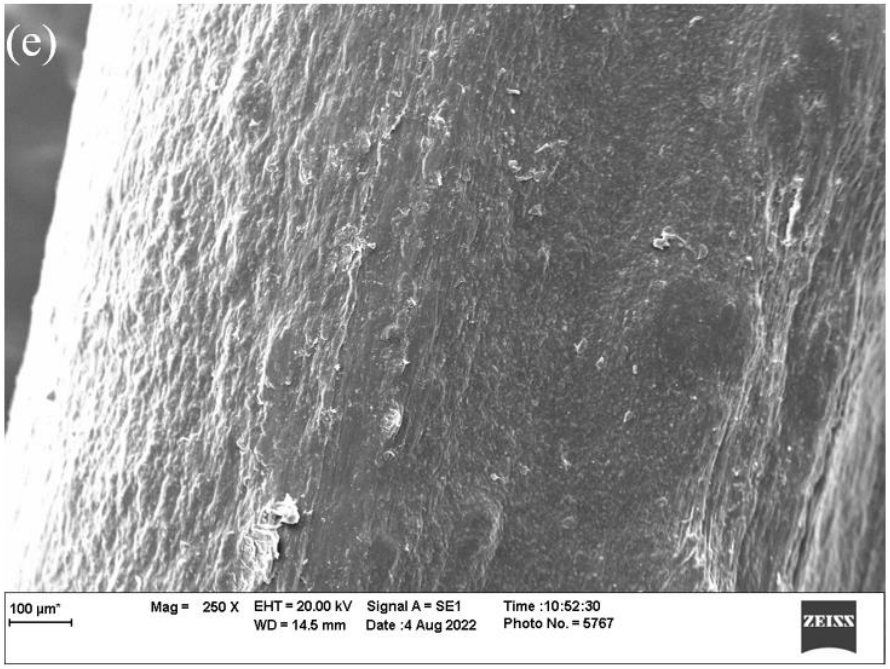

Figure 7.10. SEM images showing the surfaces of (a) PLA, (b) PLA_TPU30_PEG2, (c) PLA_TPU30_PEG5, (d) PLA_TPU40_PEG1, and (e) PLA_TPU40_PEG4.

7.3.7. 3D printed fabric structure

A plain weave fabric structure (Figure 7.11) having 8 warp yarns and 5 weft yarns was 3D printed in horizontal orientation using the PLA_TPU_30_PEG5 composite filament. The spacing between the yarns is 10 mm. The width of the 3D printed fabric is 70 mm along weft direction whereas the length is 40 mm along the warp direction. Several fibrils can be seen in the printed part. A weft yarn as indicated by an ellipse is broken while 3D printing. The inconsistency in warp yarns is clearly visible indicated by the arrows. The reason for this is the non-uniform extrusion of filament during the printing process, which happened due to the inconsistent diameter of filament that was produced using the extruder. This defect in the filament affected the print quality, dimensional accuracy, and the overall properties of the printed parts. The work related to improving the print quality and fabric properties will be considered in our future research.

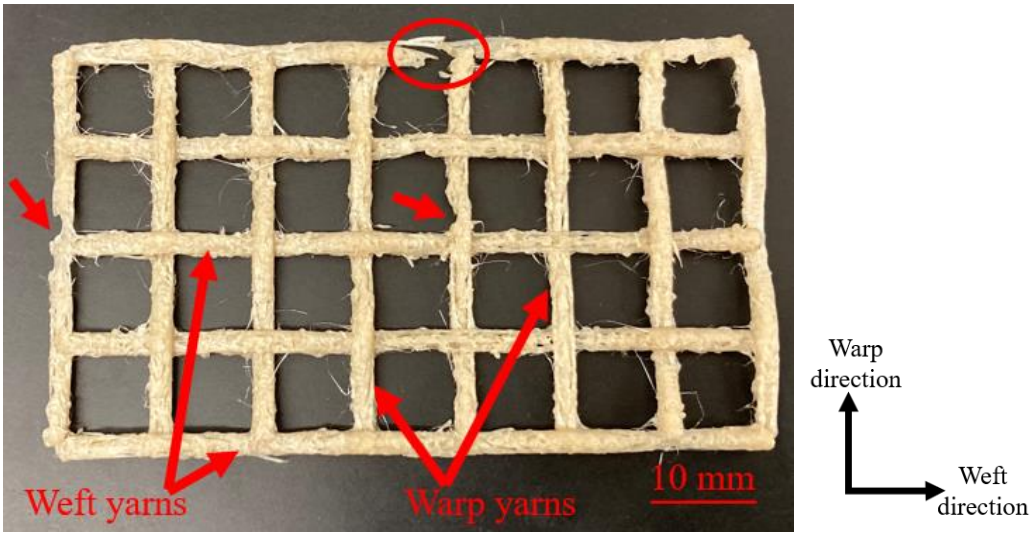

Figure 7.11. 3D printed plain weave fabric structure using PLA_TPU30_PEG5 composite filament.

7.4. Conclusions

Different polymers such as PLA, TPU and PEG are blended in different proportions and extruded to obtain composite filaments. The amount of TPU content in the composition is kept constant either being 30% or 40%. PLA and PEG are added in varying weight percentages. The filaments produced had varying diameters, but the optimal range was considered for this study. The following conclusions can be drawn from this work:

(i) The tensile test results showed that the yield stress of the composite filaments decreased significantly but the ultimate tensile stress was in the same range compared to pure PLA filament. Moreover, the Young's modulus of composite filaments also decreased compared to pure PLA filament whereas the elongation at break increased by more than 550%. This reveals the fact that the flexibility and ductility of composites increased which might be due to the presence of soft segments in TPU.

(ii) The thermal analysis showed that the glass transition temperature of PLA filament is almost the same in all the composites, which was observed using DSC. TGA results revealed that the onset thermal degradation temperature of composite filaments was around 285 °C which is slightly lower than that of pure PLA filament.

(iii) The thermo-mechanical tests demonstrated that pure PLA filaments hold higher storage modulus than composite filaments. This implies that pure PLA filament is stiffer than composite filaments. The increase in TPU and PEG content make the filaments flexible and results in lower storage modulus. On the other hand, the initial loss modulus of the

pure PLA filament is the lowest. The increase in TPU and PEG content enhanced the molecular friction which might have caused higher loss modulus of the composite filaments.

(iv) The FTIR spectroscopy revealed that there is not any additional chemical bonding between the polymers which can affect their properties.

(v) The 3D printed plain weave fabric structure using the fused deposition modeling method with PLA_TPU30_PEG5 composite filament demonstrated the feasibility of these filaments in the 3D printing of complex structures.

7.5. References

[1] C. W. Hull, "Apparatus for Production of Three-Dmensonal Objects By Stereo Thography," 4, 575, 330, 1984.

[2] D. A. Arcos-Novillo and D. Güemes-Castorena, "Development of an additive manufacturing technology scenario for opportunity identification—The case of Mexico," *Futures*, vol. 90, pp. 1–15, 2017, doi: 10.1016/j.futures.2017.05.001.

[3] R. Melnikova, A. Ehrmann, and K. Finsterbusch, "3D printing of textile-based structures by Fused Deposition Modelling (FDM) with different polymer materials," *IOP Conf. Ser. Mater. Sci. Eng.*, vol. 62, no. 1, pp. 1–6, 2014, doi: 10.1088/1757-899X/62/1/012018.

[4] L. Partsch, S. Vassiliadis, and P. Papageorgas, "3D Printed Textile Fabrics Structures," *5th Int. Istanbul Text. Congr. 2015 Innov. Technol. "Inspire to Innov.*, no. September, pp. 3–10, 2015.

[5] K. Lussenburg, N. Van Der Velden, Z. Doubrovski, J. Geraedts, and E. Karana, "Designing with 3D Printed Textiles," *Proc. 5th Int. Conf. Addit. Technol.*, pp. 74–81, 2003.

[6] M. Beecroft, "Digital interlooping: 3D printing of weft-knitted textile-based tubular structures using selective laser sintering of nylon powder," *Int. J. Fash. Des. Technol. Educ.*, vol. 12, no. 2, pp. 218–224, 2019, doi: 10.1080/17543266.2019.1573269.

[7] Nervous System, "Kinematics Bodice," 2014. https://n-e-r-v-o-u-s.com/projects/tags/3dprint/albums/kinematics-clothing/ (accessed Nov. 03, 2021).

[8] T. Spahiu, E. Canaj, and E. Shehi, "3D printing for clothing production," *J. Eng. Fiber. Fabr.*, vol. 15, pp. 1–8, 2020, doi: 10.1177/1558925020948216.

[9] S. Kim, H. Seong, Y. Her, and J. Chun, "A study of the development and improvement

of fashion products using a FDM type 3D printer," *Fash. Text.*, vol. 6, no. 9, pp. 1–24, 2019, doi: 10.1186/s40691-018-0162-0.

[10] R. Uysal and J. B. Stubbs, "A new method of printing multi-material textiles by fused deposition modelling (FDM)," *Tekstilec*, vol. 62, no. 4, pp. 248–257, 2019, doi: 10.14502/Tekstilec2019.62.248-257.

[11] J. C. Najmon, S. Raeisi, and A. Tovar, "Review of additive manufacturing technologies and applications in the aerospace industry," *Addit. Manuf. Aerosp. Ind.*, pp. 7–31, 2019, doi: 10.1016/B978-0-12-814062-8.00002-9.

[12] S. Adanur and A. Jayswal, "Additive manufacturing of interlaced fibrous structures," *Rapid Prototyp. J.*, vol. 27, no. 4, pp. 671–681, 2021, doi: 10.1108/RPJ-05-2020-0095.

[13] M. Sakhakarmy, S. Tian, L. Raymond, G. Xiong, J. Chen, and Y. Jin, "Printability study of self-supporting graphene oxide-laponite nanocomposites for 3D printing applications," *Int. J. Adv. Manuf. Technol.*, vol. 114, pp. 343–355, 2021, doi: 10.1007/s00170-021-06870-5.

[14] M. Heidari-Rarani, N. Ezati, P. Sadeghi, and M. R. Badrossamay, "Optimization of FDM process parameters for tensile properties of polylactic acid specimens using Taguchi design of experiment method," *J. Thermoplast. Compos. Mater.*, vol. 35, no. 12, pp. 2435–2452, 2022, doi: 10.1177/0892705720964560.

[15] A. Jayswal and S. Adanur, "An overview of additive manufacturing methods, materials, and applications for flexible structures," *J. Ind. Text.*, vol. 52, pp. 1–42, 2022, doi: 10.1177/15280837221114638.

[16] A. Jayswal and S. Adanur, "Effect of heat treatment on crystallinity and mechanical properties of flexible structures 3D printed with fused deposition modeling," *J. Ind. Text.*, vol. 51, no. 2S, pp. 2616S-2641S, 2021, doi: 10.1177/15280837211064937.

[17] S. Park, W. Shou, L. Makatura, W. Matusik, and K. (Kelvin) Fu, "3D printing of polymer composites: Materials, processes, and applications," *Matter*, vol. 5, no. 1, pp. 43–76, 2022, doi: 10.1016/j.matt.2021.10.018.

[18] A. Jayswal and S. Adanur, "Characterization of polylactic acid/thermoplastic polyurethane composite filaments manufactured for additive manufacturing with fused deposition modeling," *J. Thermoplast. Compos. Mater.*, pp. 1–22, 2021, doi: 10.1177/08927057211062561.

[19] R. Singh, R. Kumar, Pawanpreet, M. Singh, and J. Singh, "On mechanical, thermal and morphological investigations of almond skin powder-reinforced polylactic acid feedstock filament," *J. Thermoplast. Compos. Mater.*, vol. 35, no. 2, pp. 230–248, 2022,

doi: 10.1177/0892705719886010.

[20] J. Holbery and D. Houston, “Natural-fiber-reinforced polymer composites in automotive applications,” *JOM*, vol. 58, no. 11, pp. 80–86, 2006, doi: 10.1007/s11837-006-0234-2.

[21] M. J. John and S. Thomas, “Biofibres and biocomposites,” *Carbohydr. Polym.*, vol. 71, no. 3, pp. 343–364, 2008, doi: https://doi.org/10.1016/j.carbpol.2007.05.040.

[22] M. M. A. Nassar, R. Arunachalam, and K. I. Alzebdeh, “Machinability of natural fiber reinforced composites: a review,” *Int. J. Adv. Manuf. Technol.*, vol. 88, no. 9, pp. 2985–3004, 2017, doi: 10.1007/s00170-016-9010-9.

[23] M. Adam Khan and A. Senthil Kumar, “Machinability of glass fibre reinforced plastic (GFRP) composite using alumina-based ceramic cutting tools,” *J. Manuf. Process.*, vol. 13, no. 1, pp. 67–73, 2011, doi: https://doi.org/10.1016/j.jmapro.2010.10.002.

[24] A. Lotfi, H. Li, D. V. Dao, and G. Prusty, “Natural fiber–reinforced composites: A review on material, manufacturing, and machinability,” *J. Thermoplast. Compos. Mater.*, vol. 34, no. 2, pp. 238–284, Apr. 2019, doi: 10.1177/0892705719844546.

[25] V. A. Yiga, S. Pagel, M. Lubwama, S. Epple, P. W. Olupot, and C. Bonten, “Development of fiber-reinforced polypropylene with NaOH pretreated rice and coffee husks as fillers: Mechanical and thermal properties,” *J. Thermoplast. Compos. Mater.*, vol. 33, no. 9, pp. 1269–1291, 2020, doi: 10.1177/0892705718823255.

[26] J. R. Dorgan, H. Lehermeier, and M. Mang, “Thermal and Rheological Properties of Commercial-Grade Poly (Lactic Acid)s,” *J. Polym. Environ.*, vol. 8, no. 1, pp. 1–9, 2000.

[27] M. A. Cuiffo, J. Snyder, A. M. Elliott, N. Romero, S. Kannan, and G. P. Halada, “Impact of the Fused Deposition (FDM) Printing Process on Polylactic Acid (PLA) Chemistry and Structure,” *Appl. Sci.*, vol. 7, no. 6, p. 579, Jun. 2017, doi: 10.3390/app7060579.

[28] R. M. Rasal and D. E. Hirt, “Toughness decrease of PLA-PHBHHx blend films upon surface-confined photopolymerization,” *J. Biomed. Mater. Res. - Part A*, vol. 88, no. 4, pp. 1079–1086, 2009, doi: 10.1002/jbm.a.32009.

[29] M. Hiljanen-Vainio, P. Varpomaa, J. Seppälä, and P. Törmälä, “Modification of poly(L-lactides) by blending: Mechanical and hydrolytic behavior,” *Macromol. Chem. Phys.*, vol. 197, no. 4, pp. 1503–1523, 1996, doi: 10.1002/macp.1996.021970427.

[30] I. Chiulan, A. N. Frone, C. Brandabur, and D. M. Panaitescu, “Recent advances in 3D printing of aliphatic polyesters,” *Bioengineering*, vol. 5, no. 2, pp. 2–18, 2018, doi: 10.3390/bioengineering5010002.

[31] O. Gordobil, I. Egüés, R. Llano-Ponte, and J. Labidi, “Physicochemical properties of

PLA lignin blends," *Polym. Degrad. Stab.*, vol. 108, pp. 330–338, 2014, doi: 10.1016/j.polymdegradstab.2014.01.002.

[32] V. Jašo, M. Cvetinov, S. S. S. Rakič, and Z. S. Petrovič, "Bio-plastics and elastomers from polylactic acid/thermoplastic polyurethane blends," *J. Appl. Polym. Sci.*, vol. 131, no. 22, pp. 1–8, 2014, doi: 10.1002/app.41104.

[33] H. Y. Mi *et al.*, "Characterization of thermoplastic polyurethane/polylactic acid (TPU/PLA) tissue engineering scaffolds fabricated by microcellular injection molding," *Mater. Sci. Eng. C*, vol. 33, no. 8, pp. 4767–4776, 2013, doi: 10.1016/j.msec.2013.07.037.

[34] Q.-W. Lu and C. W. Macosko, "Comparing the compatibility of various functionalized polypropylenes with thermoplastic polyurethane (TPU)," *Polymer (Guildf).*, vol. 45, pp. 1981–1991, 2004, doi: 10.1016/j.polymer.2003.12.077.

[35] A. Frick and A. Rochman, "Characterization of TPU-elastomers by thermal analysis (DSC)," *Polym. Test.*, vol. 23, no. 4, pp. 413–417, 2004, doi: 10.1016/j.polymertesting.2003.09.013.

[36] J. Datta and P. Kasprzyk, "Thermoplastic polyurethanes derived from petrochemical or renewable resources: A comprehensive review," *Polym. Eng. Sci.*, vol. 58, no. S1, pp. E14–E35, 2018, doi: https://doi.org/10.1002/pen.24633.

[37] L. A. Hockaday *et al.*, "Rapid 3D printing of anatomically accurate and mechanically heterogeneous aortic valve hydrogel scaffolds," *Biofabrication*, vol. 4, no. 3, pp. 1–12, 2012, doi: 10.1088/1758-5082/4/3/035005.

[38] G. M. Cruise, D. S. Scharp, and J. A. Hubbell, "Characterization of permeability and network structure of interfacially photopolymerized poly(ethylene glycol) diacrylate hydrogels," *Biomaterials*, vol. 19, no. 14, pp. 1287–1294, 1998, doi: 10.1016/S0142-9612(98)00025-8.

[39] J. Chen, S. K. Spear, J. G. Huddleston, and R. D. Rogers, "Polyethylene glycol and solutions of polyethylene glycol as green reaction media," *Green Chem.*, vol. 7, pp. 64–82, 2005.

[40] J. Milton Harris, *Poly (ethylene glycol) chemistry: biotechnical and biomedical applications*. New York, 1992.

[41] Y. Zhou, L. Luo, W. Liu, G. Zeng, and Y. Chen, "Preparation and Characteristic of PC/PLA/TPU Blends by Reactive Extrusion," *Adv. Mater. Sci. Eng.*, pp. 1–9, 2015, doi: 10.1155/2015/393582.

[42] V. Jašo, M. V. Rodić, and Z. S. Petrović, "Biocompatible fibers from thermoplastic

polyurethane reinforced with polylactic acid microfibers," *European Polymer Journal*, vol. 63. pp. 20–28, 2015, doi: 10.1016/j.eurpolymj.2014.11.041.

[43] F. Feng and L. Ye, "Morphologies and mechanical properties of polylactide/thermoplastic polyurethane elastomer blends," *J. Appl. Polym. Sci.*, vol. 119, no. 5, pp. 2778–2783, Mar. 2011, doi: 10.1002/app.32863.

[44] D. Xu, K. Yu, K. Qian, and C. B. Park, "Foaming behavior of microcellular poly(lactic acid)/TPU composites in supercritical CO2," *J. Thermoplast. Compos. Mater.*, vol. 31, no. 1, pp. 61–78, 2018, doi: 10.1177/0892705716679480.

[45] C. Kaynak and S. D. Varsavas, "Performance comparison of the 3D-printed and injection-molded PLA and its elastomer blend and fiber composites," *J. Thermoplast. Compos. Mater.*, vol. 32, no. 4, pp. 501–520, 2019, doi: 10.1177/0892705718772867.

[46] Corbion Purak, "Luminy® LX175 Product," 2016. [Online]. Available: https://cdn.shopify.com/s/files/1/0236/7897/files/TDS_Luminy_LX175_Filabot.pdf?v=1602610806.

[47] L. LifeSciences, "Pellethane 2363-90AE TPU," 2016. [Online]. Available: https://www.techkits.com/products/resin-tpunat-90a/tpunat-90a.pdf.

[48] J. Verhoeven, R. Schaeffer, J. a B, and H. E. Junginger, "The physico-chemical characterization of methacrylic acid : 2 . Effect of water , PEG 400 and PEG 6000 on the glass transition temperature," *October*, vol. 30, pp. 1946–1950, 1989.

[49] N. Alizadeh, D. P. Thorne, M. L. Auad, and A. D. N. Celestine, "Mechanical performance of vinyl ester—polyurethane interpenetrating polymer network composites," *J. Appl. Polym. Sci.*, vol. 138, no. 19, pp. 1–11, 2021, doi: 10.1002/app.50411.

[50] N. Alizadeh, R. M. Broughton, and M. L. Auad, "Graft Semi-Interpenetrating Polymer Network Phase Change Materials for Thermal Energy Storage," *ACS Appl. Polym. Mater.*, vol. 3, no. 4, pp. 1785–1794, 2021, doi: 10.1021/acsapm.0c01363.

[51] N. Saba, M. Jawaid, O. Y. Alothman, and M. T. Paridah, "A review on dynamic mechanical properties of natural fibre reinforced polymer composites," *Constr. Build. Mater.*, vol. 106, pp. 149–159, 2016, doi: 10.1016/j.conbuildmat.2015.12.075.

[52] J. Guo *et al.*, "Triply Biobased Thermoplastic Composites of Polylactide/Succinylated Lignin/Epoxidized Soybean Oil," *Polymers (Basel).*, vol. 12, no. 632, pp. 1–18, 2020, doi: 10.3390/polym12030632.

[53] N. Alizadeh *et al.*, "High-fracture-toughness acrylic–polyurethane-based graft-interpenetrating polymer networks for transparent applications," *Polym. Int.*, vol. 70, no.

5, pp. 636–647, 2021, doi: 10.1002/pi.6149.

[54] N. Alizadeh, E. Triggs, R. Farag, and M. L. Auad, “Flexible acrylic-polyurethane based graft-interpenetrating polymer networks for high impact structural applications,” *Eur. Polym. J.*, vol. 148, no. 110338, pp. 1–11, 2021, doi: 10.1016/j.eurpolymj.2021.110338.

[55] R. K. Singla, S. N. Maiti, and A. K. Ghosh, “Crystallization, Morphological, and Mechanical Response of Poly(Lactic Acid)/Lignin-Based Biodegradable Composites,” *Polym. Plast. Technol. Eng.*, vol. 55, no. 5, pp. 475–485, 2016, doi: 10.1080/03602559.2015.1098688.

[56] Q. Tang and K. Gao, “Structure analysis of polyether-based thermoplastic polyurethane elastomers by FTIR, 1H NMR and 13C NMR,” *Int. J. Polym. Anal. Charact.*, vol. 22, no. 7, pp. 569–574, 2017, doi: 10.1080/1023666X.2017.1312754.

[57] M. Nofar, M. Mohammadi, and P. J. Carreau, “Effect of TPU hard segment content on the rheological and mechanical properties of PLA/TPU blends,” *Journal of Applied Polymer Science*, vol. 137, no. 45. 2020, doi: 10.1002/app.49387.

Chapter 8

Modeling creep behavior of 3D printed structures using composite filaments

Abstract

The creep behavior of polymer composites containing different weight percentages of poly(lactic) acid (PLA), thermoplastic polyurethane (TPU) and poly(ethylene) glycol (PEG) is experimentally characterized and computationally modeled using finite element analysis (FEA). The composite filaments are manufactured with melt extrusion method by using twin-screw extruders, and then are employed in the 3D printing of creep samples. The samples are tested under a constant tensile load of 100 N. In this study, the computational model is developed by using the Generalized Voigt-Kelvin solid model and three terms in Prony series. The experimental creep displacements and strains are compared with computational results, and a good agreement between them is observed. The maximum error percentages in computational result is approximately 6 % as compared to the experimental result. Hence, it can be said that the computational model developed is reliable and can be used to study the creep behavior of similar polymers. The error percentages can still be reduced by considering a higher number of terms of Prony series in the model.

8.1. Introduction

The polymers and polymer composites having improved properties are in great demand due to their high strength and lightweight [1] [2]. They can be used in several applications including automotives, aerospace, textiles, sports, and military. For this purpose, an extensive study of their mechanical deformation behavior is necessary [3]. Generally, the elastic-plastic mechanical deformation occuring due to tensile, compression, shear or bending loads are considered while desgining the materials and structures. In real applications, the material deformations are time-dependent and deforms permanently even when subjected to loads that are below the yield strength of the materials, and this behavior is known as creep [4] [5]. The elastic-plastic deformations are modeled as instantaneous deformations and the characteristic times are orders of magnitude smaller than those of creep [6]. Therefore, considering only the conventional approach of designing the materials is not appropriate for advanced applications. The inclusion of viscoelasticity approach can give better insight about the life of materials and can precisely predict the performance and failure [7] [8] [9] [10]. The creep deformation is evident at room temperature and accelerates rapidly at elevated temperatures. It has also been

found that approximately 22% of all plastic component failures are associated with creep mechanism [4]. Therefore, it is a major source of error while designing the materials for advanced applications [5].

The creep behavior of polymers are different as compared to metals and ceramics. The reason is metals and ceramics are highly periodic crystalline structures whereas the polymers contain long molecules with a chain of atoms or cross-linked network held together by covalent bonds. The chemical bond formation is strong and directional along the chains and networks whereas the adjacent chains are bonded sideways by weak secondary Van der Waals forces. This characteristic causes the mechanical properties of polymers to behave differently than metals and ceramics [6].

The creep deformation mechanism occurs in three different stages: primary (transient) creep, secondary (steady-state) creep, and tertiary (accelerated) creep [11] [12]. The strain increases with decreasing strain rate in the primary stage, and is observed after instantaneous elastic strain. In the secondary stage, the strain increases linearly with time and most of the deformations occurs during this stage. The tertiary stage exhibits the rapid increase in strain rate and leads to creep rapture. The progressive damage such as the formation and growth of voids on grain boundaries are considered to be the main contributors of the rapid growth of the strain rate. A typical creep response of a material along with two curves A and B is presented in Figure 8.1. Curve A indicates a creep response under a constant load and B indicates under constant stress. During a creep test, the cross-sectional area of a specimen decreases and thus the axial stress increases with a constant load. The increased stress accelerates the creep and causes rapid strain in tertiary stage, as shown by curve A. On the other hand, with constant stress condition, the secondary creep dominates for a much time period and delays the creep rapture [6].

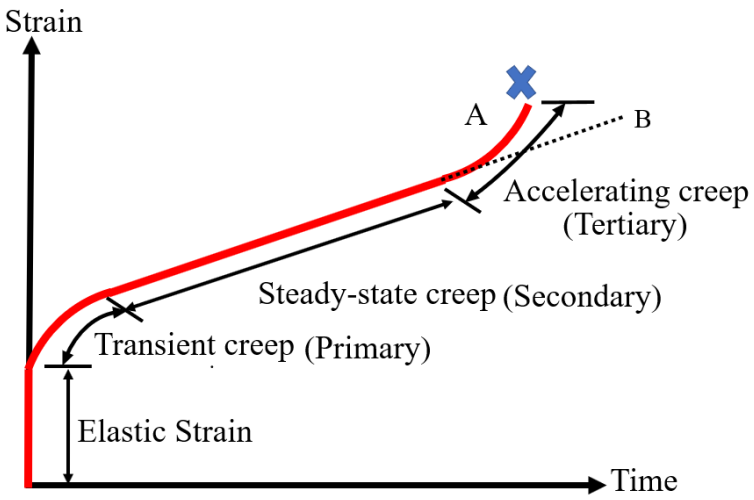

Figure 8.1. Typical creep response of a material.

In the current scenario, additive manufacturing (AM) (also known as 3D printing) is gaining popularity in almost every industry. Fused deposition modeling (FDM) is one of the methods which works on the principle of material extrusion through a nozzle. Thermoplastic polymers are generally used in FDM in the form of filaments. However, most of the polymer filaments which are readily available for FDM 3D printing do not possess both high mechanical strength, and high flexibility. This is why the use of 3D printed structures is limited for advanced applications.

The final properties of a polymer can be improved by blending of polymers depending on the compatibility between them [13][14][15][16][17][18][19][20][21]. A scientific selection of polymers and blending method becomes important. Poly(lactic) acid (PLA), thermoplastic polyurethane (TPU) and poly(ethylene) glycol (PEG) are mixed together using twin-screw extrusion method to manufacture the composite filaments for 3D printing applications and their mechanical and chemical properties are studied [14][22]. Several other researchers have studied the polymer properties of PLA/TPU composition for various applications [23] [24] [25] [26] [27] [28]. All these studies focus on elastic-plastic mechanical deformation and chemical properties investigations. Therefore, in this research, the creep behavior of polymer composites used in FDM 3D printing is studied. First, a creep experiment is conducted on all the 3D printed specimens made of polymer composite filaments. Then, a finite element analysis (FEA) approach is adopted to compare the results and develop a reliable computational model. Additionally, it helps to predict the creep behavior of other polymers and polymer composites manufactured either by 3D printing or any other methods such as injection molding, and compression molding.

This chapter is organized into different sections. In the materials and methods section, the composite filament manufacturing process is explained. In addition, the experimental creep test and finite element modeling (FEM) methods are described. In the theoretical background section, generalized Voigt-Kelvin solid model, generalized Maxwell model, and a relation between creep compliance and relaxation modulus are mentioned. In the results and discussion section, the experimental creep behavior of FDM 3D printed specimens using polymer composite filaments, finite element analysis (FEA), and the model validation are explained.

8.2. Materials and methods

8.2.1. Samples preparation

The PLA and TPU pellets were dried in oven at 60 ℃ for 12 hours and then PLA, TPU and PEG chips were blended in a defined ratio as mentioned in Table 8.1. The polymer blends were fed into twin-screw extruder (Leistritz Mic 18/GL 40D, Nuremberg, Germany) and composite filaments were obtained. The screw speed was set at 30 rpm. The composite filaments having diameters in the range of 1.70 mm to 1.80 mm were used in this research. For more information about the filamenst manufacturing and the settings, one may refer to the references [14][22]. The samples, PLA2.85 and PLA1.75 are as-purchased PLA filament of diameters 2.85 mm, and 1.75 mm respectively. All other samples listed in Table 8.1 are manufactured by using corresponding pellets and powder.

Table 8.1. Composition prepared for filament manufacturing from pellets.

Samples	PLA (wt %)	TPU (wt %)	PEG (wt%)
PLA2.85	100	0	0
PLA1.75	100	0	0
PLA	100	0	0
PLA_TPU10	90	10	0
PLA_TPU20	80	20	0
PLA_TPU30	70	30	0
PLA_TPU30_PEG3	67	30	3
PLA_TPU30_PEG4	66	30	4
PLA_TPU30_PEG5	65	30	5
PLA_TPU40	60	40	0
PLA_TPU40_PEG3	57	40	3

8.2.2. Creep test

The composite filaments were used to 3D print the specimens required for experimental creep tests. The print settings used were infill density of 100%, layer height of 0.25 mm, printing temperature of 220 ℃, and print speed of 30 mm/s. The samples of dimensions 40 mm × 10 mm × 2 mm are 3D printed using Lulzbot Taz Pro 3D printer for creep tests in horizontal (flat) directions. The creep tests of 3D printed polymer composites are performed using uniaxial tensile test configuration having a gage length of 20 mm using an Instron 5565. The creep tests are performed with a constant applied force of 100 N for 30 minutes at a room temperature (~23 ℃). The value of strain with corresponding change of time was recorded and then the creep curves are obtained.

8.2.3. Finite element modeling (FEM)

A finite element analysis was conducted to compare the creep behavior obtained from the experiments. All the analyses are performed using the commercial finite element software, ABAQUS/CAE. The sample sizes of 20 mm (length), 10 mm (width) and 2 mm (thickness) are used to establish the simplified geometric model. One end of the geometric model is fully constrained, and the other end is imposed with a constant tensile load of 100 N in x-direction, and the step time given is 1800 seconds (30 minutes). A C3D8R: an 8-node linear brick, reduced integration, hourglass control element is used in the simulation. ABAQUS/CAE used the structured meshing technique to create a mesh of hexahedral-shaped elements with a global mesh size of 0.5 mm (*Figure 8.2*).

The finite element analysis (FEA) is performed in two steps. The first step is to input the elastic material properties such as Young's modulus and Poisson's ratio. Young's modulus is calculated from Eq. *(8.4*) when time, t = 0. The second step corresponds to the analysis of time-dependent creep behavior of the materials in which Prony Series, calculated in Section 8.4.1. , are the input parameters.

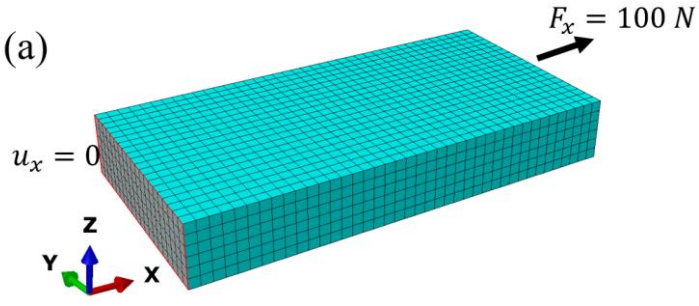

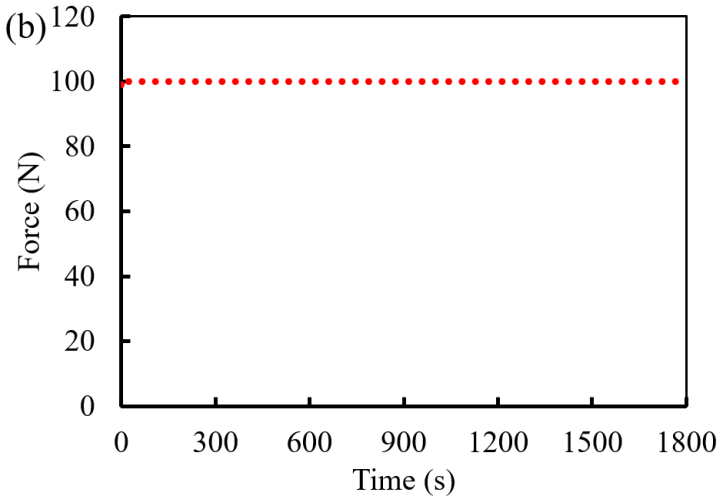

Figure 8.2. (a) Geometrical model showing the mesh and boundary conditions, and (b) Input load for creep test.

8.3. Theoretical background

8.3.1. Generalized Voigt-Kelvin solid model

The creep behavior of the 3D printed polymer composites is modeled by using a Generalized Voigt-Kelvin solid model. It consists of a series combination of one spring and *n* number of Kelvin elements as shown in Figure 8.3. A constant stress σ_0 is applied at the ends. η_i (i = 1, 2, 3, …, n) represents the viscosity of dampers in Kelvin elements.

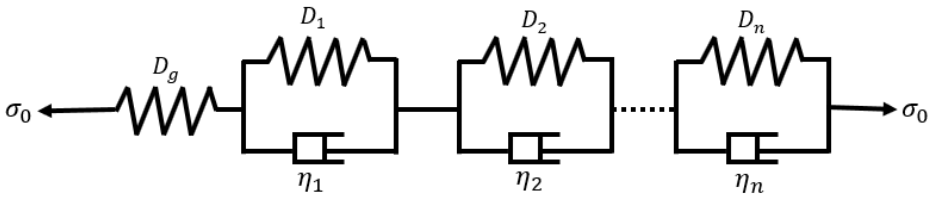

Figure 8.3. Generalized Voigt-Kelvin solid model.

The creep strain function based on the Generalized Voigt-Kelvin solid model is given by Eq. *(8.1)*.

$$\varepsilon(t) = \sigma_0 D(t) \qquad (8.1)$$

where, $\varepsilon(t)$ is creep strain function, t is time variable, σ_0 is constant applied stress, and $D(t)$ is creep compliance function, which is given by Eq. *(8.2)*.

$$D(t) = D_g + \left[\sum_{i=1}^{n} D_i \left(1 - e^{\frac{-t}{\rho_i}}\right)\right] \qquad (8.2)$$

where, D_g is glassy compliance, and D_i (i = 1, 2, 3, ……., n) are creep compliances, ρ_i (i = 1, 2, 3, ……, n) are retardation times, and n is the positive integers.

8.3.2. Generalized Maxwell model

The stress relaxation behavior of the 3D printed polymer composites is modeled by using a Generalized Maxwell model. It consists of a parallel combination of one spring and *n* number of Maxwell elements as shown in Figure 8.4. A constant strain ε_0 is applied at the ends. η_i (i = 1, 2, 3, …, n) represents the viscosity of dampers in Maxwell elements.

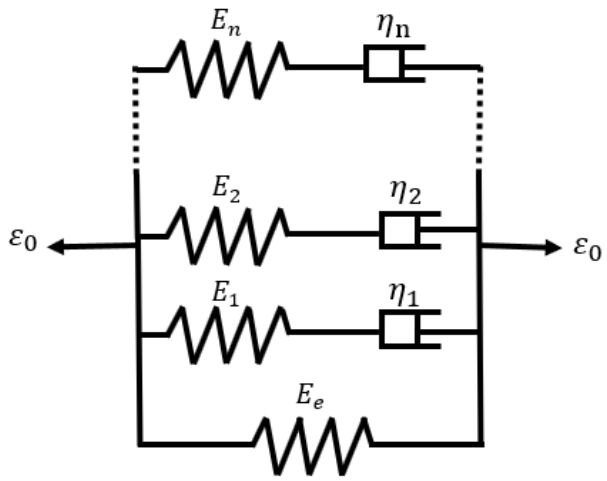

Figure 8.4. Generalized Maxwell model.

The stress relaxation function based on the Generalized Maxwell model is given by Eq. *(8.3*).

$$\sigma(t) = \varepsilon_0 E(t) \qquad (8.3)$$

where, $\sigma(t)$ is stress relaxation function, t is time variable, ε_0 is constant applied strain, and $E(t)$ is relaxation modulus function, which is given by Eq. *(8.4*).

$$E(t) = E_e + \left[\sum_{i=1}^{n} E_i e^{\frac{-t}{\tau_i}}\right] \qquad (8.4)$$

where, E_e is equilibrium modulus, and E_i (i = 1, 2, 3, ……., n) are relaxation moduli, τ_i (i = 1, 2, 3, ……, n) are relaxation times, and $\tau_i = \frac{\eta_i}{E_i}$. The equation *(8.4*) is known as Prony Series of the materials and is useful to describe the viscoelastic properties in ABAQUS CAE software.

8.3.3. Conversion between Creep Compliance and Relaxation Modulus

The viscoelastic properties of polymers are time-dependent, and hence to convert the creep compliance to relaxation modulus, Laplace transformation method should be adopted. The Laplace transform functions are given by Eq. *(8.5*) and *(8.6*).

$$\widetilde{D}(s) = \mathcal{L}\{D(t)\} \tag{8.5}$$

$$E(t) = \mathcal{L}^{-1}\left(\frac{1}{s^2\widetilde{D}(s)}\right) \tag{8.6}$$

where, $\widetilde{E}(s) = \frac{1}{s^2\widetilde{D}(s)}$, $\widetilde{D}(s)$ and $\widetilde{E}(s)$ are the functions obtained after Laplace transformation of $D(t)$ and $E(t)$, $\mathcal{L}\{\}$ is the Laplace operator, and s is the Laplace variable.

8.4. Results and discussions

8.4.1. Creep test

The experimental creep test data is post processed and creep compliance curve is obtained. The experimental compliance curve is fitted with compliance function shown by Eq. *(8.2)* in MATLAB using Curve Fitting Toolbox for 3 terms with constraints $D_g > 0$, $D_i > 0$ and $\rho_i > 0$. The fit options were adjusted to obtain fitted parameters with Goodness of fit value as $R^2 > 0.99$. It can be concluded that the two curves show good fitting over time and have similar trend [29]. The curve fitting of experimental compliance and Kelvin Model's compliance is presented in Figure 8.5. The obtained parameters D_g, D_1, D_2, D_3, ρ_1, ρ_2, and ρ_3 are shown in Table 8.2. Therefore, after substituting these values in Eq. *(8.2)*, the creep compliance equation, for PLA2.85 material, can be re-written as Eq. *(8.7)*. Similarly, the compliance equations can be written for other samples prepared in this study (see Appendix E).

$$D(t) = 0.005702 + 0.0004325\left(1 - e^{-\frac{t}{9.81}}\right) + 0.0003421\left(1 - e^{-\frac{t}{69.24}}\right) + 0.0003531\left(1 - e^{-\frac{t}{908.20}}\right) \tag{8.7}$$

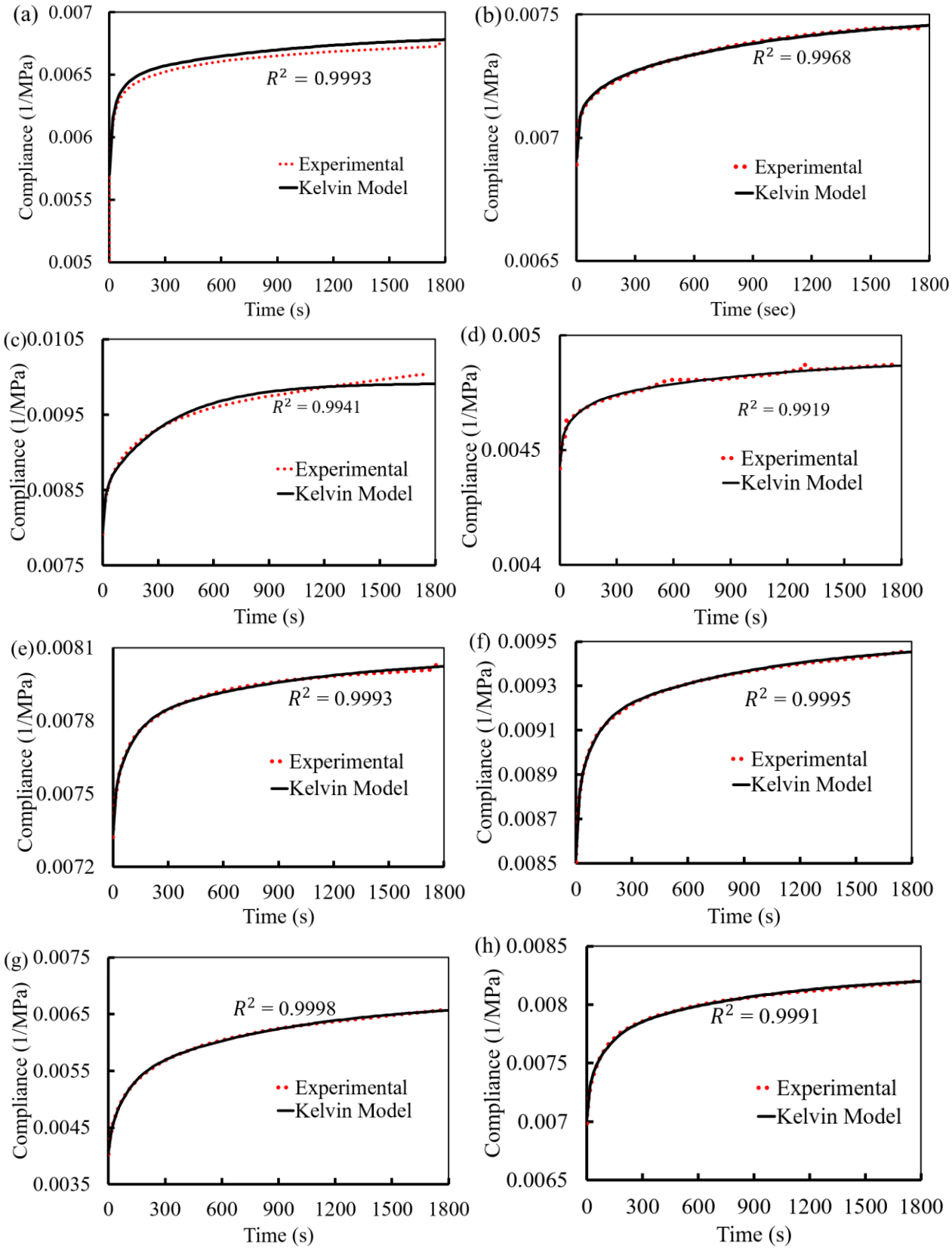
(a)
Compliance (1/MPa)
0.007
0.0065
0.006
0.0055
0.005
R^2 = 0.9993
Experimental
Kelvin Model
0 300 600 900 1200 1500 1800
Time (s)
(b)
Compliance (1/MPa)
0.0075
0.007
0.0065
R^2 = 0.9968
Experimental
Kelvin Model
0 300 600 900 1200 1500 1800
Time (sec)
(c)
Compliance (1/MPa)
0.0105
0.0095
0.0085
0.0075
R^2 = 0.9941
Experimental
Kelvin Model
0 300 600 900 1200 1500 1800
Time (s)
(d)
Compliance (1/MPa)
0.005
0.0045
0.004
R^2 = 0.9919
Experimental
Kelvin Model
0 300 600 900 1200 1500 1800
Time (s)
(e)
Compliance (1/MPa)
0.0081
0.0078
0.0075
0.0072
R^2 = 0.9993
Experimental
Kelvin Model
0 300 600 900 1200 1500 1800
Time (s)
(f)
Compliance (1/MPa)
0.0095
0.0093
0.0091
0.0089
0.0087
0.0085
R^2 = 0.9995
Experimental
Kelvin Model
0 300 600 900 1200 1500 1800
Time (s)
(g)
Compliance (1/MPa)
0.0075
0.0065
0.0055
0.0045
0.0035
R^2 = 0.9998
Experimental
Kelvin Model
0 300 600 900 1200 1500 1800
Time (s)
(h)
Compliance (1/MPa)
0.0085
0.008
0.0075
0.007
0.0065
R^2 = 0.9991
Experimental
Kelvin Model
0 300 600 900 1200 1500 1800
Time (s)

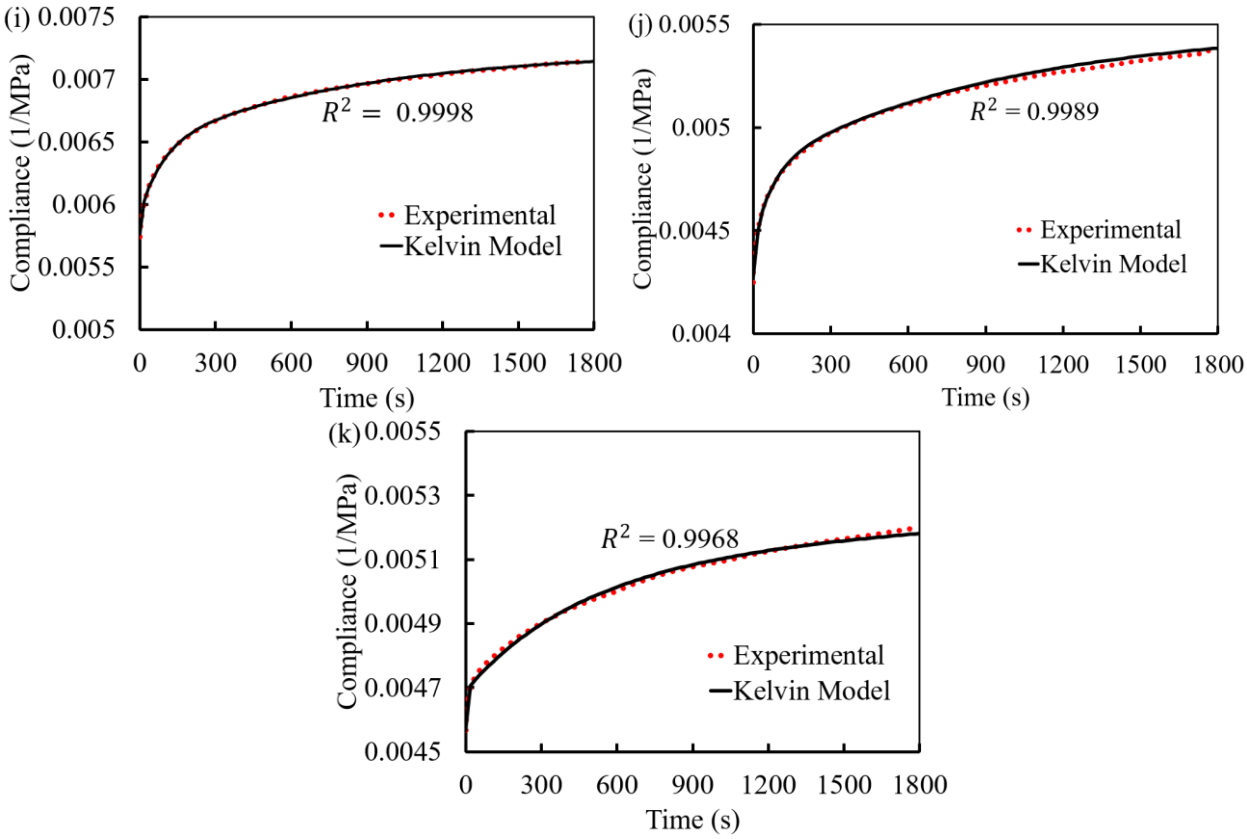

Figure 8.5. Curve fitting of compliances obtained from the creep test with compliance of Generalized Kelvin Model. (a) PLA2.85, (b) PLA1.75, (c) PLA, (d) PLA_TPU10, (e) PLA_TPU20, (f) PLA_TPU30, (g) PLA_TPU30_PEG3, (h) PLA_TPU30_PEG4, (i) PLA_TPU30_PEG5, (j) PLA_TPU40, and (k) PLA_TPU40_PEG3.

Table 8.2. Creep compliances and retardation times obtained after curve fitting in MATLAB Curve Fitting Toolbox.

Materials	Compliances (MPa^{-1})				Retardation times (s)		
	D_g	D_1	D_2	D_3	ρ_1	ρ_2	ρ_3
PLA2.85	5.702e-03	4.325e-04	3.421e-04	3.531e-04	9.81	69.24	908.20
PLA1.75	6.915e-03	1.722e-04	1.046e-04	3.106e-04	9.88	98.97	947.10
PLA	7.935e-03	1.348e-04	4.560e-04	1.391e-03	1.13	17.30	361.90
PLA_TPU10	4.431e-03	1.219e-04	1.390e-04	2.082e-04	9.82	96.8	966.7
PLA_TPU20	7.336e-03	1.525e-04	2.958e-04	2.785e-04	9.80	97.54	927.10

PLA_TPU30	8.524e-03	2.643e-04	3.433e-04	3.748e-04	9.74	91.61	924.10
PLA_TPU30_PEG3	4.045e-03	2.893e-04	9.810e-04	1.429e-03	9.92	95.13	866.00
PLA_TPU30_PEG4	7.012e-03	2.471e-04	4.526e-04	5.584e-04	9.83	96.39	875.70
PLA_TPU30_PEG5	5.759e-03	1.806e-04	5.228e-04	7.747e-04	9.54	92.54	849.10
PLA_TPU40	4.270e-03	1.677e-04	3.586e-04	6.951e-04	9.85	75.41	960.10
PLA_TPU40_PEG3	4.567e-03	1.241e-04	3.354e-04	2.672e-04	4.02	425.30	1983.00

Since the compliance is a function of time, Laplace transformation method is used to convert it to relaxation modulus function. The Prony series obtained from relaxation modulus equation will be used in ABAQUS CAE software to model the creep behavior of the materials. Using Eqs. *(8.5*), *(8.6*), and *(8.7*), the relaxation modulus equation, for PLA2.85 material, can be derived as shown in Eq. *(8.8*). Similarly, the relaxation modulus equations can be transformed for other samples prepared in this study (see Appendix E).

$$E(t) = 146.42 + 12.59e^{-0.1097t} + 8.47e^{-0.0152t} + 7.90e^{-0.00116t} \qquad (8.8)$$

Comparing Eq. *(8.4*) and Eq. *(8.8*), the coefficients of relaxation modulus and associated relaxation times can be evaluated.

At $t = 0,\ E_0 = \ E(0) = 175.38\ MPa$

$$E_1 = 12.59\ MPa, \quad \tau_1 = \frac{1}{0.1097} = 9.12\ s$$

$$E_2 = 8.47\ MPa, \quad \tau_2 = \frac{1}{0.0152} = 65.79\ s$$

$$E_3 = 7.90\ MPa, \quad \tau_3 = \frac{1}{0.00116} = 862.07\ s$$

Using the values of the obtained coefficients, the Prony Series coefficients can be calculated by using Eq. *(8.9*). The Prony Series parameters are shown in Table *8.3*.

$$g_i = \frac{E_i}{E_0} \qquad (8.9)$$

where, $\boldsymbol{E_i}$ are the coefficients of the Prony Series, $\boldsymbol{E_0}$ is the relaxation modulus at *t* = 0, and $\boldsymbol{g_i}$ are the dimensionless Prony Series coefficients.

Table 8.3. Prony Series used in the finite element analysis.

Materials	Modulus (MPa)				Relaxation times (s)			Prony Series		
	E_0	E_1	E_2	E_3	τ_1	τ_2	τ_3	g_1	g_2	g_3
PLA2.85	175.38	12.59	8.47	7.90	9.12	65.79	862.07	0.0718	0.0483	0.0450
PLA1.75	144.61	3.53	2.06	5.73	9.64	97.56	907.93	0.0244	0.0143	0.0396
PLA	126.02	2.12	6.71	16.35	1.11	16.37	312.5	0.0168	0.0532	0.1297
PLA_TPU10	225.68	6.09	6.53	8.99	9.56	93.98	925.93	0.0269	0.0289	0.0398
PLA_TPU20	136.31	2.80	5.09	4.39	9.60	93.81	892.86	0.0206	0.0374	0.0322
PLA_TPU30	117.32	3.56	4.28	4.28	9.45	88.18	887.86	0.0304	0.0365	0.0365
PLA_TPU30_PEG3	247.22	17.46	43.98	37.51	9.24	77.22	686.81	0.0706	0.1779	0.1517
PLA_TPU30_PEG4	142.61	4.93	8.15	8.61	9.49	90.74	816.99	0.0346	0.0571	0.0604
PLA_TPU30_PEG5	173.64	5.40	13.88	16.18	9.24	84.98	759.13	0.0311	0.0799	0.0932
PLA_TPU40	234.19	9.09	17.02	25.98	9.47	69.73	840.34	0.0388	0.0727	0.1109
PLA_TPU40_PEG3	218.96	5.80	14.60	9.66	3.91	396.51	1883.24	0.0265	0.0667	0.0441

8.4.2. Finite element analysis (FEA)

The finite element analysis (FEA) was performed on all 3D printed rectangular test coupons made of composite filaments using ABAQUS. The computational model was created in two steps. The first step is to analyze the elastic behavior by supplying the values of Young's modulus and Poisson's ratio. Young's modulus is calculated from the stress relaxation equation when the time is zero, and the Poisson's ratio of 0.33 is used for all the samples. The second step is to create the viscous model of the materials by inputting the values of Prony Series calculated in section 8.4.1. The viscoelastic model is defined in the time domain, where the requested parameters are g_i, k_i, and τ_i. The g_i terms are the normalized Prony coefficients for shear (deviatoric) beahvior, the k_i terms are the normalized Prony coefficients for volumetric behavior, and the τ_i values are the relaxation times of Prony series. In this study, the volume changes in the material is not considered and therefore, the only input parameters are g_i and τ_i. Only three terms of the Prony series are considered. The input parameters for creep model in ABAQUS are listed in Table 8.3. A representative creep displacement contour of PLA2.85

is shown in Figure 8.6. A maximum creep displacement is observed to be 0.5885 mm at the end of 30 minutes. The contours of all other samples are shown in Appendix F.

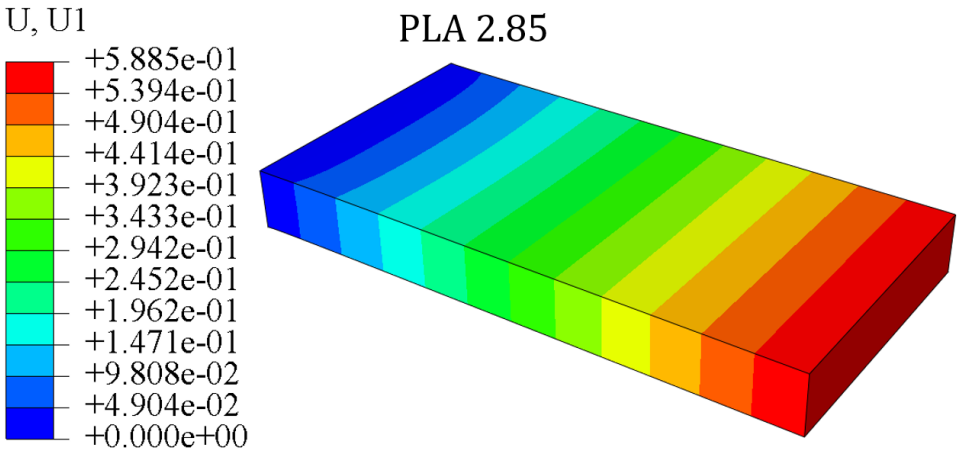

Figure 8.6. Creep displacement contours for PLA2.85.

The creep results are presented in Figure 8.7 and Figure 8.8. It is observed that the creep deformation mechanisms are seen in different stages. First, the instantaneous elastic strain region is seen followed by a smaller region of primary (transient) creep. Primary creep is the first stage of creep deformation where the strain increases rapidly and reaches an equilibrium. The second creep stage is secondary (steady-state) creep where the creep deformation is slow and constant and most of the deformations takes place in this stage. The tertiary (accelerated) creep deformation is not seen during the 30 minutes experiments because of low force applied. However, it may occur after a longer period of time. The generalized Voigt-Kelvin model and the finite element model (FEM) are able to predict the instantaneous elastic strain region, primary creep region, and secondary creep region successfully. Therefore, the model is reliable, and can be used to design 3D printed structures for applications.

PLA2.85 and PLA1.75 are as-purchased PLA filaments of diameters 2.85 mm and 1.75 mm respectively, whereas PLA is the filament manufactured from pellets in this work. PLA2.85 and PLA1.75 have almost similar creep displacement of approximately 0.6 mm at the end of 30 minutes. PLA has a slightly higher creep displacement of 0.69 mm after the test. Hence, it can be said that their creep behavior is somewhat similar. PLA_TPU10, PLA_TPU20, PLA_TPU30, and PLA_TPU40 have creep displacements of approximately 0.45 mm, 0.75 mm, 0.70 mm, and 0.57 mm, respectively at the end of the test. PLA_TPU30_PEG3, PLA_TPU30_PEG4, PLA_TPU30_PEG5, and PLA_TPU40_PEG3 have creep displacements of 0.54 mm, 0.70 mm, 0.69 mm, and 0.53 mm, respectively after 30 minutes. These data reveal

that they have almost similar creep behavior in the given time period. The same nature is true for creep strains since they are the derivatives of displacement. The reason might be the lower force applied which is not sufficient enough to bring significant deformation in the materials. Another reason might be the testing time. For better visualization of creep deformation, a longer testing time is recommended.

8.4.3. Model Validation

Figure 8.7 and Figure 8.8 show the results obtained for creep displacement and creep strain respectively. The tensile creep test results are compared with those obtained from finite element analysis (FEA). The error pecentages are calculated at 600 s, 1200 s, and 1800 s. It is found that the maximum error is approximately 6% in creep displacement and 4.5% in creep strain for PLA_TPU30_PEG3 sample at 1800 s. This shows a fact that a good agreement between experiments and FEA is observed over the tested time period. Table 8.4 demonstrates the error percentages calculated for all other samples. The computational model performs well for all the samples and successfully predicts the creep behavior over a defined time period. Therefore, the model can be considered reliable to predict the creep behavior of 3D printed polymer composites. This model can also be used to study the creep behavior of similar polymers while designing for advanced applications. Additionally, the model uses only three terms of Prony series; therefore, it can be further improved by considering the higher number of terms of Prony series.

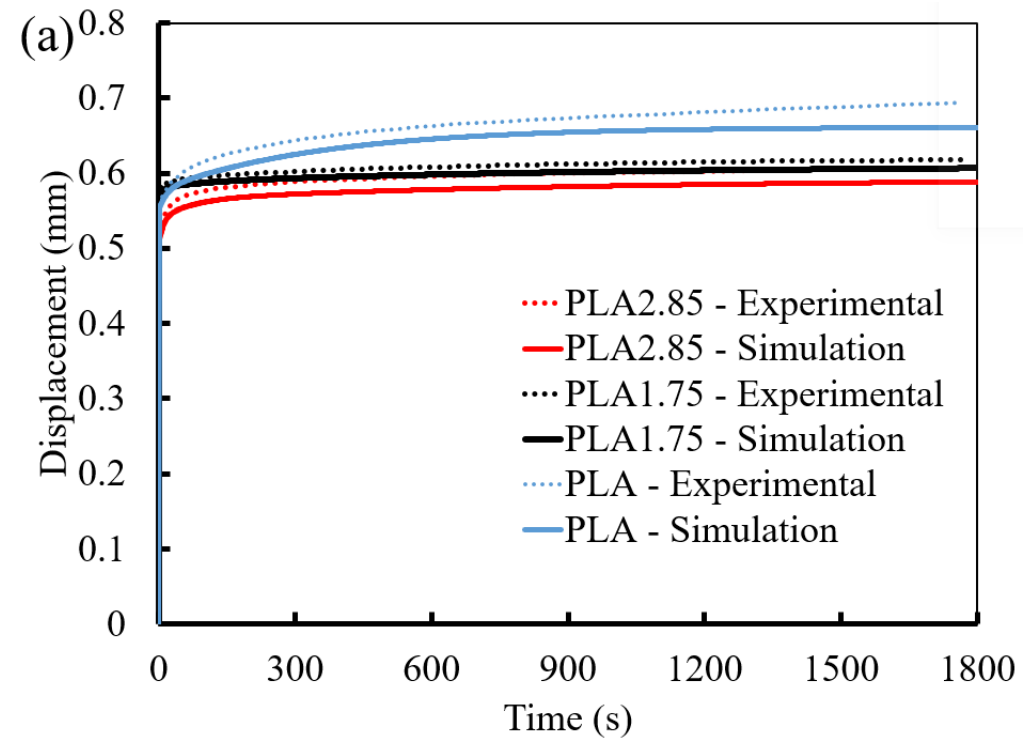
(a)
Displacement (mm)
0.8
0.7
0.6
0.5
0.4
0.3
0.2
0.1
0
0
300
600
900
1200
1500
1800
Time (s)
PLA2.85 - Experimental
PLA2.85 - Simulation
PLA1.75 - Experimental
PLA1.75 - Simulation
PLA - Experimental
PLA - Simulation

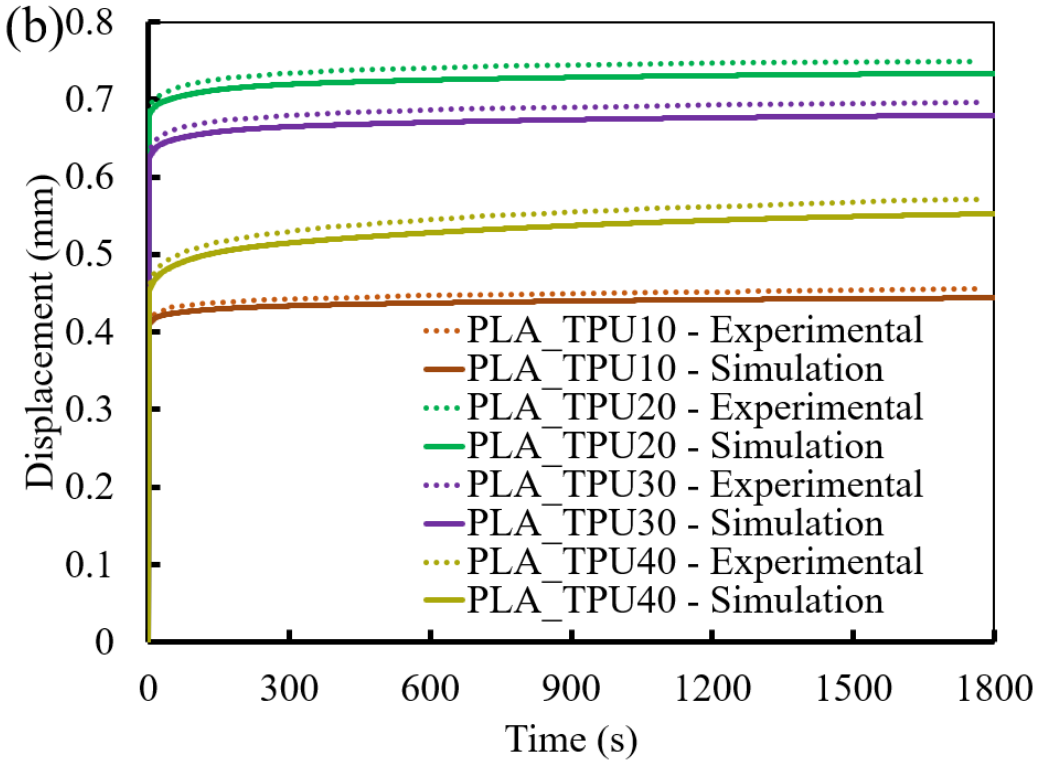
(b)
Displacement (mm)
0.8
0.7
0.6
0.5
0.4
0.3
0.2
0.1
0
0
300
600
900
1200
1500
1800
Time (s)
PLA_TPU10 - Experimental
PLA_TPU10 - Simulation
PLA_TPU20 - Experimental
PLA_TPU20 - Simulation
PLA_TPU30 - Experimental
PLA_TPU30 - Simulation
PLA_TPU40 - Experimental
PLA_TPU40 - Simulation

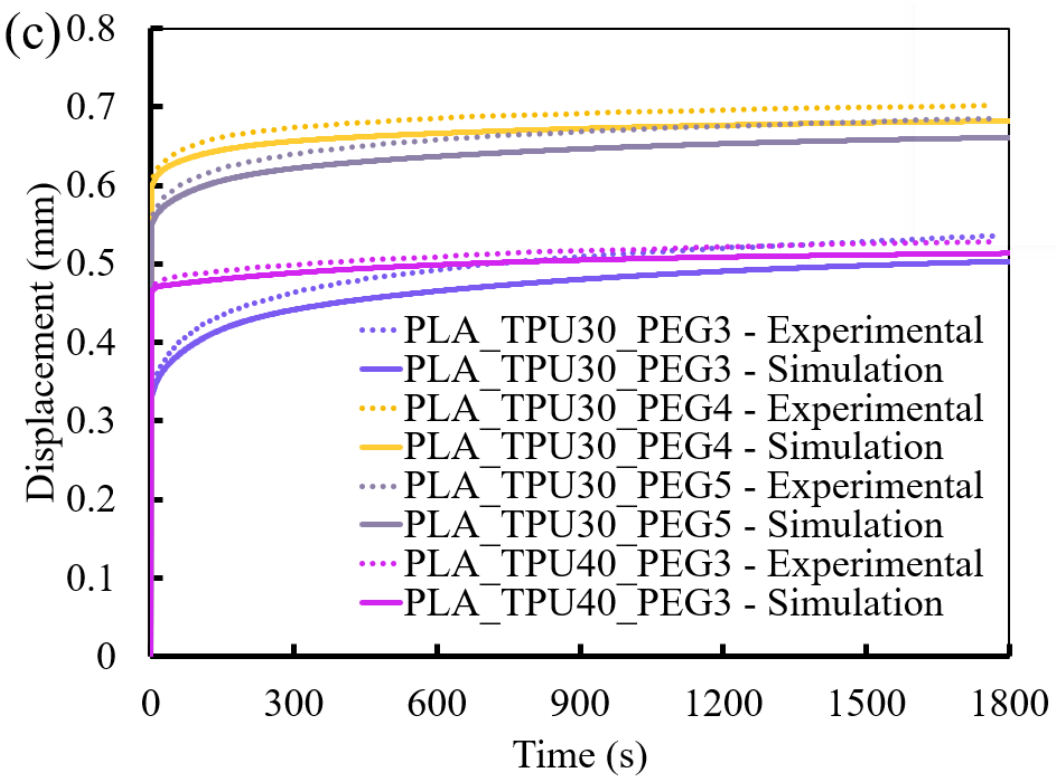

Figure 8.7. Comparison of creep displacements obtained from experiments and FEA.

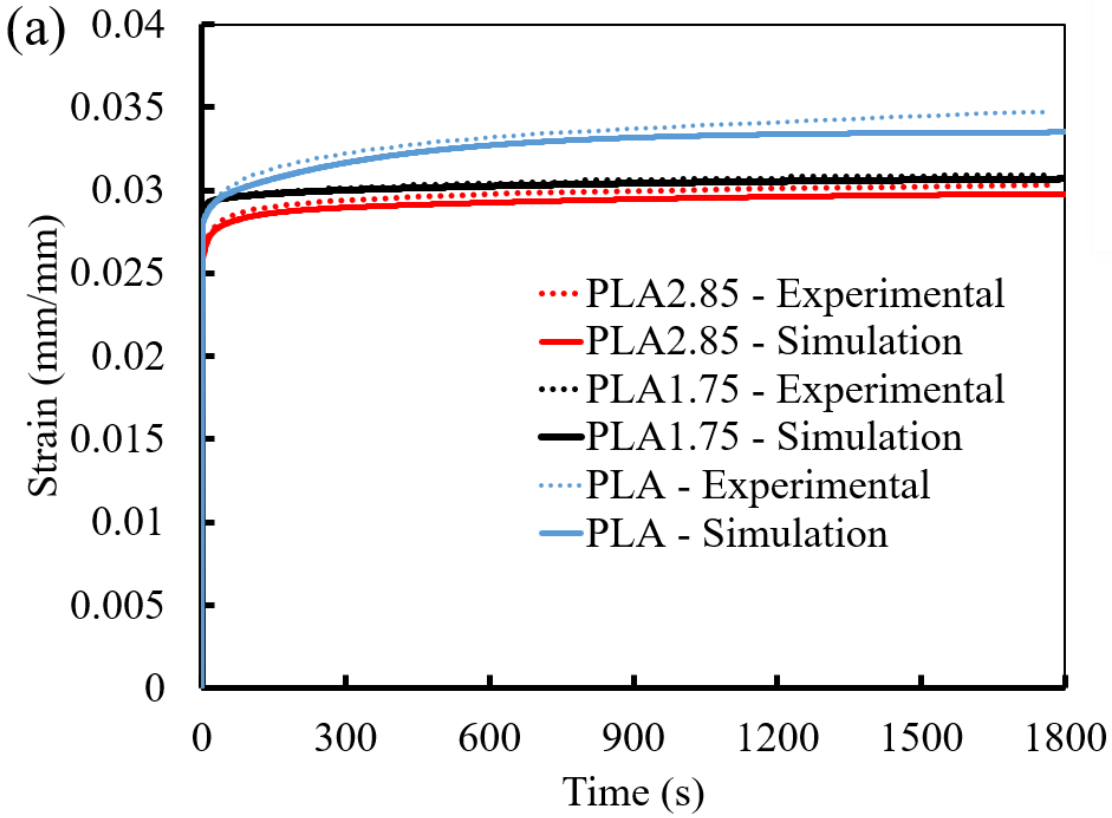

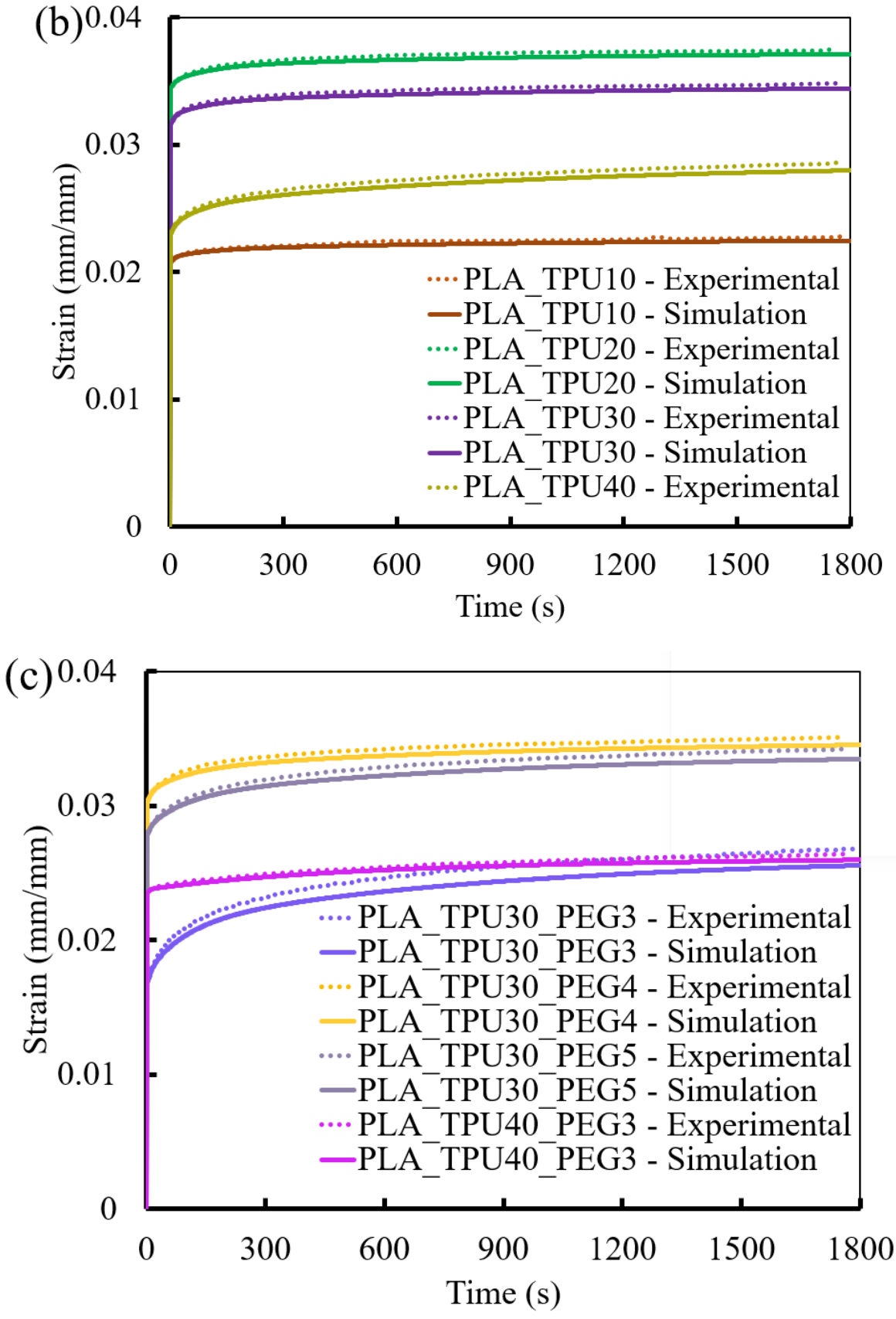

Figure 8.8. Comparison of strains obtained from experiments and FEA.

Table 8.4. Error percentages in displacements and strains obtained from experiments and FEA.

Samples	Displacements at different times (mm)			Strains at different times (mm/mm)		
	600 s	1200 s	1800 s	600 s	1200 s	1800 s
PLA2.85	a: 0.596 b: 0.578 c: 3.02	a: 0.603 b: 0.585 c: 2.98	a: 0.607 b: 0.588 c: 3.13	a: 0.0298 b: 0.0292 c: 2.01	a: 0.0301 b: 0.0296 c: 1.66	a: 0.0304 b: 0.0298 c: 1.97
PLA1.75	a: 0.608 b: 0.598 c: 1.64	a: 0.615 b: 0.604 c: 1.79	a: 0.617 b: 0.607 c: 1.62	a: 0.0304 b: 0.0302 c: 0.66	a: 0.0307 b: 0.0305 c: 0.65	a: 0.0309 b: 0.0307 c: 0.65
PLA	a: 0.663 b: 0.645 c: 2.71	a: 0.681 b: 0.685 c: -0.59	a: 0.694 b: 0.661 c: 4.75	a: 0.0332 b: 0.0327 c: 1.51	a: 0.0341 b: 0.0334 c: 2.05	a: 0.0347 b: 0.0335 c: 3.46
PLA_TPU10	a: 0.447 b: 0.437 c: 2.24	a: 0.451 b: 0.442 c: 1.99	a: 0.455 b: 0.444 c: 2.42	a: 0.0224 b: 0.0221 c: 1.34	a: 0.0226 b: 0.0223 c: 1.33	a: 0.0228 b: 0.0225 c: 1.32
PLA_TPU20	a: 0.741 b: 0.725 c: 2.16	a: 0.747 b: 0.731 c: 2.14	a: 0.749 b: 0.734 c: 2.00	a: 0.0370 b: 0.0367 c: 0.81	a: 0.0373 b: 0.0369 c: 1.07	a: 0.0375 b: 0.0371 c: 0.04
PLA_TPU30	a: 0.687 b: 0.670 c: 2.47	a: 0.693 b: 0.676 c: 2.45	a: 0.696 b: 0.679 c: 2.44	a: 0.0343 b: 0.0339 c: 1.17	a: 0.0346 b: 0.0342 c: 1.16	a: 0.0348 b: 0.0344 c: 1.15
PLA_TPU30_PEG3	a: 0.493 b: 0.465 c: 5.68	a: 0.520 b: 0.491 c: 5.58	a: 0.536 b: 0.503 **c: 6.16**	a: 0.0246 b: 0.0236 c: 4.06	a: 0.0260 b: 0.0249 c: 4.23	a: 0.0268 b: 0.0256 **c: 4.48**

PLA_TPU30_PEG4	a: 0.685 b: 0.666 c: 2.77	a: 0.695 b: 0.677 c: 2.59	a: 0.702 b: 0.682 c: 2.85	a: 0.0342 b: 0.0337 c: 1.46	a: 0.0347 b: 0.0342 c: 1.44	a: 0.0351 b: 0.0345 c: 1.71
PLA_TPU30_PEG5	a: 0.659 b: 0.637 c: 3.34	a: 0.675 b: 0.653 c: 3.26	a: 0.685 b: 0.661 c: 3.50	a: 0.0329 b: 0.0322 c: 2.13	a: 0.0337 b: 0.0331 c: 1.78	a: 0.0343 b: 0.0335 c: 2.33
PLA_TPU40	a: 0.545 b: 0.528 c: 3.12	a: 0.561 b: 0.544 c: 3.03	a: 0.572 b: 0.552 c: 3.50	a: 0.0272 b: 0.0267 c: 1.84	a: 0.0280 b: 0.0275 c: 1.79	a: 0.0286 b: 0.0279 c: 2.45
PLA_TPU40_PEG3	a: 0.509 b: 0.499 c: 1.96	a: 0.521 b: 0.509 c: 2.30	a: 0.529 b: 0.513 c: 3.02	a: 0.0254 b: 0.0252 c: 0.79	a: 0.0260 b: 0.0257 c: 1.15	a: 0.0264 b: 0.0259 c: 1.89

Note: 8.1. a – Experimental results, b – FEA results, and c – Error percentage.

8.5. Conclusions

In this work, customized composite filaments are manufactured using twin-screw extrusion method from pellets and powder. PLA is a material having high mechanical strength, and TPU is a polymer having high flexibility are used in the form of pellets and blended together. PEG powder is used as a plasticizer in varying proportions to enhance the properties of the composite filaments. The resulting composite filaments are used in 3D printing of the creep samples. The creep test is performed, and the computational model is developed and then the results are compared. The following conclusions can be drawn from this work:

(i) The tensile creep test is performed for all the 3D printed samples using polymer composite filaments manufactured. The creep displacements for all the samples are nearly 0.6 mm. This demonstrates that they have almost similar creep behaviors for the time tested although the polymers blended are of different nature. The reasons might be the application of lower force and a short time period of testing. Therefore, it is recommended to supply higher force and increase the test time period.

(ii) The experimental creep behavior is compared with that of computational model and found that the maximum error between the results is almost 6% among all the samples.

This proves that the model developed is showing a good correlation with the experiment, and thus is reliable to predict the creep behavior. This model can be used for other polymers and polymer composites manufactured from different methods such as 3D printing, injection molding and compression molding.

(iii) Only three terms of generalized Voigt-Kelvin and Maxwell model are used in this study and are still able to successfully predict the instantaneous elastic strain range, primary creep region, and secondary creep region. The tertiary creep region is not seen during the tests because of lower force and a short time period.

(iv) Although the computational model is able to predict the behavior with higher accuracy, it can still be improved by increasing the number of terms in the Prony series.

8.6. References

[1] J. Bochnia and S. Blasiak, "Stress relaxation and creep of a polymer-aluminum composite produced through selective laser sintering," *Polymers (Basel).*, vol. 12, no. 830, 2020, doi: 10.3390/POLYM12040830.

[2] X. Duan, H. Yuan, W. Tang, J. He, and X. Guan, "A phenomenological primary–secondary–tertiary creep model for polymer-bonded composite materials," *Polymers (Basel).*, vol. 13, no. 2353, pp. 1–19, 2021, doi: 10.3390/polym13142353.

[3] A. D. Drozdov, R. Høj Jermiin, and J. de Claville Christiansen, "Lifetime Predictions for High-Density Polyethylene under Creep: Experiments and Modeling," *Polymers (Basel).*, vol. 15, no. 2, 2023, doi: 10.3390/polym15020334.

[4] J. A. Jansen and J. N. Nemec, "Creep rupture failure under conditions of static strain," in *Proceedings of the Annual Technical Conference and Exhibition of the Society of Plastics Engineers (ANTEC 2014)*, 2014.

[5] G. G. Trantina, "Creep analysis of polymer structures," *Polymer Engineering & Science*, vol. 26, no. 11. pp. 776–780, 1986, doi: 10.1002/pen.760261109.

[6] J. Li and A. Dasgupta, "Failure-Mechanism Models for Creep and Creep Rupture," *IEEE Trans. Reliab.*, vol. 42, no. 3, pp. 339–353, 1993, doi: 10.1109/24.257816.

[7] R. M. Guedes, "Lifetime predictions of polymer matrix composites under constant or monotonic load," *Compos. Part A Appl. Sci. Manuf.*, vol. 37, no. 5, pp. 703–715, 2006, doi: 10.1016/j.compositesa.2005.07.007.

[8] A. Chudnovsky, Z. Zhou, H. Zhang, and K. Sehanobish, "Lifetime assessment of engineering thermoplastics," *Int. J. Eng. Sci.*, vol. 59, pp. 108–139, 2012, doi: 10.1016/j.ijengsci.2012.03.016.

[9] E. Lainé, C. Bouvy, J. C. Grandidier, and G. Vaes, “Methodology of Accelerated Characterization for long-term creep prediction of polymer structures to ensure their service life,” *Polym. Test.*, vol. 79, no. 106050, 2019, doi: 10.1016/j.polymertesting.2019.106050.

[10] M. Sattar, A. R. Othman, S. Kamaruddin, M. Akhtar, and R. Khan, “Limitations on the computational analysis of creep failure models: A review,” *Eng. Fail. Anal.*, vol. 134, no. 105968, 2022, doi: 10.1016/j.engfailanal.2021.105968.

[11] K. C. Hung, T. L. Wu, Y. L. Chen, and J. H. Wu, “Assessing the effect of wood acetylation on mechanical properties and extended creep behavior of wood/recycled-polypropylene composites,” *Constr. Build. Mater.*, vol. 108, pp. 139–145, 2016, doi: 10.1016/j.conbuildmat.2016.01.039.

[12] X. Wang, J. Shi, J. Liu, L. Yang, and Z. Wu, “Creep behavior of basalt fiber reinforced polymer tendons for prestressing application,” *Mater. Des.*, vol. 59, pp. 558–564, 2014, doi: 10.1016/j.matdes.2014.03.009.

[13] S. Park, W. Shou, L. Makatura, W. Matusik, and K. (Kelvin) Fu, “3D printing of polymer composites: Materials, processes, and applications,” *Matter*, vol. 5, no. 1, pp. 43–76, 2022, doi: 10.1016/j.matt.2021.10.018.

[14] A. Jayswal and S. Adanur, “Characterization of polylactic acid/thermoplastic polyurethane composite filaments manufactured for additive manufacturing with fused deposition modeling,” *J. Thermoplast. Compos. Mater.*, pp. 1–22, 2021, doi: 10.1177/08927057211062561.

[15] R. Singh, R. Kumar, Pawanpreet, M. Singh, and J. Singh, “On mechanical, thermal and morphological investigations of almond skin powder-reinforced polylactic acid feedstock filament,” *J. Thermoplast. Compos. Mater.*, vol. 35, no. 2, pp. 230–248, 2022, doi: 10.1177/0892705719886010.

[16] J. Holbery and D. Houston, “Natural-fiber-reinforced polymer composites in automotive applications,” *JOM*, vol. 58, no. 11, pp. 80–86, 2006, doi: 10.1007/s11837-006-0234-2.

[17] M. J. John and S. Thomas, “Biofibres and biocomposites,” *Carbohydr. Polym.*, vol. 71, no. 3, pp. 343–364, 2008, doi: https://doi.org/10.1016/j.carbpol.2007.05.040.

[18] M. M. A. Nassar, R. Arunachalam, and K. I. Alzebdeh, “Machinability of natural fiber reinforced composites: a review,” *Int. J. Adv. Manuf. Technol.*, vol. 88, no. 9, pp. 2985–3004, 2017, doi: 10.1007/s00170-016-9010-9.

[19] M. Adam Khan and A. Senthil Kumar, “Machinability of glass fibre reinforced plastic (GFRP) composite using alumina-based ceramic cutting tools,” *J. Manuf. Process.*, vol.

13, no. 1, pp. 67–73, 2011, doi: https://doi.org/10.1016/j.jmapro.2010.10.002.

[20] A. Lotfi, H. Li, D. V. Dao, and G. Prusty, “Natural fiber–reinforced composites: A review on material, manufacturing, and machinability,” *J. Thermoplast. Compos. Mater.*, vol. 34, no. 2, pp. 238–284, Apr. 2019, doi: 10.1177/0892705719844546.

[21] V. A. Yiga, S. Pagel, M. Lubwama, S. Epple, P. W. Olupot, and C. Bonten, “Development of fiber-reinforced polypropylene with NaOH pretreated rice and coffee husks as fillers: Mechanical and thermal properties,” *J. Thermoplast. Compos. Mater.*, vol. 33, no. 9, pp. 1269–1291, 2020, doi: 10.1177/0892705718823255.

[22] A. Jayswal, J. Liu, G. Harris, and S. Adanur, “Thermo-mechanical properties of composite filaments for 3D printing of fabrics,” *J. Thermoplast. Compos. Mater.*, pp. 1–26, 2023, doi: 10.1177/08927057231163489.

[23] Y. Zhou, L. Luo, W. Liu, G. Zeng, and Y. Chen, “Preparation and Characteristic of PC/PLA/TPU Blends by Reactive Extrusion,” *Adv. Mater. Sci. Eng.*, pp. 1–9, 2015, doi: 10.1155/2015/393582.

[24] V. Jašo, M. V. Rodić, and Z. S. Petrović, “Biocompatible fibers from thermoplastic polyurethane reinforced with polylactic acid microfibers,” *European Polymer Journal*, vol. 63. pp. 20–28, 2015, doi: 10.1016/j.eurpolymj.2014.11.041.

[25] H. Y. Mi *et al.*, “Characterization of thermoplastic polyurethane/polylactic acid (TPU/PLA) tissue engineering scaffolds fabricated by microcellular injection molding,” *Mater. Sci. Eng. C*, vol. 33, no. 8, pp. 4767–4776, 2013, doi: 10.1016/j.msec.2013.07.037.

[26] F. Feng and L. Ye, “Morphologies and mechanical properties of polylactide/thermoplastic polyurethane elastomer blends,” *J. Appl. Polym. Sci.*, vol. 119, no. 5, pp. 2778–2783, Mar. 2011, doi: 10.1002/app.32863.

[27] D. Xu, K. Yu, K. Qian, and C. B. Park, “Foaming behavior of microcellular poly(lactic acid)/TPU composites in supercritical CO2,” *J. Thermoplast. Compos. Mater.*, vol. 31, no. 1, pp. 61–78, 2018, doi: 10.1177/0892705716679480.

[28] C. Kaynak and S. D. Varsavas, “Performance comparison of the 3D-printed and injection-molded PLA and its elastomer blend and fiber composites,” *J. Thermoplast. Compos. Mater.*, vol. 32, no. 4, pp. 501–520, 2019, doi: 10.1177/0892705718772867.

[29] Y. Wang *et al.*, “Measurement of viscoelastic properties for polymers by nanoindentation,” *Polym. Test.*, vol. 83, no. 106353, 2020, doi: 10.1016/j.polymertesting.2020.106353.

Chapter 9
Summary and potential future works

9.1. Summary

Additive manufacturing (AM) is transforming the manufacturing industries and getting popular in several applications including textiles, electronics, aerospace, automotives, and sports. It allows to fabricate the complex objects depending on the CAD model and appropriate print settings. It has been adopted in almost every industry for fabricating prototypes or for research work. It makes the manufacturing faster and minimizes waste generation.

Fabrics and clothing are one of the basic needs of human beings. With the increase in global human population, the demand for fabrics and clothing is skyrocketing and should be fulfilled immediately. Therefore, the growth in textile industries has led to a high level of consumption and waste generation. Most fabrics are dumped as landfills after consumption and remains in the soil for decades, contributing to solid waste production. Fabric waste is one of the major sources of pollution in the world. Moreover, the traditional manufacturing methods are quite complicated, expensive, and time-consuming. It should also be kept in mind that soon the globe will not be able to handle additional solid waste anymore. Hence, a scientific selection of materials, and manufacturing processes comes into play.

In this dissertation, the design and additive manufacturing of fabric structures is proposed in the first part. In addition, novel polymer materials are also manufactured to use in 3D printing of the structures. The first part of the dissertation constitutes chapter 3, chapter 4 and chapter 5, whereas the second part constitutes chapter 6, chapter 7 and chapter 8.

In chapter 2, a literature review on current AM methods and materials which are commonly used for fabrication of flexible structures such as fabrics was presented. FDM and SLS methods were reviewed for 3D printing of fabrics, and DIW for 3D printing of flexible electronic components. The most common materials used are PLA, ABS, TPU and nylon. Different fabric designs have been investigated by the researchers. Some of the designs are plain weave, knitted, braided and many other innovative structures. Most of the researchers have only 3D printed structures and have not their mechanical properties. Moreover, literature also lacks studies on printing process parameters. This creates a future research direction on 3D printing of fabrics.

In Chapter 3, different complex fabric structures such as plain weave, twill weave, weft-knitted fabrics and braid structures were designed, and 3D printed using fused deposition modeling (FDM) method. Poly(lactic) acid (PLA) filament was used in this research to fabricate the samples. The weft knitted fabrics were 3D printed in horizontal orientation whereas the plain weave, twill weave and braid designs were 3D printed in vertical orientation. The mechanical test results showed that the warp yarns are stronger than the weft yarns, which results in a stronger fabric in warp direction. It was also found that the knitted fabrics had good flexibility in both course and wale directions, but the flexural strength in course direction is significantly lower than in wale direction. The compression tests on braids revealed that they are capable of holding failure displacement of more than 25 mm. The microscopic images revealed that the printed samples contained voids which contributed to the reduction in mechanical properties.

In chapter 4, a post-processing method is proposed to improve the mechanical property of 3D printed 2/1 twill weave and dog-bone samples. For this purpose, heat treatment method was adopted, and the samples were heated treated at various temperatures (50 ℃, 75 ℃, 100 ℃, 125 ℃) for 1 hour. This research investigated the effects of heat treatment on mechanical properties and crystallinity for 3D printed samples. It was found that the mechanical properties of 3D printed samples depend on heat treatment at various temperatures and the geometry of the structure. When the samples were heated above the glass transition temperature, their crystallinity increased. The reason might be due to increased polymeric chain mobility and sufficient time to recrystallize, which lacked during 3D printing process. Due to the interlacing nature of the fabrics, a significant improvement in mechanical properties were not observed although crystallinity was increased. On the other hand, the mechanical properties and crystallinity both increased for dog-bone samples.

In chapter 5, a multi-physics computational model was used to predict a coupled thermal-mechanical-viscoelastic properties of 3D printed fabrics. In this research, a unit cell of plain weave fabric structure is 3D printed using PLA. The tensile and compression properties were experimentally characterized in a closed thermal chamber maintained at temperatures of 60 ℃, 65 ℃, and 70 ℃. The computational model was employed to replicate the experiments and then the results were compared. It was found that the error percentages in the peak forces were 23.60% at 60 ℃, −8.85 % at 65 ℃, and –6.25 % at 70 ℃. A better agreement in peak

forces was seen for unit cells above T_g. Hence, this computational model was further used to predict the behavior of a larger fabric structure having 6 warp yarns and 6 weft yarns.

In chapter 6, a novel PLA/TPU composite filaments were manufactured, and the mechanical and chemical properties were characterized. It was investigated that the ultimate tensile strength and stiffnesses decreased for all the samples whereas the elongation increased significantly. This might have happened due to the presence of the soft segment of TPU. The thermal analysis showed the presence of phase difference between the polymers which indicates their immiscibility. However, a small improvement in the immiscibility was also observed. The thermogravimetric graphs demonstrated that the onset of thermal decomposition is 367 ℃ for pure PLA and lower for composite samples and displayed multi-stage degradation of the samples due to the presence of various functional groups having different thermal decomposition behavior. The DSC results showed that the crystallinity of the samples increased which was also seen under polarized optical microscope (POM).

In chapter 7, the effect of a plasticizer such as PEG in the PLA/TPU composite filaments were studied. The amount of TPU was fixed to either 30 % or 40 %, and PLA and PEG were added in varying amount. It decreased the yield strength of the materials, but the UTS was almost in the same range as that of pure PLA filament. The Young's modulus decreased as compared to PLA, whereas the elongation at break increased by more than 550 %. The presence of soft segment of TPU and the plasticizing effect of PEG might have played an important role to increase the elongation. The thermal analysis indicated that the glass transition temperature of the samples remained almost similar. The onset thermal degradation temperature of composite filaments was around 285 ℃ which is slightly lower than that of pure PLA filaments. The thermo-mechanical tests revealed that the pure PLA filament held higher storage modulus lower initial loss modulus among all the samples. The addition of TPU and PEG increased the molecular friction which might have caused higher loss modulus of the composite filaments. FTIR results demonstrated that the filaments were not affected by the chemical reaction between the different functional groups of the polymers. Finally, a plain weave fabric structure was 3D printed using the PLA_TPU30_PEG5 composite filament and demonstrated the feasibility of the manufactured filaments in 3D printing applications.

In chapter 8, the creep behavior of composite filaments manufactured previously in chapters 6 and 7 were studied using experiment and computational modeling. The composite filaments were used in 3D printing of the creep samples. The creep test is performed using

Instron 5565 universal testing machine under a constant load of 100 N, and the displacement and strain graphs as a function of time were generated. To develop the computational model, three terms of Prony series were considered. Finally, the results obtained from experiments and computation were compared and found that the maximum error between the results is almost 6 % among all the samples. This verifies that the model developed is reliable to predict the creep response of 3D printed polymers. This model and the procedures proposed can also be used to predict the creep response of materials manufactured from other methods such as injection molding and compression molding.

9.2. Potential future works

Since the research on additive manufacturing of fabrics is new and this dissertation will contribute to the knowledge of 3D printing of fabrics and materials. As a result, the whole additive manufacturing, materials, and textile industry will benefit. However, a very broad domain of research has been opened with this dissertation. Following are the potential future works that can be performed to move a step forward to realize the feasibility of 3D printed fabrics.

- Chapter 3: In this work, 2/1 twill weave fabric structure is studied and the yarns used were 1 mm in diameter, and the spacing between them is 3 mm (figure 3.10). The weft knitted fabric structure studied had yarn diameter of 2.54 mm and height of each loop is 27.14 mm (figure 3.15). All the braid structures had a yarn diameter of 2 mm (Figure 3.17). The diameter of the yarns, yarn spacing, and height of loop are high. The density of yarns can be increased by decreasing the diameter and the spacing between them to make the design close to a real fabric. In addition, the design of experiments (DOE) method can be adopted to explore the process-structure-properties relationships of products. This project can be further extended to 3D print a large fabric structure and join them together by polymer welding, soldering, sewing or some other innovative methods to make them wearable.

  The samples manufactured using the FDM method were fragile and brittle in nature and did not hold good mechanical properties. In the future works, the additive manufacturing of fabrics using elastomeric and flexible filaments is recommended. Some other 3D printing methods such as direct ink writing (DIW) can also be considered. This method requires hydrogel or ink. Therefore, another research topic can be based on the manufacture of appropriate hydrogel or ink to perform this activity.

- Chapter 4: This research topic focused on the post-processing method to improve the mechanical properties of final products. 2/1 twill weave fabric structures were considered for this study. The samples were heat treated at different temperatures for 1 hour, and the mechanical properties and crystallinity were studied. Although the crystallinity of the samples increased, the mechanical properties were not improved. The reasons might be the curved geometry and the presence of voids in them. In the future works, research can be conducted to reduce the voids and porosity of yarns so that the mechanical properties can be improved. In addition, the study on the effect of different heat treatment times such as 10 minutes, 30 minutes, 2 hours etc. can be studied. This project can be further extended to study the other fabric designs such as plain weave, weft-knitted, braids, basket, and satin.
- Chapter 5: In this research, the yarns were modeled to slightly touch each other. Hence, this model can be modified such that the yarns can slide over each other, and coefficient of friction can be considered. In addition, the current work focuses on a coupled thermo-mechanical-viscoelastic properties only above T_g. Therefore, it is recommended to work with temperatures below it and at room temperature as well.

  This work focused only on plain weave fabrics and that's why a lot of research work is remaining for other different fabric designs.
- Chapter 6 and 7: These studies found that the yield strength and the stiffness of the material decreased significantly although the elongation at break increased by more than 550 %. Extensive research is required to achieve higher mechanical strength. Bacterial cellulose, for example, can be studied in this regard. The addition of PEG decreased the crystallinity of the materials, and the compatibility is still not good. Hence, research is required to increase crystallinity and improve the compatibility of the polymers as well.
- Chapter 8: The creep behavior of 3D printed composite filaments were studied at room temperature. It should be noted that the materials are exposed to different environmental conditions such as high or low temperature, and moisture. The effects of these parameters were not studied, which could be a potential future work. In addition, the creep performance of 3D printed and heat-treated materials is also required to study. Heat treatment is generally conducted to improve the mechanical properties of the materials.

Appendix A

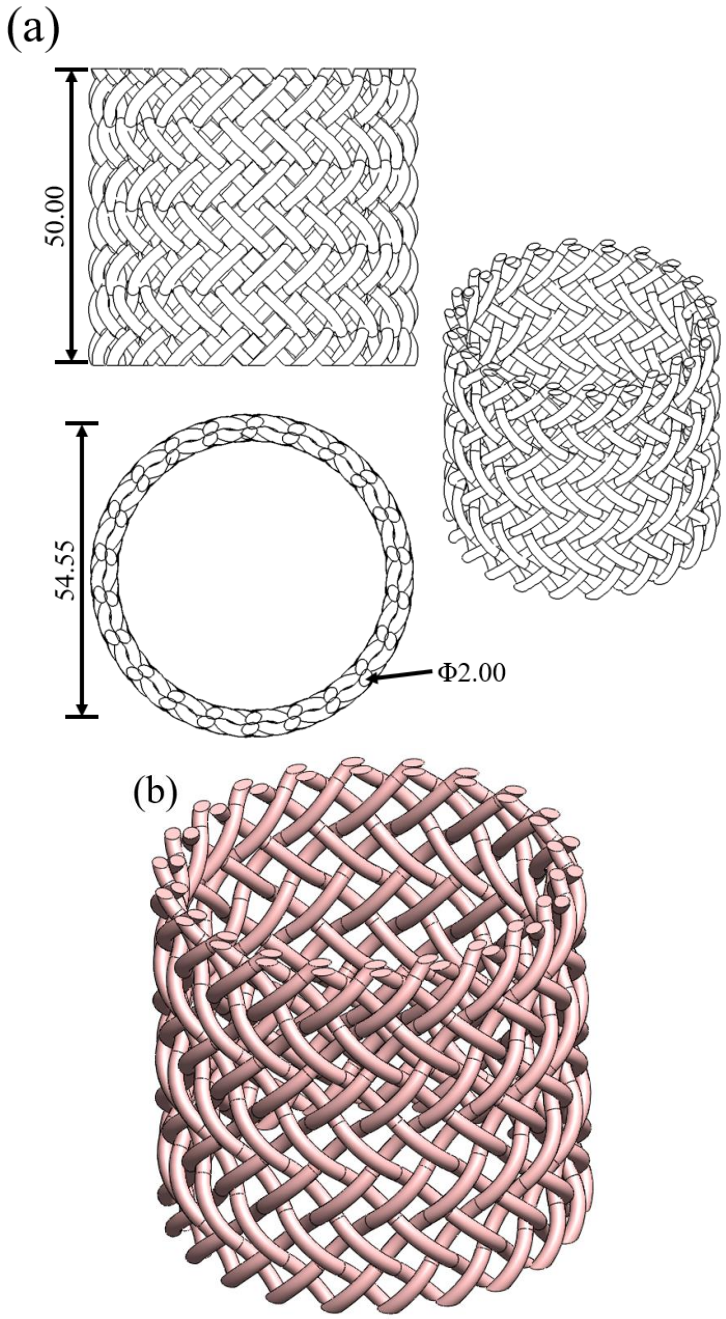

Figure A1. Design and CAD modeling of regular braid. (a) Design of braid, and (b) 3D model of braid. The dimensions are given in millimeters (mm).

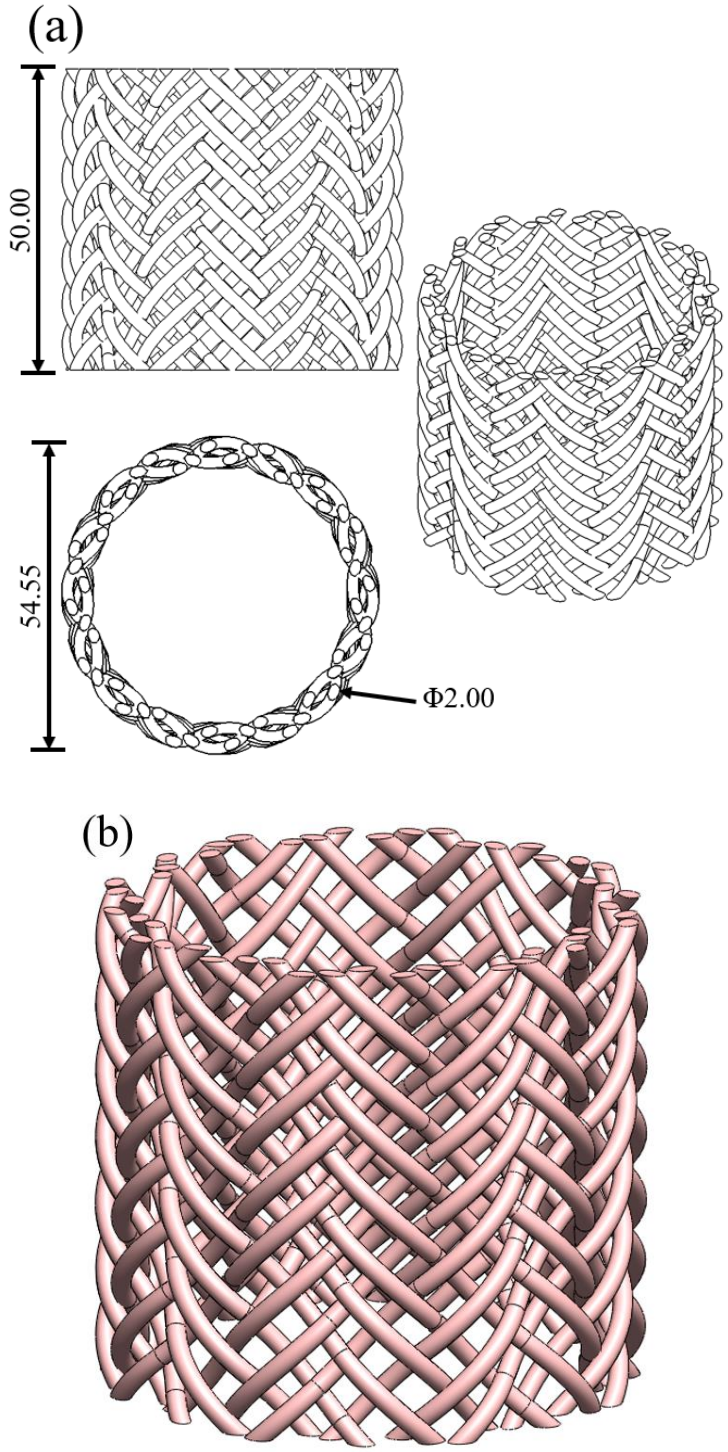

Figure A2. Design and CAD modeling of Hercules braid. (a) Design of braid, and (b) 3D model of braid. The dimensions are given in millimeters (mm).

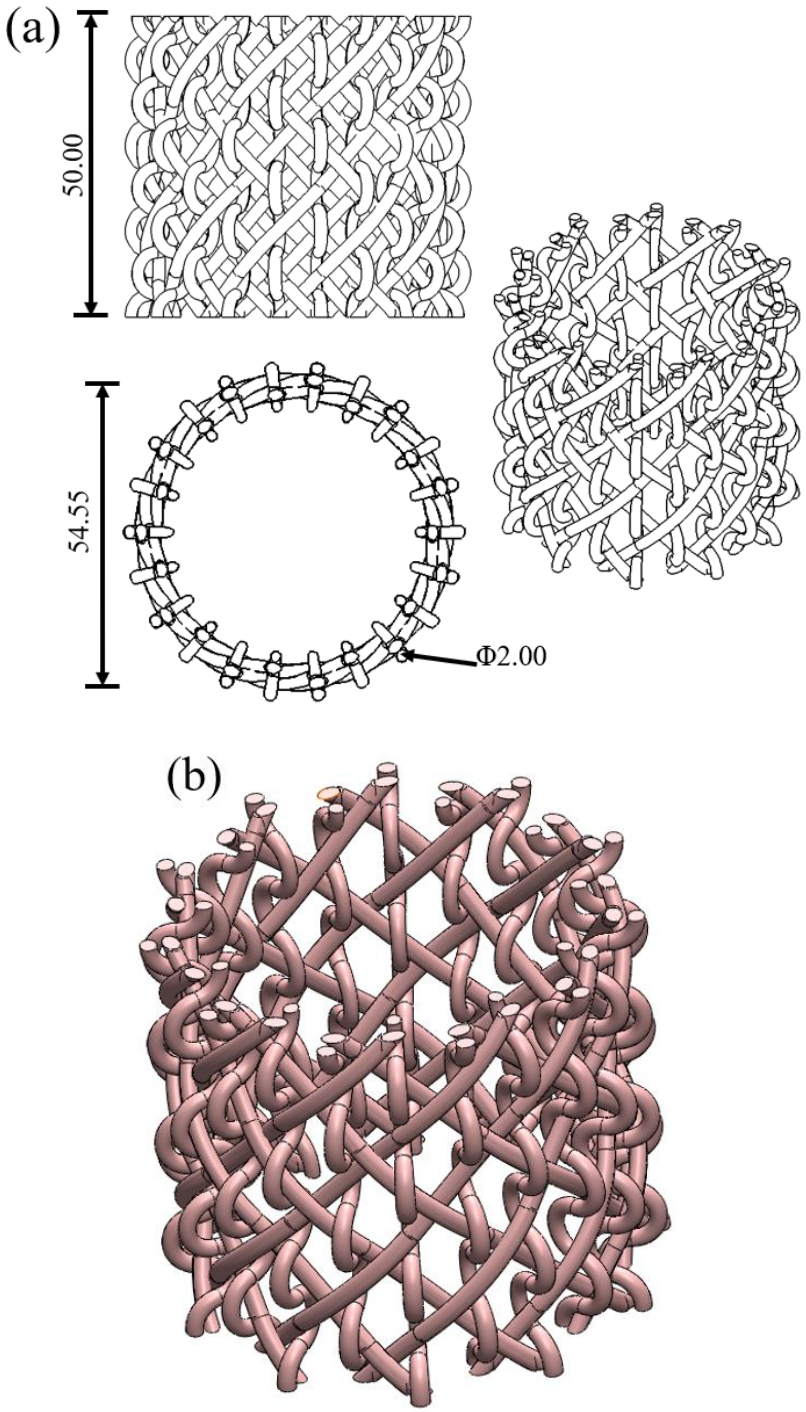

Figure A3. Design and CAD modeling of triaxial braid. (a) Design of braid, and (b) 3D model of braid. The dimensions are given in millimeters (mm).

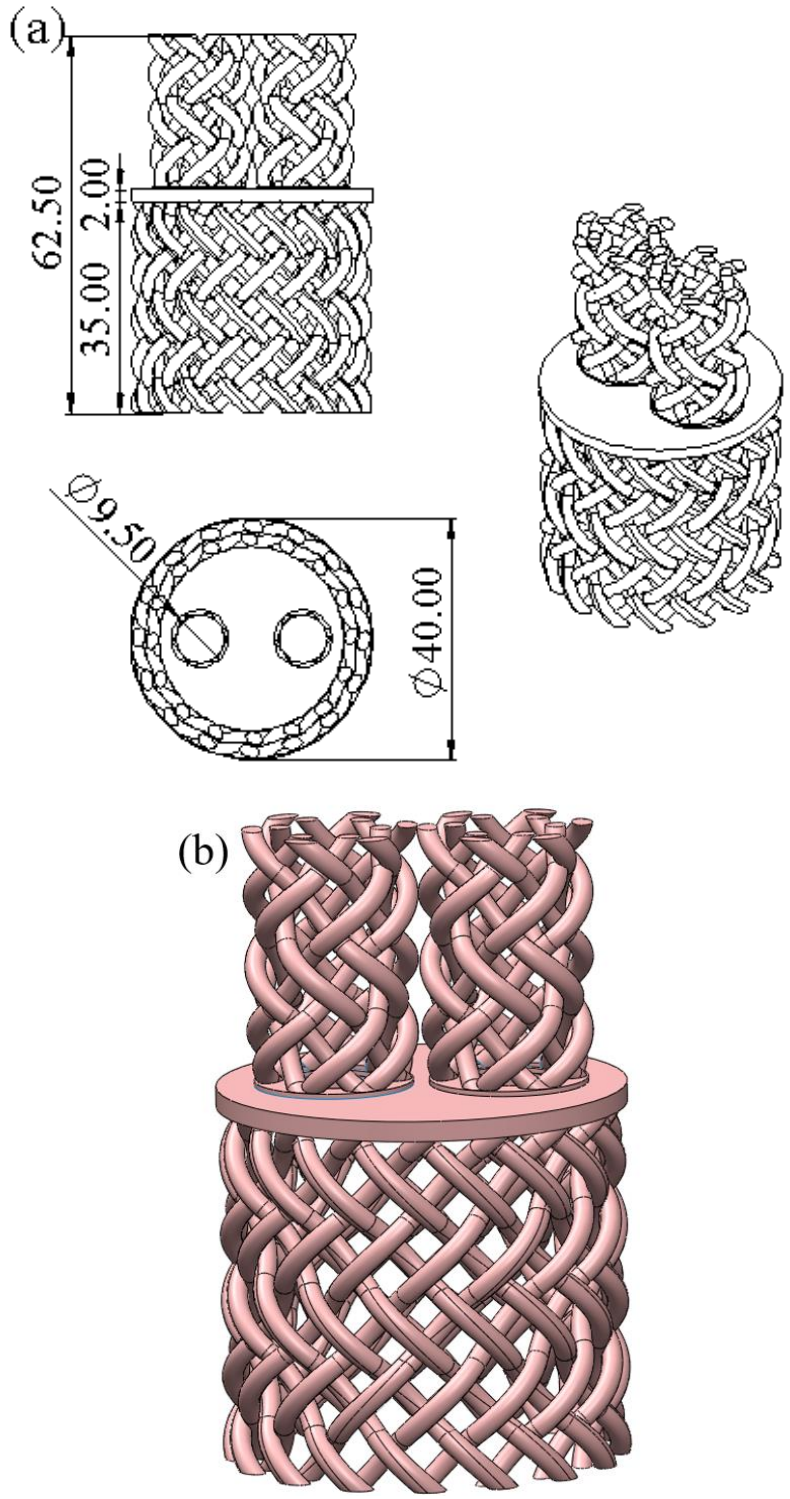

Figure A4. Design and CAD modeling of bifurcated braid. (a) Design of braid, and (b) 3D model of braid. The dimensions are given in millimeters (mm).

Appendix B

Table B1. Mechanical properties of the composite filaments manufactured for 30 wt% of TPU and varying wt% of PEG (mean ± standard error).

Samples	Yield Stress (σ_y) (MPa)	Ultimate Tensile Stress (UTS) (MPa)	Young's Modulus, E (MPa)	Elongation at break (%)
Pure PLA	47.52 ± 2.37	49.83 ± 1.26	2511.77 ± 115.50	4.64 ± 0.16
PLA_TPU30_PEG0.5	27.78 ± 1.45	45.20 ± 2.16	1541.71 ± 46.83	386.75 ± 8.55
PLA_TPU30_PEG1	27.74 ± 3.12	42.22 ± 2.80	1470.16 ± 129.68	350.61 ± 14.73
PLA_TPU30_PEG2	28.04 ± 2.15	47.16 ± 2.32	1773.04 ± 66.80	477.79 ± 13.00
PLA_TPU30_PEG3	29.10 ± 3.69	50.27 ± 3.47	1982.63 ± 73.71	477.74 ± 22.91
PLA_TPU30_PEG4	27.33 ± 1.25	55.36 ± 0.77	1849.22 ± 76.99	530.41 ± 6.40
PLA_TPU30_PEG5	26.10 ± 2.65	58.78 ± 2.73	1705.34 ± 41.89	562.07 ± 22.45

Table B2. Mechanical properties of the composite filaments manufactured for 40 wt% of TPU and varying wt% of PEG (mean ± standard error).

Samples	Yield Stress (σ_y) (MPa)	Ultimate Tensile Stress (UTS) (MPa)	Young's Modulus, E (MPa)	Elongation at break (%)
Pure PLA	47.52 ± 2.37	49.83 ± 1.26	2511.77 ± 115.50	4.64 ± 0.16
PLA_TPU40_PEG0.5	23.00 ± 4.36	51.63 ± 3.50	1518.85 ± 73.20	486.32 ± 10.94
PLA_TPU40_PEG1	30.44 ± 5.33	54.94 ± 2.01	1548.20 ± 80.48	495.82 ± 6.26
PLA_TPU40_PEG3	30.70 ± 3.75	55.90 ± 2.32	1796.84 ± 60.60	460.85 ± 7.71
PLA_TPU40_PEG4	26.05 ± 2.60	55.34 ± 1.28	1643.45 ± 128.80	512.79 ± 6.02

Table B3. p-value obtained from multiple comparison of Ultimate Tensile Stress (UTS) between PLA and the composite filaments having 30 wt% of TPU and varying wt % of PEG using Tukey test.

Samples	Pure PLA	PLA_TPU 30_PEG0.5	PLA_TPU 30_PEG1	PLA_TPU 30_PEG2	PLA_TPU 30_PEG3	PLA_TPU 30_PEG4	PLA_TPU 30_PEG5
Pure PLA		0.80865	0.29657	0.98372	1	0.65552	0.14566
PLA_TPU30 _PEG0.5	0.80865		0.97199	0.9968	0.73784	0.06944	0.00614
PLA_TPU30 _PEG1	0.29657	0.97199		0.76009	0.23881	0.00859	6.07543E-4
PLA_TPU30 _PEG2	0.98372	0.9968	0.76009		0.96543	0.22029	0.02594
PLA_TPU30 _PEG3	1	0.73784	0.23881	0.96543		0.73372	0.18623
PLA_TPU30 _PEG4	0.65552	0.06944	0.00859	0.22029	0.73372		0.94565
PLA_TPU30 _PEG5	0.14566	0.00614	6.07543E-4	0.02594	0.18623	0.94565	

Table B4. p-value obtained from multiple comparison of Ultimate Tensile Stress (UTS) between PLA and the composite filaments having 40 wt% of TPU and varying wt % of PEG using Tukey test.

Samples	Pure PLA	PLA_TPU40 _PEG0.5	PLA_TPU40 _PEG1	PLA_TPU40 _PEG3	PLA_TPU40 _PEG4
Pure PLA		0.97802	0.50296	0.3377	0.43036

PLA_TPU40_PEG0.5	0.97802		0.82941	0.66251	0.76445
PLA_TPU40_PEG1	0.50296	0.82941		0.99797	0.99994
PLA_TPU40_PEG3	0.3377	0.66251	0.99797		0.99976
PLA_TPU40_PEG4	0.43036	0.76445	0.99994	0.99976	

Table B5. p-value obtained from multiple comparison of Young's Modulus (E) between PLA and the composite filaments having 30 wt% of TPU and varying wt % of PEG using Tukey test.

Samples	Pure PLA	PLA_TPU30_PEG0.5	PLA_TPU30_PEG1	PLA_TPU30_PEG2	PLA_TPU30_PEG3	PLA_TPU30_PEG4	PLA_TPU30_PEG5
Pure PLA		1.84008E-7	6.58981E-8	2.11752E-5	0.00224	1.15441E-4	4.79522E-6
PLA_TPU30_PEG0.5	1.84008E-7		0.99633	0.47439	0.01471	0.17223	0.81258
PLA_TPU30_PEG1	6.58981E-8	0.99633		0.18507	0.00323	0.04983	0.45506
PLA_TPU30_PEG2	2.11752E-5	0.47439	0.18507		0.58728	0.99484	0.99729
PLA_TPU30_PEG3	0.00224	0.01471	0.00323	0.58728		0.91752	0.26927
PLA_TPU30_PEG4	1.15441E-4	0.17223	0.04983	0.99484	0.91752		0.8865
PLA_TPU30_PEG5	4.79522E-6	0.81258	0.45506	0.99729	0.26927	0.8865	

Table B6. p-value obtained from multiple comparison of Young's Modulus (E) between PLA and the composite filaments having 40 wt% of TPU and varying wt % of PEG using Tukey test.

Samples	Pure PLA	PLA_TPU40_PEG0.5	PLA_TPU40_PEG1	PLA_TPU40_PEG3	PLA_TPU40_PEG4
Pure PLA		3.65957E-6	5.71381E-6	2.9884E-4	2.49828E-5
PLA_TPU40_PEG0.5	3.65957E-6		0.99945	0.27437	0.88417
PLA_TPU40_PEG1	5.71381E-6	0.99945		0.37746	0.9526
PLA_TPU40_PEG3	2.9884E-4	0.27437	0.37746		0.78499
PLA_TPU40_PEG4	2.49828E-5	0.88417	0.9526	0.78499	

Table B7. p-value obtained from multiple comparison of Elongation at break (%) between PLA and the composite filaments having 30 wt% of TPU and varying wt % of PEG using Tukey test.

Samples	Pure PLA	PLA_TPU30_PEG0.5	PLA_TPU30_PEG1	PLA_TPU30_PEG2	PLA_TPU30_PEG3	PLA_TPU30_PEG4	PLA_TPU30_PEG5
Pure PLA		1.61481E-7	2.59259E-8	7.39683E-9	7.39857E-9	0	0
PLA_TPU30_PEG0.5	1.61481E-7		0.60345	0.00273	0.00274	3.507E-6	1.1206E-7
PLA_TPU30_PEG1	2.59259E-8	0.60345		2.7617E-5	2.77785E-5	7.87163E-8	3.94822E-8
PLA_TPU30_PEG2	7.39683E-9	0.00273	2.7617E-5		1	0.19137	0.00627

PLA_TPU30_PEG3	7.39857E-9	0.00274	2.77785E-5	1		0.1906	0.00623
PLA_TPU30_PEG4	0	3.507E-6	7.87163E-8	0.19137	0.1906		0.73381
PLA_TPU30_PEG5	0	1.1206E-7	3.94822E-8	0.00627	0.00623	0.73381	

Table B8. p-value obtained from multiple comparison of Elongation at break (%) between PLA and the composite filaments having 40 wt% of TPU and varying wt % of PEG using Tukey test.

Samples	Pure PLA	PLA_TPU40_PEG0.5	PLA_TPU40_PEG1	PLA_TPU40_PEG3	PLA_TPU40_PEG4
Pure PLA		0	0	0	0
PLA_TPU40_PEG0.5	0		0.87721	0.12491	0.10387
PLA_TPU40_PEG1	0	0.87721		0.01841	0.46728
PLA_TPU40_PEG3	0	0.12491	0.01841		4.25241E-4
PLA_TPU40_PEG4	0	0.10387	0.46728	4.25241E-4	

Appendix C

Figure C1 presents the heat/cool/heat cycle of PLA and the composite filaments manufactured by using twin-screw extruders.

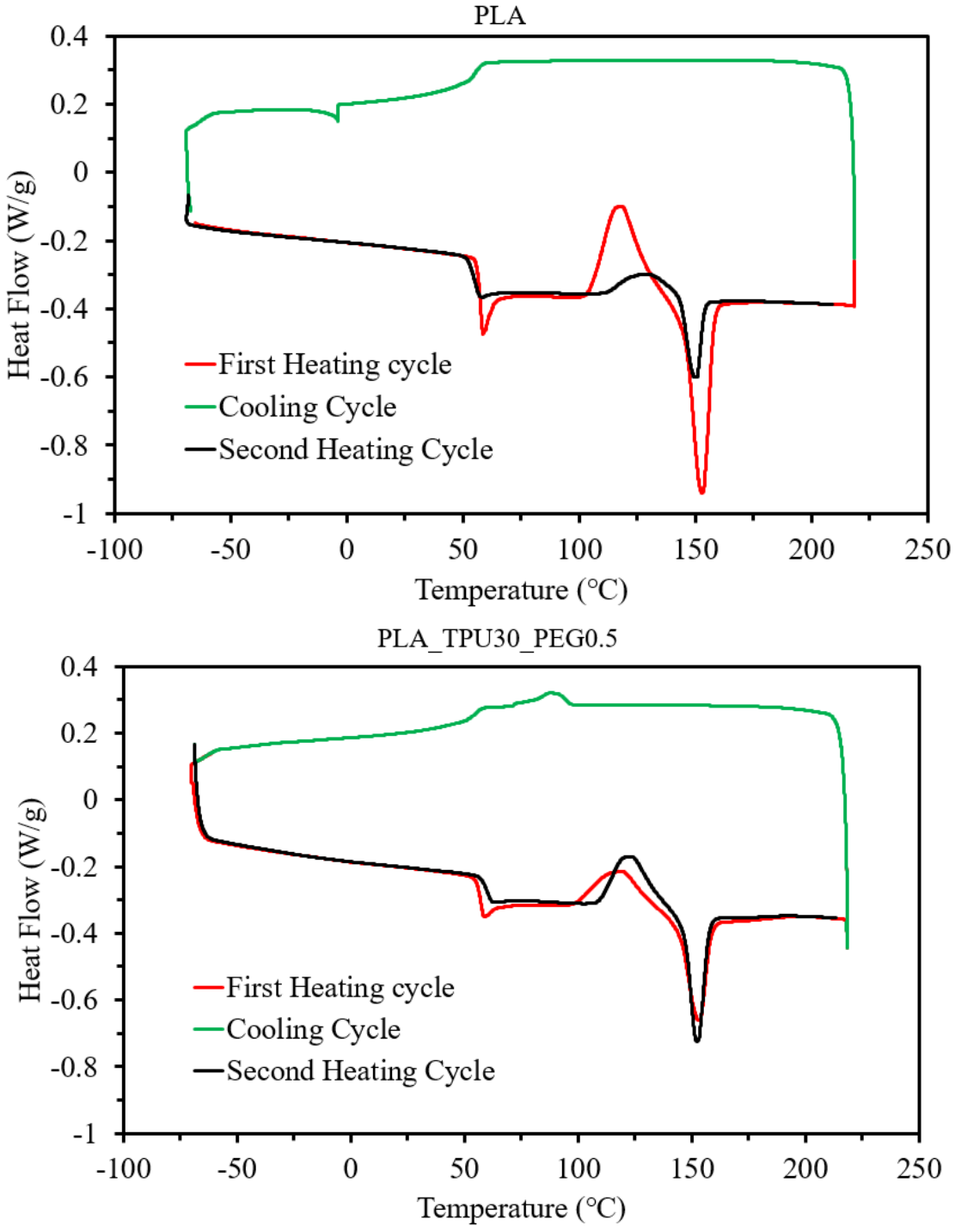

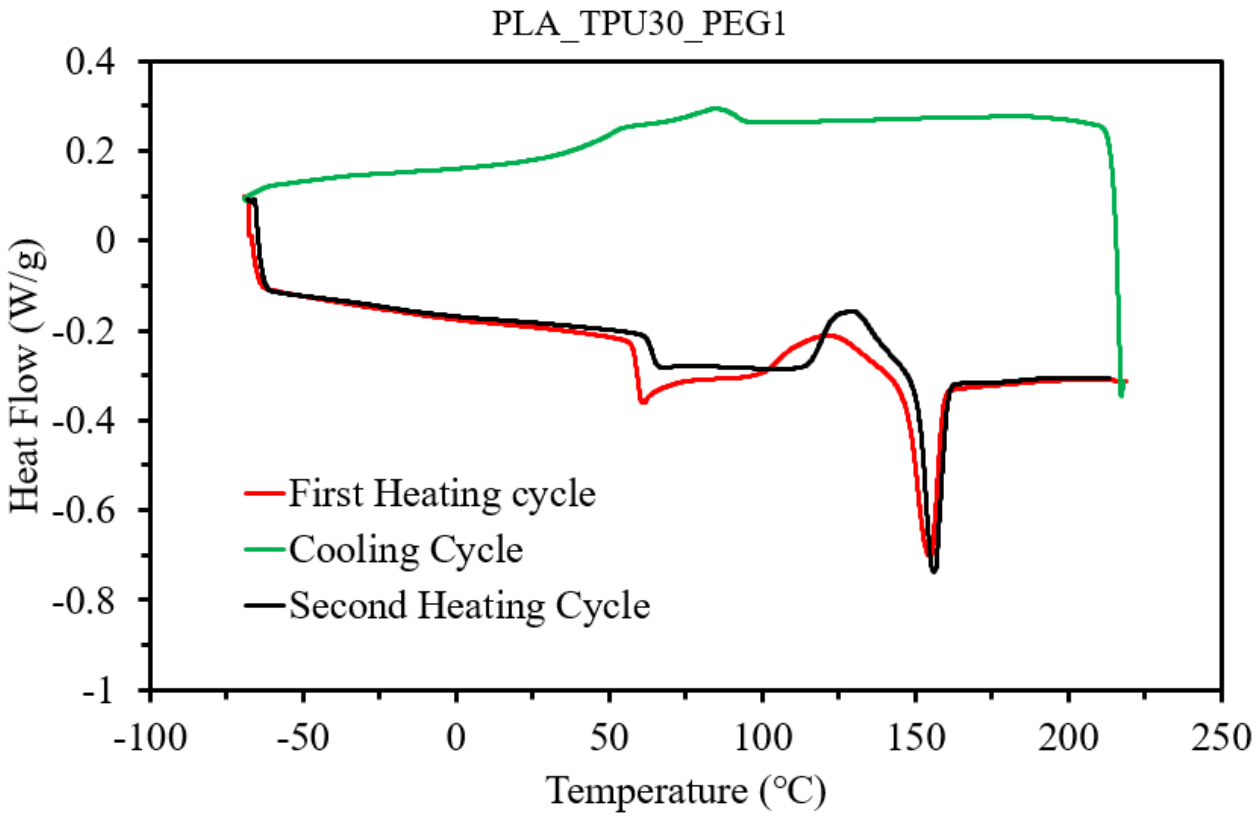
PLA_TPU30_PEG1
Heat Flow (W/g)
Temperature (°C)
First Heating cycle
Cooling Cycle
Second Heating Cycle
0.4
0.2
0
-0.2
-0.4
-0.6
-0.8
-1
-100
-50
0
50
100
150
200
250

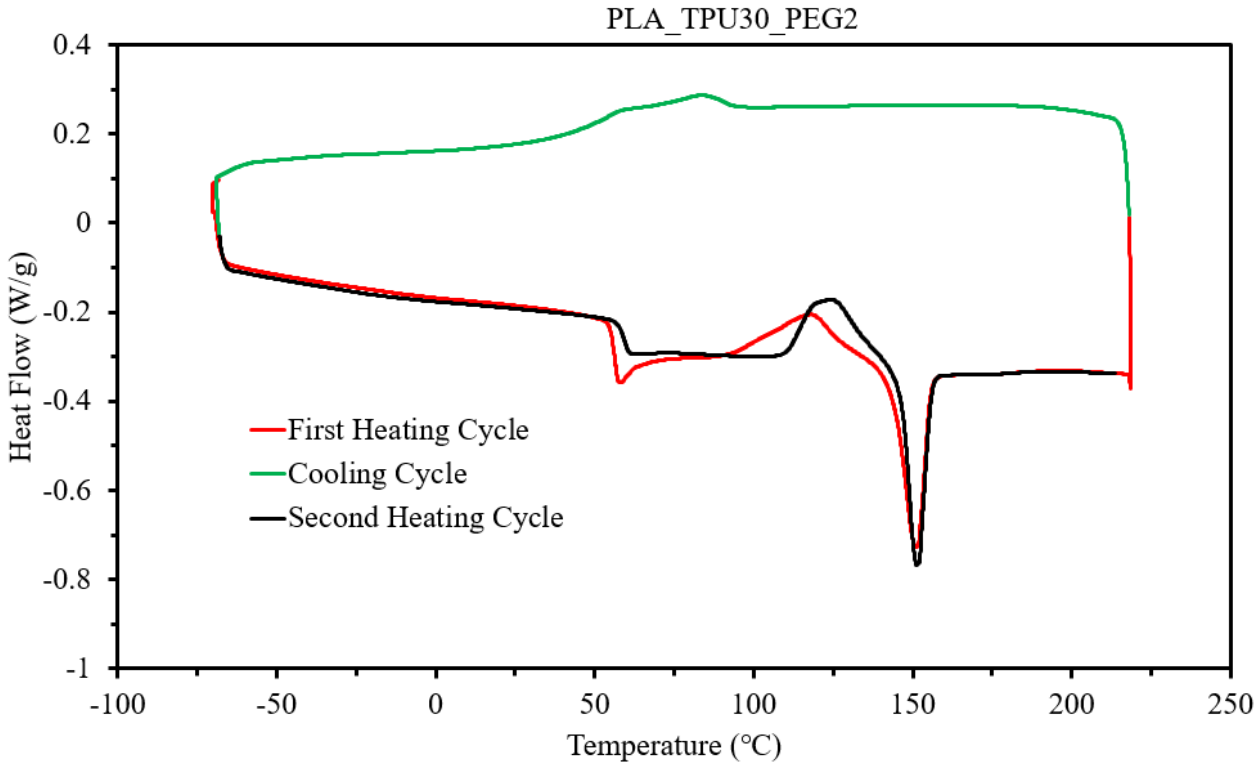
PLA_TPU30_PEG2
Heat Flow (W/g)
Temperature (°C)
First Heating Cycle
Cooling Cycle
Second Heating Cycle
0.4
0.2
0
-0.2
-0.4
-0.6
-0.8
-1
-100
-50
0
50
100
150
200
250

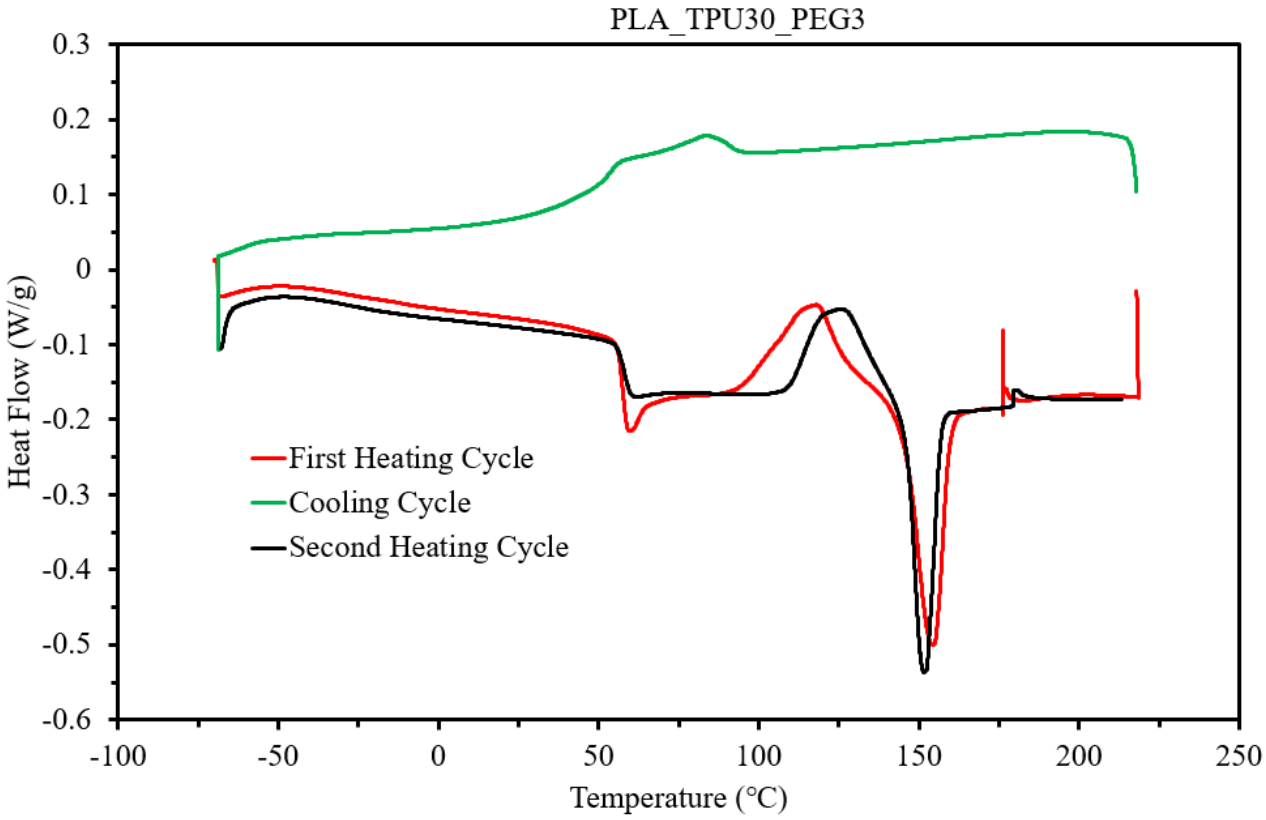
PLA_TPU30_PEG3
Heat Flow (W/g)
Temperature (°C)
First Heating Cycle
Cooling Cycle
Second Heating Cycle

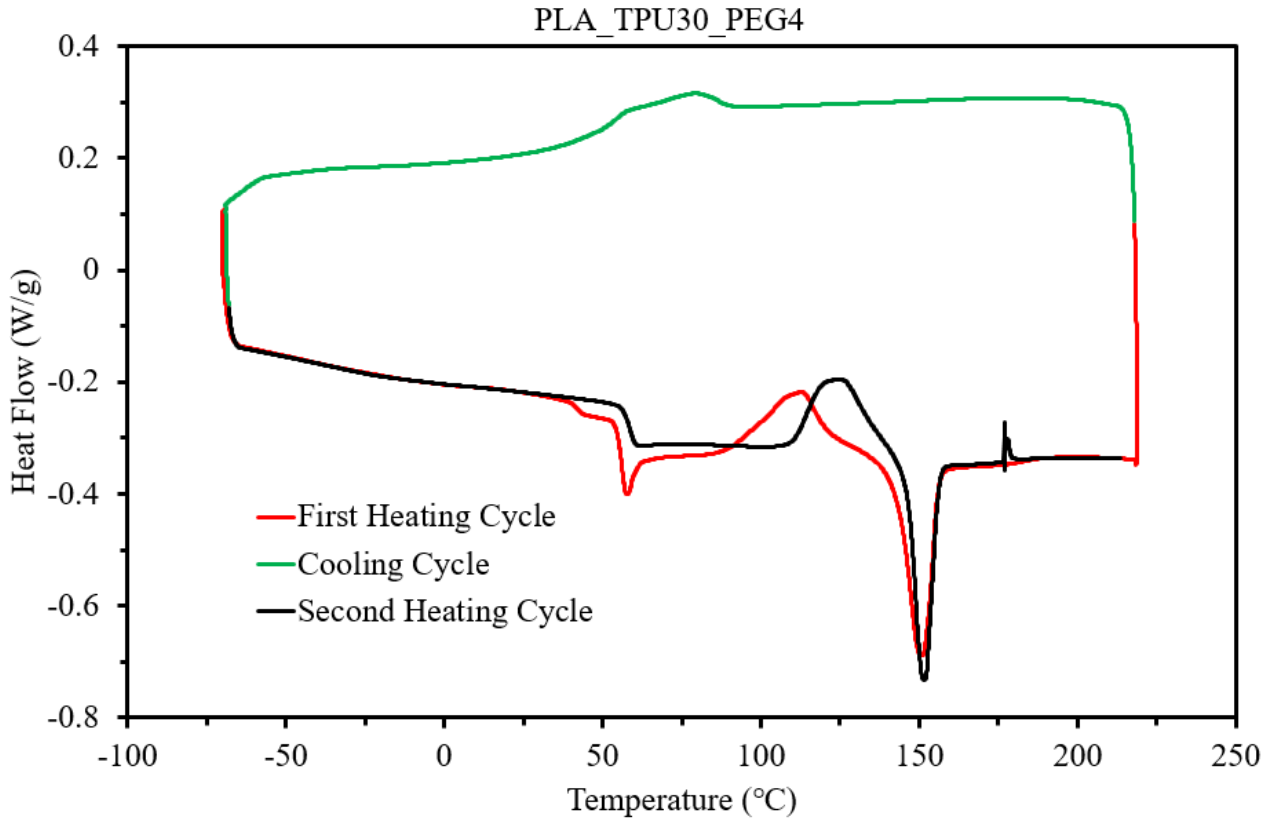
PLA_TPU30_PEG4
Heat Flow (W/g)
Temperature (°C)
First Heating Cycle
Cooling Cycle
Second Heating Cycle

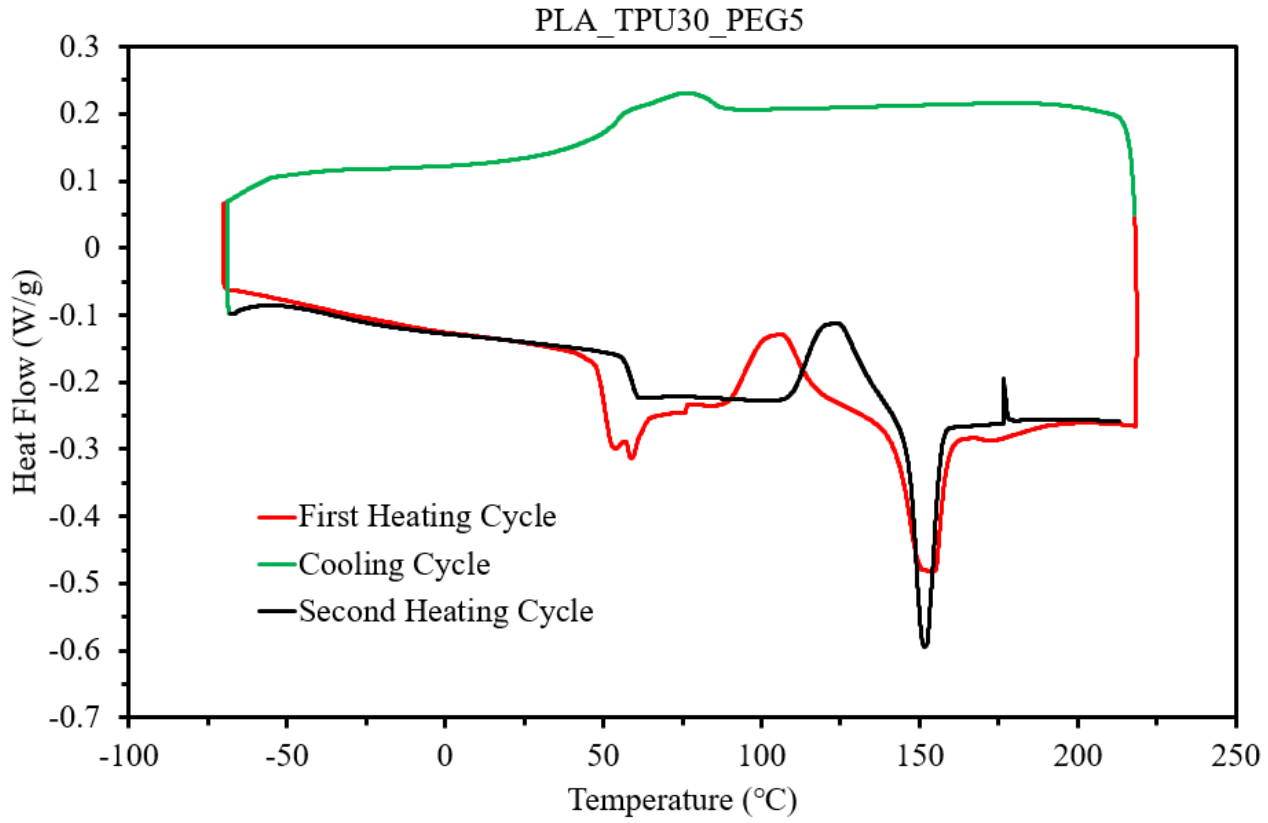
PLA_TPU30_PEG5
Heat Flow (W/g)
Temperature (°C)
First Heating Cycle
Cooling Cycle
Second Heating Cycle

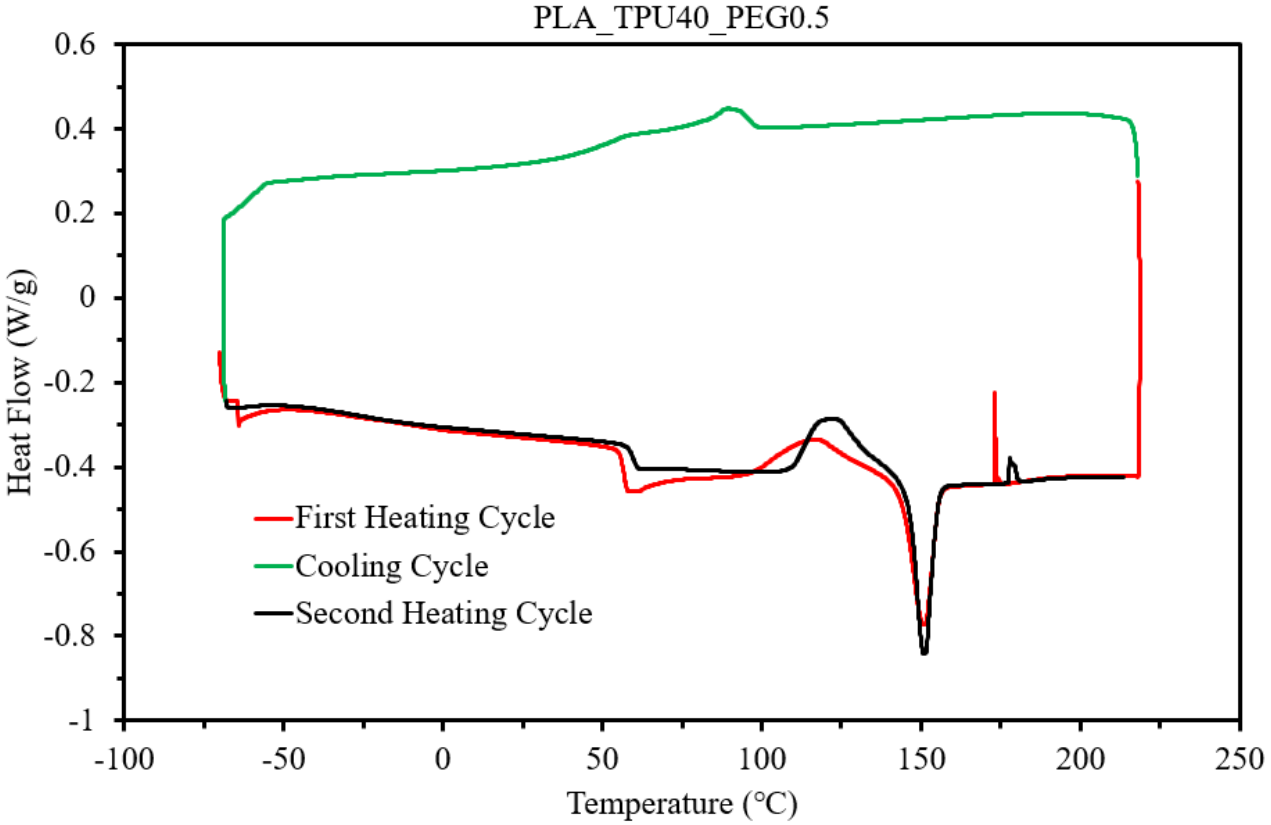
PLA_TPU40_PEG0.5
Heat Flow (W/g)
Temperature (°C)
First Heating Cycle
Cooling Cycle
Second Heating Cycle

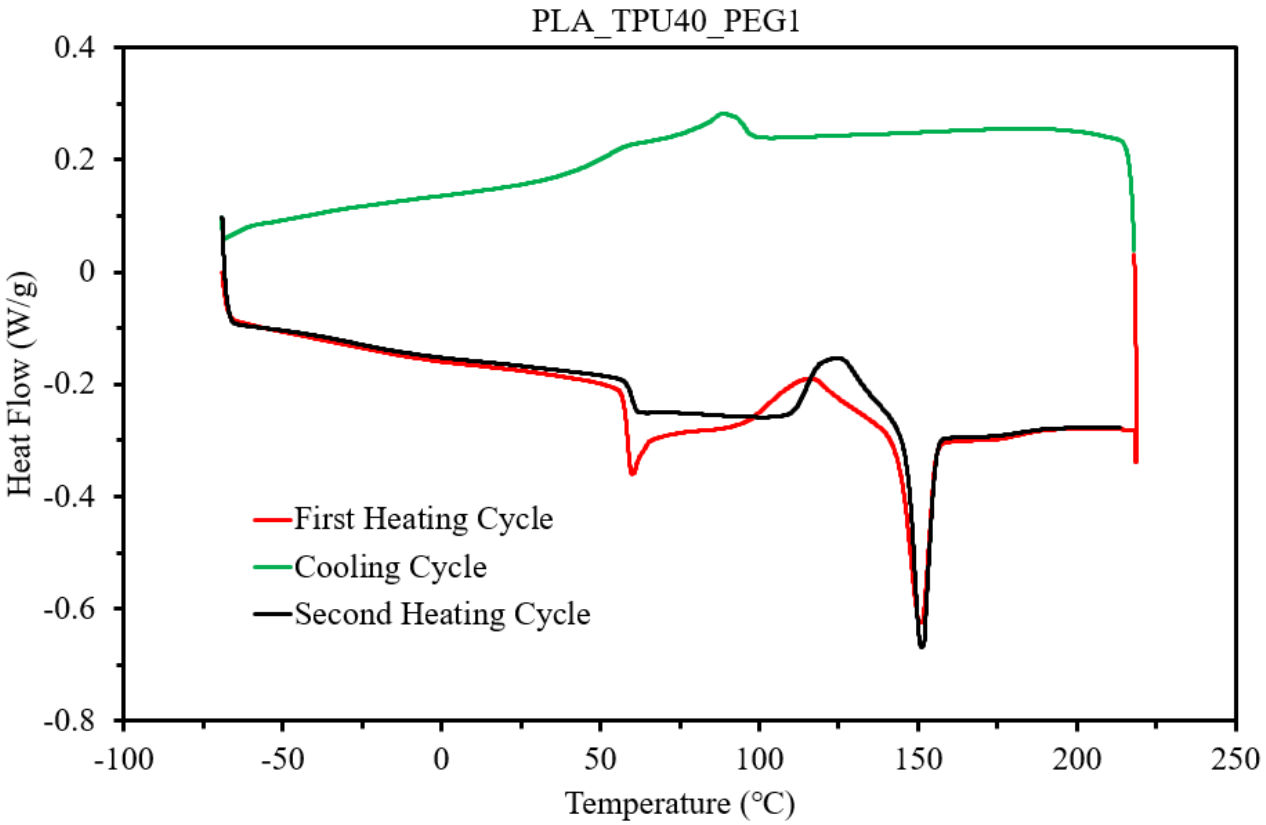
PLA_TPU40_PEG1
Heat Flow (W/g)
Temperature (°C)
First Heating Cycle
Cooling Cycle
Second Heating Cycle
0.4
0.2
0
-0.2
-0.4
-0.6
-0.8
-100
-50
0
50
100
150
200
250

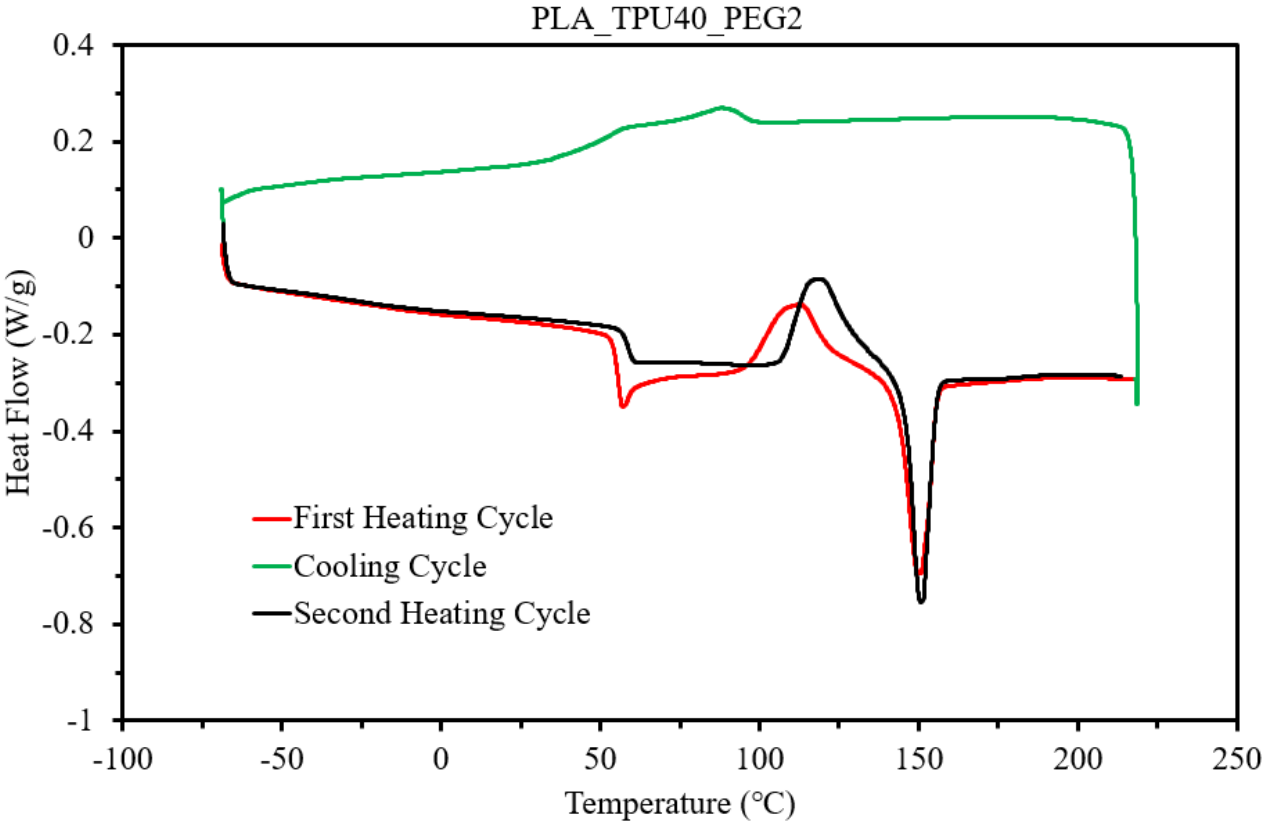
PLA_TPU40_PEG2
Heat Flow (W/g)
Temperature (°C)
First Heating Cycle
Cooling Cycle
Second Heating Cycle
0.4
0.2
0
-0.2
-0.4
-0.6
-0.8
-1
-100
-50
0
50
100
150
200
250

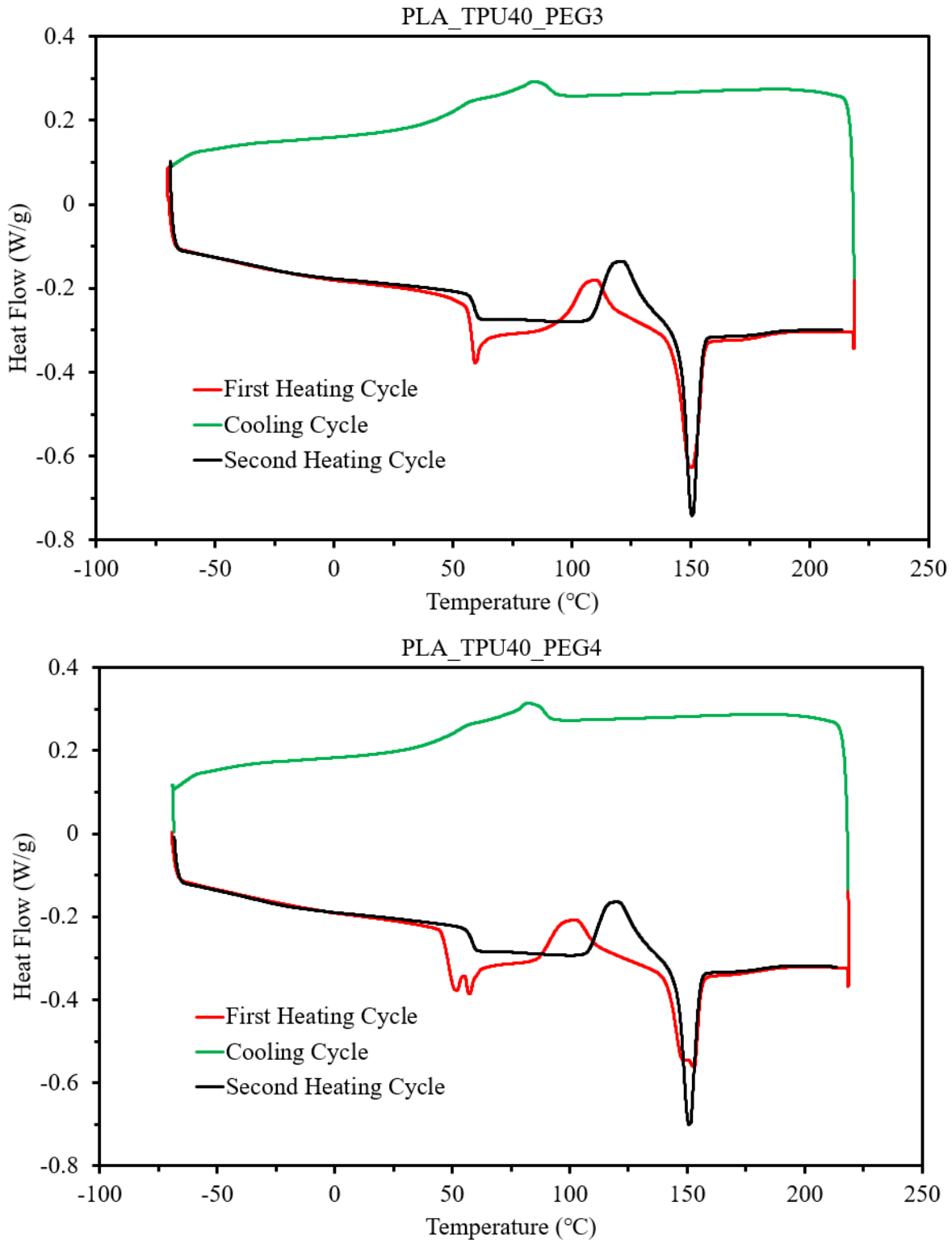

Figure C1. Heat/cool/heat cycle of PLA and the composite filaments manufactured by using twin-screw extruders.

Appendix D

Table D1. DSC results of the composite filaments obtained from the first heating cycle.

Samples	T_g (℃), PLA	T_{cc} (℃)	ΔH_{cc} (J/g)	T_m (℃)	ΔH_m (J/g)
PLA	57.47	117.55	26.51	152.86	25.50
PLA_TPU30_PEG0.5	57.43	119.09	12.99	152.29	14.68
PLA_TPU30_PEG1	56.23	118.58	14.88	151.27	15.62
PLA_TPU30_PEG2	56.18	117.89	10.09	151.28	16.68
PLA_TPU30_PEG3	55.94	116.07	13.12	151.64	15.12
PLA_TPU30_PEG4	56.25	112.81	15.24	151.22	15.29
PLA_TPU30_PEG5	58.29	105.99	10.72	151.64	14.08
PLA_TPU40_PEG0.5	56.90	116.47	9.07	150.75	14.60
PLA_TPU40_PEG1	58.92	116.30	13.50	150.69	13.72
PLA_TPU40_PEG2	55.75	112.85	17.22	150.12	18.85
PLA_TPU40_PEG3	58.05	109.74	11.58	149.89	15.53
PLA_TPU40_PEG4	56.25	102.48	14.65	152.69	13.31

Appendix E

Table E1. Summary of creep compliance and stress relaxation equations obtained for the composite filaments.

Materials	Equations
PLA2.85	$D(t) = 0.005702 + 0.0004325\left(1 - e^{-\frac{t}{9.81}}\right) + 0.0003421\left(1 - e^{-\frac{t}{69.24}}\right) + 0.0003531\left(1 - e^{-\frac{t}{908.20}}\right)$ $E(t) = 146.42 + 12.59e^{-0.1097t} + 8.47e^{-0.0152t} + 7.90e^{-0.00116t}$
PLA1.75	$D(t) = 0.006915 + 0.0001722\left(1 - e^{-\frac{t}{9.88}}\right) + 0.0001046\left(1 - e^{-\frac{t}{98.97}}\right) + 0.0003106\left(1 - e^{-\frac{t}{947.10}}\right)$ $E(t) = 144.61 + 3.53e^{-0.10372t} + 2.06e^{-0.01025t} + 5.73e^{-0.0011t}$
PLA	$D(t) = 0.007935 + 0.0001348\left(1 - e^{-\frac{t}{1.13}}\right) + 0.000456\left(1 - e^{-\frac{t}{17.30}}\right) + 0.001391\left(1 - e^{-\frac{t}{361.90}}\right)$ $E(t) = 100.84 + 2.12e^{-0.9t} + 6.71e^{-0.06109t} + 16.35e^{-0.0032t}$
PLA_TPU10	$D(t) = 0.004431 + 0.0001219\left(1 - e^{-\frac{t}{9.82}}\right) + 0.000139\left(1 - e^{-\frac{t}{96.80}}\right) + 0.0002082\left(1 - e^{-\frac{t}{966.70}}\right)$ $E(t) = 204.08 + 6.09e^{-0.10464t} + 6.53e^{-0.01064t} + 8.99e^{-0.00108t}$
PLA_TPU20	$D(t) = 0.007336 + 0.0001525\left(1 - e^{-\frac{t}{9.80}}\right) + 0.0002958\left(1 - e^{-\frac{t}{97.54}}\right) + 0.0002785\left(1 - e^{-\frac{t}{927.10}}\right)$ $E(t) = 124.03 + 2.80e^{-0.10418t} + 5.09e^{-0.01066t} + 4.39e^{-0.00112t}$
PLA_TPU30	$D(t) = 0.008524 + 0.0002643\left(1 - e^{-\frac{t}{9.74}}\right) + 0.0003433\left(1 - e^{-\frac{t}{91.61}}\right) + 0.0003748\left(1 - e^{-\frac{t}{924.10}}\right)$ $E(t) = 105.19 + 3.56e^{-0.10584t} + 4.28e^{-0.01134t} + 4.28e^{-0.001126t}$

PLA_TPU30_PEG3	$D(t) = 0.004045 + 0.0002893\left(1 - e^{-\frac{t}{9.92}}\right) + 0.000981\left(1 - e^{-\frac{t}{95.13}}\right) + 0.001429\left(1 - e^{-\frac{t}{866}}\right)$ $E(t) = 148.27 + 17.46e^{-0.108282t} + 43.98e^{-0.01295t} + 37.51e^{-0.001456t}$
PLA_TPU30_PEG4	$D(t) = 0.007012 + 0.0002471\left(1 - e^{-\frac{t}{9.83}}\right) + 0.0004526\left(1 - e^{-\frac{t}{96.39}}\right) + 0.0005584\left(1 - e^{-\frac{t}{875.70}}\right)$ $E(t) = 120.92 + 4.93e^{-0.105311t} + 8.15e^{-0.01102t} + 8.61e^{-0.001224t}$
PLA_TPU30_PEG5	$D(t) = 0.005759 + 0.0001806\left(1 - e^{-\frac{t}{9.54}}\right) + 0.0005228\left(1 - e^{-\frac{t}{92.54}}\right) + 0.0007747\left(1 - e^{-\frac{t}{849.10}}\right)$ $E(t) = 138.18 + 5.40e^{-0.10816t} + 13.88e^{-0.011768t} + 16.18e^{-0.001317t}$
PLA_TPU40	$D(t) = 0.00427 + 0.0001677\left(1 - e^{-\frac{t}{9.85}}\right) + 0.0003586\left(1 - e^{-\frac{t}{75.41}}\right) + 0.0006951\left(1 - e^{-\frac{t}{960.10}}\right)$ $E(t) = 182.10 + 9.09e^{-0.10553t} + 17.02e^{-0.01434t} + 25.98e^{-0.00119t}$
PLA_TPU40_PEG3	$D(t) = 0.004567 + 0.0001241\left(1 - e^{-\frac{t}{4.02}}\right) + 0.0003354\left(1 - e^{-\frac{t}{425.30}}\right) + 0.0002672\left(1 - e^{-\frac{t}{1983}}\right)$ $E(t) = 188.90 + 5.80e^{-0.2556t} + 14.60e^{-0.002522t} + 9.66e^{-0.000531t}$

Appendix F

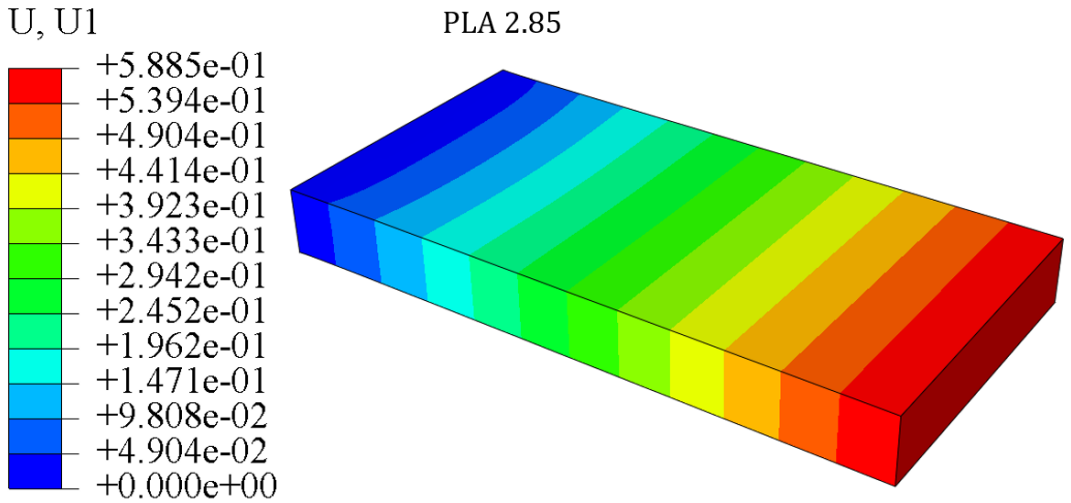
U, U1
+5.885e-01
+5.394e-01
+4.904e-01
+4.414e-01
+3.923e-01
+3.433e-01
+2.942e-01
+2.452e-01
+1.962e-01
+1.471e-01
+9.808e-02
+4.904e-02
+0.000e+00
PLA 2.85

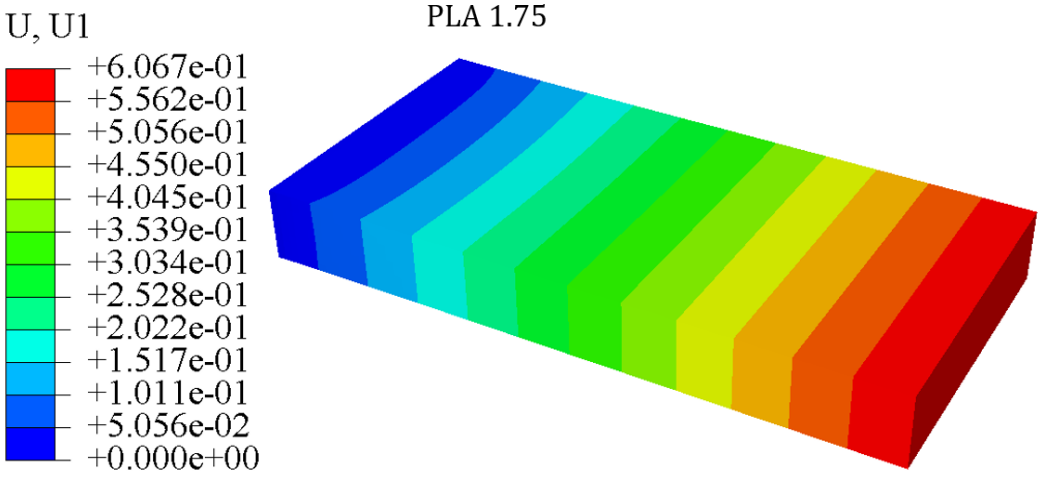
U, U1
+6.067e-01
+5.562e-01
+5.056e-01
+4.550e-01
+4.045e-01
+3.539e-01
+3.034e-01
+2.528e-01
+2.022e-01
+1.517e-01
+1.011e-01
+5.056e-02
+0.000e+00
PLA 1.75

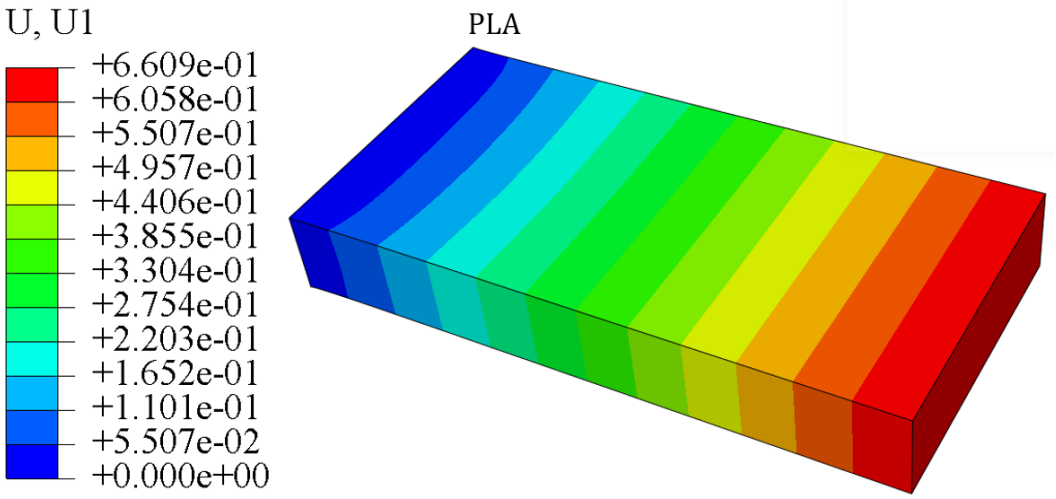
U, U1
+6.609e-01
+6.058e-01
+5.507e-01
+4.957e-01
+4.406e-01
+3.855e-01
+3.304e-01
+2.754e-01
+2.203e-01
+1.652e-01
+1.101e-01
+5.507e-02
+0.000e+00
PLA

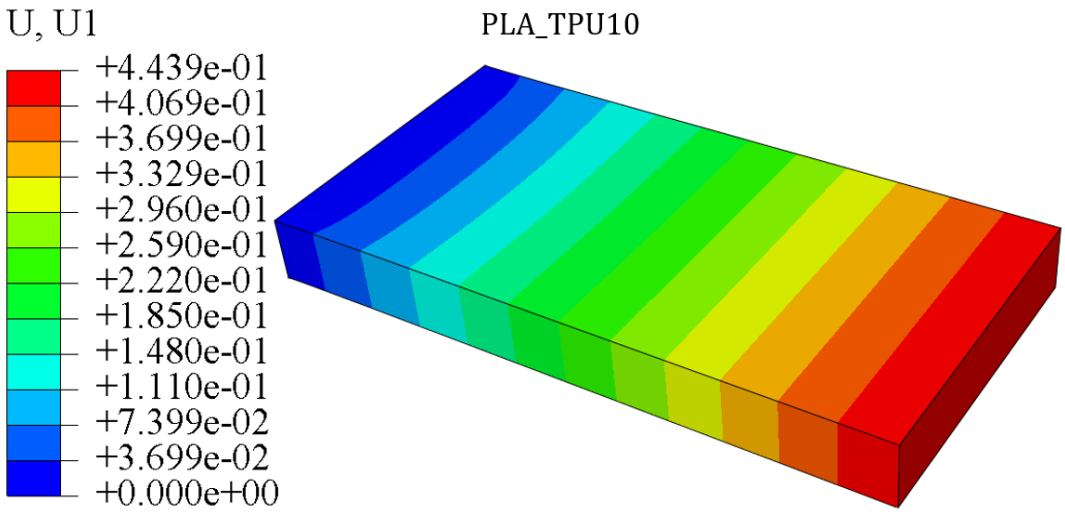
U, U1
+4.439e-01
+4.069e-01
+3.699e-01
+3.329e-01
+2.960e-01
+2.590e-01
+2.220e-01
+1.850e-01
+1.480e-01
+1.110e-01
+7.399e-02
+3.699e-02
+0.000e+00
PLA_TPU10

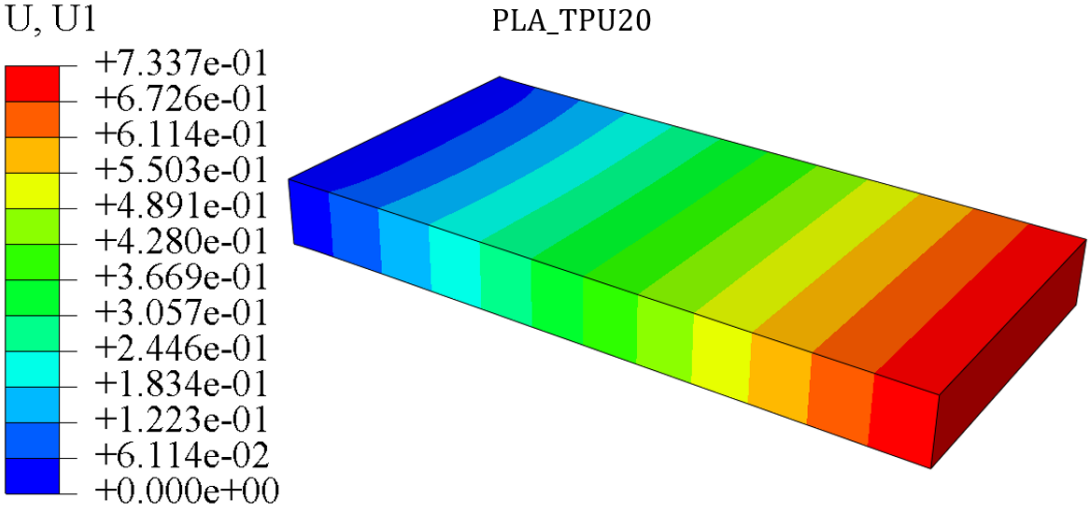
U, U1
+7.337e-01
+6.726e-01
+6.114e-01
+5.503e-01
+4.891e-01
+4.280e-01
+3.669e-01
+3.057e-01
+2.446e-01
+1.834e-01
+1.223e-01
+6.114e-02
+0.000e+00
PLA_TPU20

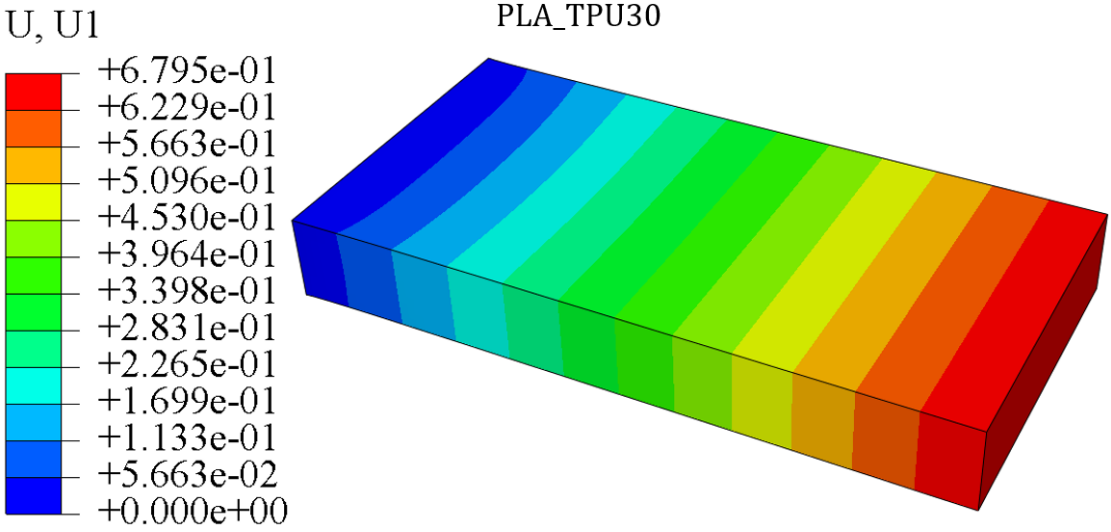
U, U1
+6.795e-01
+6.229e-01
+5.663e-01
+5.096e-01
+4.530e-01
+3.964e-01
+3.398e-01
+2.831e-01
+2.265e-01
+1.699e-01
+1.133e-01
+5.663e-02
+0.000e+00
PLA_TPU30

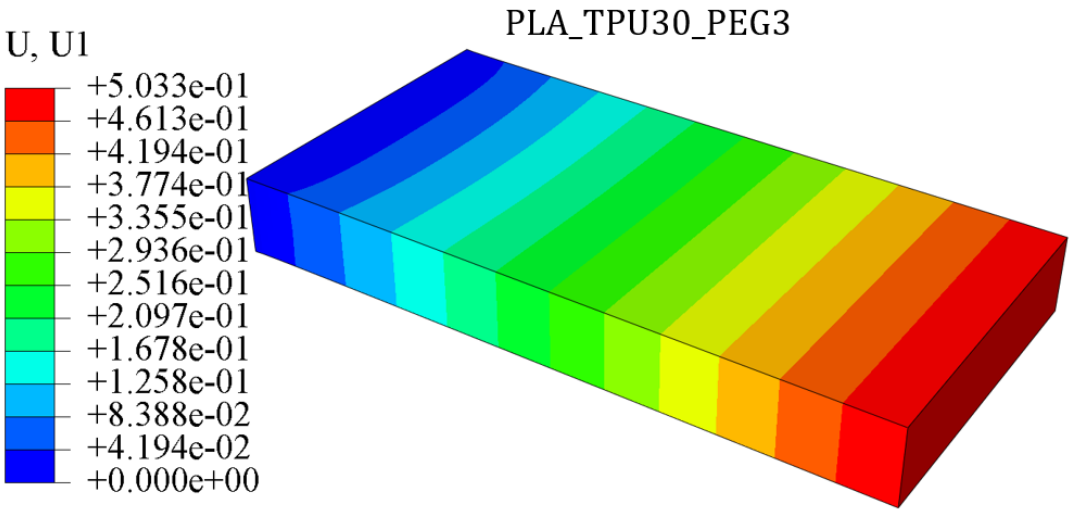
PLA_TPU30_PEG3
U, U1
+5.033e-01
+4.613e-01
+4.194e-01
+3.774e-01
+3.355e-01
+2.936e-01
+2.516e-01
+2.097e-01
+1.678e-01
+1.258e-01
+8.388e-02
+4.194e-02
+0.000e+00

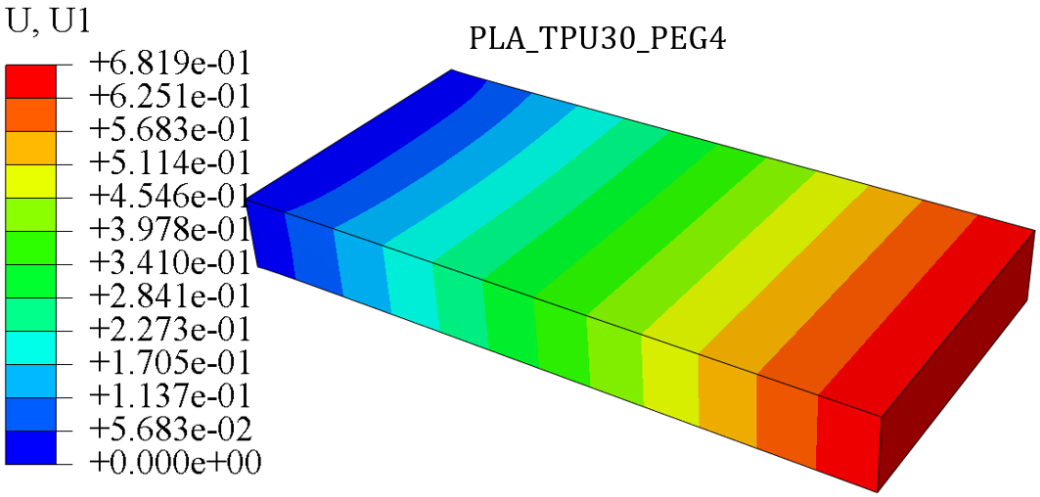
PLA_TPU30_PEG4
U, U1
+6.819e-01
+6.251e-01
+5.683e-01
+5.114e-01
+4.546e-01
+3.978e-01
+3.410e-01
+2.841e-01
+2.273e-01
+1.705e-01
+1.137e-01
+5.683e-02
+0.000e+00

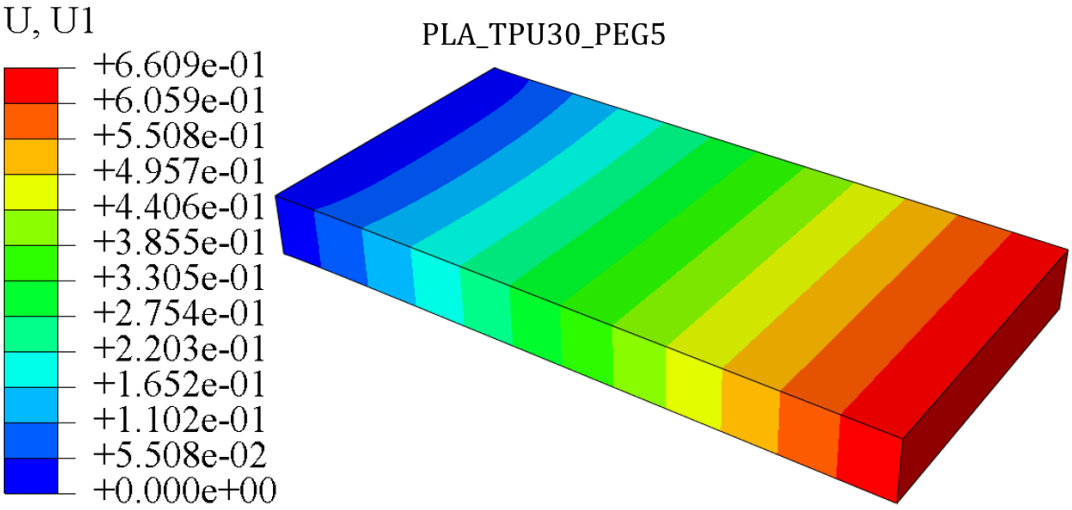
PLA_TPU30_PEG5
U, U1
+6.609e-01
+6.059e-01
+5.508e-01
+4.957e-01
+4.406e-01
+3.855e-01
+3.305e-01
+2.754e-01
+2.203e-01
+1.652e-01
+1.102e-01
+5.508e-02
+0.000e+00

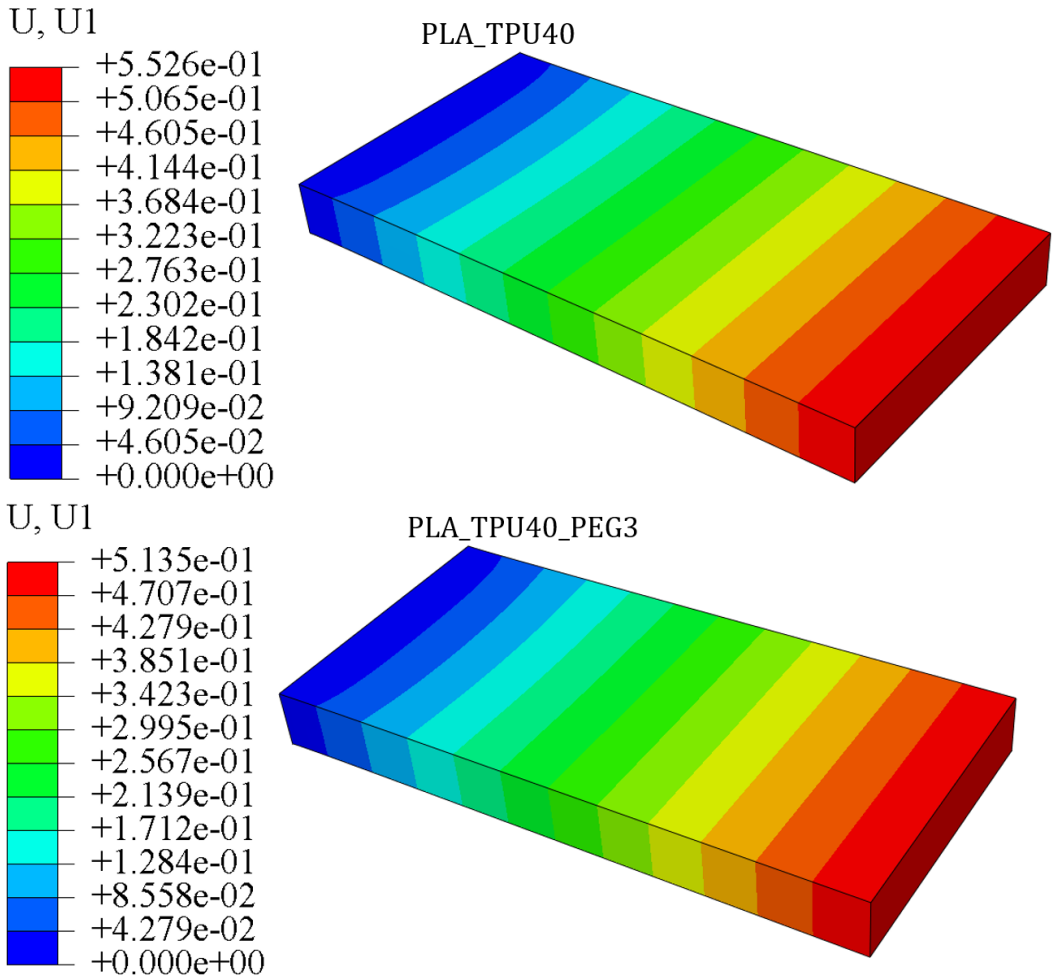

Figure F1: Contours showing creep displacements obtained from computational analysis using ABAQUS.